Experimental Investigation of the Effects of Aerodynamic and Structural Parameters on Transonic Buffeting

M.Sc. Tim Christopher Korthäuer

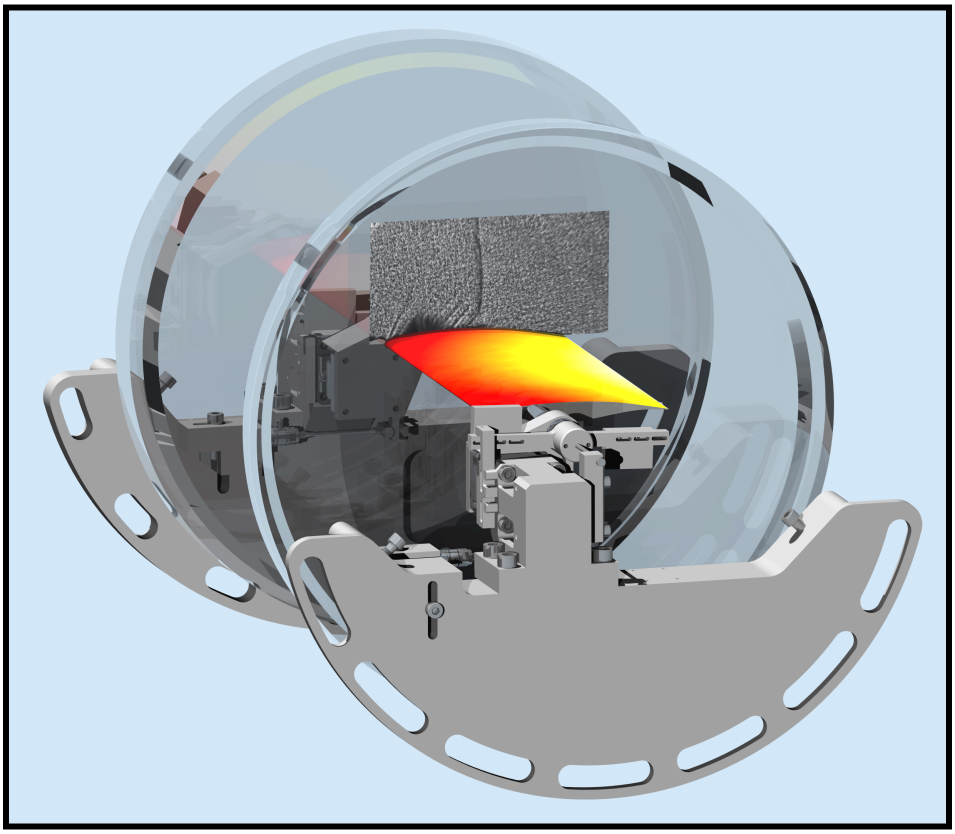

Vollständiger Abdruck der von der
Fakultät für Luft- und Raumfahrttechnik
der Universität der Bundeswehr München
zur Erlangung des akademischen Grades eines

Doktor-Ingenieurs (Dr.-Ing.)

angenommenen Dissertation.

Gutachter:
1. Univ.-Prof. Dr. Christian J. Kähler
2. Apl. Prof. Dr. Christian Breitsamter

Diese Dissertation wurde am 06.09.2023 bei der Universität der Bundeswehr München eingereicht und durch die Fakultät für Luft- und Raumfahrttechnik am 14.02.2024 angenommen. Die mündliche Prüfung fand am 06.03.2024 statt.

Acknowledgement

I would like to take the opportunity to thank the people who made this dissertation possible and provided me with support in the last few years.

First of all, I would like to thank Prof. Christian Kähler, who gave me the chance to join his team at the Institute of Fluid Mechanics and Aerodynamics and to work on the HOMER project. Furthermore, I am grateful for his trustful and ever-optimistic supervision, support, and creative input.

Secondly, I want to thank Prof. Christian Breitsamter and Prof. Lars Zigan for taking the time to evaluate my work and leading the examination process as members of the committee.

I would like to thank Sven Scharnowski and Alessandro Accorinti for the great teamwork in the wind tunnel and the project. I very much enjoyed our time together. Sven was a great mentor and supervisor, always ready to provide support in different matters ranging from the dissertation to technical issues and questions. Alessandro Accorinti was the best project and office buddy and the most reliable friend one could wish for in a now-and-again demanding time. Special thanks for all the interesting discussions and exchanges and the calming, ever-supportive way in all situations.

For the enjoyable time between the office and the lab, I would like to thank all my colleagues. I will always remember the joyful times and particularly fruitful mensa discussions. Thanks for all the fun hours at the football pitch, swimming pool, or volleyball court. Furthermore, it was great to not have to search for more than one minute to find a helping hand at the institute.

Last but not least, I am especially thankful to my family and friends for always backing me up and providing moral support and help, whenever needed. It is great to know, there is always someone there to rely on.

Abstract

Transonic shock buffet plays a substantial role in the limitation of the flight envelope of commercial aircraft. This flow unsteadiness appears in compressible flows around a wing at sufficiently high angles of attack or Mach number. The phenomenon is associated with a mostly periodic shock-wave/boundary-layer interaction.
If the structural natural frequencies of the wing are similar to this “natural” buffet frequency, a fluid-structure interaction may be induced. The resulting coupled oscillation of compression shock, fluid, and structure, called transonic buffeting, can lead to high-amplitude wing oscillations and structural failure. Numerical research has shown that structural participation can alter the onset point of shock oscillations. Furthermore, the typology of the fluid-structure interaction was found to present different natures: the classical structural excitation by the aerodynamic phenomenon of buffet, the frequency lock-in where the coupled oscillation appears at the natural pitch frequency, and the intermediate transition, so-called “veering” region.

This doctoral thesis presents a systematic experimental investigation of transonic buffeting in a cumulative form based on three journal publications with the aim of providing an experimental validation of the numerical observations. For this purpose, an experimental setup is designed, manufactured, and integrated in the Trisonic Wind Tunnel Munich. The design consists of a lightweight, two-dimensional, supercritical wing (OAT15A) with an optional pitching degree of freedom and variable torsional spring stiffness and mass distribution. Two optical measurement techniques are deployed for the non-intrusive observation of the flow-induced density gradient field (background-oriented schlieren) and the structural displacements of the wing (digital image correlation).
The first configuration of the fixed, rigid wing with inhibited pitching flexibility sets the basis of this work by providing an overview of the natural buffet characteristics in the given facility. The flow development is characterized for various angles of attack and Mach numbers with particular attention to the steady shock motion (regular or inverse), the onset points and the dominant shock oscillation frequencies.

Two subsequent detailed measurement campaigns with released pitching flexibility were conducted, whereby the distinct fluid-structural interaction of transonic buffeting with limit-cycle oscillations of the wing was obtained. The first campaign focused on the effect of structural flexibility with the aim of providing experimental validation for an alteration of the buffet(ing) onset characteristics. By comparison with the natural buffet case, a shift and a change of slope of the onset boundary were detected, which provided proof for the numerical works available in the literature. In the second campaign, the natural pitch frequency (close to the natural buffet frequency) and the mass ratio, as well as the angle of attack were varied at a constant Mach number. The aim was the investigation of the different patterns of transonic buffeting and the respective dominant modes. The experimental results confirm the existence of the regions of fluid-dominated, veering, and structurally-dominated interaction. The latter, transonic frequency lock-in, is detected for natural pitch frequencies above the natural buffet frequency and presents high but limited pitch amplitudes. Furthermore, the effects of mass ratio and natural pitch frequency on the corresponding shock and pitch amplitudes and respective region boundaries are presented and discussed. A substantial effect of the mass ratio on the onset boundary of buffeting and, unexpectedly, the resulting pitch amplitude for frequency lock-in were discovered.

The experimental observations highlight the importance of the application of experiments or simulations of fluid-structure coupling during the aircraft development to consider the limiting effects of transonic buffet(ing).

Kurzzusammenfassung

Transonic Shock Buffet spielt eine wesentliche Rolle bei der Begrenzung des Flugbereichs von Verkehrsflugzeugen. Es tritt in kompressiblen Strömungen um einen Flügel bei Erhöhung des Anstellwinkels oder der Machzahl auf. Charakteristisches Merkmal von Buffet ist meist eine periodische Stoß-Grenzschicht-Interaktion.
Wenn die strukturellen Eigenfrequenzen des Flügels in der Nähe dieser „natürlichen“ Buffetfrequenz liegen, kann es zu einer Strömungs-Struktur-Wechselwirkung kommen. Die sich daraus ergebende gekoppelte Schwingung von Verdichtungsstoß, Strömungsablösung und Struktur – genannt Transonic Buffeting – kann zu Flügelschwingungen hoher Amplitude und Strukturversagen führen. Numerische Untersuchungen haben gezeigt, dass eine Beteiligung der Struktur den Auftrittspunkt der Stoßschwingungen verändern kann. Darüber hinaus wurde festgestellt, dass sich die Strömungs-Struktur-Wechselwirkung in verschiedenen Formen ausprägt: als klassische strukturelle Anregung durch die Buffet-Stoßbewegung (Fluid-Mode), als von der Strukturfrequenz (Struktur-Mode) dominierte Interaktion (“Frequency Lock-in”) oder als die dazwischenliegende Übergangsform (“Modal Veering”).

Diese kumulative Dissertation basiert auf drei Artikeln, die in Fachzeitschriften erschienen sind und stellt eine systematische experimentelle Untersuchung des Transonic Buffeting vor. Zu diesem Zweck wurde ein Versuchsaufbau für den Trisonischen Windkanal München entworfen, gefertigt und aufgebaut. Der Aufbau bestand aus einem leichten, zweidimensionalen, superkritischen Flügel (OAT15A) mit optionalem Nick-Freiheitsgrad und variabler Torsionssteifigkeit und Massenverteilung. Zwei optische Messtechniken wurden zur nichtinvasiven Beobachtung des strömungsinduzierten Dichtegradientenfeldes (background-oriented Schlieren) und der strukturellen Oberflächenverschiebungen des Flügels (digital image correlation) eingesetzt.
Die erste Konfiguration mit starrem Flügel und unterbundenem Nickfreiheitsgrad bildet die Grundlage dieser Arbeit, indem sie einen Überblick über das natürliche Buffetverhalten in der gegebenen Versuchsanlage schafft. Die Strömungsentwicklung wurde für verschiedene Anstellwinkel und Machzahlen charakterisiert. Besonderes Augenmerk lag auf der zeitlich gemittelten Stoßbewegung (regulär oder invers), dem Auftrittspunkt des Phänomens und den dominanten Stoßschwingungsfrequenzen.
Die zwei anschließenden Messkampagnen, durchgeführt am Flügel mit elastisch gelagertem Nickfreiheitsgrad, zeigen die ausgeprägte Fluid-Struktur-Interaktion des Transonic Buffeting mit Grenzzyklusschwingungen des Flügels.
Das Ziel der ersten Kampagne lag in der Überprüfung der Abhängigkeit der Auftrittsgrenze des Buffet(ing) von der strukturellen Flexibilität. Der Vergleich mit dem natürlichen Buffetfall ergab eine Steigungsänderung und Verschiebung der Auftrittsgrenze, was einen experimentellen Beweis für die in der Literatur verfügbaren numerischen Arbeiten liefert.
In der zweiten Kampagne wurden die natürliche Nickfrequenz (nahe der natürlichen

Buffetfrequenz) und das Massenverhältnis sowie der Anstellwinkel bei konstanter Machzahl variiert. Das Ziel hierbei lag hierbei in der Charakterisierung der auftretenden Formen des Transonic Buffeting und den jeweils dominanten Moden. Die experimentellen Ergebnisse bestätigen die Existenz von Regionen mit fluid- und strukturdominierter Wechselwirkung sowie dem dazwischenliegenden Übergangsbereich. Die strukturdominierte Interaktion (Freqeuncy Lock-in) trat bei Nickeigenfrequenzen oberhalb der natürlichen Buffetfrequenz auf und wies hohe, aber begrenzte Nickamplituden auf. Darüber hinaus wurden zur phänomenologischen Charakterisierung die Auswirkungen des Massenverhältnisses und der Nickeigenfrequenz auf die entsprechenden Stoß- und Nickamplituden sowie die jeweiligen Grenzen bestimmt und diskutiert. Dabei wurde ein erheblicher Einfluss des Massenverhältnisses auf die Auftrittsgrenze des Buffetings und – unerwarteterweise – auf die daraus resultierende Nickamplitude bei Frequency Lock-in festgestellt.

Die experimentellen Beobachtungen machen deutlich, wie wichtig der Einsatz von Experimenten oder Simulationen zur Strömungs-Struktur-Kopplung im Rahmen der Flugzeugentwicklung ist, um die limitierenden Auswirkungen von Transonic Buffet(ing) zu berücksichtigen.

Contents

List of Figures

Nomenclature

Abbreviations

AoA	Angle of attack
BOS	Background oriented schlieren
CAD	Computational fluid dynamics
CFD	Computer-aided design
CFRP	Carbon-fiber reinforced polymer
COS	Coordinate system
CPSD	Cross power spectral density
CSD	Computational structural dynamics
DLR	German Aerospace Center
DoF	Degrees of freedom
EASA	Euopean Union Aerospace Safety Agency
FLI	Frequency lock-in
FM	Fluid mode
FSI	Fluid-structure interaction
LCO	Limit-cycle oscillations
NACA0012	Symmetrical airfoil profile designed by National Advisory Committee for Aeronautics
OAT15A	Supercritical airfoil profile degined by ONERA
PIV	Particle image velocimetry
PMMA	Poly-methyl-methacrylate
PSD	Power spectral density
PSP	Pressure-sensitive paint
RANS	Reynolds-averaged Navier-Stokes
ROM	Reduced-order modeling
SDoF	Single degree of freedom
SM	Structural mode
SWBLI	Shock-wave-boundary-layer interactions
TWM	Trisonic Wind Tunnel Munich
VWS	Vertical wall suction

Symbols

α	Angle of attack, °
Δ	Image displacement, pixels
γ	Specific heat ratio
μ	Mass ratio
ρ	Density, kg/m^3
ε	Deflection angle

c	Chord length, m
D	Damping coefficient
d	Thickness, m
F	Focal length
f	Frequency, Hz
Fi	Flutter index
h	Vertical location of elastic/rotational axis, m
I	Inertia around rotational axis, kgm^2
K	Stiffness factor
k	Reduced frequency, defined by $\pi fc/U_\infty$
k_{GD}	Gladstone-Dale coefficient
k_{FC}	Full-chord based reduced frequency, defined by $2\pi fc/U_\infty$
L	Aerodynamic lift, N
M	Mach number
m	Total mass of all moving parts, kg
M^*	Critical Mach number
M_{ae}	Aerodynamic moment, Nm
p	Pressure, Pa
P_{xy}	Cross power spectral density of signals x and y
R_{xy}	Cross-correlation function of signals x and y
Re	Reynolds number
S	Structural coupling factor, K
s	Span, m
St	Strouhal number
T	Temperature, K
t	Time, s
u	Stream-wise velocity, m/s
x	Stream-wise coordinate, m
y	Span-wise coordinate, m
Y_{A}	Distance density gradient - lens, m
Y_{D}	Distance background pattern - density gradient, m
Y_{i}	Distance lens - image plane, m
z	Vertical coordinate, m

Subscripts

0	Stagnation/total conditions
1	In front of the shock
2	Behind the shock
∞	Inflow conditions
θ	Pitch angular direction
b	Buffet
h	Heave
s	Shock

1

Introduction

1.1. Motivation

The research and development of modern commercial aircraft are driven by the pursuit of higher safety and optimized economic and ecological efficiency. Over the last decades, those requirements have led to a domination of turbo jet-propelled aircraft (“Airliners”) in the sector of mid and long-range flight. They operate at high flight speeds (high subsonic to transonic Mach numbers) and high altitudes with reduced drag and consequently provide the currently best trade-off between fuel consumption and operative costs.

Fig. 1.1 presents a schematic overview of the flight envelopes of different types of aircraft and the corresponding limiting factors. Regarding the cost-efficiency of airliners, a further increase in cruise speed is hindered by transonic buffet as indicated by the boundary of the green flight envelope (Badcock et al., 2011; Giannelis et al., 2017; Gao and Zhang, 2020). This aerodynamic phenomenon appears when an airplane operates in the vicinity of its critical Mach number. It is characterized by unsteady flow, which induces strong load fluctuations on the wing structure. The resulting adverse effects range from reduced aerodynamic efficiency and passenger discomfort right up to structural fatigue or failure. Both the latter pose a significant danger to aircraft and passenger safety. Despite recent developments that provide promising approaches to inhibit or delay the phenomenon (Nitzsche et al., 2022; D’Aguanno, 2023), a universal physical explanation of the buffet mechanism has not yet been found (Giannelis et al., 2017). Consequently, transonic buffet remains a critical boundary for the safe flight operation defined by aviation safety agencies like the Euopean Union Aerospace Safety Agency (EASA, 2023).

Besides the increase of flight speed, another driving factor in civil aircraft development is the enhancement of fuel efficiency - on both the propulsion as well as the structural systems. Along with the intensified development of adaptive wing structures, the techniques of additive-layer manufacturing or (tailored) composite materials have become particularly important. Being used more frequently in series productions of major aircraft manufacturers, they lead to reduced structural mass and less fuel consumption. As a consequence, structural characteristics are altered. Regarding the wings, this change is accompanied by a variation in the boundary of the so-called classical

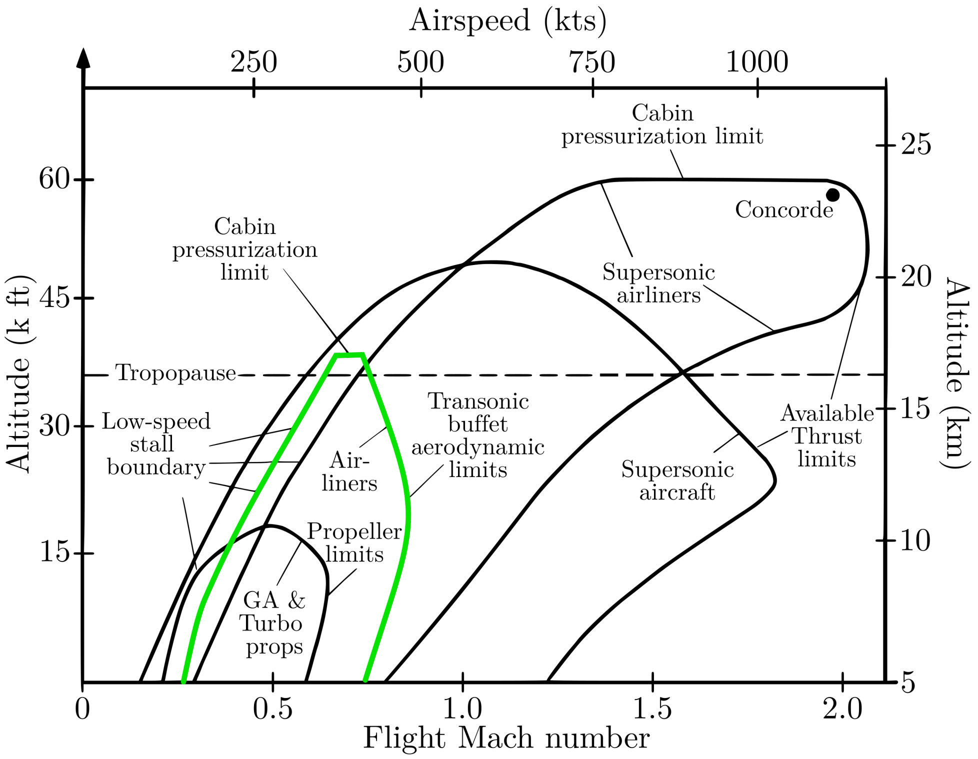

Figure 1.1: Schematic overview of various flight envelopes. Adapted from Leishman, 2022.

flutter, the avoidance of which is another crucial design requirement (EASA, 2023). Furthermore, the structural alteration may facilitate an interaction between the wing and the unsteady flow of transonic buffet and lead to strong dynamic structural excitation called transonic buffeting. This phenomenon of fluid-structural interaction is the object of this doctoral thesis.

As recent numerical works have proved, this interplay potentially shifts the buffet onset boundary, which is classically treated as an aerodynamic problem only (Nitzsche et al., 2019; Gao et al., 2018). Based on these findings, different works have recommended an adaptation of the classical design process of aircraft. The coupled fluid-structural analysis in an early stage is proposed, rather than the separate investigation of aerodynamic (transonic buffet) and structural limitations (classical flutter) and a conclusive, validating flight test. By this, awareness of detrimental interacting effects is established and design adaptations are still easily viable (Nitzsche et al., 2022; Gao and Zhang, 2020).
So far, the underlying research results are based on numerical computations only, which is why this work provides the first systematic experimental investigation for a supplementary and validating insight into the phenomenon of transonic buffeting.

1.2. Structure of this Thesis

This cumulative doctoral thesis is based on three scientific publications regarding the phenomena of transonic buffet and buffeting. As the works are focused on the experimental results, the additional chapters of this thesis provide supplementary and necessary information about the theoretical background and the methodology and put the publications in context.

In Chapter 2, the necessary physical and theoretical basics regarding transonic buffet and flutter are presented. Following this, the latest knowledge of transonic buffeting is summarized, in particular concerning the effects of parametric variations.

Chapter 3 gives a thorough overview of the methodology of this work. It presents the experimental facility and the designed setup and mechanism. Particular focus is set on the application of the optical measurement techniques that were used to determine both fluid and structural characteristics.

The experimental results are given in Chapter 4 in the form of scientific publications. The first publication in Section 4.1 focuses on transonic buffet on a wing without pitching flexibility (Accorinti et al., 2022). The subsequent publications describe the effects of various fluid and structural parameters on the transonic buffeting phenomenon with elastically suspended wing. Section 4.2 concentrates on the variation of buffet onset (Korthäuer et al., 2023a), while Section 4.3 sets the focus on the nature of the fluid-structural interaction and the respective influence of structural parameters (Korthäuer et al., 2023b).

In Chapter 5, all significant experimental observations regarding the nature of transonic buffeting are summarized. Finally, thoughts, ideas, and open points for continual investigations with the designed setup and the optical measurement techniques are shared.

2

Physical and Theoretical Basics

2.1. Airfoils in Transonic Flow

2.1.1. Transonic Flow and Shock Waves

Transonic flows are characterized by free stream flow velocities near the speed of sound, typically around the Mach number range of $0.8 < M_\infty < 1.2$. In Figure 2.1, the schematic of an exemplary airfoil at high subsonic inflow conditions ($M_\infty \approx 0.8$) is shown for zero-incidence (left) and a small angle of attack (AoA) (right). The acceleration of the flow around the leading edge and on the curved surface increases the local flow velocity above supersonic speed. The local Mach number exceeds the critical Mach number, $M > M^*$, which is the free-stream Mach number accompanying the first local occurrence of supersonic speed. At zero-incidence, two locally restricted supersonic regions are created, on both the pressure and suction sides of the airfoil (see Fig. 2.1a). Airfoils inclined with a positive AoA typically present a supersonic region solely on the airfoil suction side (see Fig. 2.1b). With an increase in AoA, the supersonic region extends downstream due to the convex curvature of the airfoil.

At moderate AoA and Mach numbers, a steady, normal compression shock wave terminates the supersonic region. Under the assumption of a calorically perfect gas, the

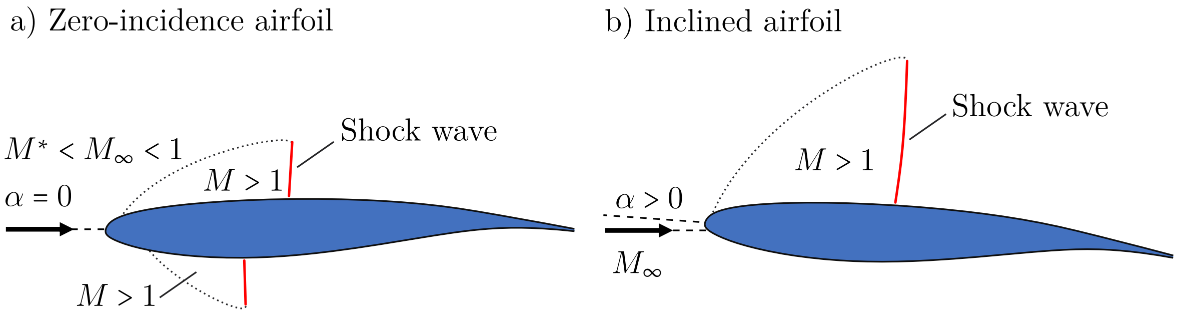

Figure 2.1: Transonic flow around a supercritical airfoil at zero (left) and positive incidence (right).

one-dimensional continuity, momentum, and energy equations can be used to derive the relations of the flow properties across the shock (Anderson, 2011):

$$M_2^2 = \frac{1 + \frac{\gamma-1}{2} M_1^2}{\gamma M_1^2 - \frac{\gamma-1}{2}} \tag{2.1}$$

$$\frac{p_2}{p_1} = 1 + \frac{2\gamma}{\gamma+1}\left(M_1^2 - 1\right) \tag{2.2}$$

$$\frac{\rho_2}{\rho_1} = \frac{u_1}{u_2} = \frac{(\gamma+1)M_1^2}{2 + (\gamma-1)M_1^2} \tag{2.3}$$

$$\frac{T_2}{T_1} = \left[1 + \frac{2\gamma}{\gamma+1}\left(M_1^2 - 1\right)\right]\left[\frac{2 + (\gamma-1)M_1^2}{(\gamma+1)M^2 - 1}\right] \tag{2.4}$$

where γ is the specific heat ratio (for air at standard conditions $\gamma = 1.4$), p is the static pressure, T the static temperature, ρ the density, and u the flow velocity in streamwise direction. The subscripts 1 and 2 refer to the locations in front of and behind the shock in the flow direction, respectively.

As the shock is a in stream-wise direction spatially very limited phenomenon, it can be described as a flow discontinuity. The static pressure, temperature and density experience a strong rise across the shock, where the ratios depend on the Mach number in front of the shock M_1 solely for a constant heat ratio (see Eqs. (2.2) to (2.4)). The higher M_1, the stronger the resulting shock and the rising effect on the static flow properties. The Mach number M_2 and the flow velocity u_2 after the shock, however, are reduced in an inverse manner, where the resulting M_2 is always subsonic in the case of a normal shock (see Eqs. (2.1) and (2.3)).

The static pressure at the trailing edge on the suction side of the airfoil plays an important role for transonic buffet(ing). In presence of a shock, it is a result of the expansion in front of the shock, the shock-induced pressure gradient, and the subsequent subsonic compression behind the shock. According to the "equality condition" (also known as "Kutta condition"), it needs to be approximately equal to the trailing edge static pressure on the airfoil pressure side. In addition to this, the static pressure at the trailing edge should be compatible with the free-stream static pressure, so far that the discrepancy has to be small enough to be adaptable by the viscous flow of the wake ("compatibility condition") (Anderson, 2011; Lee, 2001; Pearcey, 1958).

2.1.2. Steady Shock Motion

The satisfaction of the aforementioned conditions can be used as an explanation for the typical evolution of the shock wave on a supercritical airfoil approaching higher incidence, as shown in Fig. 2.2. With increasing AoA at a constant Mach number, the flow is progressively accelerated, the supersonic region enlarges, the shock wave strengthens (see Eq. (2.1)), and shifts towards the aft section of the airfoil (see Fig. 2.2a). During this "regular" shock motion, the share of the shock-induced pressure recovery rises, while the share of the subsonic compression is reduced (Pearcey, 1958).

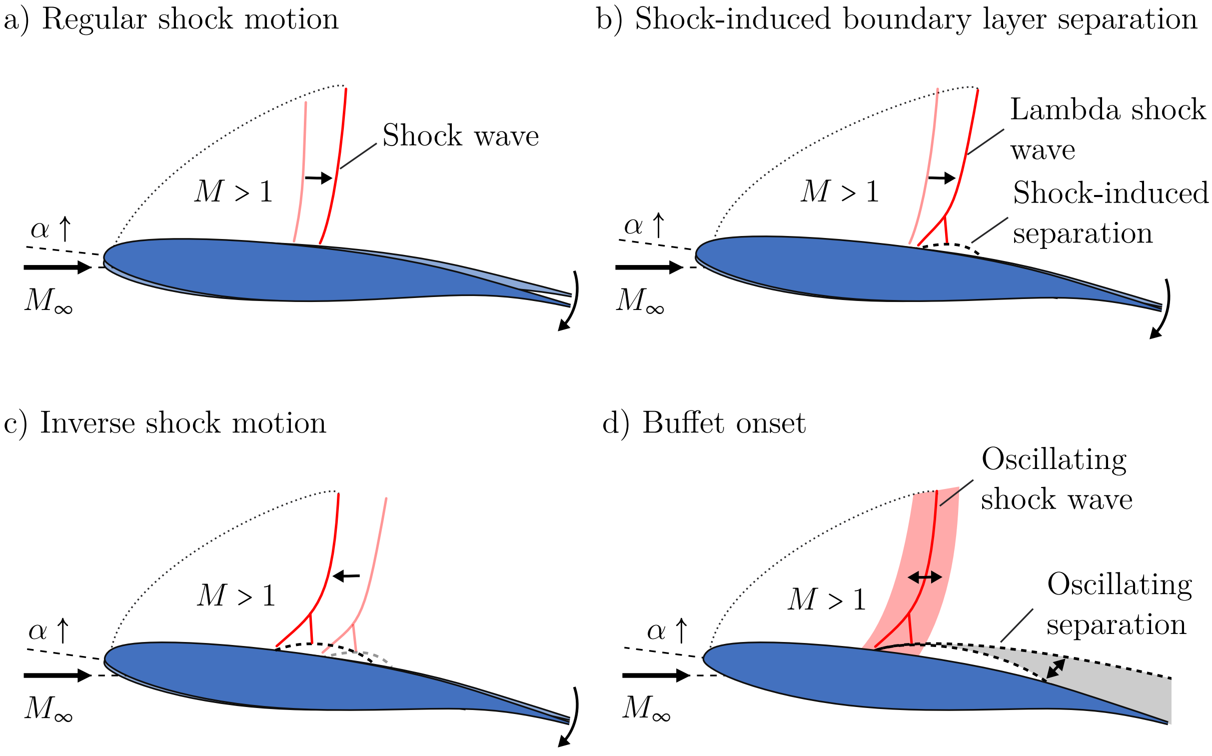

Figure 2.2: Typical evolution of the transonic flow on a supercritical airfoil with increasing AoA.

Boundary Layer Separation

At a certain AoA/Mach number, the positive, adverse pressure gradient induces a boundary layer separation at the shock foot and/or in proximity to the trailing edge. In the case of a separation bubble emerging from the shock foot, the bubble acts as a wedge. The result is a near-surface oblique shock that represents the foreleg of a lambda shock wave, as illustrated in Fig. 2.2b. At some distance from the surface, this foreleg meets a second shock wave originating from the boundary of the separation bubble. Both transition into a single normal shock wave (Babinsky and Harvey, 2011). As a significant flow separation is a necessary condition for the occurrence of transonic buffet, a lambda shock wave is a good indicator for approaching the buffet regime (Giannelis et al., 2017).

Inverse Shock Motion in Pre-buffet Conditions

With the presence of a boundary layer separation, any further increase in the AoA progressively enlarges the separated region and the effective curvature of the airfoil. The pressure distribution and recovery are significantly affected, which leads to an inverse, upstream-directed motion of the steady shock (see Fig. 2.2c). This effect is accounted to the satisfaction of the equality and compatibility conditions by a limitation of the extent of the separation area (rather than a further strength-increasing regular shock motion). Consequently, the inverse shock motion is a sign of the presence of a spatially limited but significant boundary layer separation (Pearcey, 1958). As will be shown in

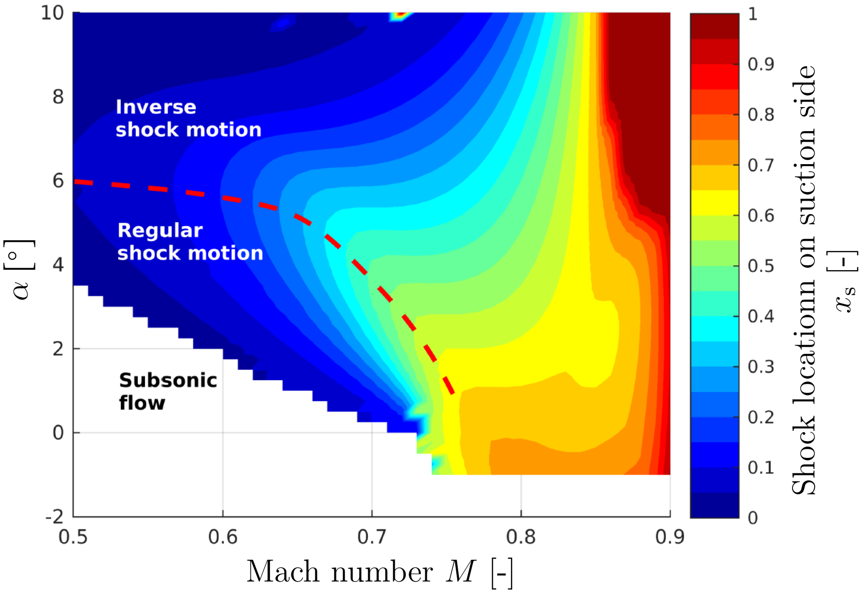

Figure 2.3: Regions of regular and inverse shock motion with respect to Mach number and angle of attack. The color scale represents the mean shock location on the suction side of the airfoil. Adapted with permission from Nitzsche et al. (2019).

Section 4.1, the inverse shock motion was found to be an intermediate step between the first occurrence of separation and buffet onset during the raise of the AoA at a constant Mach number (Accorinti et al., 2022). For the case of fixed AoA and increasing Mach number, however, the required conditions may be satisfied without an inverse shock motion. This is accounted to a lowering of both the static pressure upstream of the shock but also in the free-stream, which results in an easier satisfaction of the compatibility condition (Pearcey, 1958).

In Fig. 2.3 the color-coded steady shock locations for different combinations of AoA and Mach number are displayed. The results are based on two-dimensional, quasi-steady, numerical Reynolds-Averaged-Navier-Stokes (RANS) simulations of the transonic flow around an OAT15A airfoil (Nitzsche et al., 2019). The red dashed line represents the inversion line separating the regions of regular and inverse shock motion for an increase in AoA. In recent literature, the term "pre-buffet conditions" is often used to describe the range of Mach numbers and AoA, at which an inverse shock motion appears and the shock buffet region is approached.

2.1.3. Transonic Shock Buffet

Ultimately, after a further rise in AoA or the Mach number, the shock wave becomes unsteady and starts to oscillate in the stream-wise direction (see Fig. 2.2d). This flow unsteadiness is denoted as transonic shock buffet and has been of interest since the 1950s (Hilton and Fowler, 1947; McDevitt and Okuno, 1985; Lee, 2001; Jacquin et al., 2009; Giannelis et al., 2017). Initially, the shock motions resemble inharmonic, low-amplitude vibrations. By further increasing the AoA or Mach number, the motions become stronger and present harmonic oscillations that are termed as fully established shock buffet. Typical reduced buffet frequencies range from $0.16 < k = \pi f c / u_\infty < 0.22$, where f is the frequency, c the airfoil chord length, and u_∞ the inflow velocity.

Buffet Typology

Transonic shock buffet on wings has been observed on two-dimensional wing sections, infinite rectangular wings, finite rectangular wings with single- or double-sided clamping, as well as swept wings with or without taper and fuselage. The basic principle of transonic buffet – the stream-wise oscillating shock wave on the wing suction side – is always an inherent part. However, three-dimensional effects emerging from wall boundary layers, the sweep angle or wing tip flow alter the buffet's phenomenological appearance substantially. Additional information regarding these alterations can be found in Section 4.1 and Accorinti et al. (2023a). Despite the fact that most of the recent publications focus on three-dimensional shock buffet (Iovnovich and Raveh, 2015; Dandois, 2016; Crouch et al., 2019; Sugioka et al., 2022), this work treats transonic shock buffet on a double-sided clamped, rectangular wing. Reducing as much complexity as possible for the "natural" buffet case – the one on a rigid, fixed wing – allows a clean investigation of the effects of added structural flexibility.

Depending on airfoil shape and/or flow conditions, the rectangular wing exhibits different types of shock buffet. A typological distinction can be found in the early literature, for instance in Tijdeman (1977), Mabey (1981), and Gibb (1983). Supplementary information regarding the distinction is presented in Section 4.1 (Accorinti et al., 2022). The present work concentrates on shock buffet of the so-called type IIA, which is characteristic of modern supercritical airfoils at positive AoA. It exhibits a permanently present shock wave that oscillates in a mostly harmonic manner on the airfoil suction side, solely.

A typical cycle consists of the following steps: during the upstream motion, the shock wave strengthens, which increases the extent of the flow separation, possibly all the way to the trailing edge. As a consequence, the shock exhibits a lambda shape – as shown for the steady case in Section 2.1.2. Towards its most upstream turning point, the shock starts to weaken until it reverses its motion. The boundary layer reattaches and the shock appears normal. In its normal form, the shock travels downstream. At the most downstream turning point, the boundary layer tends to separate again, leading to a new cycle.

Multiple theories and observations regarding type IIA have been published, but an explanatory physical mechanism remains missing. As the theoretical considerations regarding the origin of the self-sustained shock-wave-boundary-layer interactions (SWBLI) on a fixed, rigid airfoil exceed the scope of this work, the reader is redirected to the introduction of Section 4.1 and the work of Giannelis et al. (2017). Nevertheless, also the present work will offer a basis for prospective theoretical investigations regarding transonic buffet as will be elaborated in Section 5.2.

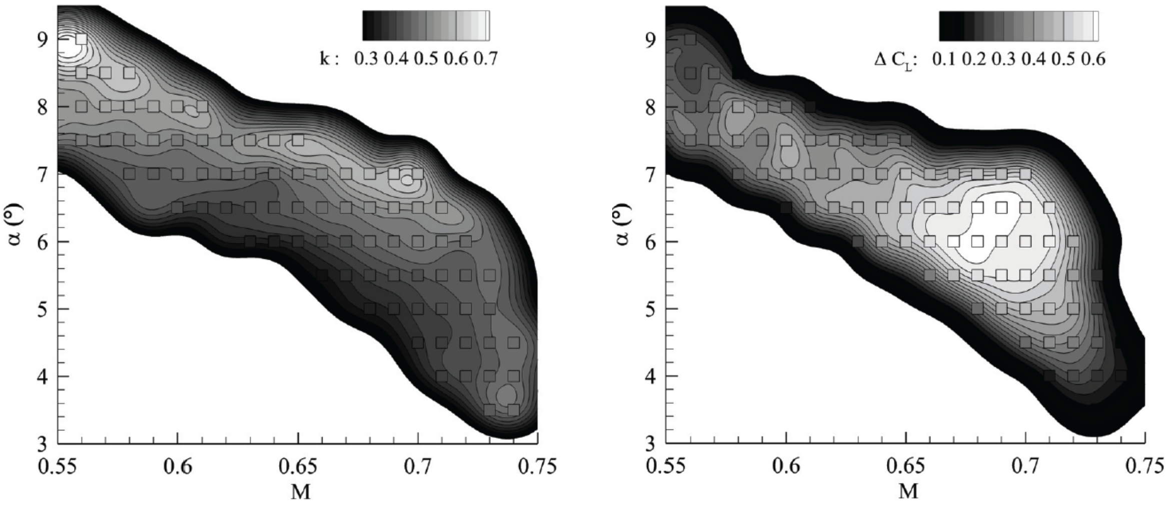

Figure 2.4: Computationally determined buffet boundaries of an OAT15A airfoil with dominant reduced frequencies – here defined by $k = 2\pi fc/u_\infty$ – (left) and amplitudes of lift coefficient (right), both based on the fluctuations of the lift coefficient. Reproduced from Giannelis et al. (2018). Copyright ©2023 Elsevier Masson SAS. All rights reserved.

Buffet Boundaries and Characteristics

In the transonic regime, the Mach number and the AoA of a fixed, rigid wing form a monotonously decreasing, lower boundary where an increase of either can induce onset of type IIA buffet (Pearcey, 1958; Mabey, 1989; Crouch et al., 2007; Jacquin et al., 2009; Sartor et al., 2015; Giannelis et al., 2018). Figure 2.4 shows the numerically determined buffet region for multiple combinations of AoA and Mach number, as well as the corresponding buffet frequency (left) and amplitude of lift fluctuations (right). As one can see, transonic buffet only appears in a narrow band of AoA and Mach number throughout transonic conditions.

Towards the offset or upper buffet boundary, the shock oscillations diminish until at a particular high AoA or Mach number, the shock wave remains steadily close to the leading edge inducing a permanent substantial flow separation from shock foot to the trailing edge (Anderson, 2011). The exact locations of the buffet boundaries are very sensitive. In experiments, they highly depend on the boundary conditions of the experimental setup/wind tunnel, such as the pressure distribution and the correction measures used to account for wall boundary-layer growth or blockage (Accorinti et al., 2022). In numerical simulations, the turbulence model plays – besides the boundary conditions – a significant role and can induce major variations to the boundaries or even suppress the phenomenon completely (Nitzsche et al., 2019; Giannelis et al., 2018). Consequently, this results in highly varying buffet boundaries throughout the literature, highlighting the complexity of the phenomenon and the need for careful consideration of experimental and modeling approaches (Accorinti et al., 2022).

Moreover, the definition of the on-/offset criterion is not unambiguous. Different criteria have been defined, and techniques have been employed to determine the boundary locations. Exemplary approaches are the detection of increased fluctuations in surface pressure (McDevitt and Okuno, 1985; Jacquin et al., 2009) or lift (Iovnovich and Raveh, 2012; Giannelis et al., 2018), the transition from negative to positive modal damping (bifurcation points) by system stability analysis (Crouch et al., 2007; Nitzsche et al., 2019), or simply the analysis of the shock position itself, as used in this work (Accorinti et al., 2022; Korthäuer et al., 2023a; Korthäuer et al., 2023b).

A common method that is applied for the identification of transonic buffet is the global stability analysis of the flow equations. It is widely accepted – since firstly proposed by Crouch et al. (2009) – that buffet represents an unstable global fluid mode, which is characterized by the coupled shock oscillation and pulsation of the separated boundary layer. In this sense, the pre-buffet flow field can be characterized as a lightly damped dynamic system, whose damping is reduced to zero at buffet onset. Consequently, the stability analysis is nowadays the means of choice for the determination of on- and offset boundaries and the attributes of the phenomenon (Sartor et al., 2015; Giannelis et al., 2017; Gao et al., 2018; Nitzsche et al., 2019; Poplingher et al., 2019; Gao and Zhang, 2020; Timme, 2020).

Transonic buffet is mainly characterized by the dominant frequency of the shock motion and its amplitude. As Fig. 2.4, left shows, a change of the dominant frequency with aerodynamic parameters is to be expected. An increase in AoA or Mach number induces a higher shock oscillation frequency for most of the buffet range. At a particular combination of AoA and Mach number, a global maximum of the lift fluctuations is reached (Fig. 2.4, right), which then diminishes rapidly with approaching the offset boundary.

Given the high sensitivity of transonic buffet and its onset boundaries – even without structural interaction – a solid analysis of the phenomenon on a fixed, rigid wing ("natural" buffet) under the respective facility's boundary conditions is crucial. The first research objective of this thesis is consequently defined as:
The experimental determination of the facility-specific buffet boundaries and shock motion characteristics (research objective 1).

The required steps are:

a. the design of an experimental setup allowing the conduction of aerodynamic experiments on a fixed, rigid two-dimensional wing (see Section 3.2);

b. the deployment of non-intrusive measurement techniques to capture the shock behavior and to verify the wing rigidity (see Section 3.3); and

c. the systematic variation of aerodynamic parameters and analysis of the shock characteristics.

The corresponding work and results are presented in Section 4.1 in form of the scientific publication by Accorinti et al. (2022).

2.2. Fluid-structure Interaction & Dynamic Aeroelasticity

The term fluid-structure interaction (FSI) typically describes the interaction between a fluid (such as a liquid or gas) and a movable or deformable object (such as a construction, bridge, or aircraft wing). Where FSI is the more common, general term to describe any deformation or movement of a body in any kind of fluid, aeroelasticity is a more specific term. It mainly refers to air as the fluid and concentrates on the dynamic behavior of flexible structures under aerodynamic forces (Bungartz and Schäfer, 2006). The so-called "Collar" triangle depicted in Figure 2.5 describes the interaction of aerodynamic, inertia, and elastic forces for a flexible structure (Collar, 1978). While static aeroelasticity, stability and control, and vibration are the results of the interaction of two of the three kinds of forces, respectively, dynamic aeroelasticity is determined by an interaction of all three forces (Wright and Cooper, 2008).

This section will give a brief description of the most common forms of dynamic aeroelastic problems on aircraft and leads to the key phenomenon of this doctoral thesis, the non-linear FSI of transonic buffeting.

2.2.1. Flutter

One of the most important dynamic aeroelastic phenomena is flutter (Collar, 1978). It describes an unstable self-excited vibration of a structure that extracts energy from the flow. It often results in catastrophic structural failure and its onset point is difficult to predict (Wright and Cooper, 2008).

The most common form, also referred to as "classical flutter", derives from the unfavourable coupling of two (or more) structural modes, such as wing bending/torsion, wing torsion/control surface elevation, or wing torsion/engine motion. The aerodynamic forces and their phase relation enable the coupling and lead to an amplification of the structural mode(s). At constant structural characteristics (natural frequency,

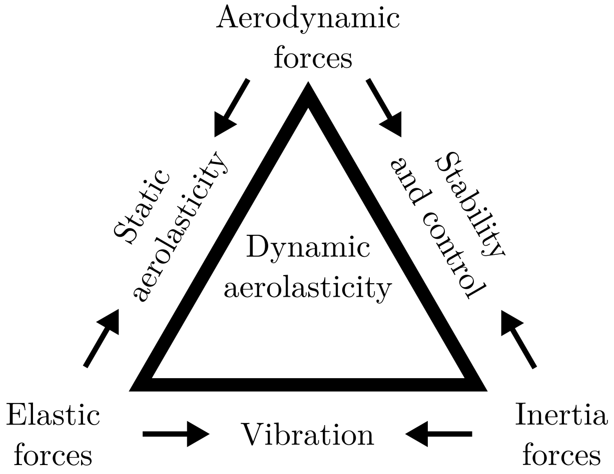

Figure 2.5: Collar's triangle of forces (Collar, 1978)

mass distribution, and moment of inertia), the flow dynamic pressure is the key parameter determining the occurrence of the phenomenon (Gao and Zhang, 2020). Typically, beyond some critical speed (or flutter speed), a small initial disturbance can induce self-sustained oscillations. The determination of the critical flutter speed and the consequent flutter frequency is typically obtained from stability or eigenvalue analysis of a flutter model under consideration of structural and aerodynamic modeling. At the point of flutter onset, the hitherto positive damping turns negative, and the corresponding mode becomes unstable.

Structural System

The typical, theoretical structural model used for the investigation of airfoil or wing section flutter is presented in Fig. 2.6. The structural system of equations of motion for an airfoil with a pitch and a heave degree of freedom (DoF) is:

$$\begin{bmatrix} m & S_\theta \\ S_\theta & I \end{bmatrix} \begin{pmatrix} \ddot{h} \\ \ddot{\alpha} \end{pmatrix} + \begin{bmatrix} D_\mathrm{h} & 0 \\ 0 & D_\theta \end{bmatrix} \begin{pmatrix} \dot{h} \\ \dot{\alpha} \end{pmatrix} + \begin{bmatrix} K_\mathrm{h} & 0 \\ 0 & K_\theta \end{bmatrix} \begin{pmatrix} h \\ \alpha \end{pmatrix} = \begin{pmatrix} L \\ -M_\mathrm{ae} \end{pmatrix} \tag{2.5}$$

where

- α is the pitch angle, and h is the vertical location of the elastic/rotational axis (heave motion),
- L and M_ae are the aerodynamic lift and moment,
- c is the airfoil's chord length,
- m is the mass of all moving parts,
- $S_\theta = x_\theta mc$ is the structural coupling parameter based on the distance x_θ between elastic/rotational axis and center of gravity,
- I is the moment of inertia around the rotational axis,
- $K_\mathrm{h} = m(2\pi f_\mathrm{h})^2$ is the stiffness factor for the heave motion with the natural heave frequency f_h (or heave eigenfrequency),
- $K_\theta = m(2\pi f_\theta)^2$ is the stiffness factor for the pitch motion with the natural pitch frequency f_θ (or pitch eigenfrequency), and
- D_h and D_θ are the respective damping coefficients.

By coinciding locations of the elastic axis and center of gravity, so that $x_\theta = 0$, the structural coupling between the heave and the pitch modes can be inhibited as $S_\theta = 0$. In wind-off conditions, heave and pitch motion would consequently be decoupled. On the aerodynamic (right-hand) side of the equation, however, further coupling coefficients are represented. This leads to a generally coupled mode shape in wind-on conditions, explaining the coupling in classical wing bending/torsion flutter (or in the 2D case, a coupled heave and pitch motion).

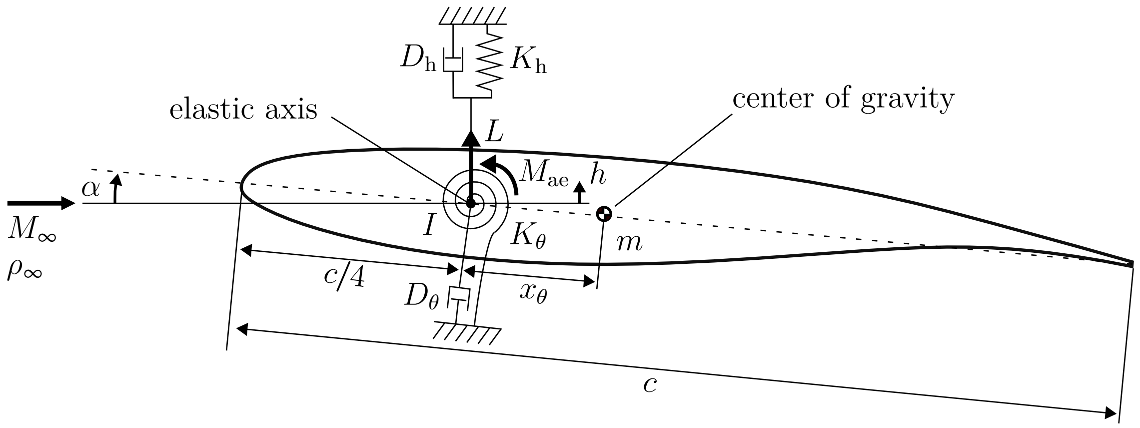

Figure 2.6: Structural model for an airfoil or wing section with two DoFs.

If the heave-DoF is fully inhibited, $h = 0$, the equation is reduced to a 1-DoF pitch motion:

$$I\ddot{\alpha} + D_\theta\dot{\alpha} + K_\theta\alpha = -M \tag{2.6}$$

The Eqs. (2.5) and (2.6) are the typical basis for the structural part of the stability analysis and the determination of flutter boundaries in literature (Giannelis et al., 2017; Nitzsche et al., 2022; Gao and Zhang, 2020).

One of the most significant parameters for aeroelastic interactions is the mass ratio

$$\mu = \frac{m}{\rho_\infty \pi (c/2)^2} = \frac{4m}{\rho_\infty \pi c^2} \tag{2.7}$$

It relates the excited mass of the system m and the exciting "mass" by the inflow density ρ_∞ in a non-dimensional manner.
Furthermore, the structural natural frequencies, f_α and f_h are of major importance. Typically in the frame of aeroelasticity, the frequency is presented in the reduced form, where two definitions are most common. One, going back to the US-American work of Theodorsen (1935), is referring to the half-chord as reference length:

$$k = \frac{2\pi f c/2}{u_\infty} = \frac{\pi f c}{u_\infty} \tag{2.8}$$

The other definition is based on the works of Frazer and Duncan (1931) and Collar (1978) from the UK. It refers to the full chord and results in

$$k_{FC} = \frac{2\pi f c}{u_\infty} \tag{2.9}$$

Beside these two definitions, also the frequency ratio with respect to the buffet frequency f/f_b is common, rarely also the Strouhal number $St = fc/u_\infty$. In this work, the definition by Theodorsen (1935) is employed but attentive reading of additional comparative literature is recommended. In the latter, the flutter index $Fi = 2/(k_\theta\sqrt{\mu})$ is often used as a combined structural parameter for the presentation of the flutter boundary. As both parameters k_θ and μ will be investigated separately, the flutter index is not utilized in this work.

Non-linear Flutter & Limit Cycle Oscillations

Structural amplitudes during flutter may eventually exceed any structurally tolerable level unless some form of non-linearity in the system leads to a limitation of the motion (Wright and Cooper, 2008; Nitzsche et al., 2019). Non-linearities can emerge from structural, aerodynamic, and control system phenomena. At this point linear analysis fails to predict the flutter speed and more sophisticated methods are required (Wright and Cooper, 2008).

Structural non-linearity can be expected from large deflections, non-uniform stiffness effects (e.g. stiffening pylon attachments), or play in structural joints or control surface attachments. Control-based non-linearities emerge from control surface deflection, actuation mechanisms or multiple simultaneously applied control laws. An aerodynamic flow can be considered linear when changes in fluid properties (such as presssure) are proportionally related to changes induced by the shape or motion of a body in the flow (such as the velocity field). Even under consideration of small disturbances, transonic flow is highly non-linear. The non-linearities are based on the geometry of the supercritical airfoils (which are mostly cambered and of high thickness), the combined presence of sub- and supersonic regions, (moving) shock waves and flow separation, as well as their interaction (transonic buffet) (Wright and Cooper, 2008; Bendiksen, 2011; Dowell et al., 2003).

A typical manifestation of non-linearities are limit-cycle oscillations (LCO). The excessive rise of the amplitude of an undamped oscillation is hereby limited, as soon as the non-linear region is reached. Figure 2.7 shows the temporal evolution and limitation of a harmonic pitching LCO (left) and the corresponding phase plane (Rooij, 2017). The resulting amplitude is highly dependent on various parameters such as structural characteristics (e.g. damping, natural frequency, location of the center of gravity or

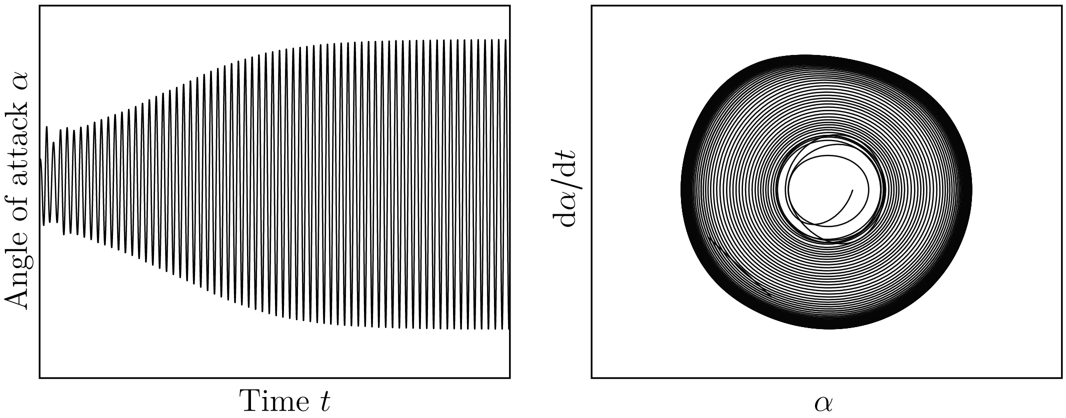

Figure 2.7: Exemplary limit-cycle oscillation of the angle of attack over time (left) and in the phase plane, plotted against its temporal derivative (right). Adapted from Rooij (2017).

elastic axis), aerodynamic parameters (e.g. AoA, flow velocity, location of transition) and combined ones (e.g. the mass ratio) (Dowell et al., 2003; Schewe et al., 2003; Dowell, 2010; Bendiksen, 2011; Braune and Hebler, 2019).

Non-linear FSI in Transonic Flow

The most common forms of FSI based on non-linear effects of the transonic flow are the transonic dip, transonic buzz, and transonic buffeting (Gao and Zhang, 2020). The transonic dip describes a substantial lowering of the linear flutter boundary in the transonic regime, particularly for swept wings. Figure 2.8 presents a schematic of the linearly-modeled and experimentally observed flutter boundaries for different airfoil thicknesses, adapted from Doggett et al. (1959) and Wright and Cooper (2008). Compressibility effects altering the phase relation between the aerodynamic forces are deemed responsible for the transonic dip (Isogai, 1979). Furthermore, a high dependency on other factors such as the mass ratio, the AoA, or the airfoil thickness was observed. Consequently, this multi-parametric dependent phenomenon plays a major role in the limitation of the flight envelope (Bendiksen, 2011). Transonic buzz describes the self-excited single-degree-of-freedom (SDoF) flutter of the control surface. It is initiated by a control surface deflection and is attributed to an interaction of shock wave and control surface (Zhang et al., 2015; Gao and Zhang, 2020). Transonic buffeting stands for the structural interaction with shock buffet, hence an oscillation of the shock wave on the suction side coupled with a structural flutter motion. Despite the limitation of the amplitude, the eventual high level of wing oscillations might be above structural capabilities and could induce severe structural failure. At the least,

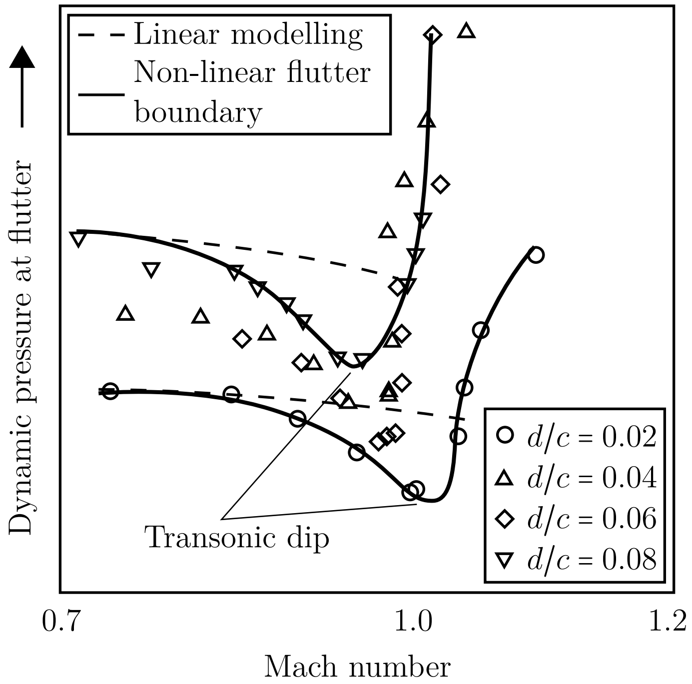

Figure 2.8: Linearly-modeled and experimentally determined non-linear flutter boundaries in dependency of airfoil thickness. Adapted from Doggett et al. (1959).

fatigue will limit the components' life cycle – also with low-level oscillations. It is the focus of this work and the phenomenon and its characteristics will be presented in the following section.

2.2.2. Transonic Buffeting

A structural excitation in association with transonic buffet may occur when the structural natural frequencies of the 2D wing are located in the proximity of the dominant natural buffet frequency. The resulting aeroelastic phenomenon is known as transonic buffeting. Even without the presence of structural non-linearities, the non-linear nature of the flow itself hereby leads to limit-cycle oscillations of the airfoil (Dowell et al., 2003).

A typical buffeting cycle is shown in Fig. 2.9. It presents a fully established buffeting cycle with limited amplitude recorded in the frame of the experimental campaign presented by Scharnowski et al. (2022). The natural pitch frequency was set similarly to the buffet frequency. The color code presents the stream-wise flow velocity measured by particle image velocimetry (PIV). At $t = 0.0\,\mathrm{ms}$, the shock wave is found in its most downstream location and appears straight, indicating an attached boundary layer. The airfoil pitch, however, reaches its maximum with a delay at $t = 1.0\,\mathrm{ms}$, where the lower part of the shock wave already starts its upstream motion. It is inclined, which coincides with a separated boundary layer. Starting from $t = 2.0\,\mathrm{ms}$, the angle of attack decreases. The major part of the shock wave is found in its upstream motion, it appears very inclined, and strong boundary layer separation is present. At $t = 3.0\,\mathrm{ms}$ the shock foot has reached its upstream reverse point, the lower shock part straightens, and the boundary layer reattaches. The airfoil pitch and the upper part of the shock, however, are delayed and continue in their direction up to $t = 4.0\,\mathrm{ms}$. Starting from $t = 5.0\,\mathrm{ms}$ the shock front appears mostly straight and is entirely found in its downstream journey, accompanied by a decrease in pitch. The boundary layer remains fully attached during the downstream motion, indicating a weaker shock and pressure gradient. Between $t = 8.0\,\mathrm{ms}$ and $t = 9.0\,\mathrm{ms}$ the downstream reverse point is reached and a new cycle commences.

Modern methods of coupled numerical simulations (computational fluid dynamics and structural dynamics (CFD/CSD) are a good tool for the analysis of coupled fluid-structure phenomena, such as transonic buffeting. Given the high computational effort and cost required for sufficiently time-resolved simulations, different approaches are being developed to reduce the complexity of calculations whilst aiming for the preservation of similar results. The review work of Giannelis et al. (2017) gives a thorough overview of the instituted methods. Gao et al. (2017) – among others – applied the promising technique of reduced-order-modeling for the prediction of transonic buffet(ing) and obtained well-matching results compared to his reference points from coupled CFD/CSD simulations. Nevertheless, uncertainties of new methods remain and the limitations of such approaches are yet to be determined, which emphasizes the need for validation data. While fully coupled numerical methods like CFD/CSD provide data for that cause, also here some inevitable uncertainty factors persist, such

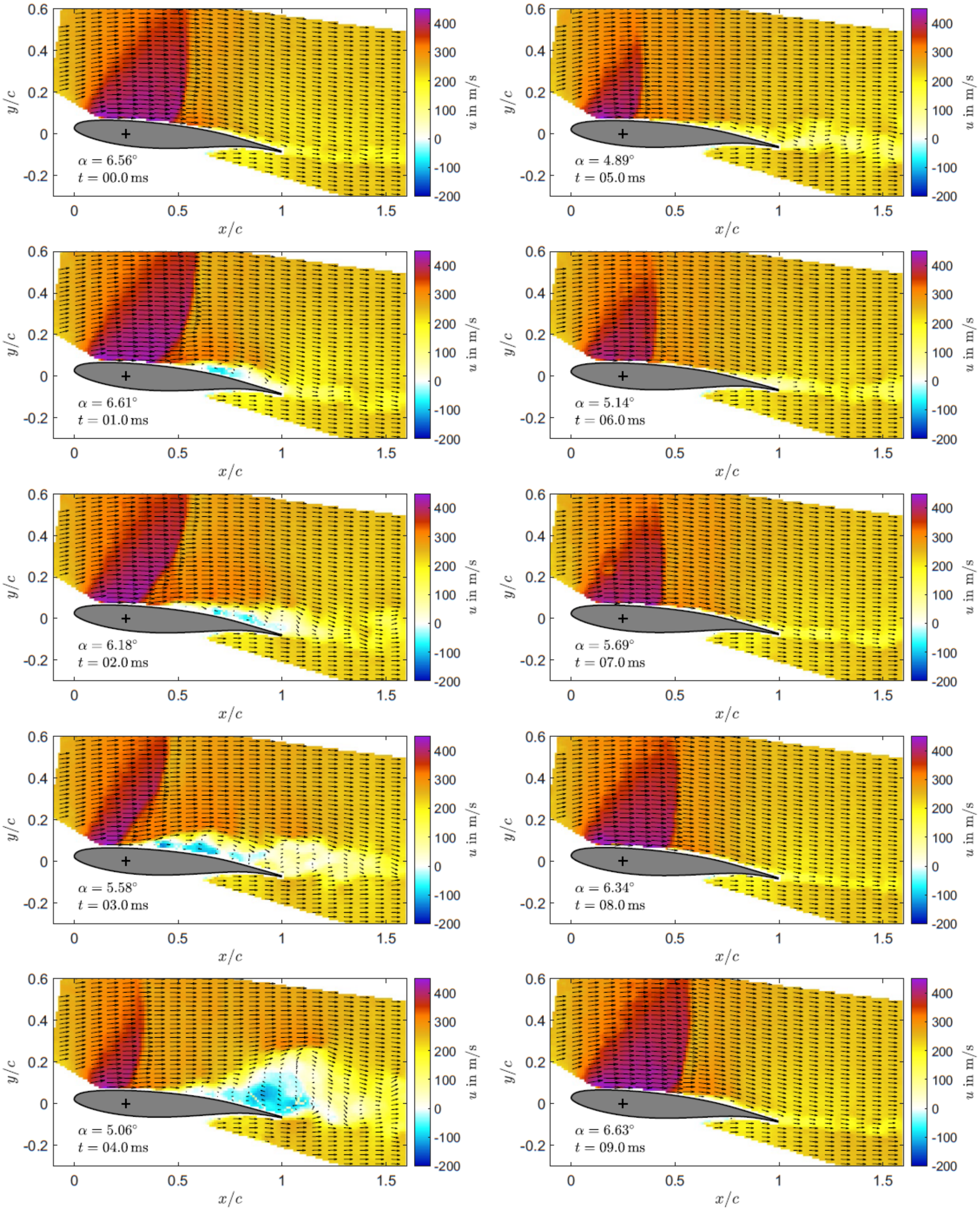

Figure 2.9: Evolution of the velocity field around an oscillating airfoil in successive time steps for one buffeting cycle obtained from PIV measurements. The color code represents the stream-vise velocity component u. Reprinted from Scharnowski et al. (2022).

as turbulence modeling (Nitzsche et al., 2019). Consequently, experimental investigations continue to be the tool of choice to validate and complement the computationally obtained data. For this reason, aeroelastic experiments are conducted in the transonic regime with focus on transonic buffet with and without the influence of pitch flexibility by using a specifically designed setup (see the summary of research objectives and required steps Section 2.3).

Phenomenological Excitation

Several studies regarding transonic buffeting have been conducted over the last decades. Distinctions can be based on several characteristics, such as the airfoil model, the method (experimental or computational; fully coupled or reduced-order modeling), the parametric range (aerodynamic and structural), and the excitation method (self-induced or forced by pitch motion, heave motion, or deflection of control surfaces).
The application of forced excitation offers the benefits of a highly controlled, less risky approach to the phenomenon. Typically, frequency and amplitude are prescribed by the exciter and in case of need the oscillations can be suppressed, hence a high damping is applied. The energy budget analysis allows a simple evaluation of the state of the interaction, whether it is stable - the exciter adds energy to the system to maintain the oscillation - or unstable - the exciter extracts energy from the system and dampens the oscillation to maintain the given amplitude. The higher the energy extraction, the higher would be the corresponding natural amplitude. A drawback of this approach is the assumption of a certain designated pattern of motion, such as a harmonic oscillation. In particular for structural interaction with developed shock buffet, where the upstream shock excursion may be faster than the downstream one (Scharnowski et al., 2022), such an assumption is questionable. The additional adjustable parameters of frequency and amplitude can provide further insight into the underlying mechanisms. But they come with the drawback of additional computational or experimental costs, or limited capacity for other important parametric variations, such as Mach number, AoA, mass ratio, or natural pitch frequency.

The method of self-induced excitation, in contrast, bears frequency and amplitude as result of the FSI and reduces the parametric space. Given the high number of other important parameters and the availability of several computational works on the topic, the approach of self-excited experiments was chosen for this work. However, the risk of an uncontrollably large model motion is higher. The implementation of appropriate safety mechanisms is essential (see Section 3.2).

In the following section, some essential research results, setting the basis for this thesis will be presented: the numerical discoveries regarding transonic buffeting, its variable onset boundaries, and modal interaction with frequency lock-in (FLI). A summary of additional works related to the topics can be found in Sections 4.2 and 4.3 (Korthäuer et al., 2023a; Korthäuer et al., 2023b).

Variation of Onset Characteristics

With the upcoming approach of the global modal analysis of the flow (see Section 2.1.3), the combined numerical analysis of both fluid and structural modes became the focus of the latest aeroelastic research on the topic. From the combined analysis it appeared that the different modes of fluid and structure show coupling potential. Kou et al. (2017) showed that the coupling of fluid and structural modes leads to the premature onset of vortex-induced vibrations on a cylinder, for which the onset Reynolds number could be more than halved. Similar to this, the modal interaction on an airfoil in transonic flow may lead to reduced damping, and consequently bifurcation characteristics may be affected, i.e. buffet(ing) onset. Otherwise put, structural natural frequencies in a certain range can affect buffet onset and potentially even the operating envelope of aircraft (Gao et al., 2018; Nitzsche et al., 2019).

Firstly reported by Nitzsche (2009) – based on forced excitation of control surfaces – other groups have found compliant results, confirming an onset in the pre-buffet regime (with respect to natural buffet onset). As an example, Fig. 2.10, left, shows the onset boundaries determined by reduced-order modeling of an elastically suspended NACA0012 airfoil with pitching DoF (Gao et al., 2018). The single red markers represent comparative CFD/CSD results that confirm the ROM-based findings. The differently colored areas denote the dominant unstable mode, the structural pitching mode (SM, gray), or the unstable fluid mode (FM, green), whichever drives the coupled unsteadiness. The angle of attack α, the natural pitching frequency k_θ, and the mass ratio μ are varied. All three parameters affect the natural buffet onset boundary. For the range of $0 < k_\theta < 0.35$, higher k_θ or lower μ both lead to a lowering of the onset AoA. Above, only k_θ shows an effect, where an increase has a stabilizing effect, i.e. it results in a higher onset AoA. The orange dashed line approximately represents the natural buffet frequency and separates the two regions of dominant unstable modes.

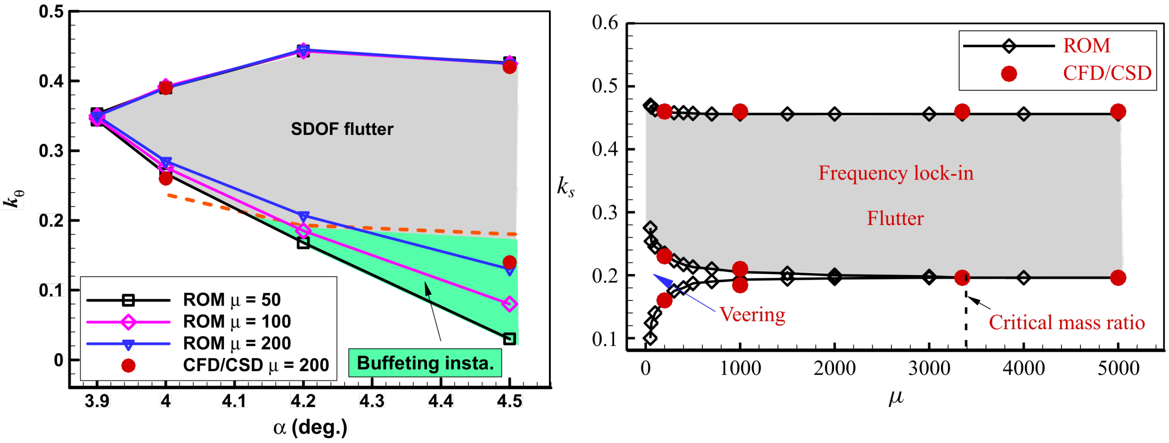

Figure 2.10: Onset boundaries and phenomenological classification of a NACA0012 airfoil at $M = 0.7$ in dependence on AoA and structural characteristics. Left: Natural pitch frequency k_θ and AoA (reproduced from Gao et al. (2018). Copyright ©2023 Elsevier Masson SAS. All rights reserved.). Right: Natural pitch frequency (here denoted as k_s) and mass ratio μ (reproduced with permission from Gao et al. (2017)).

The reduction of the onset boundary by introducing structural flexibility has high relevance for the aircraft design envelope. Real wing structures are never infinitely stiff and their characteristics may be unfavorably altered – for example by modern manufacturing processes. Therefore, it is recommended by the authors of Nitzsche et al. (2019) and Gao et al. (2018) to consider coupled effects in an early stage of the aircraft development process. Based on this important finding and the remaining uncertainty due to its numerical character, another research objective is defined:
The experimental determination of the onset boundaries of a wing with elastically-suspended pitching DoF in dependence of the natural pitch frequency (research objective 2).

The required steps are:

a. the design of an experimental setup allowing the conduction aeroelastic experiments on a two-dimensional wing with optional elastically-suspended pitching DoF, variable natural pitching frequency, mass ratio, and mass distribution;
b. the deployment of appropriate measurement techniques; and
c. the systematic variation of aerodynamic and structural parameters, as well as the reliable determination of onset boundaries.

The work and results regarding this objective are presented in Section 4.2 in form of the scientific publication by Korthäuer et al. (2023a).

Modal Interaction and Frequency Lock-in

The work of Gao and Zhang (2020) gives a thorough review of transonic aeroelastic phenomena under consideration of the interaction of structural and fluid modes. Figure 2.11 presents the modal interaction of the fluid mode (the shock oscillation, “F”) and the structural mode (the pitch mode, “S”). The complex-valued results in (a) and (b) were obtained from the eigenvalue analysis of the ROM model and represent the modal frequency (imaginary part) and the negative modal damping (real part), respectively. The two modal branches illustrate eigenvalue loci for varying natural pitch frequencies k_θ (in this figure denoted as k_s). In Fig. 2.11(a), the two branches swap their associated modes. Branch B in blue, initially following the fluid mode with a buffet frequency of $k_\mathrm{b} \approx 0.2$, swaps to the structural mode on the diagonal and vice versa for branch A in black. This phenomenon, where the mode shapes of a system change as their frequencies cross each other, is referred to as modal veering. Figure 2.11(b) shows the corresponding modal damping: at low k_θ, the damping of branch B, associated with the fluid mode, is negative (positive real part) and, consequently, the mode is unstable. After veering, the now associated structural mode is unstable instead. At $k_\theta \approx 0.46$ branch B crosses the stability limit and the structural mode becomes stable.

The plots in Fig. 2.11(c) and (d) stem from a coupled CFD/CSD simulation and represent the resulting coupled aeroelastic frequency and the pitching amplitude, respectively. In region (1) the unstable fluid mode leads to a low-amplitude structural excitation (classical dynamic excitation or forced vibration) at the buffet frequency. In the veering region (2), as the mode shapes are exchanged, the coupled frequency

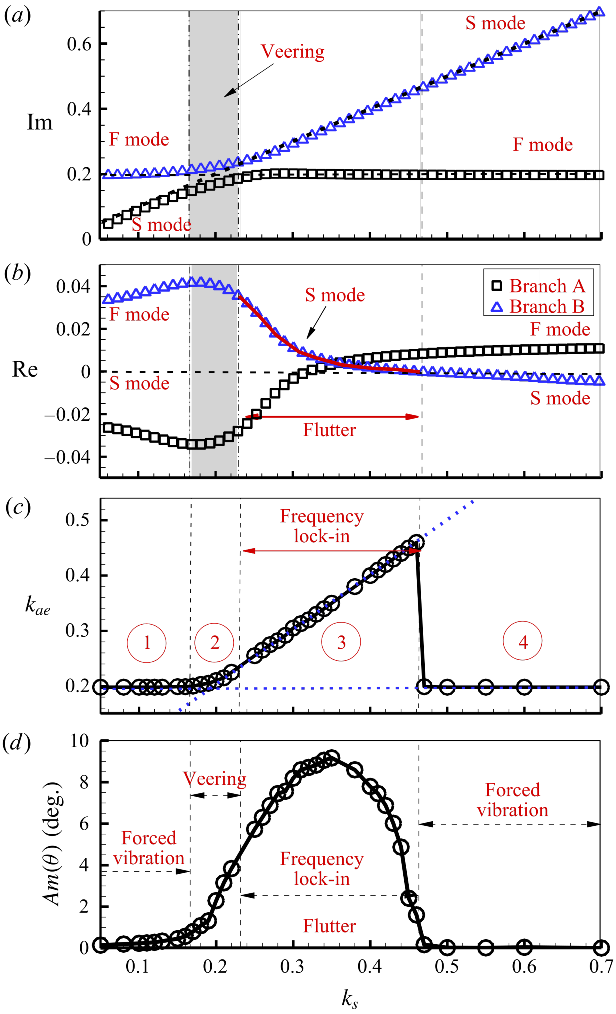

Figure 2.11: Modal development (a and b), coupled aeroelastic frequency (c) and pitch amplitude (d) for an increase in the natural pitch frequency throughout the regions of forced vibration, veering, and FLI. Reproduced with permission from Gao et al. (2017).

transitions from the buffet one to the natural pitch frequency. At the same time, the pitch amplitude increases strongly. The region (3), where the coupled frequency follows the natural pitch frequency is called the frequency lock-in (FLI) region. The amplitude rises to a high level until, $k_\theta = 0.35$, where the two branches A and B intersect, the maximum amplitude is reached before dropping again. When branch B becomes stable at $k_\theta \approx 0.46$, the coupled frequency suddenly returns to the buffet frequency, and a typical dynamic structural excitation (forced vibration) is obtained at a low pitch amplitude (region (4)). In numerical simulations with forcedly-excited pitching motion by Raveh and Dowell (2011), it was shown that the pitch-frequency related range of the lock-in phenomenon can be extended if the prescribed amplitude was set high enough.

The phenomenon of FLI contradicts the classical theory of dynamic structural excitation, where the structure is excited by a dominant fluid phenomenon. In this case, the amplitude would show maximum response (a resonance peak) for a natural pitch frequency $k_\theta = k_\mathrm{b} \approx 0.2$. The coupled frequency in (c) would not lock into the structural frequency but remain at k_b.

Parametric Space of Interest

The relevant parametric space for aeroelastic phenomena is rather large as both aerodynamic and structural parameters affect their occurrence and characteristics. For transonic buffeting, the parameters of Mach number, angle of attack, natural pitch frequency, mass ratio, and structural damping play the most significant role. Various works have varied these or related parameters (such as flutter index or dynamic pressure) over a wide range (as summarized in Korthäuer et al. (2023b)).

Nevertheless, for the phenomena of interest – the premature buffet(ing) onset and transonic FLI – it is of importance to set the parameters in the correct range. As has been shown in Fig. 2.4, the aerodynamic parameters of AoA and Mach number define the natural buffet range. The work of Accorinti et al. (2022), presented in Section 4.1, is consequently used to determine the relevant range in the particular experimental facility and its boundary conditions. As the Figs. 2.10 and 2.11 show, the most important structural parameter is the natural pitch frequency (also called pitching eigenfrequency). In order to facilitate modal interaction, the natural pitch frequency should be varied in the vicinity of the expected buffet frequency, which again also depends on the AoA. It should be adaptable, approximately in the range of $0.1 < k_\theta < 0.5$ to be low enough to represent the fully FM-dominated region but to also cover the veering, FLI, and drop-back to FM-dominance. From an experimental point of view, covering such a large range without substantial design adaptations is very challenging, as will be elaborated in Section 3.2.2.

The role of the other substantial structural parameter – the mass ratio – is twofold: it needs to be set in the correct range, low enough to obtain modal veering (see Fig. 2.11), but high enough to avoid static divergence and classical torsion-bending flutter (Nitzsche et al., 2022). On the other hand, it was found to have a significant effect on the frequency-related width of both the veering and the FLI region, as shown in the top plots in Fig. 2.12 adapted from Giannelis et al. (2016). Inherent for aeroelastic phenomena, structural damping is the third important parameter. As shown in the bottom two plots of Fig. 2.12, it has a substantial effect on the resulting pitching amplitude and the upper end of the FLI region.

On the basis of the presented numerical results a final research objective is defined as: **The experimental verification of the regions of transonic FLI, the fluid-dominated structural excitation, and the intermediate veering region on a wing with elastically-suspended pitching DoF** (research objective 3).

Complementary to the steps of research objective 2, the additional steps required are:

a. the systematic variation of aerodynamic and structural parameters like the AoA, the natural pitch frequency, and the mass ratio; and

b. the analysis of the parametric effects and the corresponding manifestation of aeroelastic interaction.

The work and results are presented in Section 4.3 in form of the scientific publication by Korthäuer et al. (2023b).

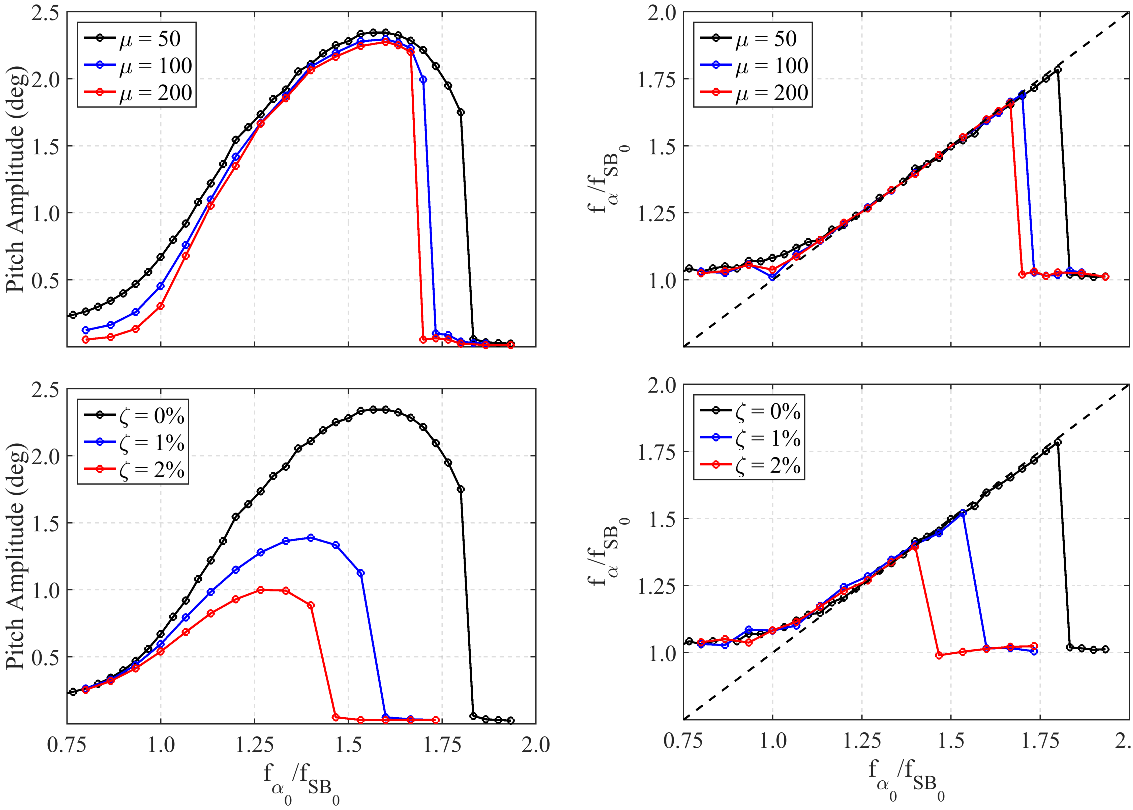

Figure 2.12: Effects of mass ratio (upper plots) and structural damping (lower plots) on the pitch amplitude (left) and the pitch frequency ratio (right). The subscripts 'α_0', 'α', and 'SB_0' stand for the natural pitch frequency, the measured pitch frequency and for natural shock buffet frequency, respectively. Reproduced with permission from Giannelis et al. (2016).

2.3. Research Objectives

The numerical findings regarding transonic buffet (see Section 2.1.3) and buffeting (see Section 2.2.2) set the basis for the research objectives of this doctoral thesis:

1. **The experimental determination of the facility-specific buffet boundaries and shock motion characteristics.**

   The steps required for this are:

   a. the design of an experimental setup allowing the conduction of aerodynamic experiments on a fixed, rigid two-dimensional wing;
   b. the deployment of non-intrusive measurement techniques to capture the shock behavior and to verify the wing rigidity; and
   c. the systematic variation of aerodynamic parameters and analysis of the shock characteristics.

   The work and corresponding results are presented in Section 4.1 in form of the scientific publication by Accorinti et al. (2022).

2. **The experimental determination of the onset boundaries of a wing with elastically-suspended pitching DoF in dependence of the natural pitch frequency.**

   The necessary steps for this are:

   a. the enhancement of the experimental setup to allow the conduction of aeroelastic experiments on a two-dimensional wing with optional elastically-suspended pitching DoF, variable natural pitching frequency, mass ratio, and mass distribution;
   b. the deployment of non-intrusive measurement techniques to capture the shock behavior and the wing motion and deformation; and
   c. the systematic variation of aerodynamic and structural parameters, as well as the reliable determination of onset boundaries.

   The work and results regarding this objective are presented in Section 4.2 in form of the scientific publication by Korthäuer et al. (2023a).

3. **The experimental verification of the regions of transonic FLI, the fluid-dominated structural excitation, and the intermediate veering region on a wing with elastically-suspended pitching DoF.**

   Complementary steps to the ones of research objective 2 are:

   a. the systematic variation of aerodynamic and structural parameters like the AoA, the natural pitch frequency, and the mass ratio; and
   b. the analysis of the parametric effects and the corresponding manifestation of the aeroelastic interaction.

The work and results are presented in Section 4.3 in form of the scientific publication by Korthäuer et al. (2023b).

For the sake of experimental efficiency, the steps 1a and 2a are combined in the design of an adaptive setup of which further information is presented in Section 3.2. Similar to this, the selection of non-intrusive measurement techniques was made far-seeing to fulfill the requirements of steps 1b and 2b. Detailed information is given in Section 3.3.

3

Methodology

The following chapter gives a more thorough insight into the methodology of this work than presented in the scientific publications at hand.
It is structured as follows: in Section 3.1, the experimental facility is presented. Section 3.2 describes the integrated experimental setup and Section 3.3 provides information about the applied measurement and data analysis techniques.

3.1. Experimental Facility

3.1.1. Overview

The experiments presented in this work were perfomed in the Trisonic Wind Tunnel of the University of the Bundeswehr Munich (TWM). Figure 3.1 shows a schematic of the facility. The blow-down type wind tunnel consists of two pressure tanks that are pressurized up to 20 bar with dry air provided by three compressors. In the operational state of an open gate and control valve, the air is discharged into the environment. The control valve controls the total pressure of the flow in the settling chamber within a range of 1.3 bar to 5 bar and an uncertainty of approx. 0.1 % at the here-used total pressure. It can consequently be used as a control mechanism for the Reynolds number. The settling chamber integrates two fine metal meshes and a honeycomb mesh to reduce flow fluctuations. The free-stream turbulence level for the here-considered Mach number range is approximately 1.3 %, based on the velocity fluctuations in stream-wise direction (Scharnowski et al., 2018). Two adjustable throats, the Laval nozzle and the diffuser allow the operation at Mach numbers in the range of $0.2 < M < 3.0$. The Laval nozzle, located in between the settling chamber and the test section, is partially closed for supersonic experiments and accelerates the flow above sonic speed, while the diffuser is fully opened. For flows up to the sonic speed, the Laval nozzle remains open, whereas the diffuser cross section is used to control the Mach number in the test section.

In Fig. 3.2 the operational range of the TWM is presented. In order to keep comparability to most previous experimental and numerical results (Jacquin et al., 2009; Crouch et al., 2009; Gao et al., 2017), a total pressure of $p_0 = 1.5\,\text{bar}$ was selected for the experiments to obtain a chord-based Reynolds number $Re_\text{c} \approx 3 \cdot 10^6$, where the model chord length was $c = 0.15\,\mathrm{m}$. Black markers indicate the experimental operating points for this work and highlight the capabilities of the facility, in particular regarding future investigations.

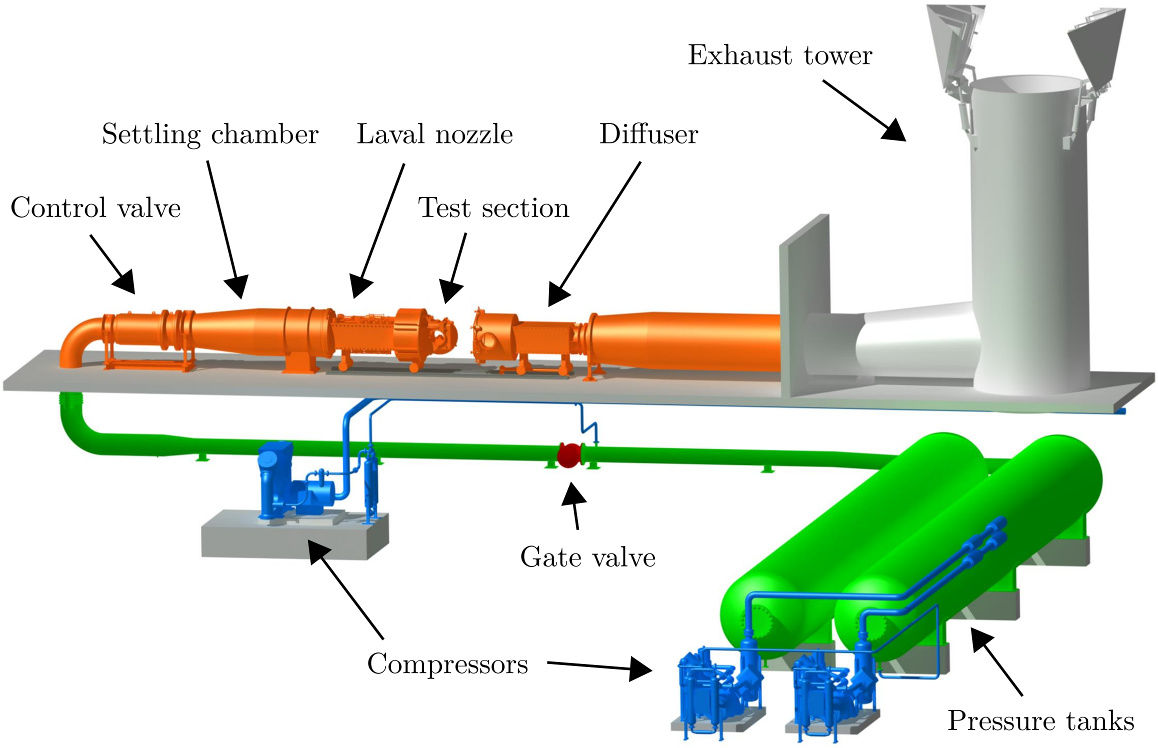

Figure 3.1: Schematic of the Trisonic Wind Tunnel Munich.

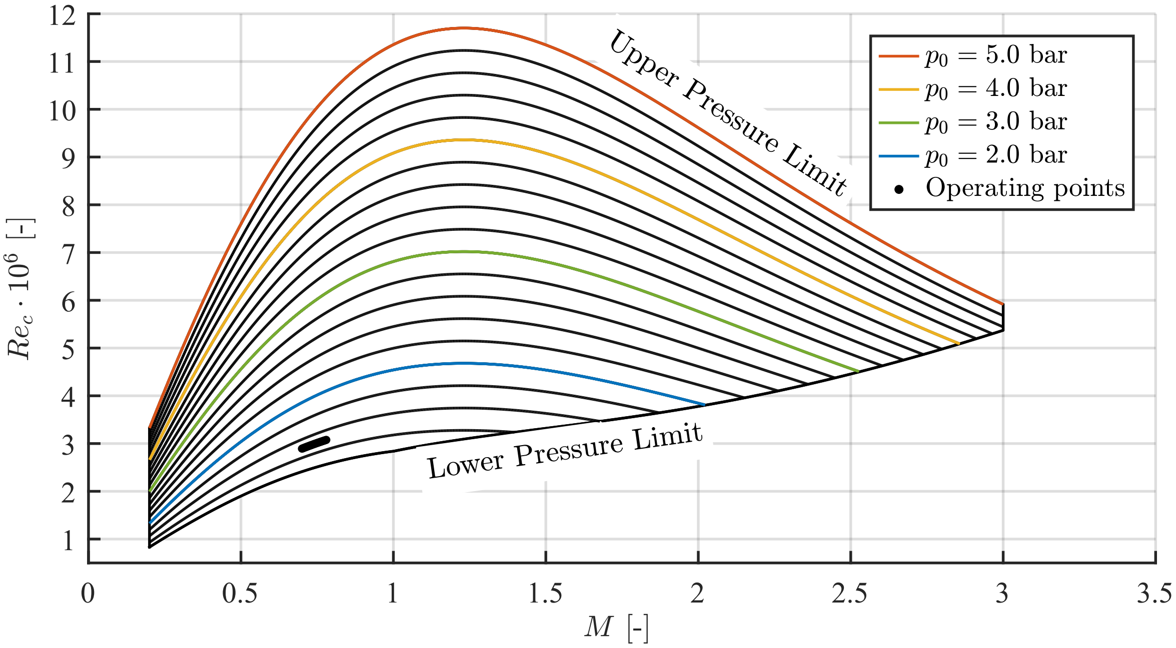

Figure 3.2: Operational range of the TWM and operating points of the presented work.

3.1.2. Test Section

The facility's rectangular test section of 0.3 m width and 0.68 m height is optimized for aerodynamic profile testing. It is enclosed by a circular plenum chamber. Slots in the horizontal walls allow pressure equalization with the test section. The plenum consequently provides an optimized distribution of pressure loads on the wind-tunnel structure when operated in extreme conditions. Furthermore, plenum pressure adaptation may be used for horizontal boundary-layer suction. The following wind tunnel corrections were applied in the test section. The horizontal, slotted walls were set to a diverging angle to compensate for the flow acceleration based on the increasing boundary layer displacement thickness and consequent buoyancy effects. The horizontal suction was not employed. On the vertical walls, a suction mechanism, exploiting the positive pressure difference between test section and diffuser, was applied (see Fig. 3.4).

The divergence and suction settings were optimized in advance to obtain a constant stream-wise wall pressure distribution throughout the empty test section for all relevant Mach numbers. The resulting angle of each horizontal wall was 0.08° along the complete test section length of 1.8 m. In Fig. 3.3 the Mach number distribution along the test section is displayed. The colored lines and the error bars represent respectively the linearly interpolated time-averages and the standard deviations of the Mach numbers. As one can see, the application of divergence and vertical wall suction (VWS) reduces the stream-wise increase in the flow velocity significantly and can lead to a rather constant Mach distribution throughout the whole test section. Since the side windows prohibit air suction in the range of $-1.2 < x/c < 1.7$, a slight increase of the Mach number occurs. Nevertheless, an optimum of suction settings for minimized boundary layer effects was found. A more detailed description of the facility and its characterization can be found in Scheitle and Wagner (1991).

In order to avoid possible damages to the high-quality and expensive glass side win-

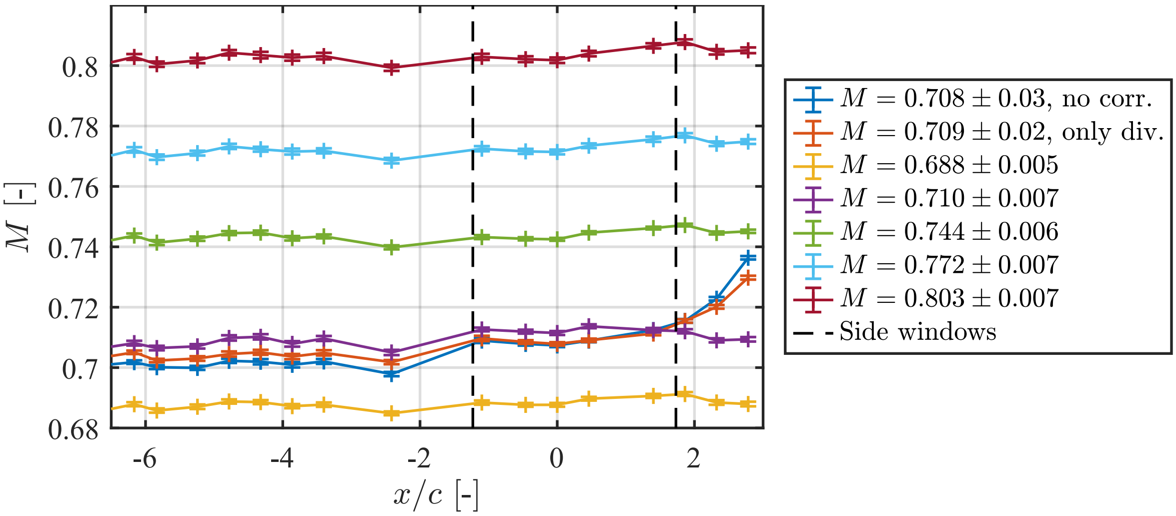

Figure 3.3: Mach number distribution along the test section with and without the boundary layer correction methods of divergence and vertical wall suction.

dows during the aeroelastic experiments, they were replaced by a pair of tempered Poly-methyl-methacrylate (PMMA) windows, which were customized for enhanced optical and mechanical access. For this, a concentric hole serving as shaft feedthrough was drilled into the plain circular windows before tempering, which was expected to reduce mechanical stresses from the manufacturing process. Despite this post-treatment, Schlieren measurements revealed substantial refractive-index gradients in the windows, in particular in the region of the drilled hole, which obstructed the application of the technique during wind tunnel runs (see Fig. 3.12). Due to this, the conventional Schlieren setup was replaced by background-oriented Schlieren, which is less sensitive to minor variations in density (see Section 3.3.1). Figure 3.4 right shows the options for optical access to the model from the top and the side of the test section that were provided and used during the experiments. Furthermore, the hydraulic mechanism for the rotation of the windows is shown, which allows for a precise adjustment of the window and model angle. This way, an in-run variation of the AoA can be performed, which was used for the determination of the buffet(ing) onset boundaries in Sections 4.1 and 4.2.

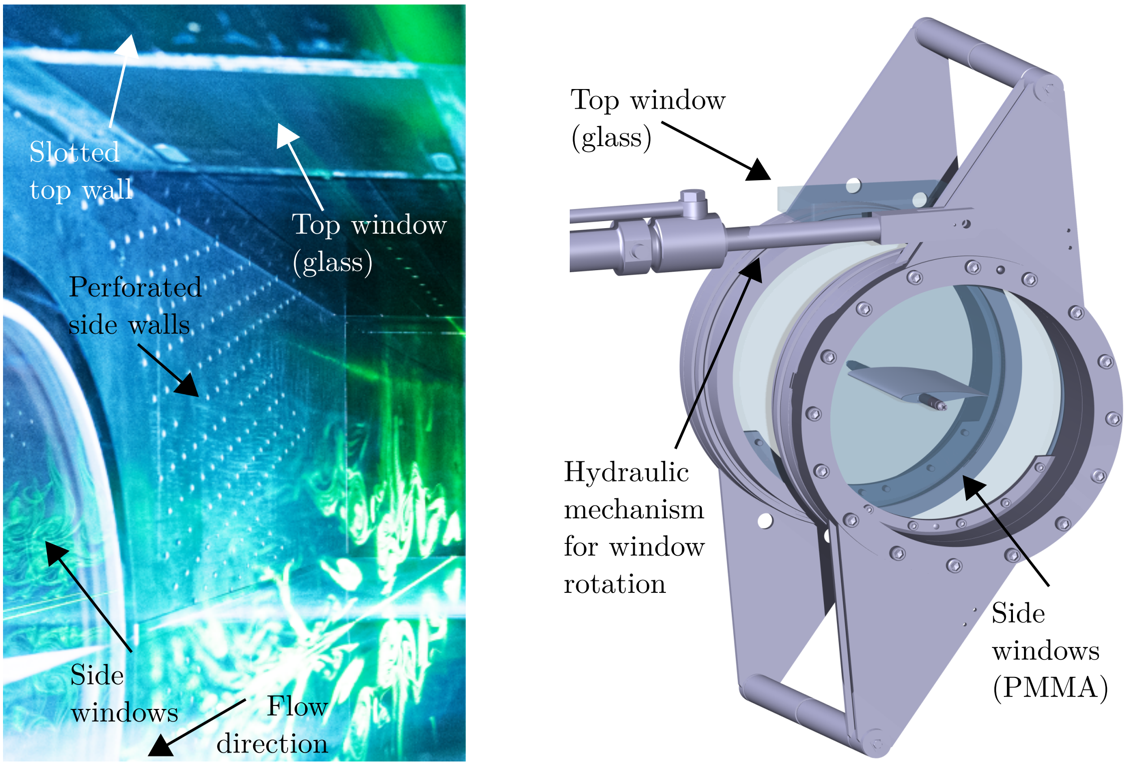

Figure 3.4: Photograph of the test section with suction slots and holes (left, Photo: C. Siebold, Universität der Bundeswehr). Options of optical access to the TWM test section (right).

3.2. Experimental Setup

In collaboration with the DLR Institute of Aeroelasticity (Göttingen, Germany) an experimental setup was designed for a spring-mounted two-dimensional wind-tunnel model with an optional pitching DoF. The capability of simultaneous 3D-force and aerodynamic moment measurements on either wing side – while maintaining optical access – was of major importance in the design process.

3.2.1. Wind-tunnel Model

After the publication of Jacquin et al. (2009), the supercritical airfoil profile OAT15A became a benchmark for the analysis of transonic buffet (e.g. Crouch et al. (2009) and Giannelis et al. (2017)) and was therefore selected for this campaign. Figure 3.5 shows the airfoil profile with a thickness of 12.3% of the chord. In order to allow reliable manufacturing, the original shape was minimally upscaled and cut off to obtain a trailing edge with finite thickness of 0.5% of chord, i.e. 0.75 mm.

The two-dimensional rectangular wing, shown in Fig. 3.6, had a span width of s = 298 mm, a chord length of c = 152 mm, and a thickness of d = 18.4 mm. Consequently, the wing introduced a maximum blockage of 3.5% in the test section at the highest angle of attack. Due to the resulting aspect ratio of 1.96 the presence of a clean 2D flow could not be assumed. However, detailed investigations of the span-wise shock front have revealed that despite 3D effects closer to the walls, the 2D characteristics of shock buffet remain dominant (Accorinti et al., 2023a). Boundary layer tripping was applied at x/c = 7% on both the suction and the pressure sides to maintain comparability to other experiments. For this, a line of circular stickers with a diameter of 3 mm, a thickness of 60 µm, and span-wise spacing of 6 mm was used, as shown in Fig. 3.6.

The wing integrated a hollow steel shaft and was manufactured from carbon-fiber-reinforced polymer (CFRP) by Weberschock Development (Gleichen, Germany) to maintain maximum stiffness inside the wing at a simultaneously low experimental mass ratio. An evaluation of the obtained rigidity was performed in Korthäuer et al. (2023b) and revealed a mostly stiff behavior with only minor bending and torsion. A circular pocket located close to the leading edge allowed for the insertion of extra weight for major adjustments of the weight and inertia distribution, which was not needed for the present work. The hollow shaft allowed the integration of cables and tubes. For

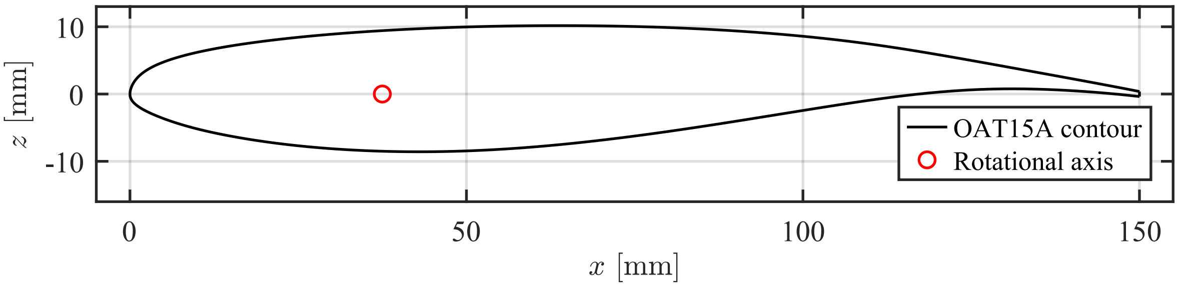

Figure 3.5: OAT15A airfoil profile with location of the rotational axis at 25% of chord.

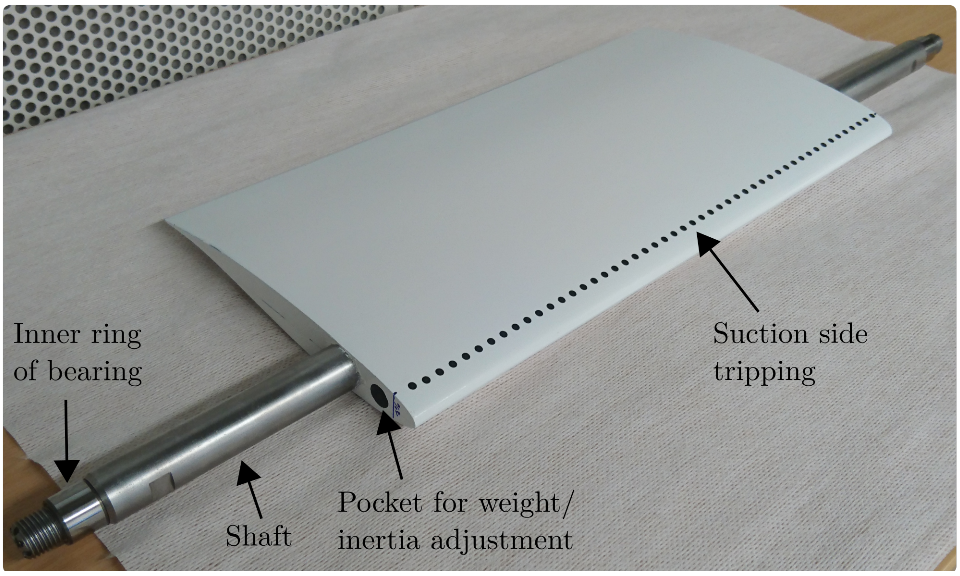

Figure 3.6: Photograph of the two-dimensional rectangular wing with integrated shaft at $x/c = 25\%$ of chord and tripping dots at $x/c = 7\%$.

subsequent measurement campaigns, a second version of the model was constructed, integrating pressure and temperature sensors to provide reference data for PIV and pressure-sensitive paint (PSP) experiments. In the present work, the focus was on the first safe operation and the use of purely optical measurement techniques, which is why the integration of sensors was omitted.

3.2.2. Structural Mechanism

Figures 3.7 and 3.8 show the complex realization of the experimental setup for the conduction of transonic buffeting experiments with reduced DoF as a photograph from the wind-tunnel test section with all corresponding parts and a CAD model (computer-aided design), respectively. The presented setup provided a compromise for all previously described functions. The wing was spring-mounted with a pitching DoF at reduced heave motion. Furthermore, the capability of simultaneous 3D-force and aerodynamic moment measurements on either wing side was given at the drawback of increased bending flexibility. The optical access of most of the wings's suction side surface was provided.

The rotational axis was defined by the steel shaft, located at 25% of chord. It was fed through the concentric holes in both side windows of the test section and supported in the plenum chamber by self-aligning bearings. The distance between windows and bearings had to be higher than expected due to the need of force introduction in the measurement plane of the 3D-force balances, which in turn increased the free shaft length and allowed additional vertical bending outside of the wing. After passing the bearings, the shaft was connected to a set of lever arms. The lower, vertical lever arm overtook the role of the torsional spring whose stiffness could be adjusted by setting its length and cross-section. Adjustments weights were connected to the side arms in order to adjust the moment of inertia and the center of gravity. For the sake of

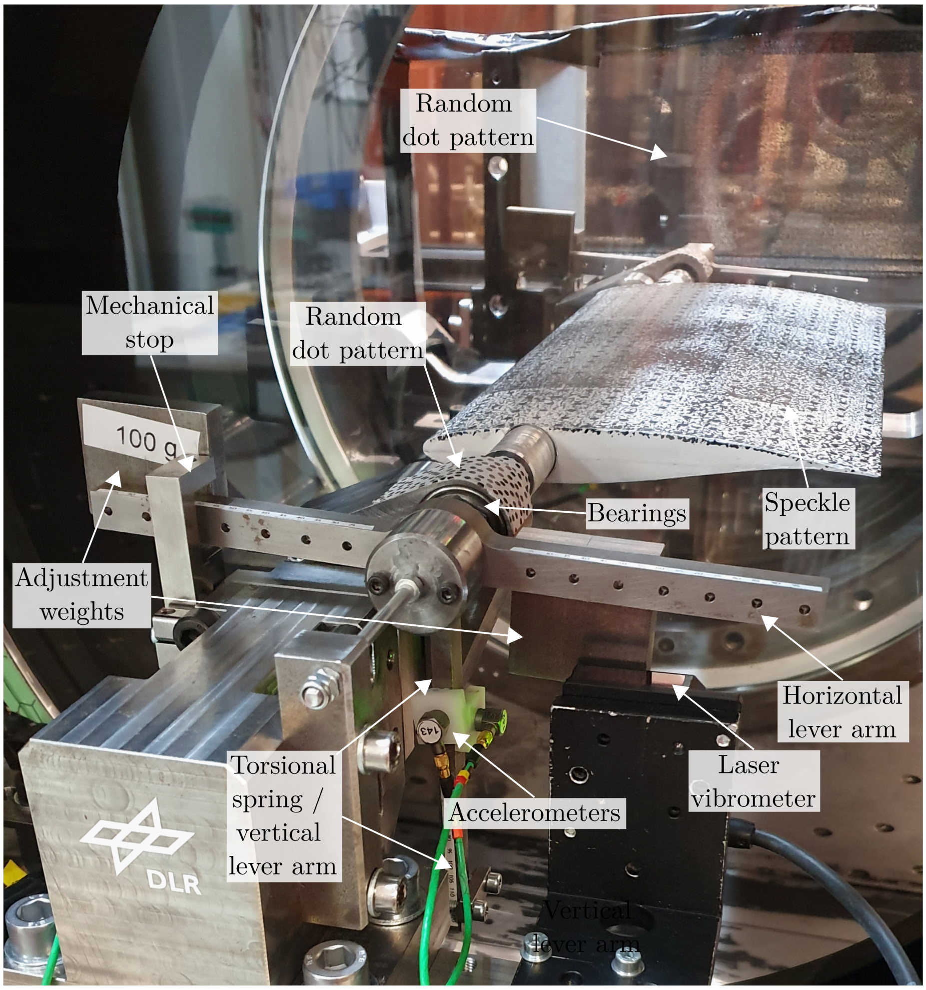

Figure 3.7: Photo of the mechanic implementation of the spring-mounted rigid wing with a pitching and reduced heave DoF, as well as applied measurement techniques.

reduced structural coupling in wind-off conditions, the latter was set to coincide with the rotational axis for all flexible cases. Accelerometers on the vertical lever arm and a laser-vibrometer on the horizontal lever arms were used to obtain online information about the current amplitude and frequency of the pitch motion. A mechanical stop was used on the lever arms to limit the maximum pitch amplitude to 2.5°. Wind tunnel runs exhibiting excessive pitch amplitudes close to the limit were interrupted prematurely to avoid structural damage.

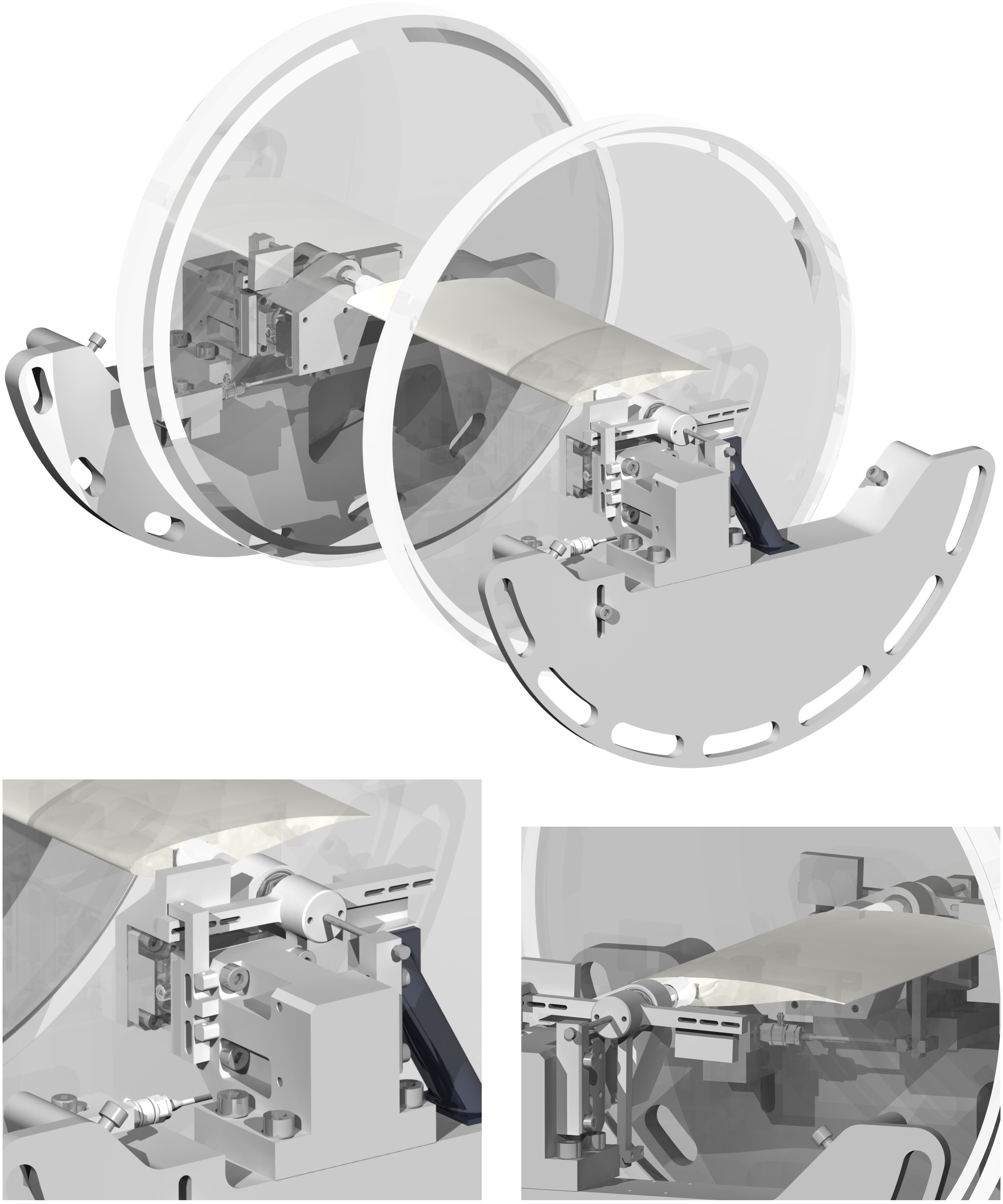

Figure 3.8: CAD model of the spring-mounted wing model with a pitching DoF and the structural mechanism attached to the wind-tunnel window frame.

3.3. Measurement Techniques

In order to observe, identify and quantify the phenomena of transonic buffet and buffeting (described in Sections 2.1.3 and 2.2.1), it is of paramount importance to study in detail the dominant features of the flow field as well as the structural motion. As numerical and experimental investigations have shown, the phenomenon of transonic buffet is highly sensitive to boundary conditions (Accorinti et al., 2022; Nitzsche et al., 2019), which leads to the conclusion that the intrusion of measurement probes may also alter the characteristics of the phenomena. Furthermore, despite the expectation of limited structural amplitudes (LCO) in the aeroelastic experiments and the provided safety measures, structural damage to the wing, the mechanism, or even the facility could not be fully precluded upfront. The deployment of optical measurement techniques allowed spatially and temporally highly-resolved, non-intrusive measurements at low risk of harming the equipment. No expensive, integrated sensors had to be subjected to possible detriment.

Two techniques were chosen for the presented wind-tunnel campaigns as designated by steps 1b and 1b (see Section 2.3). Background-oriented Schlieren (BOS) was used to determine regions of varying density gradients and to detect the location of the shock front and will be described in Section 3.3.1. The technique of digital image correlation (DIC) was used for deformation measurements of the wing and will be explained in Section 3.3.2.

3.3.1. Background-Oriented Schlieren

Background-oriented Schlieren (BOS) is an optical measurement technique for the visualization of variations of density gradients in compressible and thermal flows. It is based on the same principle as Schlieren photography and shadowgraphy, namely variations of the media's refraction index due to changes in the density. The lateral deflection of light rays is based on the linear relation of a fluid's density and its refraction index, which is described by the Gladstone-Dale equation

$$n - 1 = k_{\mathrm{GD}}\rho \tag{3.1}$$

for gaseous media, where n is the refractive index, ρ is the fluid density and $k_{\mathrm{GD}} \approx 0.23\,\mathrm{cm}^3\,\mathrm{g}^{-1}$, the Gladstone-Dale coefficient for air at standard conditions. Unlike these classical Schlieren methods, BOS applies correlation techniques on a background pattern to determine the variation in reafractive index.

Measurement principle

In Fig. 3.9, the schematic of a BOS setup is presented, which illustrates the underlying principle for measurements of density variations in the horizontal direction (x) on an airfoil. The setup consists of an illuminated background plane containing a random pattern, which is positioned behind the measurement volume. The typical size of the background pattern structures (e.g. a random dot) in the image should range on the order of 3 to 5 pixels (Raffel, 2015). In the case of uniform density in the measurement

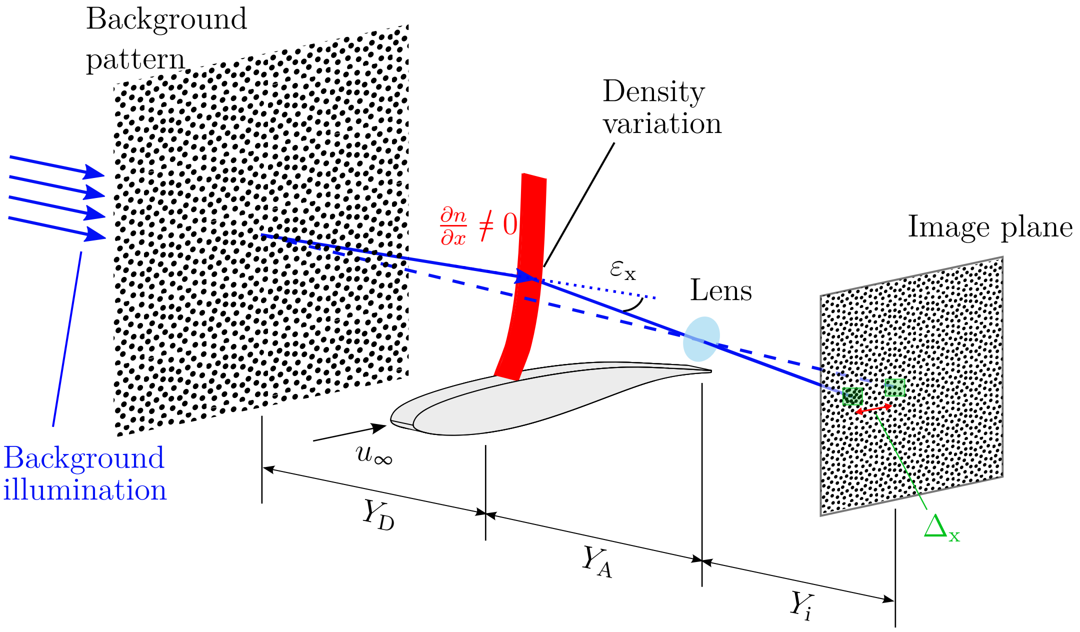

Figure 3.9: BOS working principle for an exemplary density variation created by the formation of a shock on a supercritical airfoil.

volume (for instance, when the wind tunnel is at rest), light rays passing the pattern will maintain their direction when traversing the volume so that the background pattern appears unaltered on the image plane after passing a lens or lens system (e.g. dashed line). If the some of the scattered light rays transit density gradients, they are deflected by the angle ε_x and ultimately reach the image plane at a different position deviating by Δ_x (solid line). Consequently, the corresponding pattern additionally appears at a different position in the image plane.

The resulting deflection angle ε_x is an integrated quantity depending on all variations of the refractive index n encountered along the light path

$$\varepsilon_\mathrm{x} = \frac{1}{n_0} \int \frac{\partial n}{\partial x}\, dy \tag{3.2}$$

where n_0 is a reference refractive index.

Under the assumption of paraxial recording and small deflection angles $\varepsilon_\mathrm{x} \approx \tan \varepsilon_\mathrm{x}$, the following formula for the image displacement has been derived by Raffel (2015)

$$\Delta_\mathrm{x} = F \left(\frac{Y_\mathrm{D}}{Y_\mathrm{D} + Y_\mathrm{A} - F} \right) \varepsilon_\mathrm{x} \tag{3.3}$$

where Y_D is the distance between the background pattern and the location of the density gradient, and Y_A the distance between the location of the density gradient and the lens. F represents the focal length of the lens.

The following practical considerations are derived from Eq. (3.3) in the work of Raffel (2015) regarding a focusing problem inherent to the BOS technique and the required trade-off in positioning of its components:

- Higher sensitivity, i.e. a larger image displacement Δx for the same ε_{x} is obtained for large Y_{D} and small Y_{A}. This contradicts the need of sharp imaging of the density gradients, which requires focusing on their location.
- At the same time, the imaging system should be focused on the background pattern to obtain a maximum contrast in the images for subsequent cross-correlation.
- As a compromise, it is suggested to position the background pattern closer to the object (the density gradient) than the camera, but to maintain the same order of magnitude for both their distances.
- To reduce the consequent image blur, small apertures are recommended for BOS imaging. They come with the additional beneficial reduction of spherical and chromatic lens aberrations. Consequently, to maintain sufficient contrast in the image, an intense background pattern illumination is required.
- On the other hand, to reduce blurring effects of temporal integration, snapshots as instantaneous as possible are desired. This requires a short exposure time with a high amount of light, which is why it was refrained from using an aperture.

Implementation of BOS at the Experimental Facility

In Fig. 3.10, the implementation of the BOS setup at the TWM is schematically displayed. Figures 3.7 and 3.14 provide additional photographs from inside the test section and the plenum chamber, respectively. In Table 3.1 the experimental parameters of the BOS measurements are summarized.

The conventional Schlieren illumination system of the TWM consists of an LED (Luminus CBT-120-B-C11-KM301, 462 nm), a dot aperture and a parabolic mirror. It was used to provide parallel light, which passed through the test section in the span-wise direction. The random dot pattern was printed on a transparent foil in a total area of 14 cm × 28 cm. It was mounted in between light source and test section, due to the

Parameter	Value	Unit
Camera	HS Vision Phantom V2640	
Dynamic range	12	bit
Pixel size	13.5 × 13.5	µm
Acquisition rate	1000	Hz
Exposure time	20	µs
Image resolution	1024 × 640	pixels
Optical magnification	16.6	
Interrogation window size	8 × 8	pixels
Window overlap	50	%
Displacement field resolution	256 × 160	

Table 3.1: Overview of the experimental parameters used for the BOS measurements and evaluation.

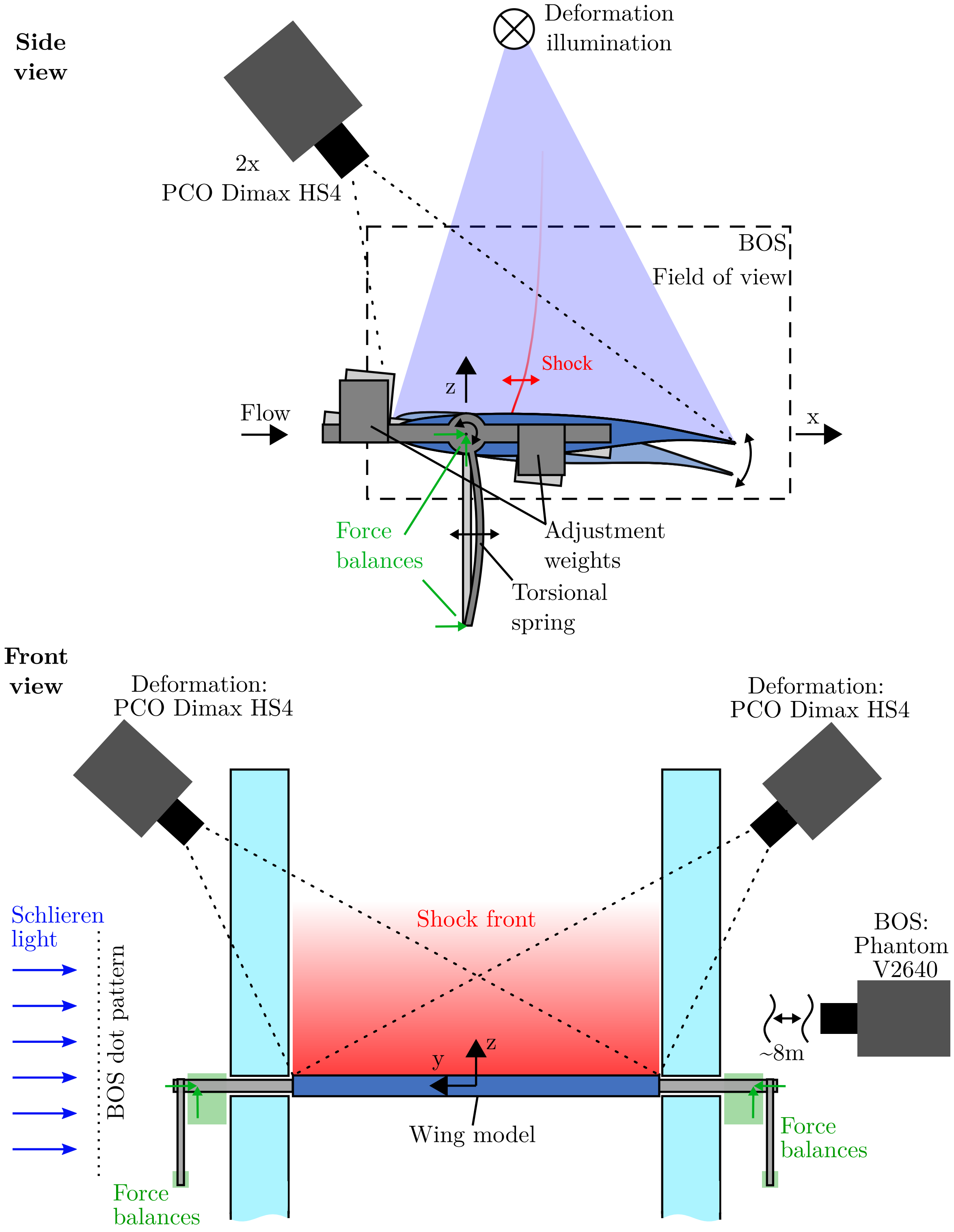

Figure 3.10: Sketch of the experimental setup including the spring-mounted rigid wing with a pitching DoF and reduced heave DoF and the applied measurement techniques.

spatial limitation by the plenum chamber rather close to the test section. It provided the required high-contrast background (as shown in the top row of Fig. 3.11). The pattern was composed of randomly positioned dots of 2 – 3 pixels in diameter that covered approx. 40% of the total area. Due to the mechanical stresses in the window and the concomitant refraction, the dot pattern was modified and appeared more as a speckle pattern, though it remained a granularity size of approx. 3 – 5 pixels. Images of the pattern were recorded in the displayed field of view (in Fig. 3.10, top) from the opposite side of the test section by a high-speed camera (Phantom V2640) with an image rate of 1000 Hz.

BOS Measurement Procedure

The typical procedure of BOS measurements is constituted of the following steps:

Reference image - Recording of a set of reference images in the undisturbed state, i.e. in flow-off conditions, typically right before or after the experiment. Consequent averaging reduces the effect of small fluctuations on the reference image. The top-left image in Fig. 3.11 shows the averaged raw-image in flow-off conditions. Patches were applied in the regions of the wing and other structural parts. Due to the distortion by the window and the trade-off in setting the focus, the dot pattern was altered to a more-speckle-like pattern. Nevertheless, the uniqueness and the contrast of the resulting pattern remained sufficient for evaluation. The indicated region of strong light distortion in the vicinity of the rotational axis is based on strong variations in density in the PMMA window from manufacturing.

Image acquisition with flow - Acquisition of a set of images in flow-on conditions, which contain distortions to the background pattern based on the regions of varying density gradients. In the top-right image of Fig. 3.11, an instantaneous raw image is displayed. Even without further evaluation, strong density gradients become visible, in particular at the shock front. The transition tripping at $x/c = 7\%$ introduces an oblique shock wave and further small shocklets in the first half of the chord become visible. The blurry region in the wake of the airfoil indicates the presence of density gradients, presumably a shear layer due to the pressure difference at the trailing edge induced by the boundary layer separation on the suction side.

Image correlation - A two-dimensional cross-correlation between flow-on images and the reference image is applied. For this, interrogation windows are successively shifted along the image in both directions of which each position results in a displacement vector (see Section 3.3.4). Typical evaluation methods being applied in other correlation-based techniques can be utilized (e.g. PIV, see Raffel et al. (2018)). In the present work, the displacement vector fields were obtained by analysis with the PIV evaluation tools of LaVision Davis 10.1. Figure 3.11, bottom, shows the color-coded displacement field Δ_x in stream-wise direction for the given example. Reliable displacement values could be obtained everywhere but in the region of the rotational axis (optical distortion) and in the right side of the field of view (spherical aberration). Despite the strong distortion in the region of the rotational axis, a correlation between the two images remained possible to some degree reducing the invalid region to a smaller extent as shown in the raw images.

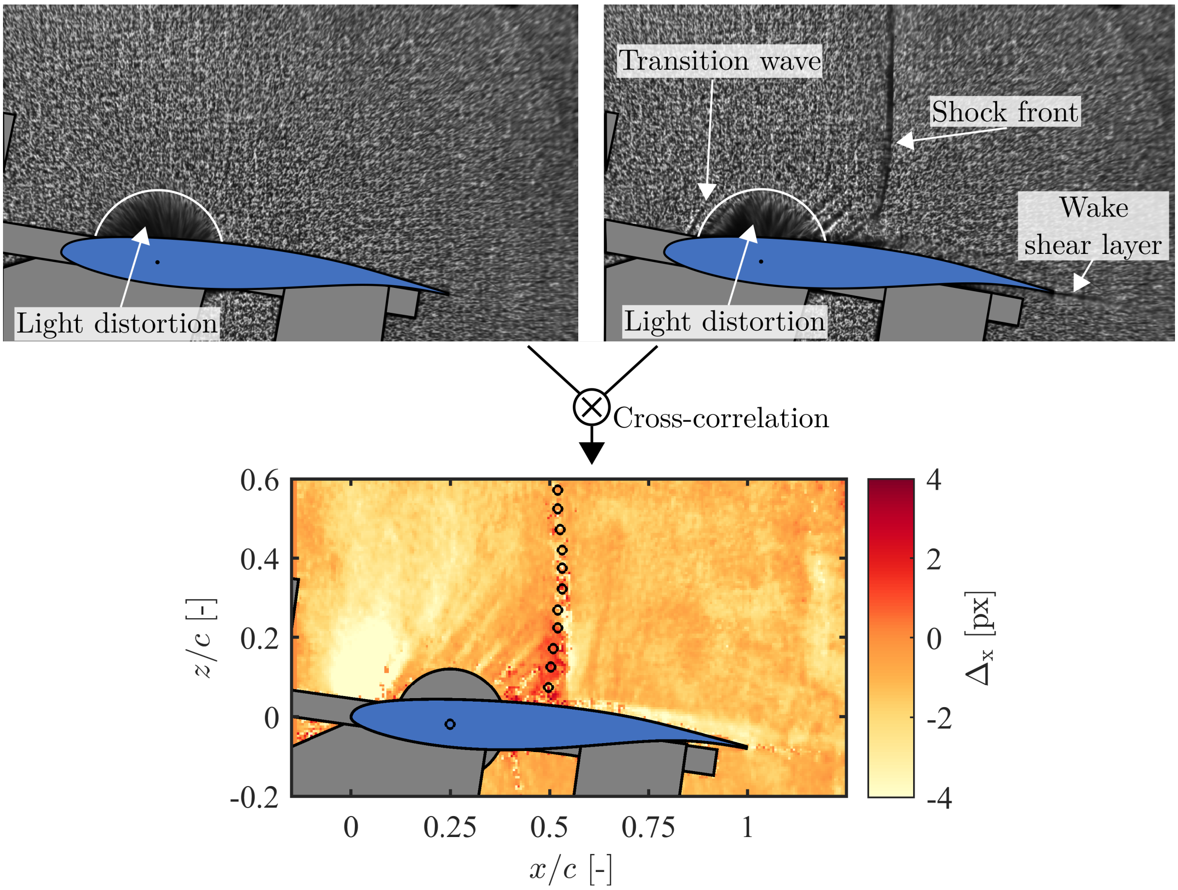

Figure 3.11: Top: Raw BOS images showing the background dot pattern in both states, the reference image at flow-off conditions (left) and an instantaneous image at $M = 0.74$. Bottom: The corresponding color-coded field of displacements in x-direction. Black circles represent the automatically determined shock position at different heights. Patches were applied in the regions of the wing and other structural parts for all images.

Image analysis - The obtained displacement vector fields were post-processed in MatLab. Based on the maximum stream-wise displacements, which correspond to the stream-wise density gradients, the shock locations at several heights were detected on the wing suction side (black circles in the bottom image of Fig. 3.11). For more details see Accorinti et al. (2022).

The Benefits and Limitations of BOS

Susceptibility to optical distortions - In contrast to classical schlieren, the principle of cross-correlation for the evaluation of BOS allows the presence of a higher flow-independent optical distortion. As long as the altered background retains a pattern of sufficient contrast and granularity (e.g. not given for the circular region in Fig. 3.11), the measurements are not impaired. Given the availability of a high-precision Schlieren setup at the TWM, its applicability for the given experiment was evaluated in the first place. Figure 3.12 shows the color-coded image intensity based on the classical Schlieren setup measuring the streamwise density gradients. The left image shows the absolute intensities at wind-off conditions. The high sensitivity of the setup allowed for a precise determination of the flow-independent refractive index in the two side windows at wind-off conditions. It clearly presents a circular pattern indicating mechanical stress from the manufacturing process. However, already these comparatively minor light deflections, lead to a locally exceeded dynamic range of the camera and consequent loss of information. The right image shows the color-coded intensity of a run at $M = 0.72$, which was corrected by subtracting the reference (wind-off) image. At these aerodynamic conditions no shock but only compression waves towards the trailing become visible. Well reproduced regions of acceleration at the leading edge and the wave structures farther from the surface in the aft section above the suction side are visible. However, areas close to the surface and in the center region display a discontinuous intensity difference, due to the insufficient dynamic range, which makes the results unreliable.

Spatial resolution - Besides the generally favored, higher sensitivity of the classical Schlieren setup at the TWM, another drawback of BOS is the lower resulting spatial

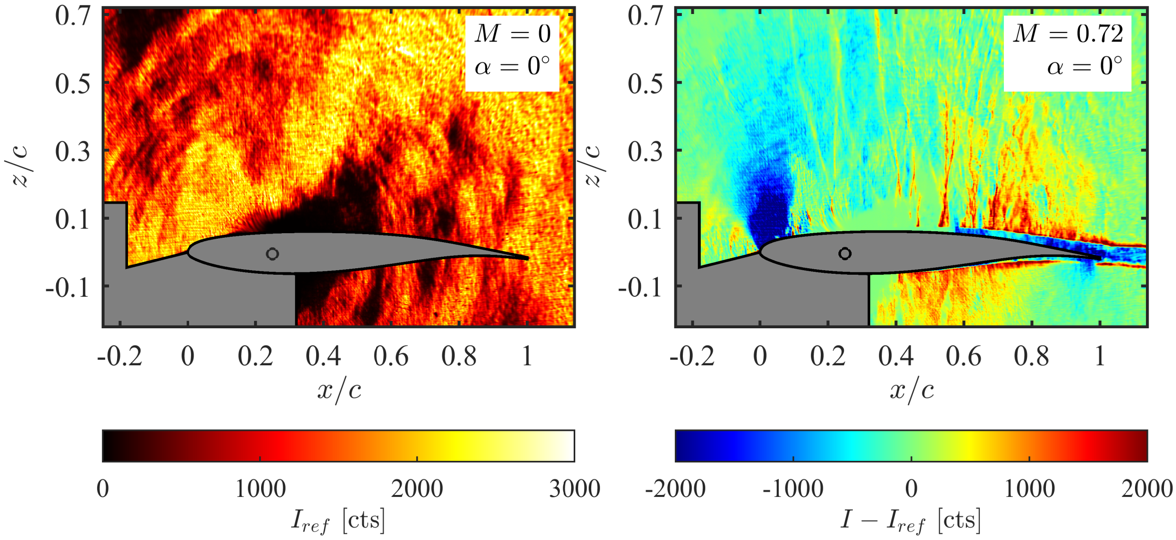

Figure 3.12: Exemplary results of classical Schlieren measurements exhibiting strong distorting effects by the PMMA windows. Left: image at flow-off conditions with color-coded absolute image intensity; right: color-coded wind-on image corrected by the intensities of the wind-off image.

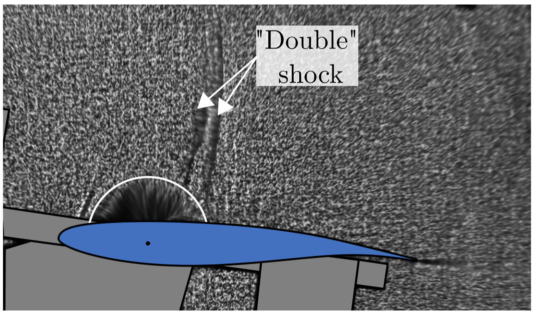

Figure 3.13: Raw BOS image presenting two shocks, presumably due to a span-wise curvature of the shock front.

resolution. The principle of cross-correlation reduces the spatial resolution by a factor up to the size of the interrogation windows (see Table 3.1).

Integrative principle - Both classical and background-oriented Schlieren are integrative measurement techniques, i.e. all density gradients encountered along the light path result in a single integrated quantity that does not allow the determination of its - in this case span-wise - single contributions. Other techniques allow a planar evaluation but come at higher experimental complexity (e.g. focused Schlieren or particle image velocimetry). In Fig. 3.13, an instantaneous BOS image is shown, which presents two dominant regions resembling two separate shocks or shock fronts. These are the result of the span-wise integration of an oblique shock front or 3D effects due to interaction with the side wall boundary layer. Given the integrative principle, the span-wise origin of the single contributions can not be traced back and the algorithm-based determination of the shock location might obtain an unambiguous result. However, the influence of such an event was deemed minor, as the appearance of a “double” shock only rarely happened (Accorinti et al., 2022).

Optical accessibility - Given sufficient frontal illumination of the pattern, BOS can also be applied in facilities that do not allow two-sided optical access (no necessity of illuminating from the back). For instance, in Accorinti et al. (2023a) the surface pattern applied to the suction side of the wing was used for the analysis of the span-wise shock formation in buffet conditions.

Overall, the experimental simplicity, reliability, and robustness of BOS, including the correlation-based digital analysis, are the main advantages of the technique (Raffel, 2015) and reason for its application in this work.

3.3.2. Stereo Digital Image Correlation

Measurement Principle and Implementation at the Experimental Facility

Given the importance of their interaction with the flow, three-dimensional structural surface displacements of the wing were measured via stereo digital image correlation (DIC). It is a non-intrusive, optical measurement technique that is generally used to analyze the displacement and deformation of a surface. It was invented in the early 1980s (Sutton et al., 1983) and has become a standard technique when it comes to structural surface measurements.

Surface images are captured by one or more cameras. Depending on the application, different configurations and calibration methods are typically applied for the determination of surface displacements, whereas the measurement principle remains similar. By the use of correlation algorithms between subsequent images, the movement of distinct surface features is tracked. The resulting displacement data can be used to evaluate the surface deformation or motion under load or to calculate strain, stress, and other mechanical properties of the observed object.
The following paragraph will give an overview about the measurement principle and the final implementation at the TWM. Recommendations are based on the detailed work about the technique of Schreier et al. (2009) and Hartley and Zisserman (2004).

Camera configuration - While for the detection of planar motions or deformations a single camera setup is sufficient, the reconstruction of three-dimensional surfaces, as in the present case, either requires a highly rigid model that is not deformed under loads (assumption of a rigid-body movement) or, in case of a deforming structure, the combination of multiple cameras to extract the additional depth information. As the actual degree of rigidity of the wing was unknown before the experiments, a stereo configuration of two high-speed cameras (PCO Dimax HS4) was installed to observe the suction side of the wing from two directions through the side windows of the test section. In Fig. 3.10, the positioning of the cameras is schematically shown and Fig. 3.14 presents a photo of the actual implementation at the TWM. The two cameras were mounted on the rotating window frame on either side of the test section at a maximum height to obtain the highest possible observation angle and to not obstruct the light path for the BOS measurements. Due to the restrictive mounting space in the plenum chamber and the cameras' extensive sizes, the optical axis had to be aligned parallel to the flow direction. Mirrors allowed for the indirect observation of the wing surface. Figure 3.18 displays images from both cameras, observing the wing suction side through the mirrors.

The resulting observation angle of 60° was lower than the recommended 15 – 35°. The lower the angle, the higher is the in-plane displacement accuracy and the better are the cross-correlation results. Higher observation angles however increase the out-of-place displacement accuracy, which is of particular interest for the pitch and heave motion of the wing (Sutton et al., 1983; Rory Bigger et al., 2018). As will be shown in the following paragraphs, the setup provided satisfactory results with the high observation angles. However, this resulted in two consequences: firstly, the optical magnification factor strongly varied depending on the location on the wing surface and ranged from

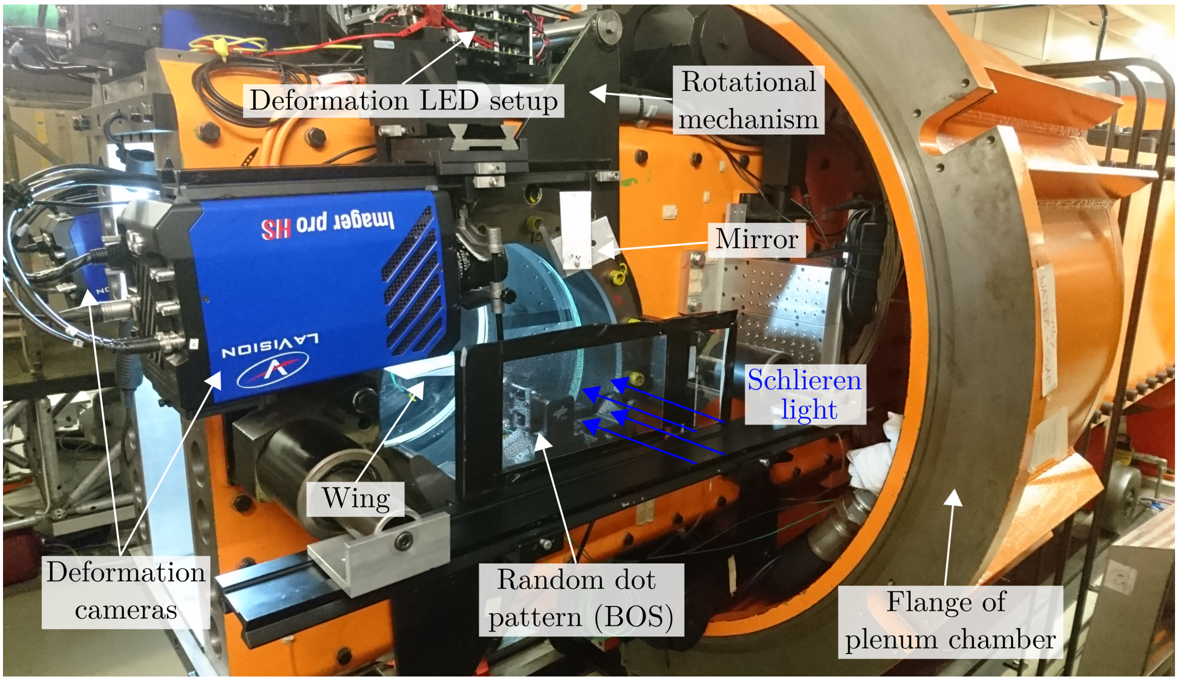

Figure 3.14: Photo of the test section showing the location of the high-speed deformation cameras and the installation of the background dot pattern for BOS.

$4.56 < M_{\text{DIC}} < 7.31$. The consequent strong perspective distortion demands for a sufficiently adapted surface pattern and complicates the cross-correlation between images of the different cameras. Secondly, the necessity of sharp imaging over a long range along the optical axis required appropriate optical adaptation (small aperture) and consequently a strong surface illumination to provide enough signal. Furthermore, the observation through the PMMA windows of a thickness of 50 mm introduced image distortions and required a more complex calibration method.

Surface pattern - The distinct surface features to be tracked in DIC can be inherent to the object's surface (cracks, edges, or patterns) or manually applied to the surface (speckle pattern). As the wing's surface was immaculate, it did not contain any features for tracking, but required the manual application of a pattern. The optimal feature size (and distance between features) ranges from 3 to 5 pixels, where it is of major importance to maintain a high contrast and randomness to ensure optimized results (Rory Bigger et al., 2018). For a high contrast of the surface pattern – which is essential for good correlation results – the wing was painted with a base layer of signal-white two-component acrylic paint (Mipa 2 K PUR-HS). The overlaying dull black speckles were created by roll-painting a light layer of water-based black paint on a rough sponge, which was then iteratively imprinted on the wing. Due to the paint dullness, reflections could be reduced. The application of the sponge created randomly shaped patterns, which improve correlation results. Figure 3.15 shows the wing with the applied surface pattern. The additional underlying regular dot pattern was applied for preliminary tests and remained to avoid surface impairment during its removal. The resulting pattern led to a distinct feature size in each camera ranging from 3 to 10 pixels for the far end and 10 to 30 pixels at the close end of the wing. It allowed sufficient granular

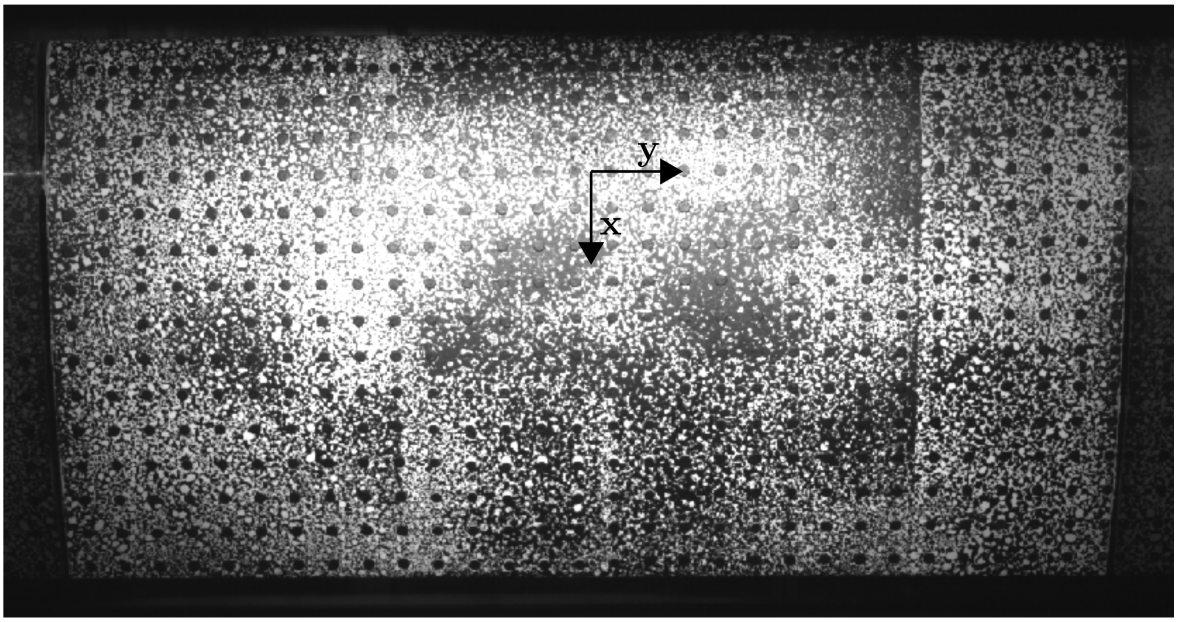

Figure 3.15: Top view of the wing suction side with applied DIC speckle pattern.

features even at the far end for the consequent process of image cross-correlation.

Optical considerations and illumination - A Zeiss Distagon objective lens with a focal length of $F = 35\,\mathrm{mm}$ was used for both cameras allowing the capturing of the entire upper wing surface. The application of a Scheimpflug adapter was not possible without interfering with the BOS field of view or reducing the AoA range. Given the comparatively large range of required depth of focus, a $(F/11)$-aperture provided a compromise for sufficiently sharp imaging of all wing regions at simultaneous sufficient light intensity. The rather small aperture and the need for high frequency recording and consequent low exposure time led to the requirement of strong surface illumination. A set of four high-power LEDs (Luminus CBM-120-UVX, 410 nm) was installed on top of the test section to illuminate the wing surface in pulsed mode to allow unblurred images at maximized intensity. The illumination setup was optimized for measurements using PSP and provided the highest light intensity possible given the restricted mounting space.

Camera calibration - Similar to human vision, the utilization of a stereo camera setup allows for the calculation of depth information based on the two varying images of the same object. This requires two basic steps, a correlation of the two camera images to determine the corresponding locations of a distinct feature in the respective camera images, and secondly, a calibration that relates those feature locations on the camera images with respect to the three-dimensional world coordinates. In the case of an undistorted projection of the object on the imaging plane (or only minor radial distortion by an objective lens), a pinhole model can be used for the camera calibration. It is based on intrinsic and extrinsic camera parameters that can be determined by multiple arbitrary recordings of a calibration target, containing known, well-defined markers. The three-dimensional camera position is hereby defined with respect to the world coordinate system (x^w, y^w, z^w) and allows for an affine transformation in

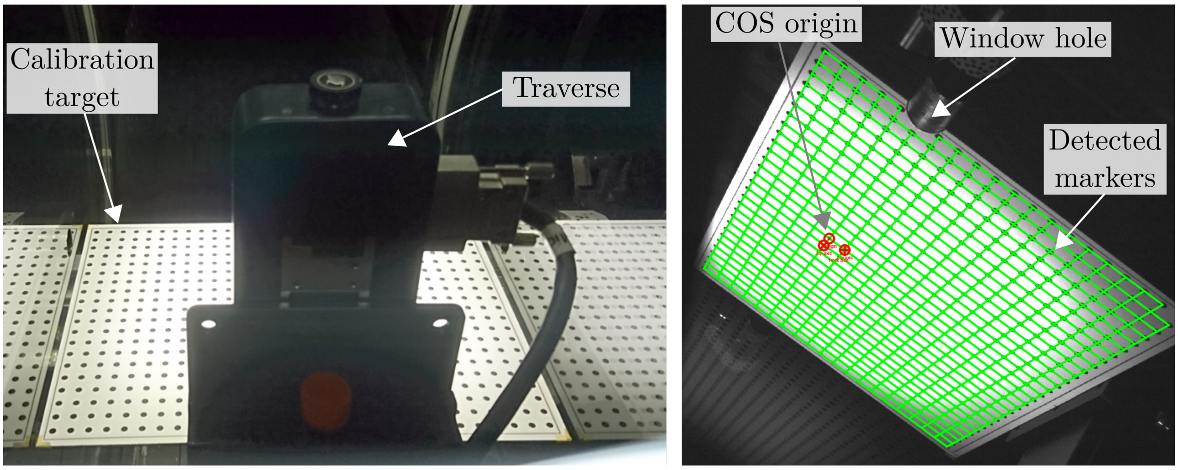

Figure 3.16: Co-planar calibration process: Calibration target mounted on traverse in the test section (left) and exemplary calibration image showing detected circular markers and the selected origin for the coordinate system.

homogenous coordinates from the world to the image coordinates (x^1, y^1) of camera 1. However, the required inverse transformation matrix for the determination of a three-dimensional surface from a single recorded two-dimensional image does not exist. This explains the necessity of a second, equally calibrated camera for a relation of world coordinates (x^w, y^w, z^w) to the image coordinates (x^2, y^2) of camera 2. Under consideration of the epipolar constraint, which geometrically defines a relation between the two image planes, the reconstruction of a three-dimensional surface is possible (Schreier et al., 2009).

Due to the thick side windows, the projected image of the wing was distorted, which introduced major errors in the application of the pinhole model. For this reason, a co-planar calibration was applied, according to Soloff et al. (1997). The calibration target of a size of 200 mm × 290 mm provided markers in the ranges of $-55\,\mathrm{mm} < x < 135\,\mathrm{mm}$ and $-140\,\mathrm{mm} < y < 140\,\mathrm{mm}$, respectively. It was precisely positioned horizontally in the test section and defined the coordinate system (COS) origin aligned with the center of the holes in the windows, as shown in Fig. 3.16, right. This position later corresponded to the location of the rotational axis. As a next step, the pattern was vertically traversed through the measurement volume in the range of $-40\,\mathrm{mm} < z < 40\,\mathrm{mm}$ by steps of 2.5 mm (see Fig. 3.16, left). For each of those co-planar target locations, a stereo set of calibration images was recorded. By automatic detection the respective image coordinates of the markers could be determined for each camera. The combination with the exactly known real-world marker positions, resulted in a cloud of defined points in space and the corresponding image coordinates of both cameras. The intrinsic and extrinsic camera parameters were determined from these coordinates. A third order polynomial was fitted by a least-squares optimization and allowed for the correction of the relation of image coordinates $(x^1, y^1)^{-1}$ and $(x^2, y^2)^{-1}$ with the world coordinates $(x^w, y^w, z^w)^{-1}$ in the calibrated volume.

Figure 3.17 shows the dewarped calibration target, reconstructed from both camera images, and the locations of the target markers in the underlying coordinate systems

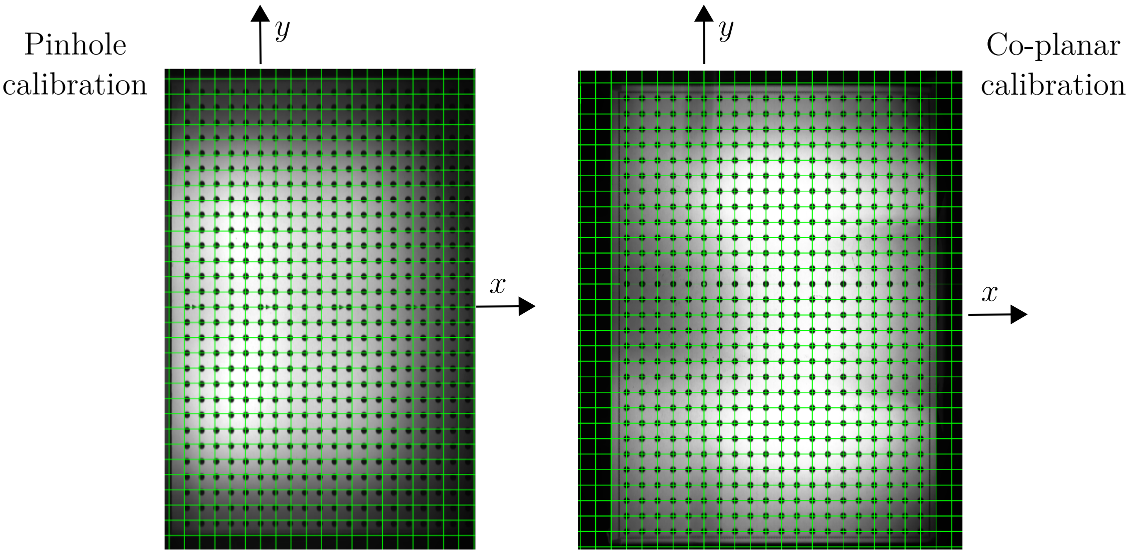

Figure 3.17: Result of calibration process: Surfaces of the calibration target reconstructed from both camera images for a pinhole calibration model (left) and the co-planar calibration (right).

represented by the green grid. For the pinhole calibration on the left, a good agreement is only obtained in the vicinity of the selected COS origin. Deviations towards the outer image regions are based on the refraction in the thick side windows. The equivalent result for the co-planar calibration (right) shows a good agreement in all regions of the target and hereby provides a solid basis for sophisticated deformation measurements.

DIC Measurement Procedure

For the process of DIC-based deformation measurements the software LaVision Davis 10.1 was used. After the co-planar calibration, the typical procedure for the determination of wing displacements consisted of the following steps, which are displayed schematically in Fig. 3.18. In Table 3.2 the resulting measurement parameters of the technique are summarized.

Parameter	Value	Unit
Camera	PCO Dimax HS4	
Dynamic range	12	bit
Pixel size	12 × 12	µm
Acquisition rate	1000	Hz
Exposure time	200	µs
Image resolution	1392 × 1392	pixels
Optical magnification	4.56 to 7.31	
Interrogation window size	19 × 19	pixels
Window overlap	6	pixels
Surface field resolution	281 × 575	vectors

Table 3.2: Overview over the experimental parameters used for the stereo DIC measurements and evaluation.

Wind-off images and initial surface reconstruction - Before and/or after the experiments, a set of images (at least one per camera) is recorded without flow, as shown for the top pair in Fig. 3.18 ($t = 0$). For an initial surface reconstruction $\mathbf{S}(0)$, corresponding regions in both camera images have to be found. This is accomplished by cross-correlation of both images in shifting interrogation windows (i, j) with a certain overlap. Due to the highly distorted camera images, shape functions have to be applied to the interrogation areas, which comes at high computational effort. Without, the determination of a sufficient correlation is very unlikely. This is exemplarily shown for the corresponding interrogation areas marked by the red frame in the top of Fig. 3.18. Once the image coordinates of the best corresponding patterns

$$\begin{pmatrix} x^1_{i,j}(0) \\ y^1_{i,j}(0) \\ x^2_{i,j}(0) \\ y^2_{i,j}(0) \end{pmatrix}$$

are found, the acquired calibration function can be applied to translate the coordinates into the world coordinate system

$$\begin{pmatrix} x^w_{i,j}(0) \\ y^w_{i,j}(0) \\ z^w_{i,j}(0) \end{pmatrix}$$

Hereto, the calibration provides a line of sight for each image point on which the found

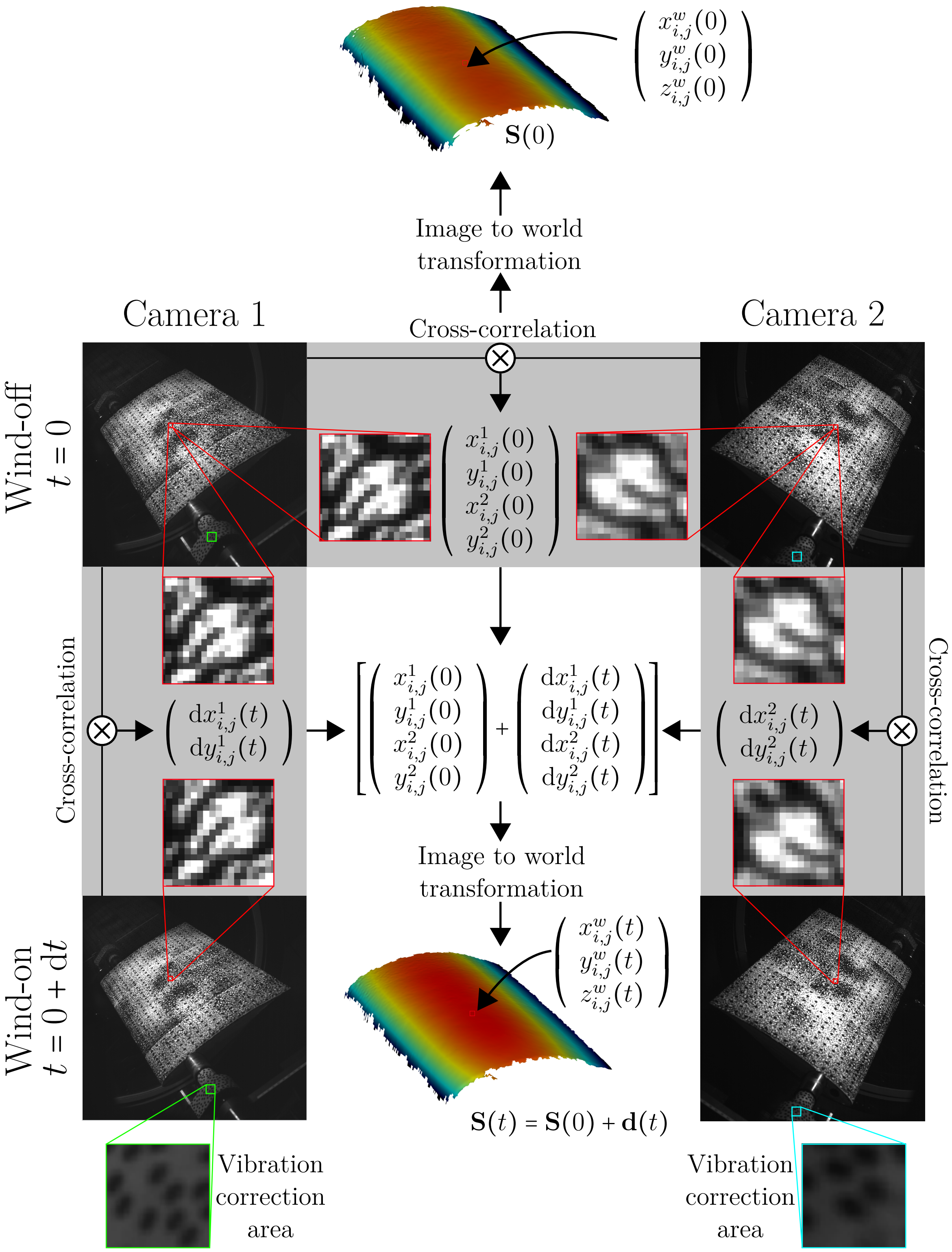

Figure 3.18: Schematic of DIC measurement procedure with reference to wind-off images.

interrogation area is located in the 3D world. Ideally, the lines of sight of the two cameras will intersect in 3D space at the object position belonging to that interrogation area. In reality, they will hardly intersect, but there will be a 3D world location with the smallest distance, which is defined as the object point. By this, the whole surface $\mathbf{S}(0)$ can be reconstructed for every image pair – also at wind-on conditions (see Fig. 3.18).

Reprojection error - If the defined object point is now projected back into the camera images using the calibration data, there is a deviation in the image from the correlated to the back-projected position (reprojection error). This error can be used to describe the uncertainty of the surface reconstruction (Lin et al., 2020). In Fig. 3.19 the spatial distribution of the reprojection error is presented. Regions close to the windows with higher distortion and/or poor correlation quality present a higher deviation of up to 0.38 %. Besides this, the error can locally reach up to 0.2 % due to lower correlation values, whereas most of the surface ranges in between 0.03 % to 0.13 %. As can be seen for $\mathbf{S}(0)$ in Fig. 3.18, at the leading edge and close to span-wise ends, the reconstruction is limited when not both cameras provide information of a certain area (e.g. obstruction of line of sight) or the correlation coefficient remains too low (e.g. due to unsharp imaging, strong refraction, pattern structures of the wrong size or insufficient contrast due to illumination).

Wind-on images - At experimental conditions both cameras record images at the selected frame rate. Here, a total number of 13000 images was recorded with a frame rate of 1000 Hz for the runs of continuous AoA variation, while at constant conditions 5000 images were acquired.

Camera vibration correction - Due to wind-tunnel and camera vibrations, the recorded wind-on images were corrected with respect to the reference images. For this, the random dot pattern attached to the fixed mechanical parts outside the test section served as fixed reference. By cross-correlation of a selected region of that pattern, marked by the green/turquoise rectangles in Fig. 3.18, the vibration-based shift of

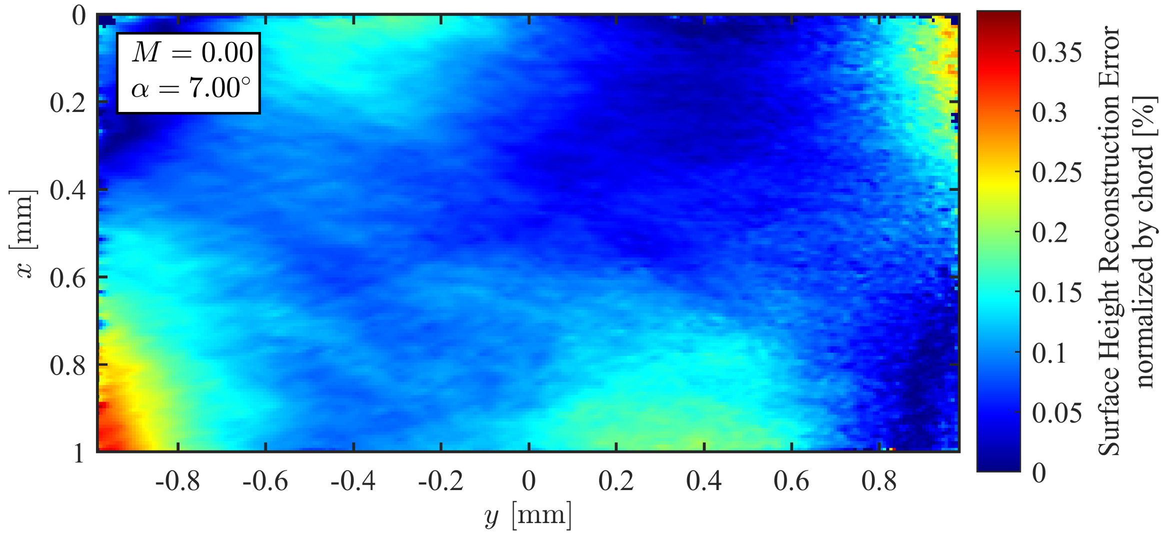

Figure 3.19: Surface height reconstruction error of DIC measurements at wind-off conditions.

each camera could be extracted and used for the correction of the entire set of images. By this, the introduction of artificial displacements or impaired correlation results could be prevented.

Image displacements and surface reconstruction - After the vibration correction, the surfaces for each point of time in the experiment are reconstructed. Given the two, highly-distorted camera images, the computational effort of cross-correlating was expected to be very high. Due to this, the evaluation of displacements relative to the respective reference (wind-off) image for each camera was chosen as a more effective method. The two camera images that were recorded at a certain point of time t during the experiment were thus not correlated with each other but with the respective reference (wind-off) image as shown on the left and right in Fig. 3.18, respectively. As a result, the image based displacements

$$\begin{pmatrix} \mathrm{d}x^1_{i,j}(t) \\ \mathrm{d}y^1_{i,j}(t) \end{pmatrix} \text{ and } \begin{pmatrix} \mathrm{d}x^2_{i,j}(t) \\ \mathrm{d}y^2_{i,j}(t) \end{pmatrix}$$

for each interrogation area (i, j) are obtained. Given the lower distortion of the correlating areas, the determination of their displacement is more efficient (Schreier et al., 2009). By addition of the displacements to the reference image coordinates at $t = 0$, the image coordinates for t are obtained

$$\begin{pmatrix} x^1_{i,j}(t) \\ y^1_{i,j}(t) \\ x^2_{i,j}(t) \\ y^2_{i,j}(t) \end{pmatrix} = \left[\begin{pmatrix} x^1_0 \\ y^1_0 \\ x^2_0 \\ y^2_0 \end{pmatrix} + \begin{pmatrix} \mathrm{d}x^1_{i,j}(t) \\ \mathrm{d}y^1_{i,j}(t) \\ \mathrm{d}x^2_{i,j}(t) \\ \mathrm{d}y^2_{i,j}(t) \end{pmatrix} \right] \tag{3.4}$$

The consequent translation into world coordinates by application of the calibration function allows for a more efficient surface reconstruction $\mathbf{S}(t)$ at any point of time t. The actual three-dimensional displacement with respect to the wind-off conditions can be determined by vector-wise subtraction of the wind-off surface:

$$\mathbf{d}(t) = \mathbf{S}(t) - \mathbf{S}(0) \tag{3.5}$$

Figure 3.20 shows the resulting vertical displacement for an exemplary wind-tunnel run with fixed wing in natural buffet conditions at $\overline{M} = 0.74$ and $\overline{\alpha} = 6.48°$. The deformation of the wing and the consequences for the experiments are discussed in Section 4.3 (Korthäuer et al., 2023b).

In Fig. 3.21 the instantaneous spatial distribution of the stereo reconstruction error is displayed. It represents an additional source of uncertainty, which is based on the reprojection of the results of temporal correlation of the images, similar to the surface height reconstruction error in Fig. 3.19. The shock front clearly induces an increased uncertainty that rises on both sides towards the respective span ends. These are the most critical regions as the camera's respective observation distances differ the most, the distortion of the pattern by the shock is consequently as different as it can get. At $y = -0.35\,\%$, the stereo reconstruction is lower because both cameras experience a similar distortion. In similarity to BOS, the stereo reconstruction error represents the optical footprint of high density gradients. By evaluation of its characteristics, it allows the determination of dominant shock oscillation frequencies and relative amplitudes. It may actually be used as a redundant or replacing technique for BOS if no accurate determination of shock locations is required.

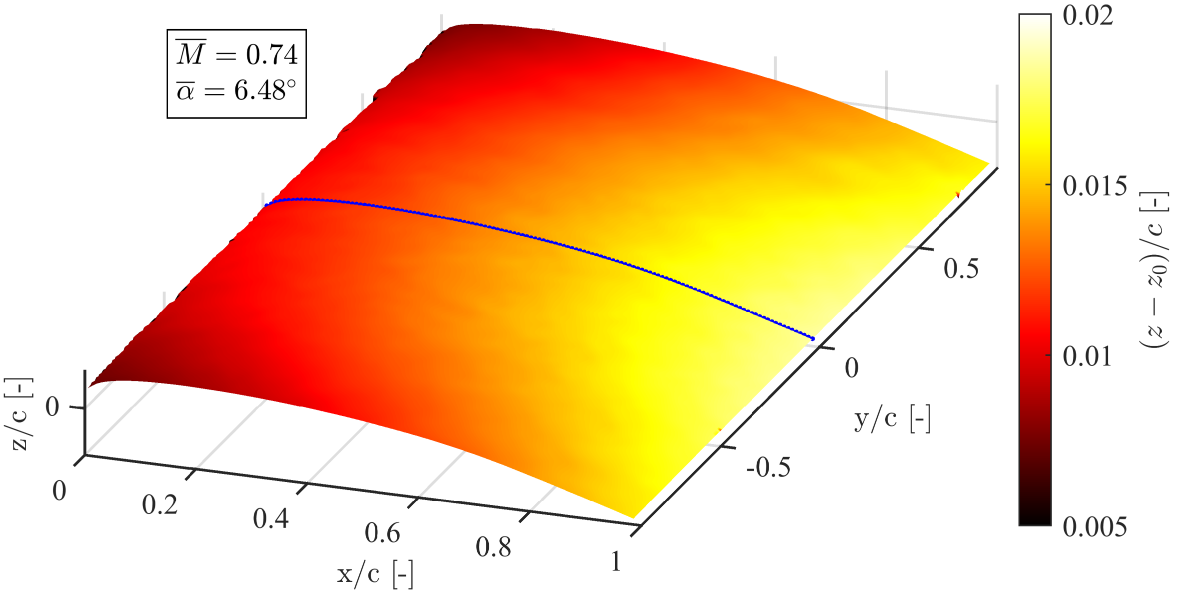

Figure 3.20: Averaged surface with color-coded vertical displacement field obtained by DIC measurements with center cut highlighted in blue.

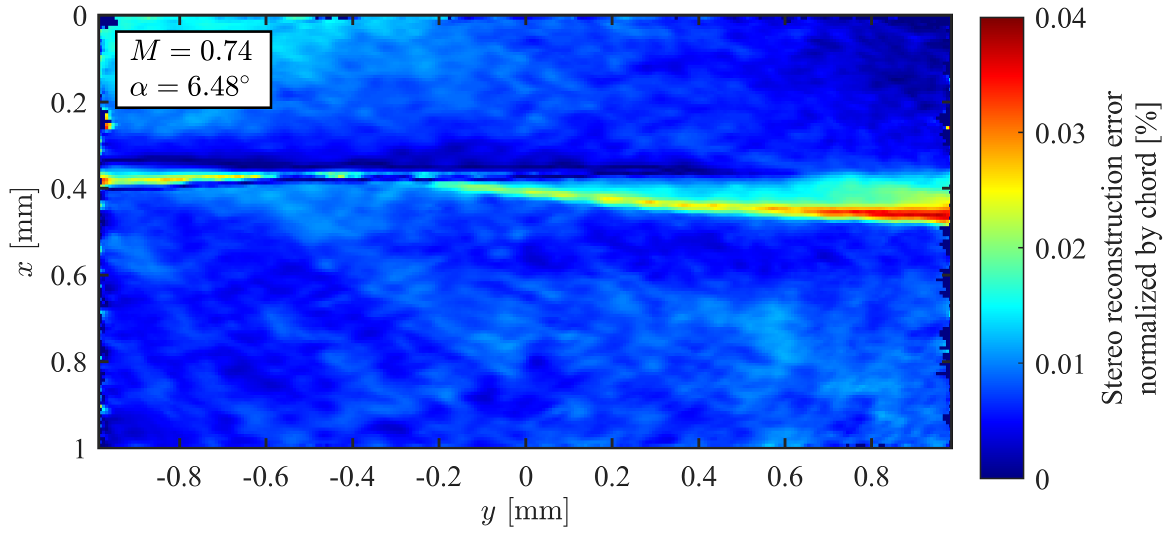

Figure 3.21: Instantaneous distribution of the stereo reconstruction error of DIC measurements at wind-on conditions.

Transformation to Airfoil Coordinates

In order to evaluate the aerodynamically important quantities angle of attack α, the heave motion z_{A} and the surge motion x_{A}, the surface data was post-processed in MatLab. For this, a least-squares fitting algorithm was programmed that allowed for the determination of the optimal transformation of one arbitrary curve to match another. Therefore, the rotation angle α and the translation of its rotational center $(x_{\mathrm{A}}, z_{\mathrm{A}})$ - in this case the shaft axis - were varied to fit the original OAT15A contour to the contour of a chord-wise cut through the measured surface. This procedure has - to the author's best knowledge - been firstly applied to retrieve airfoil coordinates from suction surface measurements and proofed to be a successful tool.

Figure 3.22 shows the fitting result for the exemplary blue center cut at $y/c = 0$ in Fig. 3.20. The black dashed curve represents the 'original' OAT15A contour, which is transformed (red) to match the measured surface contour (blue). The resulting transformation values are displayed in the top right corner. Figure 3.23 presents the resulting span-wise distribution of the transformation results α, x_{A}, and z_{A} for the exemplary run with $M = 0.74$. Black lines represent the mean values and the gray regions show the fluctuations based on the standard deviation. Towards the span-wise wing ends, the results become unreliable due to missing information in the surface data and consequent low fit quality. In the region of $-0.9 < y/c < 0.9$, the estimated values show a rather even distribution for the angle of attack α with slight increase towards high y/c. The surge motion x_{A} presents a stronger trend indicating a slightly oblique wing positioning. The heave motion z_{A} clearly shows wing bending with a pronounced region towards lower y/c. The partially negative values stem from mounting the wing shaft slightly below the coordinate system y-axis, which was defined concentric through both window holes. The lower mounting allowed a free heave motion without structural interference of the windows.

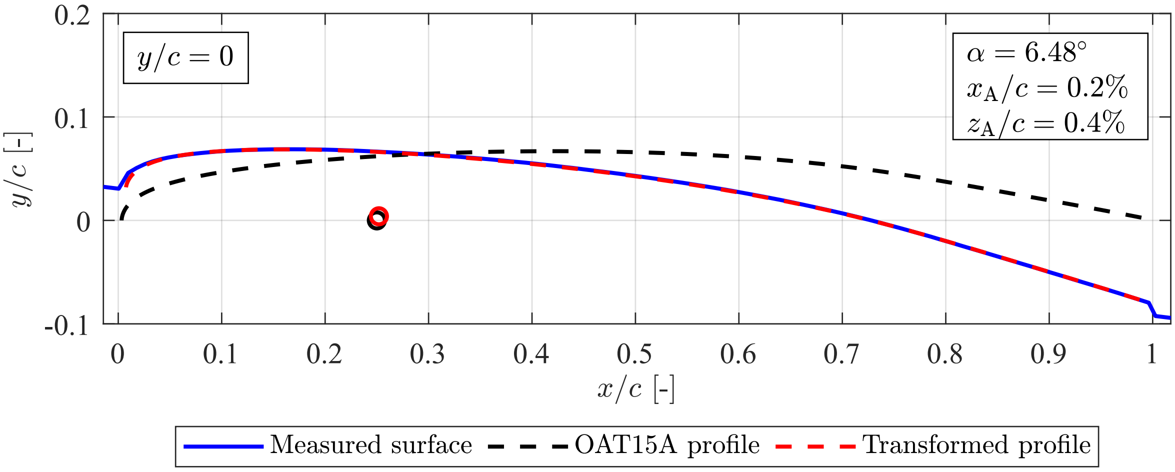

Figure 3.22: Transformation principle from world to wing coordinates for an instantaneous measurement at $M = 0.74$ on the fixed wing in transonic buffet conditions at the center chord $y/c = 0$.

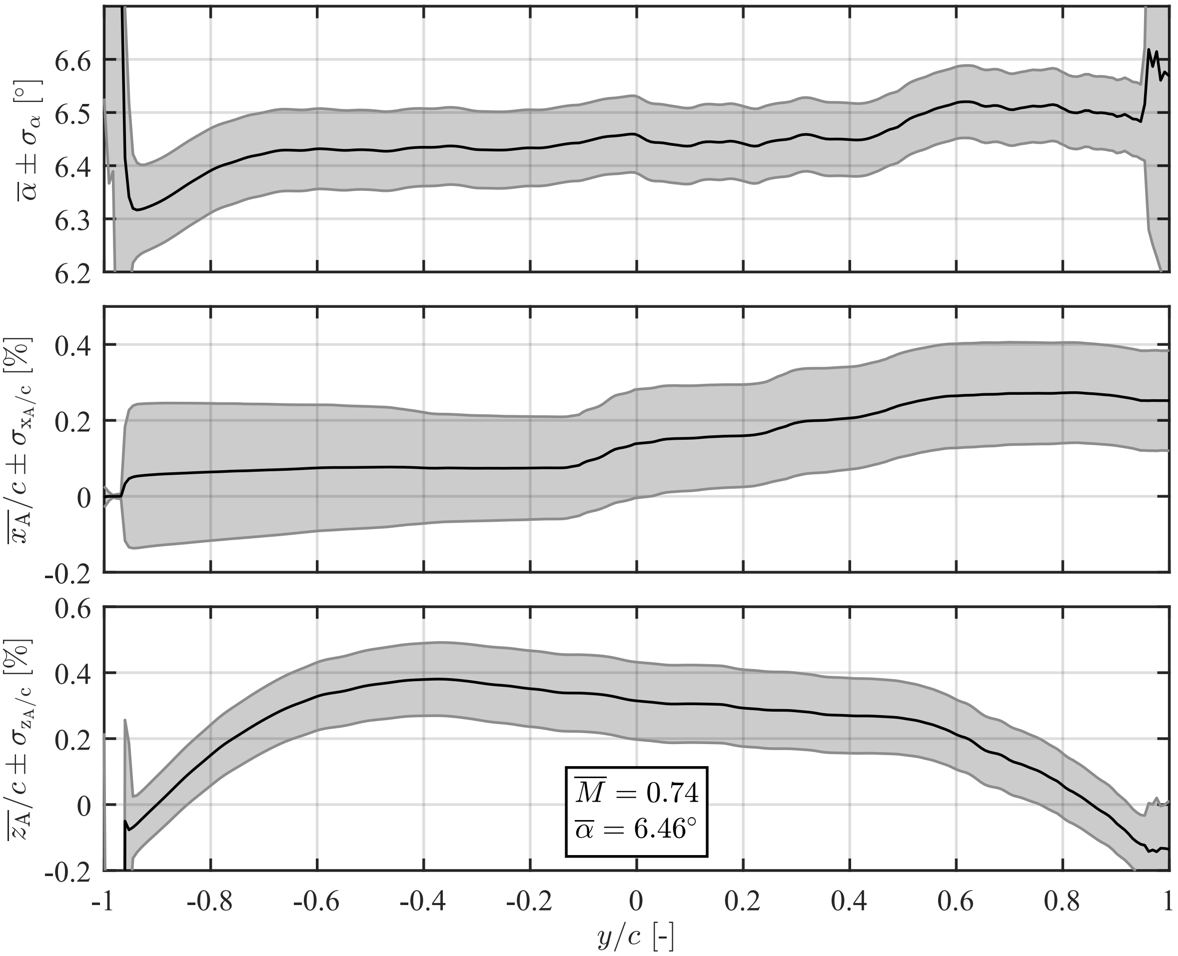

Figure 3.23: Spanwise distribution of wing deformation in airfoil coordinates for the AoA (top) and the horizontal and vertical axis locations x_A (middle) and z_A (bottom), respectively.

The Advantages and Limitations of DIC

Hereinafter, a summary of the advantages and limitations of DIC surface measurements is given.

Intrusiveness - As it is based on imaging, DIC is a low-intrusive measurement technique. However, the surface pattern may add some extra roughness to the wing surface. In the present case, the pattern thickness of approx. 50 µm exceeds the viscous sublayer thickness (approx. 10 µm). According to Schlichting and Gersten (2006), the boundary layer ranges between hydraulically smooth and fully rough. Consequently, the influence of the surface roughness on the flow is not entirely negligible but could not be quantitatively identified. Effects on the behavior of laminar-turbulent transition or the separation behavior during buffet remain subject of future detailed investigation.

Scalability of accuracy, resolution and measurement area - Depending on the application, the desired accuracy and measurement area can be highly variable. The resolution is not restricted to discrete sensor positions. With the same equipment and sufficient mounting space, both small or large areas can be observed at higher or lower accuracy and resolution, respectively. Multiple cameras may be deployed to increase the field of view at constant accuracy and resolution.

Susceptibility to density variations - Small variations in density and the consequent artificial surface displacements are mostly compensated by the use of a second camera, which is unlikely to experience the same distortion. The consequent correlation result may be altered but usually remains a good match. In the present experiments, the shock wave introduced strong density gradients, which locally increased the uncertainty in the surface reconstruction significantly (see Fig. 3.21). Given the continuous surface, and in this case, the rather high rigidity of the measurement object, it can be concluded that the measurements were not significantly altered by these effects. The additional step of airfoil profile fitting described in Section 3.3.2 compensates for all remaining locally confined artificial displacements along the chord.

3.3.3. Supportive Techniques

Force Balances

In order to support the optical measurement techniques, multiple force balances were integrated into the setup as shown in Figs. 3.7, 3.8 and 3.10. On both ends of the wing shaft at the location of the bearings, a KISTLER 9347C triaxial balance recorded the respective axial forces F_{3x}, F_{3y}, F_{3z}. An additional one-dimensional KISTLER 9311 force balance was connected to the lower end of the vertical lever arm to measure the aerodynamic moment via the force and distance to the rotation axis.

Unexpectedly, strong non-linearity occurred in the force measurements, which were traced back to clearance in the bearings. Consequently, a fruitful dynamic calibration and its application for retrieval of the actual aerodynamic loads was not possible. Nevertheless, the force balances played an important role in the determination of the structural modes and their respective natural frequencies, as presented in Section 4.2 (Korthäuer et al., 2023a).

Accelerometers & Laser Vibrometer

Accelerometers were applied to the wing during the first sets of structural characterizations at wind-off conditions. By this, additional information could be obtained to confirm the findings from other techniques. Its was found that the spectra of the uncalibrated forces were sufficient for a wind-off structural characterization as shown in Section 4.1 (Korthäuer et al., 2023a). During the wind tunnel runs, accelerometers were attached to the vertical lever arm, and a laser vibrometer was directed onto the side arm (see Fig. 3.7). Both provided online information about the setup motion.

3.3.4. Data Processing and Analysis

This section will give a summary of the processing and analysis methods that were applied to the obtained measurement data.

2D cross-correlation

A fundamental analysis method that was used for both major measurement techniques, the BOS and DIC measurements, is the two-dimensional cross-correlation.
As shown exemplary in Fig. 3.24, two two-dimensional data arrays, in this case two PIV images with varying intensities I_A and I_B at two different time steps, are correlated. A region (or interrogation window) of a selected size (M, N) in image A (red rectangle), is successively shifted by (ξ, η) in image B. The correlation coefficients for every shift combination in the correlation plane can then calculated by

$$c(\xi,\eta) = \frac{C(\xi,\eta)}{\sqrt{\sigma_{\mathrm{I_A}}}\sqrt{\sigma_{\mathrm{I_B}}(\xi,\eta)}} \tag{3.6}$$

with

$$C(\xi,\eta) = \sum_{i=0}^{M}\sum_{j=0}^{N}\left[I_\mathrm{A}(i,j) - \mu_{\mathrm{I_A}}\right]\left[I_\mathrm{B}(i+\xi,j+\eta) - \mu_{\mathrm{I_B}}(\xi,\eta)\right] \tag{3.7}$$

$$\sigma_{\mathrm{I_A}} = \sum_{i=0}^{M}\sum_{j=0}^{N}\left[I_\mathrm{A}(i,j) - \mu_{\mathrm{I_A}}\right]^2 \tag{3.8}$$

$$\sigma_{\mathrm{I_B}}(\xi,\eta) = \sum_{i=0}^{M}\sum_{j=0}^{N}\left[I_\mathrm{B}(i,j) - \mu_{\mathrm{I_B}}(\xi,\eta)\right]^2 \tag{3.9}$$

where $\mu_{\mathrm{I_A}}$ and $\mu_{\mathrm{I_B}}(\xi,\eta)$ are the average values of the respective (shifted) region. This expresses the simplest representation of the two-dimensional evaluation. Due to higher computational efficiency, the actual computation is typically performed in the Fourier-space (Willert and Gharib, 1991). Further common enhancements are the iterative multigrid evaluation or the application of window weighting (Scarano, 2003; Scarano and Riethmuller, 2000; Raffel et al., 2018). The peak in the resulting correlation map (see Fig. 3.24, bottom) represents the most probable match of the intensity pattern from the region in image A in image B. Consequently, it describes the shift of the particles or surface pattern, depending on the technique. The subsequent shift of the selected reference region in image A, potentially with an overlap, allows the determination of the whole field of displacements. More information can be found in Raffel et al. (2018).

Statistics

Given a measured signal over time $x = \{x_1, x_2, ..., x_N\}$ with a number of samples N, the following statistical quantities were determined for the description of the phenomena:

- Arithmetic mean

$$\bar{x} = \frac{1}{N}\left(\sum_{i=1}^{n} x_i\right) = \frac{x_1 + x_2 + \cdots + x_n}{n} \tag{3.10}$$

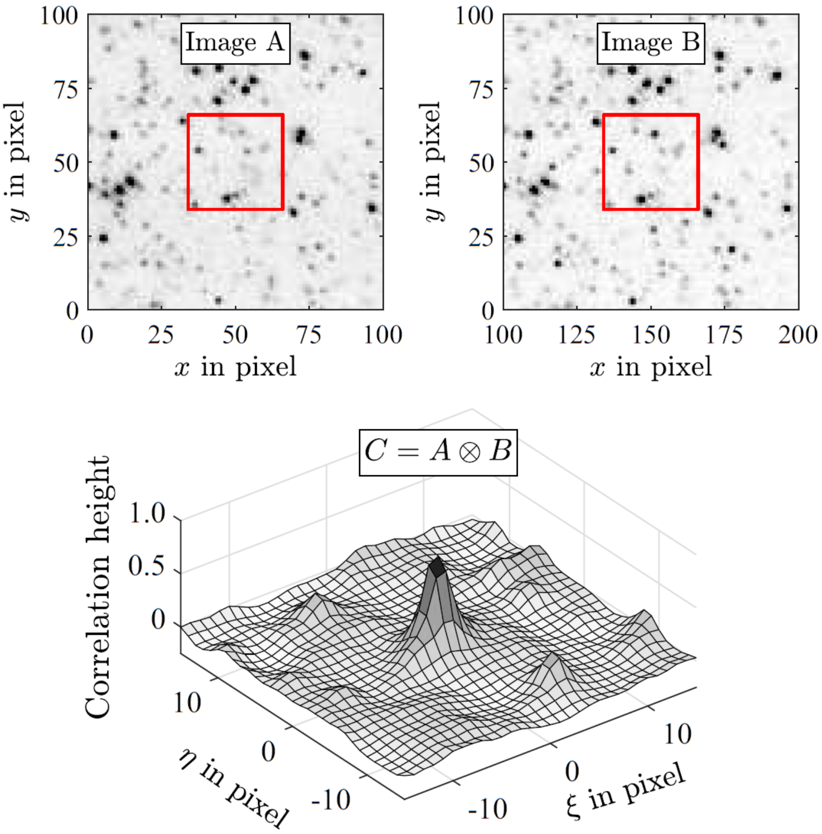

Figure 3.24: Cross-correlation scheme for PIV evaluation (Scharnowski et al., 2019).

- Standard deviation

$$\sigma_x = \sqrt{\frac{1}{N-1}\sum_{i=1}^{N}(x_i - \bar{x})^2} \tag{3.11}$$

- Percentile
  The k^{th}-percentile is the real number that satisfies the following two conditions for a real-valued cumulative probability distribution function $F(x)$:

$$\int_{(-\infty,\tilde{x}]} dF(x) \geq \frac{k}{100} \tag{3.12}$$

$$\int_{[\tilde{x},\infty)} dF(x) \geq \frac{1-k}{100} \tag{3.13}$$

- Median value
  The median value equals the 50^{th}-percentile of any real-valued cumulative probability distribution function $F(x)$, and is consequently defined as the real number

$\tilde{x}$ that satisfies the inequalities

$$\int_{(-\infty,\tilde{x}]} dF(x) \geq \frac{1}{2} \tag{3.14}$$

$$\int_{[\tilde{x},\infty)} dF(x) \geq \frac{1}{2} \tag{3.15}$$

Spectral analysis

For the analysis of the spectral content and the dominant frequencies, the power spectral density (PSD) was used. It describes the distribution of the power of a signal or time series $x(t)$ in the frequency domain. Mathematically, it represents the Fourier transform of the auto-correlation function R_{xx} and is a special case of the cross-power spectral density (CPSD), when $y(t) = x(t)$. Analogously, the CPSD is the Fourier transform of the cross-correlation R_{xy} of two different signals $x(t)$ and $y(t)$. The discrete form for two time series $x = \{x_1, x_2, ..., x_N\}$ and $y = \{y_1, y_2, ..., y_N\}$ with a number of samples N is given by

$$P_{xy}(f) = \sum_{N=-\infty}^{\infty} R_{xy}(k) e^{-i2\pi kN} \tag{3.16}$$

and

$$R_{xy}(k) = \frac{1}{N\sigma_x\sigma_y} \sum_{t=1}^{N} (x_t - \bar{x})(y_{t+k} - \bar{y}) \tag{3.17}$$

for any positive integer $k < N$.
In this work, the method of Welch (1967) was used to compute the (C)PSD, typically with a Hamming window of a length of 100 samples and 50% of overlap. The window-wise approach allows a noise-reduced determination of dominant frequencies at the cost of frequency resolution.

Phase averaged analysis

In constant operating conditions, the airfoil motion and the surrounding flow presented a highly periodic behavior, which allowed phase-based analysis of the results shown in Section 4.3 (Korthäuer et al., 2023b).
For the phase determination and the consequent phase-averaging, a sinusoidal function $\alpha(t)$ was fitted to the temporal development of the angle of attack.

$$\alpha(t) = \bar{\alpha} + \hat{\alpha} \sin(2\pi f t - \varphi) \tag{3.18}$$

This was done for successive subsets of 50 time steps to account for slight variations in frequency and amplitude of the AoA throughout the whole run. The phase relationship of each data point was accurately determined. The signals were divided into 50 groups of approx. 100 samples each, based on their phases φ_α, and the phase averaged values were computed for each group.

4

Results

The following chapter presents the results of the transonic buffet(ing) experiments in the form of three scientific publications.

The first publication, “Experimental Investigation of Transonic Shock Buffet on an OAT15A Profile” (Accorinti et al., 2022) in Section 4.1, analyses the phenomenon of transonic buffet on the wing without pitching flexibility. The focus is set on the study of shock features, the determination of inversion and onset boundaries, and the dominant shock oscillation frequencies. An excursus investigates the potential influencing character of the gap flow between window and wing, and the wall suction.

In the consequent work “Effect of Mach Number and Pitching Eigenfrequency on Transonic Buffet Onset” (Korthäuer et al., 2023a) in Section 4.2, the pitching DoF is released, allowing the wing an elastically-suspended pitching motion. The article focuses on the variation of the onset boundaries for different Mach numbers and natural pitch frequencies in comparison to the non-flexible wing. The evolution of dominant frequencies from the pre-buffet to the buffet(ing) regime is evaluated for both the flow and structural oscillations.

The article “Experimental investigation of transonic buffeting, frequency lock-in and their dependence on structural characteristics” (Korthäuer et al., 2023b) in Section 4.3 investigates the nature of the fluid-structural interaction of transonic buffeting with particular focus on the effects of structural parametric variations on the regions of FLI, veering, and classical structural excitation. Dominant frequencies and the phase relations of shock, pitch and heave motion are analyzed and presented.

AIAA Journal
Vol. 60, No. 11, November 2022

Experimental Investigation of Transonic Shock Buffet on an OAT15A Profile

Alessandro Accorinti,[*] Tim Baur,[†] Sven Scharnowski,[‡] and Christian J. Kähler[§]
Bundeswehr University Munich, 85577 Neubiberg, Germany

https://doi.org/10.2514/1.J061135

Self-sustained shock wave oscillations on airfoils, commonly defined as shock buffet, can occur under certain combinations of transonic Mach numbers M_∞ and angles of attack (AoAs) due to the interaction between the shock and the separated boundary layer. To improve the understanding of this complex phenomenon, the flow over a supercritical profile (OAT15A) was experimentally investigated for a fixed Reynolds number Re_c of 3×10^6 and numerous aerodynamic conditions within the ranges of $2.5 \text{ deg} < \text{AoA} < 6.5 \text{ deg}$ and $0.71 < M_\infty < 0.78$. Deformation and force measurements were used to assess the actual rigidity of the model and its interaction with the flow. The tracking of the shock location by means of background-oriented schlieren allowed for studying the shock features and the frequency content of the buffet flows. Furthermore, the inversion of shock motion and buffet onset, which are referred to as buffet boundaries, were estimated. The inversion of shock motion proved to be a necessary but not sufficient condition for buffet onset. The trends of the results showed a good agreement with the relevant literature cases. However, the buffet amplitude was smaller, and buffet onset occurred at considerably higher AoAs. The comparison of the literature results also revealed a general sensitivity of buffet features to both numerical and experimental parameters. For this reason, the influence of the boundary-layer suction at the vertical walls and the gap flow at the side windows on the buffet features was examined. The buffet frequencies and amplitudes were slightly affected, but the buffet boundaries appeared to be virtually insensitive to these factors. Given the large number of investigated aerodynamic conditions, these results are valuable for validation purposes of computational fluid dynamics simulations.

Nomenclature

AoA_{meas} = measured angle of attack in wind-on conditions, deg
AoA_{set} = set angle of attack in wind-off conditions, deg
c = chord, mm
f = frequency, Hz
k = reduced frequency; $\pi f c / U_\infty$
M_∞ = freestream Mach number upstream of the model
p_0 = stagnation pressure, Pa
Re_c = Reynolds number based on the chord
St = Strouhal number; $f c / U_\infty$
s = span, mm
T_0 = stagnation temperature, K
U_∞ = freestream velocity upstream of the model, m/s
x = streamwise distance from the leading edge, mm
x_A = streamwise distance of the quarter-chord from the leading edge, mm
x_s = shock position, mm
y = spanwise distance from the centerline, mm
z = vertical distance from the leading edge, mm
z_A = vertical distance of the quarter-chord from the leading edge, mm
ζ = normal distance to the upper surface, mm
σ = standard deviation

I. Introduction

SHOCK buffet results from the interaction between the shock and the separated boundary layer on the surface of a wing under certain combinations of transonic Mach numbers and angles of attack. This flow unsteadiness leads to self-sustained shock oscillations, for which the frequency is typically on the same order of magnitude as low structural eigenfrequencies, which in turn can lead to fluid–structure interaction (FSI) and reduction in aircraft performance. Two types of shock buffet have, until now, been discovered for airfoils. Type I regards biconvex sections at zero incidence and is characterized by oscillations on both the suction and pressure sides [1–3]. Type II, which occurs at positive angles of attack (AoAs) and is typical of supercritical profiles, exhibits shock oscillations solely on the suction side [4–20]. Unlike for type I, a universal working model has yet to be accepted by the scientific community. Type II is the object of this paper and is henceforth simply referred to as shock buffet.

Several necessary but not sufficient conditions for shock buffet have been determined over the years. In Refs. [5,6,8–11,13–18,20], it was shown that buffet only occurs in the case of a separated boundary layer. However, buffet arises at AoAs above which boundary-layer separation first appears. Moreover, the type of separation (separation bubble, trailing-edge separation, or complete separation) varies with model and aerodynamic conditions. According to the findings in Ref. [4], a reliable indicator of boundary-layer separation in the case of a constant Mach number is the inversion of shock motion. As the AoA increases, the flow accelerates more on the suction side and the pressure in front of the shock drops. As a consequence, the shock initially moves toward the trailing edge (Fig. 1, first image). By doing so, the overall pressure recovery (compression at the shock and continuous subsonic compression downstream of the shock) satisfies the equality and compatibility conditions at the trailing edge [4,7]. The first one states that there must be approximate equality between the pressure on the two sides of the wake at the trailing edge; the second one requires compatibility of the pressure at the trailing edge with the freestream static one, in the sense that the difference between the two pressures has to be the change that can be accommodated along the viscous flow downstream of the trailing edge. At a certain AoA, the boundary layer on the suction side separates, which tends to decrease the pressure recovery downstream of the shock. The extent

---

Received 2 August 2021; revision received 22 June 2022; accepted for publication 22 June 2022; published online Open Access 25 July 2022.

[*] Research Associate, Institute of Fluid Mechanics and Aerodynamics, Werner-Heisenberg-Weg 39; alessandro.accorinti@unibw.de.

[†] Research Associate, Institute of Fluid Mechanics and Aerodynamics, Werner-Heisenberg-Weg 39; tim.baur@unibw.de.

[‡] Research Associate, Institute of Fluid Mechanics and Aerodynamics, Werner-Heisenberg-Weg 39; sven.scharnowski@unibw.de.

[§] Full Professor, Institute of Fluid Mechanics and Aerodynamics, Werner-Heisenberg-Weg 39; christian.kaehler@unibw.de.

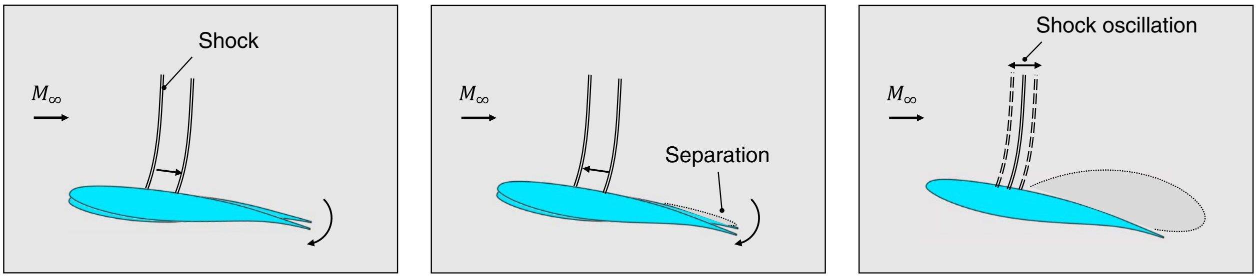

Fig. 1 Evolution of the shock motion with the increase in AoA: regular shock motion (left), inversion of shock motion (middle), and shock buffet (right).

of the separated region increases with the AoA. Once it has grown enough to significantly affect the pressure distribution on the model, the shock starts to travel toward the leading edge (Fig. 1, second image) in order to limit the extent of separation and satisfy the equality and compatibility conditions. Therefore, the inversion of shock motion at a constant Mach number and increasing AoA appears to be another necessary condition for buffet. Nonetheless, this has yet to be proved for a large range of aerodynamic conditions and different geometries. In the case of a constant AoA and increasing Mach number, the equality and compatibility conditions may be satisfied through a reduced downstream displacement rate of the shock with M_∞ instead of through an inversion. A reasonable explanation for that was again presented in Ref. [4]: increasing the Mach number not only drops the pressure in front of the shock but also the freestream pressure. Another necessary condition for buffet was suggested in Ref. [14], where it was observed, for the airfoils investigated via numerical simulations, that buffet only takes place if the shock is located downstream of the maximum curvature of the profile. However, experimental confirmation of this condition has yet to be provided.

At an AoA above which the boundary-layer separation first appears, buffet onset may occur where the shock starts to oscillate due to the interaction with the separated region (Fig. 1, third image). However, as shown in Ref. [8], a further increase in the AoA above onset is necessary to develop a fully established buffet, which displays a periodic shock motion at a dominant frequency ($0.16 < k < 0.22$ and $0.05 < St < 0.07$ are typical ranges of the buffet reduced frequency and Strouhal number, respectively). Several criteria have been proposed for buffet onset. In Ref. [4], the bursting of the separation bubble at the shock foot, which could be recognized by tracking the divergence of the pressure at the trailing edge, had been deemed responsible for the onset of the unsteadiness. However, it was shown in Refs. [11,14] that, depending on airfoil geometry and aerodynamic conditions, a separation bubble can remain present after the onset and the boundary layer can be fully separated before onset. In Ref. [1], the hypothesis had been advanced that onset occurs upon reaching a specific M_∞ in front of the shock. However, this was contradicted by the results in Ref. [11]. The so-called global modal decomposition of the transonic equations of the flow was first applied in Ref. [11] to compute the aerodynamic modes and identify the one that becomes unsteady with an increase in AoA. Buffet onset was estimated this way for different Mach numbers, AoAs, and geometries, yielding a good agreement with the experimental results of Refs. [5,8]. Also, in Ref. [15] too a global stability analysis was performed, which compared favorably with the results in Refs. [8,11]. Other work has aimed at quantifying the onset by tracking a specific variable.

For example, the divergence of normal force fluctuations was used in Ref. [6]. In Ref. [5], the onset of the unsteadiness was instead linked to the linear increase in the envelope of the time-resolved pressure at the model's surface. In Ref. [8], instead, the rise in pressure fluctuations at the model's surface was selected; whereas in Refs. [14,17], the increase in the lift coefficient fluctuations was chosen.

The characteristics of shock buffet so far presented were observed within experimental and numerical works performed on two-dimensional (2-D) wings. Only minor differences in terms of buffet frequencies and amplitudes were found via unsteady Reynolds-averaged Navier–Stokes (URANS) simulations in Ref. [21] for infinite swept wings with a sweep angle smaller than 20 deg. Even though local three-dimensional (3-D) phenomena (for instance, a nonuniform spanwise separation line) appear during some instants of the shock oscillation cycle, the overall buffet phenomenon remains 2-D-like. On the other hand, for sweep angles of ≥ 20 deg, spanwise periodic pressure perturbations were discovered: the so-called buffet cells, which travel outboard toward the wingtip. These perturbations are responsible for a periodic chordwise shock oscillation that resembles the 2-D phenomenon. However, the amplitude of shock oscillations is lower and the buffet frequency higher than the respective 2-D case (for a sweep angle of 30 deg, the buffet amplitude is half of the 2-D one and the buffet frequency is about three times the 2-D one). Moreover, for sweep angles of 15 and 30 deg, the shock position coincides with the location of maximum curvature on the upper surface. Therefore, the necessary criterion for buffet proposed by the same authors in Ref. [14] may not be valid for all 3-D cases and geometries. In Ref. [22], a broadbanded buffet frequency centered on $St = 0.26$ and between four and seven times higher than the respective 2-D case was experimentally measured on a half-wing body with a sweep angle of 30 deg. As in Ref. [21], this frequency is connected to spanwise outboard-traveling waves, for which the wavelength is approximately one chord. Besides this 3-D buffet phenomenon, a 2-D-like buffet was also found in the midspan section with a Strouhal number of 0.04. Furthermore, a Kelvin–Helmholtz instability was detected, which developed in the shear layer downstream of the shock, had a wavelength of $0.1c$, and had Strouhal numbers between one and four. In Ref. [23], the results of the experiments performed on four different half-wing bodies with a sweep angle of 30 deg were compared. Shock buffet only exhibits broadbanded Strouhal numbers higher than the respective 2-D configurations and centered on values ranging between 0.2 and 0.3. Similar to Refs. [21,22], the higher frequencies are associated with spanwise traveling structures with a distinct convection velocity. To verify whether the 3-D buffet phenomenon can be connected to a globally unsteady mode, analogously to 2-D buffet [12,15], global stability analyses were conducted in Refs. [24–27]. Besides the 2-D-like unsteady mode, spanwise modes with maxima of the growth rate for wavelengths close to 1 and 10 chords were discovered. These additional modes are stationary in the case of infinite swept wings and provide a 3-D structure to a still nominally 2-D unsteady flow. In the case of swept wings, the stationary spanwise modes become unsteady. The one with a wavelength of one chord is comparable in terms of frequency and convection speed to the one having a Strouhal number of 0.26 in Ref. [22]. Also, the 2-D unsteady mode presents similar features to the low-frequency mode acting on the midspan of the wing in Ref. [22]. On the other hand, no clear connection has yet been established between the spanwise mode with a wavelength of 10 chords and the Kelvin–Helmholtz instability found in Ref. [22], although they exhibit similar frequencies. Regarding buffet onset, the sweep angle seems to have little influence on it. The global stability analysis also proved to be a reliable tool to detect buffet onset in the 3-D case, even though the aspects of the instability seemed to differ from the 2-D buffet and seemed to resemble the stall-cell modes in low-speed flows [27]. Finally, in Ref. [26], a global stability analysis was performed together with a simulated transition to turbulence of the boundary layer. In this case, buffet onset occurred at a slightly lower AoA than in all the previous studies, which considered a fully turbulent flow. Similar results were found in the 2-D experiments presented in Ref. [16] for the case of a laminar boundary layer interacting with the shock. Compared to Ref. [8], where the transition to turbulence was fixed, not only takes buffet place at lower angles of attack but its frequency also increases.

The goal of this paper is to determine the characteristic features of 2-D shock buffet for an OAT15A profile by verifying whether the inversion of shock motion is a necessary condition for buffet onset and determining these two boundaries for several M_∞ and AoA combinations. The inversion of shock motion and buffet onset are henceforth referred to as buffet boundaries. Moreover, with the aim to expand the available experimental data for buffet validation, the time averages and the standard deviations of the shock location together with the dominant frequencies of developed buffet flows are provided. In Sec. II, the experimental setup is presented. The facility as well as the measurement techniques are first described, followed by an investigation of the model's actual rigidity and an overview of the performed runs. In Sec. III, the shock features and the buffet frequencies and boundaries determined via background-oriented schlieren (BOS) are presented. Afterward, a comparison of the main results with the relevant literature cases is made. Additionally, the influence on the buffet characteristics of two boundary conditions in the test section (namely, the boundary-layer suction at the vertical walls and the gap flow at the side windows) is discussed. Some concluding remarks are outlined in Sec. IV.

II. Experimental Setup

A. Description of the Facility

The Trisonic Windtunnel Munich (TWM) facility is a blowdown wind tunnel with a 300-mm-wide and 680-mm-high test section ideally suited for profile measurements. The facility has an M_∞ operating range from 0.2 to 3.0. The Reynolds number can be adjusted by means of the total pressure, which can be varied between 1.2 and 5.0 bar. The facility has two tanks with a total volume of 356 m^3 that are pressurized with dry air up to 20 bar above ambient pressure. This allows for a maximal run time of 100 s for the flow conditions in this work. The freestream turbulence level based on the streamwise velocity fluctuations in the TWM test section is 1.9% at $M_\infty = 0.3$ and decreases with increasing M_∞, reaching 0.45% at $M_\infty = 3.0$, as shown in Ref. [28]. More details about the facility and its characterization were provided in Ref. [29].

To compensate for the growth of the boundary layer in the test section, a boundary-layer suction is applied to the vertical walls, which are perforated and connected by pipes to the diffusor downstream of the test section. The level of applied suction can be set by varying the cross section of the pipes. Additionally, the growth of the boundary layer is limited by using a divergence of the horizontal walls; that is, the test section height increases moving downstream. In a preliminary campaign without model, the optimal configuration of suction was determined; that is, the one that together with the set divergence gave the most constant streamwise pressure distribution in the test section. The blockage effects introduced by the model are deemed to have a minor impact because the blockage ratio is below 3.5% at the highest AoA considered in this work.

B. Description of the Model and the Measurement Techniques

The model under investigation is based on the OAT15A profile, which was developed by ONERA. This airfoil became a benchmark for transonic buffet analysis after the publication of the extensive experimental campaign of Ref. [8], as evidenced by several numerical studies on this profile (Refs. [9,10,12,15,17,18]). The carbon-fiber-reinforced polymer profile has a relative thickness of 12.3%, a chord length of $c = 152$ mm, a span of $s = 298$ mm ($AR = 2$), and a trailing-edge thickness of 0.5% of the chord. Between the profile ends and the side windows of the test section, there is a gap of 1 mm, for which the effect on buffet is presented in Sec. III.E. The boundary layer is tripped at the position of $x/c = 0.07$ by applying a row of circular dots, 70 μm high and distributed every 6 mm along the span, on both the upper and lower surfaces. The position is chosen to be the same as in Ref. [8], which is a convenient one for curved wings because it is close to the location of the pressure minimum on the suction side. The height of the dots is selected to trigger the transition without overtripping. The profile is rigidly mounted in the wind tunnel to impede FSI. However, hammer tests performed on the model in the absence of flow revealed that the first three eigenfrequencies (heave, pitch coupled with surge, and pitch) are relatively low (158, 300, and 389 Hz, respectively) and close to the expected buffet frequency. Therefore, deformation measurements are used to assess the actual rigidity of the model and its interaction with the flow. BOS is employed to track the shock location.

The test section is illustrated together with the measurement equipment in Fig. 2. Structural deformations of the model are detected via stereo digital image correlation measurements [30]. A random speckle pattern is painted with a sponge on the model's upper surface in order to optimize the correlation-based deformation measurements. The pattern is expected to have negligible influence on the boundary layer because it is thinner than the tripping dots. The light coming from two light-emitting diodes (LEDs; Luminus CBM-120-UVX, 410 nm) on top of the test section is scattered by the model and reaches a PCO Dimax HS4 camera located on each side of the test section. Making use of a preceding coplanar stereo camera calibration, a correlation-based surface reconstruction is performed to obtain the 3-D components of the surface displacement. In addition, a random reference pattern is applied outside of the test section so as to correct the recorded images for camera vibrations. To perform BOS measurements from the side, a random pointlike pattern, for which the points are 2 pixels in diameter (0.5 mm) and the point density (covered area) is slightly above 40%, is installed in the background of the test section. The test section and the pattern are illuminated by an LED (Luminus CBT-120-B-C11-KM301, 462 nm) and recorded by a Phantom V2640 high-speed camera. The displacement of the background pattern between wind-off and wind-on (without and with the flow in the test section) is proportional to the density gradient at wind-on conditions. The displacement field is evaluated by performing a cross correlation between the two images, and it provides a qualitative representation of the density gradient. A more detailed description of the BOS technique can be found in Ref. [31]. The force and moment balances complete the setup (see Ref. [19] for more information). The absolute values of the measured forces and moments are not reliable due to partial coupling between them. However, the trends of their statistics and spectra with the aerodynamic parameters are expected to be correct, and hence serve as a qualitative comparison to the deformation and BOS data.

C. Determination of the Deformation and Vibration of the Model

Deformation results allow for verifying how rigid the model actually is. For the sake of simplicity, only the results of the runs with constant AoAs at $M_\infty = 0.74$ are hereinafter discussed (see Sec. II.D for the description of the performed runs). The results at the other Mach numbers are indeed quantitatively similar. Figure 3 illustrates the time-averaged vertical displacement of all the points on the upper surface of the model with respect to the wind-off conditions at $M_\infty = 0.74$ and $\mathrm{AoA}_{\mathrm{set}} = 6.5$ deg. $\mathrm{AoA}_{\mathrm{set}}$ is the set AoA in wind-off conditions. The overall deformation can be described by two contributions: a profile bending, leading to a higher vertical shift in the center region (green and blue arrows); and a positive profile rotation, resulting in a stronger vertical shift at the trailing edge (green and purple arrows).

Based on these findings, the deformation of the profile center cut is decomposed into a vertical shift and a rotation. The latter is responsible for a reduction in AoA from $\mathrm{AoA}_{\mathrm{set}}$ to $\mathrm{AoA}_{\mathrm{meas}}$, which is the measured angle of attack in wind-on conditions (see bottom of Fig. 4). As of Sec. II.D, all displayed AoAs will refer to the measured values.

In the top Fig. 4, the vertical displacement with respect to the wind-off conditions of the four points from Fig. 3 is shown for $M_\infty = 0.74$ and several $\mathrm{AoA}_{\mathrm{set}}$. Until $\mathrm{AoA}_{\mathrm{set}} = 5.5$ deg, the time average of the vertical displacement tends to grow linearly, whereas its standard deviation remains approximately constant with the $\mathrm{AoA}_{\mathrm{set}}$. At higher $\mathrm{AoA}_{\mathrm{set}}$, however, the separation of the boundary layer occurs, causing an increase in the mean aerodynamic loads with $\mathrm{AoA}_{\mathrm{set}}$ to stop. This is why the time-averaged displacement reaches a plateau. On the other hand, its standard deviation soars, indicating that the interaction between the structure and the flow intensifies.

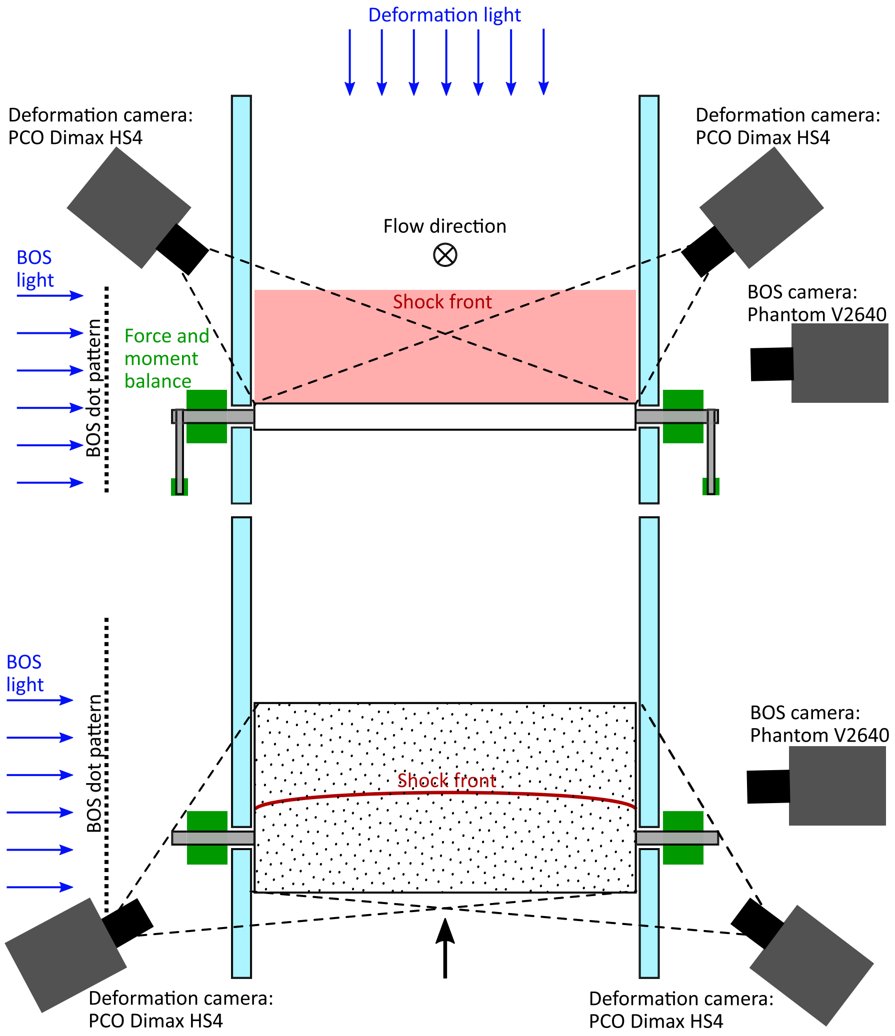

Fig. 2 Front and top views of the experimental setup.

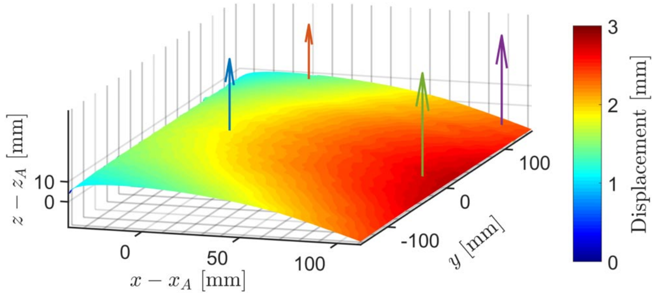

Fig. 3 Color-coded time-averaged vertical displacement of the upper surface of the model with respect to reference wind-off conditions at $M_\infty = 0.74$ and $\mathrm{AoA}_{\mathrm{set}} = 6.5$ deg. Adapted from Ref. [19].

This very same interaction can be also observed in Fig. 5, which shows the power spectral densities (PSDs) of the fluctuations of the following variables: the vertical displacement at the location of the green arrow from Fig. 3 measured by the deformation cameras (red spectrum), the shock location computed via BOS (blue spectrum), and the vertical force recorded by the 3-D force balance (green spectrum). For the computation of the PSD, the method of Welch presented in Ref. [32] is used. A window width of 100 time steps is selected for the BOS and deformation measurements. For the force measurements, instead, a window of 1000 time steps is chosen, given its 10 times higher sampling frequency. These widths ensure a sufficient number (approximately 10) of buffet cycles in the respective PSD windows. At $\mathrm{AoA}_{\mathrm{set}} = 5.0$ deg (Fig. 5, first image), no clear peak can be seen in the BOS spectrum, indicating a stable shock; whereas the first three structural eigenfrequencies (respectively, heave, pitch coupled with surge, and pitch) are present in both deformation and balance data, with values slightly different from the wind-off ones (respectively, 158, 300, and 389 Hz). By increasing the $\mathrm{AoA}_{\mathrm{set}}$ to 6.0 deg (Fig. 5, middle), a peak appears in the BOS data around 96 Hz, confirming that buffet onset has already been reached and an established periodic buffet is present. Simultaneously, a very similar peak is shown in the deformation and balance spectra, indicating an interaction between the buffet and the structural modes. Finally, at $\mathrm{AoA}_{\mathrm{set}} = 7.0$ deg (Fig. 5, third image), the buffet peak in the BOS data moves toward higher frequencies (117 Hz). The structural and balance data do not show a clear peak at the same frequency but a rather broad peak region that extends from the buffet to the heave frequency, with the latter being higher. The model can be considered rigid regarding the pitch motion because the intensity of the PSD of the pitch mode stays almost constant in prebuffet and buffet conditions. However, the same cannot be said for the heave motion because the PSD of the heave mode increases by one order of magnitude, going from 5.0 to 7.0 deg. This interaction is probably facilitated by the fact that the fluid and heave modes are getting remarkably close at higher AoAs. For this reason, the effects of the FSI between these modes on buffet onset and buffet frequencies will be investigated in future works.

D. Overview of the Performed Runs

To study the evolution of the shock features and of the buffet frequency with the aerodynamic conditions, runs with a constant M_∞ and AoA are performed. For the detection of the buffet boundaries, instead, AoA sweeps are conducted. The sampling frequency is 1 kHz for the BOS and deformation measurements, whereas the force balances record at 10 kHz. The analyzed AoAs are relatively

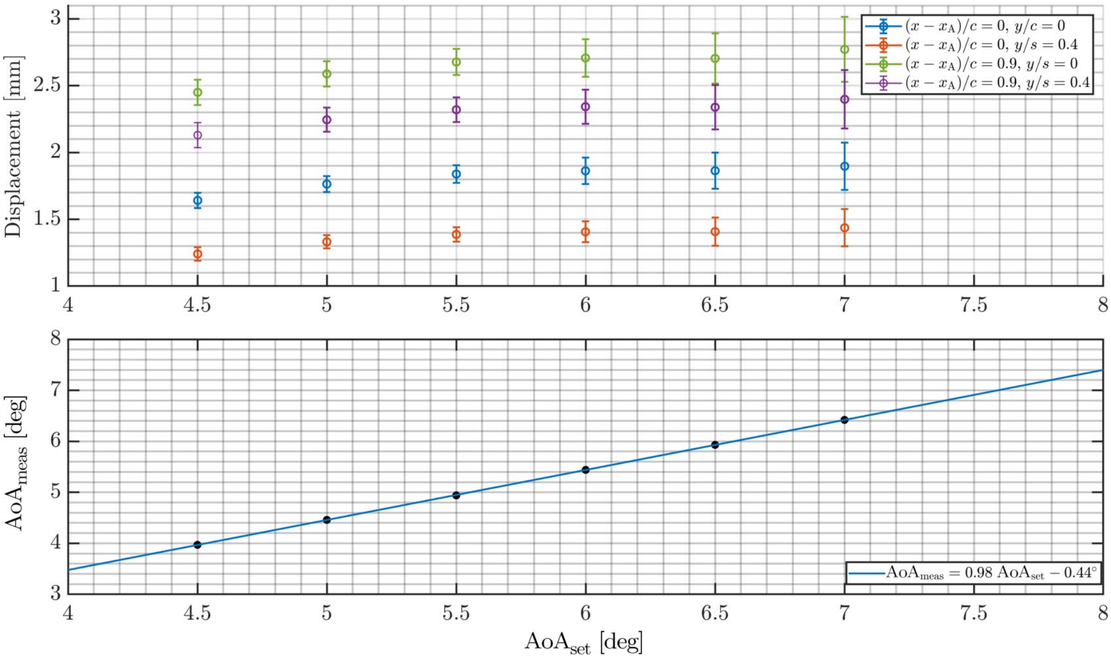

Fig. 4 **Time-averages vertical displacement of four points of the upper surface of the model with respect to reference wind-off conditions and its standard deviation as error bar at $M_\infty = 0.74$ over set AoAs (top), and measured AoAs as a function of AoA$_{\text{set}}$ (bottom). Adapted from Ref. [19].**

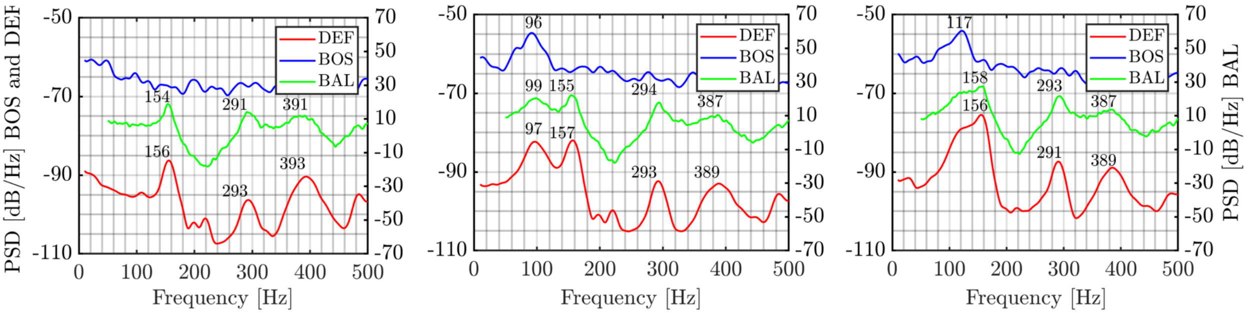

Fig. 5 **PSDs of deformation (DEF), BOS, and balance (BAL) data at $M_\infty = 0.74$. From left to right: AoA$_{\text{set}}$ = 5.0, 6.0, and 7.0 deg. Adapted from Ref. [19].**

higher than those in Refs. [8–11] due to a buffet onset delay already reported in Ref. [19]. The stagnation conditions are set to $p_0 \approx 1.5 \times 10^5$ Pa and $T_0 \approx 300$ K in order to yield a Reynolds number based on the chord equal to $Re_c \approx 3 \times 10^6$, as in Ref. [8].

In the case of the runs with constant aerodynamic conditions, the AoA and M_∞ are varied between 3.5 and 6.5 deg and between 0.72 and 0.75, respectively. The BOS data of these runs are used to obtain reliable shock statistics and buffet frequencies because they contain 10,000 samples at almost constant aerodynamic conditions for the BOS and deformation measurements. The results of these runs will be shown in Secs. III.A and III.B.

AoA sweeps are performed between 2.5 and 6.0 deg. The targeted Mach numbers are 0.71, 0.73, 0.74, 0.76, and 0.78. Due to wind-tunnel effects, M_∞ does not stay constant but decreases on average by 0.009 through the AoA sweep. The BOS data of these runs are used to estimate the buffet boundaries on a fine AoA grid. The average number of samples in 0.1-deg-spaced intervals, which are selected for the computation of the statistics, is approximately 200 for the BOS and deformation measurements. The results of these runs will be shown in Sec. III.C.

III. Results

A. Shock Features

Examples of raw wind-on BOS photographs for $M_\infty = 0.74$ and AoA = 6.5 deg are shown in Fig. 6. The two photographs correspond to the time instants of an oscillation cycle at which the shock location at a normal distance from the upper surface of 10% of the chord reaches its most downstream and upstream locations, respectively. The Mach wave observed upstream of the shock is due to the transition triggering dots. The darker circular region is caused by high mechanical stresses in the window due to a hole needed for the model mounting. Here, the distortion of the light path is so strong that no reliable information can be retrieved. The left-side image of Fig. 6 reveals a lambda-shaped region typical of transonic shock wave/boundary-layer interactions. When the shock moves upstream, the shock strength increases, which leads to a larger separation (Fig. 6, right). Three-dimensional effects at the side walls cause a deformation of the shock surface, as can be seen in the left-side image of Fig. 6. However, they remain confined to 15% of the profile span at each extremity.

By means of cross correlation between the wind-off and the wind-on BOS images, it is possible to obtain the displacement fields, which are a qualitative representation of the density gradients in the flow. The shock location is identified with the maximum displacement at each of the considered normal distances to the upper surface. Figure 7 illustrates the time averages (colored curves) and the standard deviations (shaded error bars) of the shock positions between $\zeta/c = 0.05$ and $\zeta/c = 0.55$ for several runs with constant AoAs and M_∞. The values of standard deviation reflect the unsteady nature of the shock location. However, they also comprise BOS uncertainty, which is on the order of the interrogation window size (1% of the chord), and oscillations caused by occasional jumps of the detected shock position due to spanwise deformation of the shock front. In Fig. 7 (left), the evolution of the shock front with the AoA is shown for $M_\infty = 0.74$. For an AoA between 4.5 and 5 deg, the shock travels

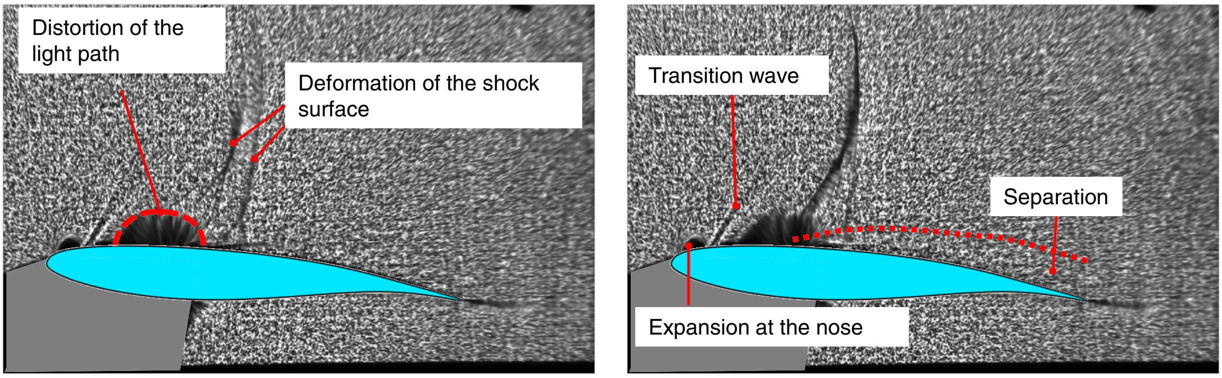

Fig. 6 Instantaneous wind-on BOS photographs for AoA = 6.5 deg and M_∞ = 0.74: most downstream (left) and upstream (right) shock locations of a buffet cycle.

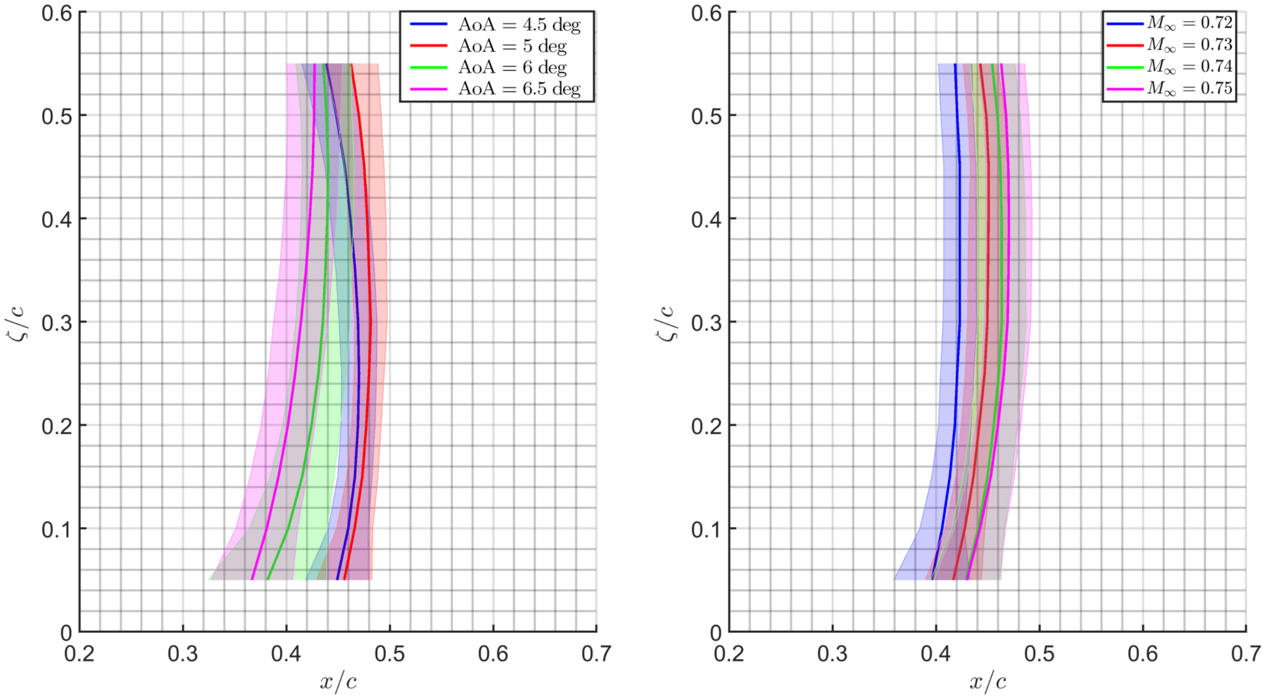

Fig. 7 Time averages (colored curves) and standard deviations (shaded error bars) of the shock front. M_∞ = 0.74 at four different AoAs (left), and AoA ≈ 5.5 deg at four different M_∞ (right).

toward the trailing edge (regular shock motion). At an AoA higher than 5 deg, however, the boundary layer has already separated because the shock starts to move toward the leading edge. As already explained in Sec. I, the inversion of shock motion limits the extent of separation and increases the pressure recovery downstream of the shock in order to satisfy the equality and compatibility conditions. Moreover, the separated region acts like a wedge, and this causes the shock front to become oblique, as described in Ref. [4]. In addition, increasing the AoA from 5 to 6 deg leads to a significant rise in the standard deviation of the shock location (developed buffet). A further increase in AoA, however, results in a lower standard deviation, which suggests buffet develops toward its offset. In Fig. 7 (right), the evolution of the shock front with M_∞ at AoA ≈ 5.5 deg is illustrated. At $M_\infty = 0.72$, separation is present at the shock foot, as is visible from the inclination of the shock front. However, different from the case with an increasing AoA, the rate of downstream shock motion with the Mach number is slowed down, but no inversion occurs. This is likely due to the fact that, as already explained in Sec. I, the freestream pressure drops with an increase in M_∞. Therefore, an inversion of shock motion is not necessarily required to meet the equality and compatibility conditions at the trailing edge. The results presented in the next sections (some of which are summarized in Table 1) refer to the shock location at a normal distance from the upper surface of 10% of the chord, i.e., $\zeta/c = 0.1$. This height is chosen in order to be as close as possible to the surface and to better compare the shock statistics and buffet frequencies with the ones available in the literature, which are mostly based on the pressure distribution at the upper surface.

B. Frequency Content of the Shock Motion

The PSD of the shock fluctuations is analyzed to detect its dominant frequencies, with a particular focus on the frequencies of the developed buffet flows. For this purpose, the BOS results of the runs with constant AoAs and M_∞ are used due to the high number of samples at fixed aerodynamic conditions. For the computation of the PSD, the method of Welch presented in Ref. [32] is used. A window width of 100 time steps is selected in order to have a sufficient number (approximately 10) of buffet cycles in it. Furthermore, the changes of the dominant reduced frequency k and of the Strouhal number St with the AoA and M_∞ are studied.

In Fig. 8, the PSDs of the fluctuations of the shock location are shown. The appearance of a clear peak in the spectrum corresponds to a developed buffet flow. At $M_\infty = 0.74$ (bottom-left in Fig. 8), for example, a developed buffet can be observed starting from AoA = 5.5 deg because a dominant peak emerges at 96 Hz in the spectrum. However, a small bump around 80 Hz appears as of AoA = 5 deg,

Table 1 Summary of results of the runs with constant M_∞ and AoAs

AoA, deg	M_∞	$\overline{x_s/c}$	$\sigma_{x_s/c}$	f_{buffet}, Hz	k_{buffet}	St_{buffet}
5.1	0.72	0.40	0.019	— —	— —	— —
5.6	0.72	0.41	0.022	— —	— —	— —
6	0.72	0.39	0.033	90	0.177	0.056
6.5	0.72	0.36	0.033	105	0.208	0.066
4.5	0.73	0.41	0.019	— —	— —	— —
5.0	0.73	0.43	0.018	— —	— —	— —
5.5	0.73	0.43	0.019	— —	— —	— —
6	0.73	0.40	0.030	98	0.193	0.061
6.5	0.73	0.37	0.032	111	0.223	0.071
4.0	0.74	0.43	0.022	— —	— —	— —
4.5	0.74	0.46	0.019	— —	— —	— —
5.0	0.74	0.47	0.018	— —	— —	— —
5.5	0.74	0.44	0.026	96	0.188	0.060
6	0.74	0.40	0.038	104	0.208	0.066
6.5	0.74	0.38	0.030	117	0.233	0.074
3.5	0.75	0.44	0.024	— —	— —	— —
4.0	0.75	0.47	0.026	— —	— —	— —
4.4	0.75	0.49	0.020	— —	— —	— —
4.9	0.75	0.47	0.021	94	0.182	0.058
5.5	0.75	0.44	0.025	104	0.208	0.066
5.9	0.75	0.41	0.034	111	0.223	0.071
6.4	0.75	0.39	0.038	120	0.238	0.076

which suggests that buffet onset may have already occurred. The buffet frequency always rises with an increase in the AoA or M_∞. At $M_\infty = 0.74$, for example, it shifts to slightly higher values with increasing AoA (from 96 to 117 Hz). Figure 9 presents the reduced buffet frequency trends with the AoAs for the four M_∞ values (the correspondent Strouhal numbers are shown in Table 1), which were obtained by linearly fitting the BOS results (colored circles). In addition, the buffet peaks in the spectrum of the vertical force are plotted as colored squares; if no buffet peak is present in the force spectrum, then its dominant peak is plotted instead. The increase in k appears to be linear with the AoA. Moreover, the slope seems to significantly drop with M_∞. For two combinations of the aerodynamic parameters (maximum AoA at the two highest Mach numbers), the buffet peak is not visible anymore in the force spectrum. Instead, a broader peak that extends from the buffet to the heave frequency is formed, with the latter being higher. For this reason, the two correspondingly colored squares in Fig. 9 approach the horizontal dashed line, which represents the wind-off value of the reduced heave eigenfrequency. Also, the BOS spectrum too in Fig. 8 shows a broader peak for these cases in comparison to the others, even if the buffet peak is still visible. As already mentioned in Sec. II.C, the fact that the fluid and heave modes get remarkably close at higher AoAs probably enhances the interaction between them. Figure 8 also reveals that the amplitude of the buffet frequency at each M_∞ reaches

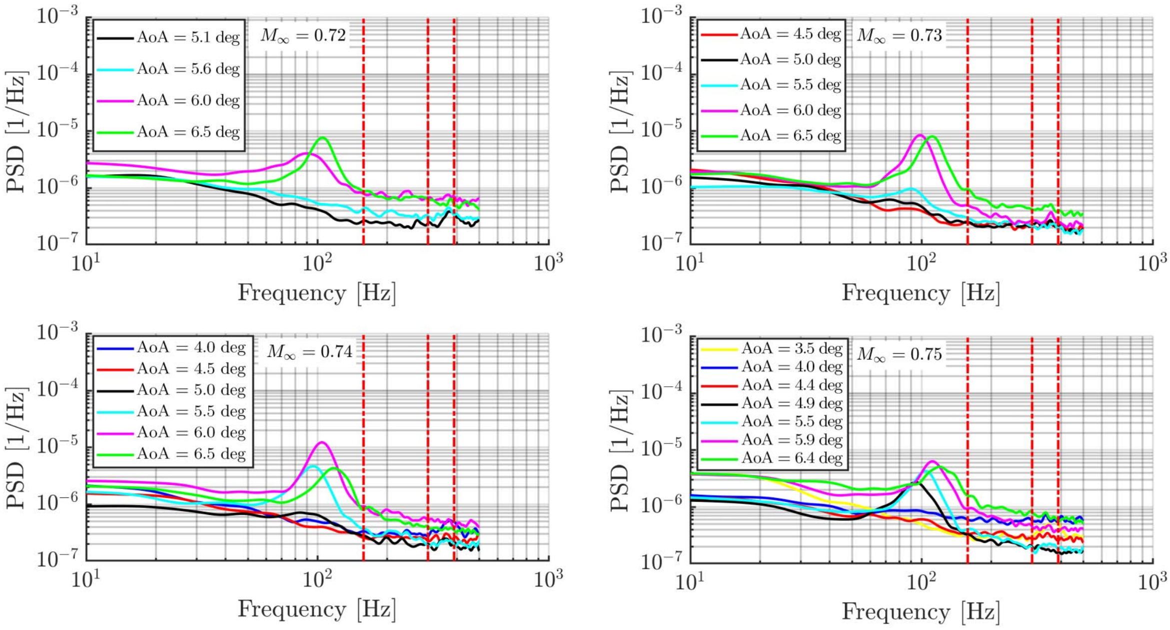

Fig. 8 PSDs of shock oscillations at several AoAs for different M_∞. The first three structural eigenfrequencies (heave, pitch coupled with surge, and pitch) are illustrated as vertical dashed lines.

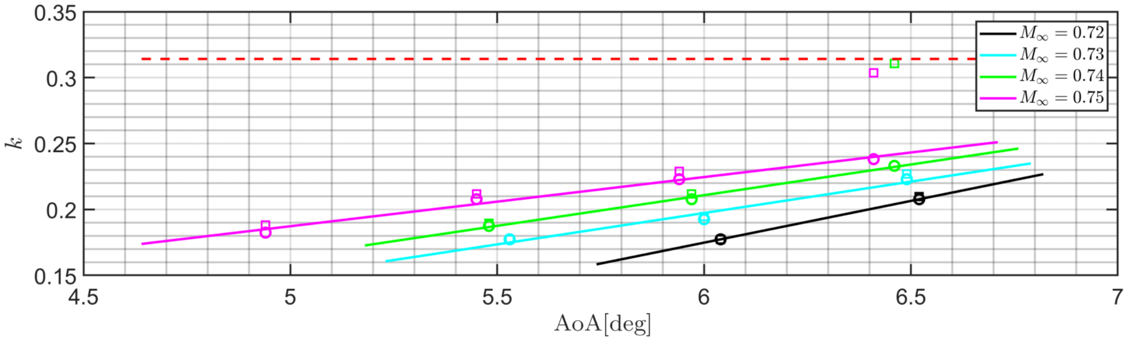

Fig. 9 Reduced frequency as a function of AoA for different M_∞: reduced buffet frequency measured via BOS (colored circles), linear interpolations of BOS buffet frequencies at each M_∞ (colored lines), reduced buffet frequencies detected via force measurements (colored squares), and wind-off value of heave eigenfrequency (dashed line).

a maximum and decreases with a further increase in the AoA as buffet moves toward its offset. Buffet offset itself is, however, outside of the range of the examined AoA. At $M_\infty = 0.74$, for example, the maximum amplitude is reached at AoA = 6.0 deg, which also constitutes the maximum in the whole range of investigated aerodynamic parameters.

C. Buffet Boundaries

The BOS results of the sweep runs are used to detect the buffet boundaries on a 0.1-deg-spaced AoA grid. For the sake of simplicity, the criterion for the detection of the buffet boundaries is hereinafter explained by plotting the results of the sweep run with $0.735 < M_\infty < 0.745$. In Fig. 10, the time average and the standard deviation of the shock location are illustrated. The most downstream time-averaged shock location is selected to track the inversion of shock motion (red dashed line). Similar to Refs. [6,8,14,17], buffet onset is identified with the rise in the fluctuations in the flow. In Ref. [6], the divergence of normal force fluctuations was used. In Ref. [8], the rise in pressure fluctuations at the model's surface was selected; whereas in Refs. [14,17], the increase in the lift coefficient fluctuations was chosen. In this paper, instead, the rise in the standard deviation of the shock location is used. However, no fixed threshold for the rate of increase in the standard deviation with the AoA is selected because this rate appears to vary with the aerodynamic conditions. Instead, the minimum of the standard deviation (blue dashed line) after the inversion of shock motion is chosen because it proves to successfully identify for all the sweep runs of the AoA at which the standard deviation begins to rise.

The evolution of the flow from regular shock motion to developed periodic buffet is shown in Fig. 11. The colored circles represent the time averages of the shock location for the five sweep runs (as already mentioned in Sec. II.D, M_∞ slightly decreases during these runs due to wind-tunnel effects) as well as for the constant runs. The most downstream shock positions at each sweep run are highlighted by the black stars. The red curve, obtained by linearly fitting the black stars, represents the inversion of shock motion in the analyzed M_∞ range. The black open circles correspond to the rise in the standard deviation of the shock location at each sweep run. By linearly fitting them, the blue curve is obtained, which represents the buffet onset boundary. As can be seen, the shock motion inversion and the onset lines have a rather similar slope. On average, buffet onset is 0.3–0.4 deg displaced toward higher AoAs with respect to the inversion of shock motion. This reinforces the conviction that the latter is a suitable, necessary but not sufficient condition for shock buffet.

D. Comparison with Literature

A comparison of the results with the relevant literature cases is hereinafter presented. First, the buffet boundaries are addressed; because no results are available in the literature regarding the inversion of shock motion, the focus of the analysis is put on buffet onset.

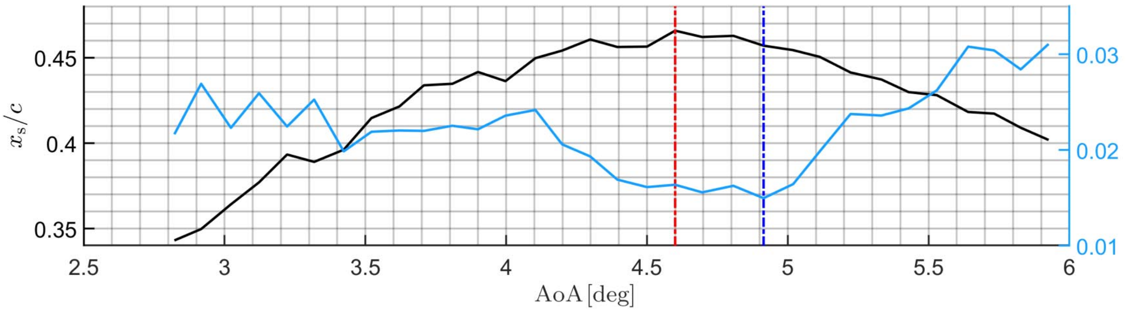

Fig. 10 Time averages and standard deviations of shock location for the sweep run with $0.735 < M_\infty < 0.745$. Red dashed line and blue dashed line highlight inversion of shock motion and buffet onset, respectively.

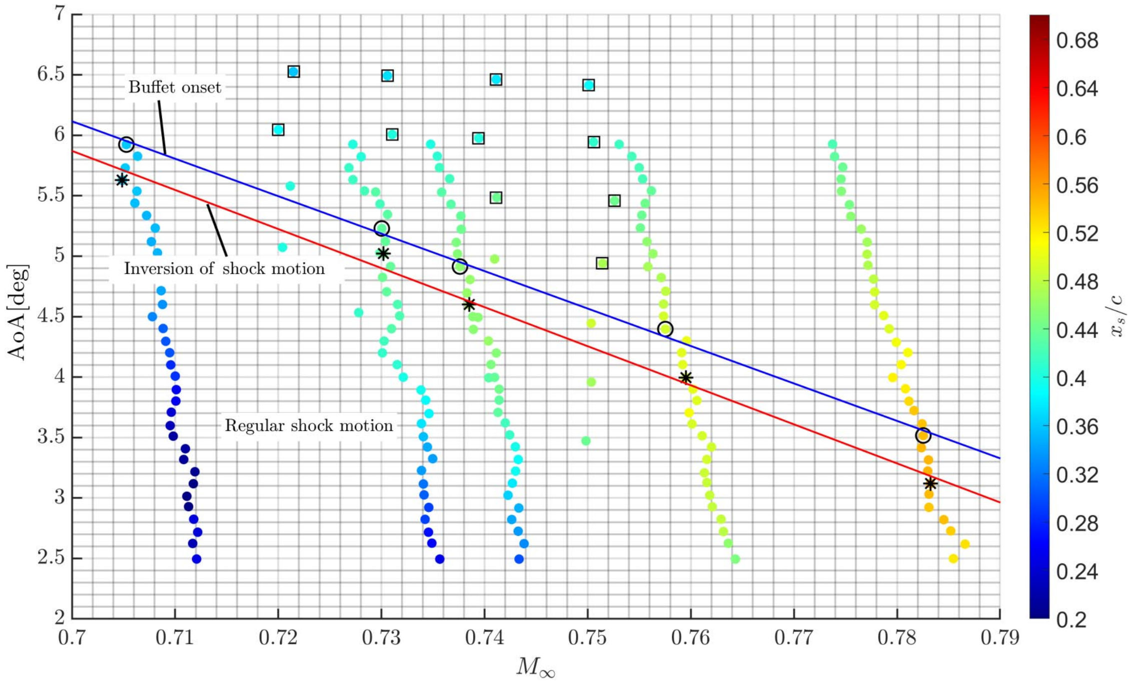

Fig. 11 Color-coded time averages of shock location as a function of M_∞ and AoA. Black stars and open black circles represent shock motion inversion and buffet onset, respectively. Red and blue lines are linear fit functions of shock motion inversion and of buffet onset, respectively. Black open squares highlight developed periodic buffet cases.

Afterward, the trends of the reduced buffet frequencies with M_∞ and the AoA are compared. Finally, the time averages and the standard deviations of the shock location of buffet flows are addressed.

The linear reduction in buffet onset with M_∞, which was described in Refs. [5,11] for the NACA0012 model, seems to also be valid for the OAT15A: at least for the investigated range of M_∞. As is visible in Fig. 11, this reduction amounts to approximately 0.3 deg for an increase of 0.01 in M_∞, which appears to be in good agreement with the one shown in Ref. [17] for the range of Mach numbers between 0.7 and 0.74. However, although in Ref. [17] the shock buffet quenches as of $M_\infty = 0.75$, in the present study, buffet is also present at Mach numbers higher than 0.74. Moreover, the shock position at an AoA above buffet onset lies downstream of the location of maximum curvature of the profile ($x/c = 0.31$) for the entire M_∞ range, which confirms the findings in Ref. [14]. Buffet onset occurs for $M_\infty = 0.73$ at AoA = 5.2 deg, which is with a delay varying between 1.5 and 2 deg with respect to the findings in Refs. [8–10,12,15,17,20]. In Ref. [18], only one out of five investigated turbulence models predicted an unsteady solution, starting at AoA = 4.5 deg.

The reduced buffet frequency at $M_\infty = 0.73$ and AoA = 3.5 deg was 0.208 in Ref. [8] and 0.215 in Ref. [12]. At the same Mach number, a similar frequency is reached in Fig. 9 at AoA = 6.2 deg. In Refs. [10,17], the frequency at $M_\infty = 0.73$ and AoA = 3.5 deg varies with the turbulence model: in Ref. [10], it is between 0.214 and 0.235; and in Ref. [17], it is between 0.217 and 0.225. In Ref. [15], it is 0.232 and equal to the one in Ref. [8] at $M_\infty = 0.74$. In Ref. [9], an increase in AoA from 3.5 to 4.5 deg is necessary when switching from a zonal detached-eddy simulation (DES) to a URANS simulation to obtain the frequency reported in Ref. [8]. In the experiments described in Ref. [20], the same frequency as in Ref. [8] was found at $M_\infty = 0.7$, which corresponds to 0.73 after correcting the blockage caused by the model. Similar to what was presented in Ref. [17], the increase in reduced buffet frequency illustrated in Fig. 9 is monotonic with the AoA. In particular, the increase in k appears to be linear with the AoA, as in the URANS simulations for a NACA0012 model at $M_\infty = 0.76$ shown in Ref. [11]. In Ref. [8], on the other hand, the increase in reduced frequency with an AoA at $M_\infty = 0.73$ is negligible. In Ref. [15], only a slight increase from 0.232 to 0.241 can be observed toward buffet offset, which is reported at AoA = 6 deg. In this regard, it was shown in Ref. [17] that the increase in reduced frequency with the AoA significantly drops with the Mach number, which can also be seen in Fig. 9. Similar to the findings in Refs. [8,12,17], the increase in reduced buffet frequency in Fig. 9 is monotonic with M_∞. The average rate of increase in k with Mach at AoA = 3.5 deg and for an interval of Mach centered on $M_\infty = 0.73$ was 0.015 for an increase of 0.01 in M_∞ in Refs. [8,12,17]. The same trend is found in Fig. 9 at AoA = 6.2 deg.

As can be extrapolated from Table 1, the time average and the standard deviation of the shock location at $M_\infty = 0.73$ and AoA = 6.2 deg are 0.39 and 0.031, respectively. In Ref. [20], the time-averaged shock position at $M_\infty = 0.7$ and AoA = 3.5 deg is almost identical (0.38), whereas the standard deviation is more than doubled (0.067). Considering that, in both of these works, the shock position is detected at a normal distance from the upper surface of 10% of the chord, its value at the surface is even more upstream due to the inclination of the shock front. In Refs. [8,17], the time average and the standard deviation of the shock location at $M_\infty = 0.73$ and AoA = 3.5 deg are, instead, 0.42 and 0.046, respectively. At AoA = 3.9 deg, the standard deviation of the shock location grows to 0.064, which is very close to the value in Ref. [20] at AoA = 3.5 deg and significantly higher than the maximum value (0.038) obtained within the entire range of the aerodynamic parameters investigated in this paper (see Table 1).

Overall, one can infer that the trends of the results (buffet onset, buffet frequency, and shock motion) with the aerodynamic parameters presented in this paper are in agreement with the literature cases. However, focusing on the comparison of the OAT15A results, the buffet amplitude is smaller and buffet onset occurs at a considerably higher AoA. It was shown in Ref. [17] that, depending on the aerodynamic condition, the buffet features can remarkably change. For example, at a higher AoA and lower M_∞, buffet can deviate from a purely harmonic behavior. In general, buffet amplitudes and frequencies are found to be strongly dependent on the aerodynamic parameters. If the effective aerodynamic conditions in the present work differ from the ones in the literature, this could explain a broader and weaker buffet peak and the delay of buffet onset. Factors that could be responsible for different effective aerodynamic conditions are as follows:

1) The first factor is FSI between heave and buffet modes. Both the experiments in Refs. [8,20] and the simulations in Refs. [9,10,12, 15,17] involve rigid models. In Sec. II.C, it was explained how the model in this study cannot be considered rigid concerning the heave mode. Especially at higher AoAs, where the buffet and the heave modes come close to each other, the dominant peak in the spectra tends to broaden and the buffet amplitude to decrease. This can simply be caused by buffet offset but could also be enhanced by the fact that some energy is transferred from the flow to the structure due to FSI. However, it is rather unlikely that FSI is responsible for the delay in buffet onset because the entire flow development (formation of shock, inversion of shock motion and buffet onset) seems to be affected by a similar delay and the interaction between fluid and heave modes becomes significant only after the buffet mode appears in the spectrum (see Fig. 5).

2) The second factor involves 3-D effects due to lower AR. It should be recalled that the AR of the model in the present study is two, whereas the model investigated in Ref. [8] had an aspect ratio of 3.4 and the one in Ref. [20] had one of 2.8. The 3-D effects may be stronger, and it cannot currently be excluded that they have an influence on the delayed flow development, with buffet onset included. As is visible in Fig. 6, one certain 3-D effect, which is also captured for the higher AR models in Refs. [8,20], is the spanwise shock front not being completely straight. However, the buffet frequencies illustrated in Fig. 9 belong to the typical 2-D buffet range (see Sec. I). This suggests that even if local 3-D effects may appear, the overall buffet phenomenon remains 2-D-like. Similar conclusions are drawn for an infinite unswept wing in Ref. [21], where a nonuniform spanwise separation line coexists with nominally 2-D buffet features. A side effect of the spanwise curvature of the shock front could be a slight alteration of the spectrum and a broader buffet peak if the shock detection algorithm jumps from one spanwise position to another at some time instants. This may happen if, for example, at a certain point of the buffet cycle, the initially detected shock that corresponds to a certain spanwise position gets weak and/or the shock that lies at another spanwise position becomes stronger. A correction of the algorithm for these possible 3-D effects is, however, currently not available.

3) A third factor is gap flow at the side walls. The gap flow at the side walls could be responsible for a reduction in effective AoA, and this could explain a delay in buffet onset as well as a reduction in buffet frequency (see Fig. 9).

4) A fourth factor includes wind-tunnel characteristics. In Ref. [8], adaptive walls that mimic an infinite domain are employed to compensate for blockage effects. On the other hand, in Ref. [20], blockage effects are present. As mentioned earlier in this paper, they are deemed responsible for the increase in effective Mach number, which causes buffet onset to occur at lower M_∞ than in Ref. [8]. In the present study, the optimal configuration of boundary-layer suction and divergence of the horizontal walls compensate for the growth of the boundary layer in the test section and provide a constant streamwise pressure distribution without the model. Blockage effects due to the model may not be negligible in transonic conditions even if the blockage ratio is small (less than 3.5%). However, blockage should lead to an increased effective Mach number [20,29], which would result in an earlier onset at lower Mach numbers with respect to Ref. [8]. In Fig. 11, instead, buffet onset at AoA = 3.5 deg is evidently displaced toward higher Mach numbers. In Ref. [29], it was shown that in the TWM, the effect of the slits in the walls, of the divergence of the horizontal walls, and (especially) of the suction on the vertical walls increases once a shock is formed on the model. In particular, higher levels of the aforementioned parameters lead to lower velocities on the profile and more upstream shock locations. Therefore, another possible explanation for the delayed flow

development observed within this work could be that the wind-tunnel settings, albeit being optimal without the model, excessively perform once the model is installed in the test section.

5) The fifth factor is the tripping of the boundary layer. In both Refs. [8,20], carborundum grains are used for the tripping of the boundary layer, albeit with different heights (102 and 140 μm, respectively). In the present study, on the other hand, a row of circular dots is employed, which are 70 μm high and distributed every 6 mm along the span. Even though the location of the tripping is identical to all the experimental groups ($x/c = 0.07$), slight differences can be expected in the thickness of the turbulent boundary layer interacting with the shock. In Ref. [16], the effects on buffet features of the boundary-layer state were investigated. Two configurations of the OALT25 airfoil, for which the design is very similar to the OAT15A but targeted for extended laminar flow, were compared: with and without the tripping of the boundary layer at $x/c = 0.07$. In the latter case, the shock becomes stronger and its location significantly shifts downstream. The amplitude of its oscillations becomes remarkably lower. Moreover, the typical 2-D buffet frequency observed in the spectrum of the pressure fluctuations for the tripping case ($St = 0.07$) is barely visible in the configuration without tripping. Instead, a new dominant frequency appears at $St = 1$, starting from lower angles of attack. The frequencies reported in Refs. [8,20] and the present work are all similar to the case with tripping in Ref. [16], which confirms that the boundary layer interacting with the flow is in all cases turbulent. However, as already mentioned, the thickness of the boundary layer at the shock location could differ and contribute to the disparities among the experiments. In the numerical works in Refs. [9,12,15], the simulated flow is fully turbulent. In Ref. [17], the influence on buffet onset of the fixed transition at $x/c = 0.07$ is found to be negligible.

E. Sensitivity of Buffet Features

In Sec. III.D, it was shown how the numerical results in Refs. [9,10,12,15,17] presented a similar buffet onset as in Ref. [8] for $M_\infty = 0.73$ (the maximum delay was found in Ref. [18] and is equal to 1.3 deg). Also, the buffet frequency too at $M_\infty = 0.73$ and AoA $= 3.5$ deg can be accurately reproduced enough (the maximum relative deviation is found in Ref. [10] and is equal to 13%). In general, however, the numerically simulated buffet features (mean shock location, shock oscillation amplitude, buffet frequency and onset, boundary-layer profiles, and fluctuations of C_L and C_p) present a significant sensitivity to the sort of analysis (global stability simulation, URANS simulation, and DES), the turbulence model, the spatial and temporal discretization, and the inclusion or not in the simulation of wind-tunnel geometry. In Sec. III.D, it was also stressed that the three experimental campaigns under examination (Refs. [8,20] and the present work) exhibit distinct buffet features at supposedly equivalent aerodynamic conditions, even though similarities can be found (e.g., the buffet frequency between Refs. [8,20] or the time-averaged shock location between Ref. [20] and the present work). It was concluded that different effective aerodynamic conditions due to structural properties and the geometry of the model, wind-tunnel characteristics, and/or sort of tripping of the boundary layer can be held accountable for discrepancies in the results. Therefore, shock buffet is also sensitive to the experimental boundary conditions. In Ref. [15], the regions of the flow that can most affect buffet features and the buffet sensitivity to several steady forcings were investigated via global mode analysis. The analysis of the adjoint global mode revealed that the boundary layer, and especially its separation point, is the region of the flow with the highest receptivity: that is, the most capable of affecting the shock amplitude and frequency by application of a harmonic forcing. Moreover, the sensitivity gradients of the global modes with respect to a steady forcing show that a streamwise momentum force in the boundary layer or in the recirculation region, a cooling of the flow, or an increase of the eddy viscosity in the attached boundary layer (similar to the experimental application of vortex generators) manage to stabilize the unstable eigenvalue.

Shock buffet is evidently an extremely sensitive phenomenon. Therefore, the effect of the two following parameters on buffet onset and amplitude is investigated and presented in this section: the boundary-layer suction of the vertical walls of the test section, and the gap flow from the lower to the upper surfaces of the model at the side windows. First, a sweep run with 2.5 deg < AoA < 5.9 deg and 0.735 < M_∞ < 0.745 is performed with a reduced suction; the cross section of the pipes connecting the test section with the diffusor is reduced by 10% with respect to the optimal configuration mentioned in Sec. II.A. Then, the original value of suction is restored and the same run is performed with a closed gap by application of silicon. These results are then compared with the original sweep. In the left-side image of Fig. 12, the mean shock position is plotted as a function of the AoA, where the shaded error bars display the standard deviation of the shock location. At lower AoAs, the decrease in boundary-layer suction causes the shock locations to move downstream, similar to what was reported in Ref. [29] and discussed in Sec. III.D. This suggests an acceleration in flow development. At a higher AoA, the differences with respect to the original case tend to disappear, except for a later inversion of shock motion, which is shifted from AoA $= 4.6$ to 4.7 deg, and a reduced level of shock oscillations. The closure of the gap moves the shock position even more downstream before the inversion point and slightly more upstream after it. Buffet onset shifts from AoA $= 4.9$ to 4.8 deg with respect to the original run. Moreover, the shock oscillations increase from a maximum $\sigma_{x_s/c}$ of 0.03 to 0.04 as compared to the original sweep. Therefore, the closure of the gap facilitates the flow development before inversion and enhances the buffet phenomenon.

The right-side plot in Fig. 12 displays the PSDs of the shock oscillations at AoA $= 5.9$ deg. Reducing suction decreases the level of shock oscillations, even though the frequency stays constant. The closure of the gap slightly increases the extent of the oscillations and moves the peak from 100 to 115 Hz. Because the buffet frequency normally rises with an increase in the AoA or M_∞, this may indicate that the closure of the gap increases the effective AoA of the profile. Even though the reduction in boundary-layer suction and the closure of the gap flow exhibit some influence on the shock location before inversion and buffet amplitude, the effect on the inversion of shock motion and onset is virtually negligible and does not explain the delay with respect to the literature cases.

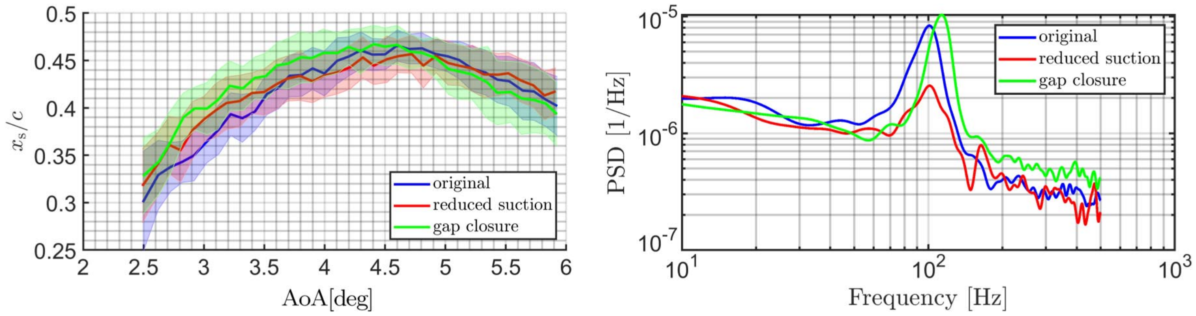

Fig. 12 Effect of reduced suction and of closure of gap on shock location for 2.5 deg < AoA < 5.9 deg and 0.735 < M_∞ < 0.745 (left) and on the PSDs of its fluctuations for $M_\infty = 0.735$ and AoA = 5.9 deg (right).

IV. Conclusions

With the aim to investigate the influence of the angle of attack and Mach number on the shock features and buffet frequency as well as accurately determine the buffet boundaries, a supercritical profile (OAT15A) was experimentally investigated at the Trisonic Windtunnel Munich by means of BOS, deformation, and force measurements.

The PSDs of the fluctuations of the shock location determined via BOS show an increase in buffet frequency with both the AoA and M_∞. In particular, the increase in reduced frequency with the AoA appears to be linear, with a decrease in slope as M_∞ increases. The amplitude of the buffet frequency at each M_∞ rises with the AoA until reaching a maximum. Then, it further decreases as buffet approaches its offset. Both buffet boundaries show a rather linear trend with M_∞. Developed buffet flows are only present at mean shock positions downstream of the location of the maximum curvature of the profile. The question arises whether, following the same principle, buffet offset is caused by the shock moving upstream of this location at a higher AoA.

The inversion of shock motion proved to be a reliable, necessary but not sufficient condition for buffet onset, with buffet onset being 0.3–0.4 deg displaced toward a higher AoA with respect to the inversion of shock motion. However, it is not obvious why developed shock buffet is delayed compared to the appearance of significant boundary-layer separation on the model. A possible explanation for this could be the following; with the increase in the AoA, the inversion of shock motion (or, in the case of an increase in M_∞, the decrease in the rate of downstream shock motion) makes it possible to satisfy the equality and compatibility conditions while keeping the flow solution stable. This is valid, however, only until a specific state and extent of boundary-layer separation (separation bubble, trailing-edge separation, or full separation), which depends on the model geometry and aerodynamic parameters. After this turning point, a further increase in AoA is only compatible with an unsteady solution; that is, shock buffet takes place. Because the inversion of shock motion and its rate are not altered after buffet onset (see Fig. 10), it may be argued that buffet is an unsteady way of satisfying the equality and compatibility conditions. The big, yet unanswered question is what happens at buffet onset that makes the solution shift from steady to unsteady. To solve this riddle, a careful analysis of the evolution with the aerodynamic parameters of the pressure field on the model, especially in proximity of the trailing edge and in the wake, is required.

The trends of the results (buffet onset, buffet frequency, and shock motion) with the aerodynamic parameters are in good agreement with the literature cases. However, focusing on the comparison of the OAT15A results, the buffet amplitude is smaller and buffet onset occurs at a considerably higher AoA. Different effective aerodynamic conditions due to FSI between heave and buffet modes, 3-D effects, the gap flow at the side walls, wind-tunnel characteristics, and/or sort of tripping of the boundary layer are deemed responsible for these disparities.

The comparison of the literature results also revealed a general sensitivity of buffet features to both numerical and experimental parameters. For this reason, the effects of the gap flow and of the boundary-layer suction on buffet onset and amplitude were investigated. Even though the reduction in boundary-layer suction and the closure of the gap flow exhibit some influence on the shock location before inversion and buffet amplitude, the effect on the inversion of shock motion and buffet onset is virtually negligible and does not explain the delay with respect to the literature cases. To understand the root cause of different flow developments and buffet features among the literature cases, a possible approach could be to compare the shock characteristics (location, strength, and inclination) and the pressure distributions (on the model, along the wind-tunnel walls and in the wake) for several numerical and experimental parameters.

Considering the large number of investigated aerodynamic conditions, this campaign constitutes a rich dataset and provides the numerical community with a valuable tool for a more complete validation of the computational fluid dynamics methods.

Acknowledgments

Financial support in the frame of the Holistic Optical Metrology for Aero-Elastic Research project from the European Union's Horizon 2020 research and innovation program under grant agreement no. 769237 is gratefully acknowledged. Additional financial support from the Universität der Bundeswehr München is also gratefully ackowledged. The authors would like to thank Jens Nitzsche, Yves Govers, Johannes Dillinger, Johannes Knebusch, and Tobias Meier from the DLR, German Aerospace Center, Institute of Aeroelasticity for their valuable contributions and expertise in the design, manufacturing, and integration of the presented setup.

References

[1] Mabey, D. G., "Oscillatory Flows from Shock Induced Separations on Biconvex Aerofoils of Varying Thickness in Ventilated Wind Tunnels," Advisory Group for Aerospace Research and Development TR 296, Aix-en-Provence, France, 1981.

[2] Gibb, J., "The Cause and Cure of Periodic Flows at Transonic Speed," Ph.D. Thesis, Cranfield Univ., Cranfield, England, U.K., 1983.

[3] Mabey, D. G., Welsh, B. L., and Cripps, B. E., "Periodic Flows on a Rigid 14% Thick Biconvex Wing at Transonic Speeds," British Royal Aircraft Establishment TR 81059, 1981.

[4] Pearcey, H. H., "A Method for the Prediction of the Onset of Buffeting and Other Separation Effects from Wind Tunnel Tests on Rigid Models," Advisory Group for Aerospace Research and Development TR 223, Neuilly-Sur-Seine, France, 1958.

[5] McDevitt, J. B., and Okuno, A. F., "Static and Dynamic Pressure Measurements on a NACA 0012 Airfoil in the Ames High Reynolds Number Facility," NASA, Scientific and Technical Information Branch TR 2485, 1985, https://ntrs.nasa.gov/citations/19850019511 [15 July 2022].

[6] Lee, B. H. K., "Oscillatory Shock Motion Caused by Transonic Shock Boundary-Layer Interaction," *AIAA Journal*, Vol. 28, No. 5, 1990, pp. 942–944.
https://doi.org/10.2514/3.25144

[7] Lee, B. H. K., "Self-Sustained Shock Oscillations on Airfoils at Transonic Speeds," *Progress in Aerospace Sciences*, Vol. 37, No. 2, 2001, pp. 147–196.
https://doi.org/10.1016/S0376-0421(01)00003-3

[8] Jacquin, L., Molton, P., Deck, S., Maury, B., and Soulevant, D., "Experimental Study of Shock Oscillation over a Transonic Supercritical Profile," *AIAA Journal*, Vol. 47, No. 9, 2009, pp. 1985–1994.
https://doi.org/10.2514/1.30190

[9] Deck, S., "Numerical Simulation of Transonic Buffet over a Supercritical Airfoil," *AIAA Journal*, Vol. 43, No. 7, 2005, pp. 1556–1566.
https://doi.org/10.2514/1.9885

[10] Thiery, M., and Coustols, E., "URANS Computations of Shock-Induced Oscillations over 2D Rigid Airfoils: Influence of Test Section Geometry," *Flow, Turbulence and Combustion*, Vol. 74, No. 4, 2005, pp. 331–354.
https://doi.org/10.1007/s10494-005-0557-z

[11] Crouch, J. D., Garbaruk, A., Magidov, D., and Travin, A., "Origin of Transonic Buffet on Aerofoils," *Journal of Fluid Mechanics*, Vol. 628, June 2009, pp. 357–369.
https://doi.org/10.1017/S0022112009006673

[12] Crouch, J. D., Garbaruk, A., Magidov, D., and Jacquin, L., "Global Structure of Buffeting Flow on Transonic Airfoils," *IUTAM Symposium on Unsteady Separated Flows and Their Control*, Springer, New York, 2009, pp. 297–306.
https://doi.org/10.1007/978-1-4020-9898-7_25

[13] Nitzsche, J., "A Numerical Study on Aerodynamic Resonance in Transonic Separated Flow," *IFASD 2009, International Forum on Aeroelasticity and Structural Dynamics*, Paper 126, Seattle, WA, June 2009, pp. 1–18, https://elib.dlr.de/61964/ [retrieved 15 July 2022].

[14] Iovnovich, M., and Raveh, D. E., "Reynolds-Averaged Navier-Stokes Study of the Shock-Buffet Instability Mechanism," *AIAA Journal*, Vol. 50, No. 4, 2012, pp. 880–890.
https://doi.org/10.2514/1.J051329

[15] Sartor, F., Mettot, C., and Sipp, D., "Stability, Receptivity, and Sensitivity Analyses of Buffeting Transonic Flow over a Profile," *AIAA Journal*, Vol. 53, No. 7, 2015, pp. 1980–1993.
https://doi.org/10.2514/1.J053588

[16] Brion, V., Dandois, J., Abart, J. C., and Paillart, P., "Experimental Analysis of the Shock Dynamics on a Transonic Laminar Airfoil," *Progress in Flight Physics*, Vol. 9, June 2017, pp. 365–386.
https://doi.org/10.1051/eucass/2016090365

[17] Giannelis, N. F., Levinski, O., and Vio, G. A., "Influence of Mach Number and Angle of Attack on the Two-Dimensional Transonic Buffet Phenomenon," *Aerospace Science and Technology*, Vol. 78, June 2018, pp. 89–101.
https://doi.org/10.1016/j.ast.2018.03.045

[18] Nitzsche, J., Ringel, L. M., Kaiser, C., and Hennings, H., "Fluid-Mode Flutter in Plane Transonic Flows," Paper 006, 2019, https://elib.dlr.de/127989/ [retrieved 15 July 2022].

[19] Accorinti, A., Baur, T., Scharnowski, S., Knebusch, J., Dillinger, J., Govers, Y., Nitzsche, J., and Kähler, C. J., "Measurements of Deformation, Schlieren and Forces on an OAT15A Airfoil at Pre-Buffet and Buffet Conditions," *IOP Conference Series: Materials Science and Engineering*, Vol. 1024, IOP Publishing, Amsterdam, 2021, Paper 012052, https://iopscience.iop.org/article/10.1088/1757-899X/1024/1/012052/meta [retrieved 15 July 2022].

[20] D'Aguanno, A., Schrijer, F. F. J., and van Oudheusden, B. W., "Experimental Investigation of the Transonic Buffet Cycle on a Supercritical Airfoil," *Experiments in Fluids*, Vol. 62, No. 10, 2021, pp. 1–23.
https://doi.org/10.1007/s00348-021-03319-z

[21] Iovnovich, M., and Raveh, D. E., "Numerical Study of Shock Buffet on Three-Dimensional Wings," *AIAA Journal*, Vol. 53, No. 2, 2015, pp. 449–463.
https://doi.org/10.2514/1.J053201

[22] Dandois, J., "Experimental Study of Transonic Buffet Phenomenon on a 3D Swept Wing," *Physics of Fluids*, Vol. 28, No. 1, 2016, Paper 016101.
https://doi.org/10.1063/1.4937426

[23] Paladini, E., Dandois, J., Sipp, D., and Robinet, J. C., "Analysis and Comparison of Transonic Buffet Phenomenon over Several Three-Dimensional Wings," *AIAA Journal*, Vol. 57, No. 1, 2019, pp. 379–396.
https://doi.org/10.2514/1.J056473

[24] Crouch, J. D., Garbaruk, A., and Strelets, M., "Global Instability in the Onset of Transonic-Wing Buffet," *Journal of Fluid Mechanics*, Vol. 881, Dec. 2019, pp. 3–22.
https://doi.org/10.1017/jfm.2019.748

[25] Paladini, E., Beneddine, S., Dandois, J., Sipp, D., and Robinet, J. C., "Transonic Buffet Instability: From Two-Dimensional Airfoils to Three-Dimensional Swept Wings," *Physical Review Fluids*, Vol. 4, No. 10, 2019, Paper 103906.
https://doi.org/10.1103/PhysRevFluids.4.103906

[26] Garbaruk, A., Strelets, M., and Crouch, J. D., "Effects of Extended Laminar Flow on Wing Buffet-Onset Characteristics," *AIAA Journal*, Vol. 59, No. 8, 2021, pp. 2848–2854.
https://doi.org/10.2514/1.J060707

[27] Plante, F., Dandois, J., Beneddine, S., Laurendeau, E., and Sipp, D., "Link Between Subsonic Stall and Transonic Buffet on Swept and Unswept Wings: From Global Stability Analysis to Nonlinear Dynamics," *Journal of Fluid Mechanics*, Vol. 908, Dec. 2021, pp. 1–40.
https://doi.org/10.1017/jfm.2020.848

[28] Scharnowski, S., Bross, M., and Kähler, C. J., "Accurate Turbulence Level Estimations Using PIV/PTV," *Experiments in Fluids*, Vol. 60, No. 1, 2019, pp. 1–12.
https://doi.org/10.1007/s00348-018-2646-5

[29] Scheitle, H., and Wagner, S., "Influences of Wind Tunnel Parameters on Airfoil Characteristics at High Subsonic Speeds," *Experiments in Fluids*, Vol. 12, No. 1, 1991, p. 90–96.
https://doi.org/10.1007/BF00226571

[30] Chu, T. C., Ranson, W. F., and Sutton, M. A., "Applications of Digital-Image-Correlation Techniques to Experimental Mechanics," *Experimental Mechanics*, Vol. 25, No. 3, 1985, pp. 232–244, https://www.researchgate.net/profile/Tsuchin-Chu/publication/227293508_Applications_of_digital-image-correlation_techniques_to_experimental_mechanics/links/55d760e708aed6a199a68265/Applications-of-digital-image-correlation-techniques-to-experimental-mechanics.pdf.

[31] Raffel, M., "Background-Oriented Schlieren (BOS) Techniques," *Experiments in Fluids*, Vol. 56, No. 3, 2015, pp. 1–17.
https://doi.org/10.1007/s00348-015-1927-5

[32] Welch, P. D., "The Use of Fast Fourier Transform for the Estimation of Power Spectra: A Method Based on Time Averaging over Short, Modified Periodograms," *IEEE Transactions on Audio and Electroacoustics*, Vol. 15, No. 2, 1967, pp. 70–73.
https://doi.org/10.1109/TAU.1967.1161901

D. E. Raveh
Associate Editor

AIAA Journal
Vol. 61, No. 1, January 2023

Effect of Mach Number and Pitching Eigenfrequency on Transonic Buffet Onset

Tim Korthäuer,* Alessandro Accorinti,† Sven Scharnowski,‡ and Christian J. Kähler§
University of the Bundeswehr Munich, 85577 Neubiberg, Germany

https://doi.org/10.2514/1.J061915

The transonic flow around an elastically suspended supercritical airfoil was experimentally investigated in order to enhance knowledge of buffet boundary dependencies and the corresponding self-excited fluid–structure interaction (buffeting). For that purpose, an experimental setup was designed, manufactured, and integrated in the Trisonic Wind Tunnel Munich. The design consisted of a rigid, two-dimensional, supercritical airfoil (OAT15A) with optional pitching degree of freedom and variable torsional spring stiffness. High-speed background-oriented schlieren measurements were used to observe the shock with its dynamics, while a high-speed stereo camera setup for correlation-based deformation measurements was implemented to track the dynamics of the structural motion. Pre-buffet and buffet flows were analyzed by a continuous increase of the angle of attack. The detailed observation of the shock position with increasing angle of attack exhibited a clear effect of Mach number and pitch eigenfrequency on the buffet phenomenon. The corresponding onset boundary clearly shifted into the "pre-buffet" regime given specific structural settings. Furthermore, the resulting fluid–structure interaction of shock and coupled pitch–heave motion showed characteristics of structural frequency lock-in for the pitch-to-buffet frequency ratios of 1.2 and the mode veering region for ratios of 1 and 0.9, indicating the transition region from fluid mode flutter to structural mode flutter.

Nomenclature

c = chord length, mm
F = uncalibrated force
f = frequency, Hz
I = moment of inertia, kg · m^2
k = reduced frequency, $\pi f c / u_\infty$
M = Mach number
m = total mass of all moving parts, kg
Re = chord-based Reynolds number
s = span width, mm
t = time, s
u = flow-velocity in streamwise direction, m/s
x = streamwise ordinate of wind-tunnel coordinate system
x_s = streamwise shock position in wing coordinate system
y = spanwise ordinate of wind-tunnel coordinate system
z = vertical ordinate of wind-tunnel coordinate system
α = angle of attack, °
γ = inertia factor, $I/(c^2 m)$
μ = mass ratio, $(m/s)/[\rho_\infty \pi (c/2)^2]$
ρ = density, kg/m^3

Subscripts

A = rotational axis
b = buffet (fixed/rigid wing)
set = set value of angle of attack, prescribed by facility
st = static
θ = pitch-angular direction
$1, x$ = streamwise component of one-dimensional force balance at lower end of pitching lever arm
$3, x$ = streamwise component of three-dimensional force balance
$3, z$ = vertical component of three-dimensional force balance
∞ = freestream

I. Introduction

THE development and operation of modern commercial aircraft is strongly driven by the demand for high cost efficiency and fuel efficiency while ensuring passenger safety. As for cost efficiency, the increase in flight speed remains a crucial parameter. At the common, high subsonic to transonic cruise speed, local flow velocities above a supercritical airfoil can exceed sonic boundaries and lead to a supersonic flow region on the airfoil suction side. This local region is terminated by a shock wave, leading to a sudden flow deceleration and pressure increase, to satisfy the subsequent higher static pressure boundary conditions of the main flow. Depending on the shock strength, boundary-layer separation may occur. At increasing flight speeds or angle of attack (AoA), the shock wave can become unsteady and result in a self-sustained shock-wave–boundary-layer interaction (SWBLI) with limited amplitudes of shock oscillations. This dynamic instability of the flow in absence of structural motion is denoted as transonic shock buffet and has been of interest since the 1950s [1–5]. Due to the associated strong load variations and possible interaction with the structure, buffet is one of the limiting factors of the flight envelope of commercial aircraft and plays a major role with respect to safety aspects [4,6,7]. Different types of shock buffet have been observed: Type I describes the phenomenon on biconvex airfoils at zero incidence where it exhibits (phase-locked) SWBLI on both pressure and suction sides, and can be well explained by a model described in [8,9]. Type II, in contrast, is characteristic for modern supercritical airfoils and exhibits shock oscillations only on the airfoil suction side at positive AoA. Transonic buffet of type II has been studied over decades, but a comprehensive physical explanation of the root cause remains missing. Multiple observations and hypotheses have been published, offering explanation of buffet and prediction of its boundaries (onset and offset) for different combinations of airfoil shapes and operating conditions.

Most intensively, the model of Lee [10] has been discussed, where down- and upstream propagating pressure waves from the model trailing edge interact with the shock front and induce the oscillations

---

Received 4 April 2022; revision received 18 August 2022; accepted for publication 27 August 2022; published online Open Access 27 October 2022.

*Research Associate, Institute of Fluid Mechanics and Aerodynamics, Werner-Heisenberg-Weg 39; tim.baur@unibw.de.

†Research Associate, Institute of Fluid Mechanics and Aerodynamics, Werner-Heisenberg-Weg 39; alessandro.accorinti@unibw.de.

‡Research Associate, Institute of Fluid Mechanics and Aerodynamics, Werner-Heisenberg-Weg 39.

§Full Professor, Institute of Fluid Mechanics and Aerodynamics, Werner-Heisenberg-Weg 39.

on the airfoil suction side. As this model was not found to be universally valid [3,11], it was adapted as described in [3,12]. The validity of the adapted buffet model outlined in [13] was not harmed by the introduction of pitching flexibility at low structural eigenfrequencies. The identification of buffet by a global flow instability [14] has been widely accepted and has become the means of choice for the numerical determination of buffet boundaries, i.e., the bifurcation points of the "unsteady" fluid mode [4,15–18]. The flowfield associated with this unsteady mode is characterized by a coupled shock oscillation and pulsation of the separated boundary layer, which was illustrated in both numerical [19] and experimental [3] results. Buffet onset was estimated this way for different Mach numbers, AoA, and geometries, yielding a good agreement with the experimental results of [2,3]. Also other buffet features, such as frequency and amplitude, were fairly predicted. Investigations of the buffet boundaries, in particular numerically, have ever accompanied the phenomenon, since it only appears in a narrow band of AoA and Mach number in transonic conditions. On a rigid wing, it was found that AoA and Mach number form a monotonous boundary, where an increase of either can induce buffet onset given a sufficiently high Mach number [3,20–24]. Before the publication of [5], a multiparametric experimental determination of buffet boundaries remained elusive. The absolute positions of the boundaries, however, vary strongly depending on the boundary conditions of the experimental facility (e.g., pressure distribution, wall boundary-layer or blockage correction measures [5]) or the applied turbulence models in numerical simulations [16,24]. Furthermore, multiple different criteria and techniques have been selected for the onset definition, ranging from an increase in surface pressure [2,3] or lift measurements [24,25], over observation of the bifurcation points [16,22] to the observation of the mere shock position statistics [5].

If the eigenfrequencies of the wing structure are on the same order of magnitude as the shock buffet frequency, the phenomenon can interact with the structure. This fluid–structure interaction (FSI) between the dynamic instability of the flow and the elastic structure is commonly known as "buffeting." It results in high-amplitude structural motion and, consequently, increased stress on the aircraft structure, eventually even in catastrophic structural failure and threatens the obligatory safety aspect. Several research groups conducted experiments or simulations under consideration of elastic wing structures in the past. The earliest computational work dealt with forced excitation of buffet and its FSI by flap or structural motions [26–28], followed by several groups that dealt with self-excitation, which can also lead to self-sustained limit-cycle oscillations of the airfoil [29–31].

With the upcoming approach of the modal analysis of the flow, the combined coupled numerical analysis under consideration of both fluid and structural modes moved into the focus of latest aeroelastic research. The detailed analysis showed that coupling between different modes can occur. This way, the modal damping and consequently bifurcation characteristics may be affected, i.e., buffet onset. In plain terms, structural eigenfrequencies in a certain range can induce a premature buffet onset [15,16]. Therefore, a separated treatment of buffet and buffeting is not deemed useful anymore for the mutually dependent phenomena, and the term "buffet" will be used in this work as the representation of an unsteady fluid mode (shock) independently from its coupling with or without the structure. Furthermore, some research groups identified the presence of atypical excitation behavior. Depending on the ratio of the structural pitch to rigid buffet frequency f_θ/f_b, an asymmetrical structural response appeared, leading to a high-amplitude response for ratios between $1 \lessapprox f_\theta/f_b \lessapprox 1.8$ with a maximum between $1.3 \lessapprox f_\theta/f_b \lessapprox 1.6$. The amplitude was hereby additionally influenced by the mass ratio and damping of the system [31,32]. Classical structural excitation, on the contrary, should lead to a maximum response at a ratio of 1 ("resonance"), as discussed in [28] for forced excitation. Additionally, the coupled frequency was found to synchronize with the structural eigenfrequency (lock-in phenomenon) for the same range of higher ratios, in contrast to classical structural excitation. For $f_\theta/f_b < 1$, a coupled motion with the same frequency as for rigid-wing buffet was obtained, the coupled motion was governed by the fluid mode [16,28,30–32]. In between, a transition or veering region was located, where the coupled frequency transitions from one state to the other. The extent of that region with respect to the structural frequency increased with reduced mass ratio [15,30,31].

In most experimental research of the past, the structural frequencies were set with a considerable distance below the buffet frequency, which led to an excitation of the structural motion at the buffet frequency (fluid mode) [13,33,34]. In [35], first experiments were shown, where the structural pitch frequency was set in the vicinity of the rigid wing buffet frequency in order to obtain a strong FSI. During the observed limit-cycle FSI, the shock oscillation locked into the slightly higher structural frequency. Special emphasis was set on the observation of the flowfield and the interaction of shock, structure, and separated boundary layer.

To conclude, the mentioned findings have emphasized the necessity of coupled fluid–structure simulations in the aircraft design process, rather than an unidirectional system without structural feedback onto the flow. The rigid-wing buffet only represents the boundary case for an infinitely stiff structural system [15,16]. The numerical basis of this research is already quite extensive, but experimental data are lacking to verify the simulations. For that reason, an experimental setup was designed by the authors to investigate the phenomenon with particular attention to the self-excitation of transonic FSI. After an extensive measurement campaign with focus on buffet onset boundaries on a mostly rigid wing [5,36,37], the pitching degree of the wing was released and the corresponding torsional spring stiffness adjusted to obtain pitching eigenfrequencies in the vicinity of the shock buffet frequency, namely, just below, approximately equal, and slightly above.

Section II gives an overview of the experimental setup and the facility, and is followed by detailed information about the deployed measurement techniques and the parametric variations in Secs. III and IV. The effect of the AoA is presented together with the underlying signal analysis procedures by reference to one wind-tunnel run in Sec. V. After the presentation of the effects of the Mach number in Sec. VI and pitch eigenfrequency in Sec. VII, an overview of the determined onset boundaries is given in Sec. VIII. Finally, the presented results are summed up, conclusions are drawn, and an outlook for future work prospects is given in Sec. IX.

II. Experimental Setup

The experiments were perfomed in the Trisonic Wind Tunnel of the Bundeswehr University in Munich (TWM). It is a blow-down-type wind tunnel with a rectangular test section of 0.3 m width and 0.68 m height. The facility allows for aerodynamic profile testing from subsonic to supersonic flows. Two adjustable throats, a Laval nozzle upstream (for supersonic speeds), and a diffusor downstream (for subsonic speeds) of the test section allow the operation at Mach numbers in the range of 0.2–3.0. Reynolds number control is established by setting the total pressure of the incoming dry air between 1.2 and 5 bar. The freestream turbulence level is approximately 1.3%, based on the velocity fluctuations in streamwise direction. A detailed description of the facility and its characterization can be found in [38,39]. Boundary-layer growth in the test section was compensated by diverging horizontal walls and by using boundary-layer suction on the vertical walls. The divergence and suction settings were optimized in advance to obtain a constant streamwise wall pressure distribution throughout the empty test section for all relevant Mach numbers. The resulting angle of each horizontal wall was 0.08° along the complete test section length of 1.8 m.

After the publication of [3], the supercritical airfoil profile OAT15A became a benchmark for transonic buffet analysis [4,14] and was therefore selected for this campaign. The airfoil introduced a maximum blockage of 3.5% in the facility at the highest AoA considered. Figure 1 shows the experimental setup for the operation of buffeting experiments with reduced degrees of freedom (DOF). Focus of the design was the best possible realization of a spring-mounted pitching DOF with reduced heave motion. Furthermore, the capability of simultaneous three-dimensional (3D) force and

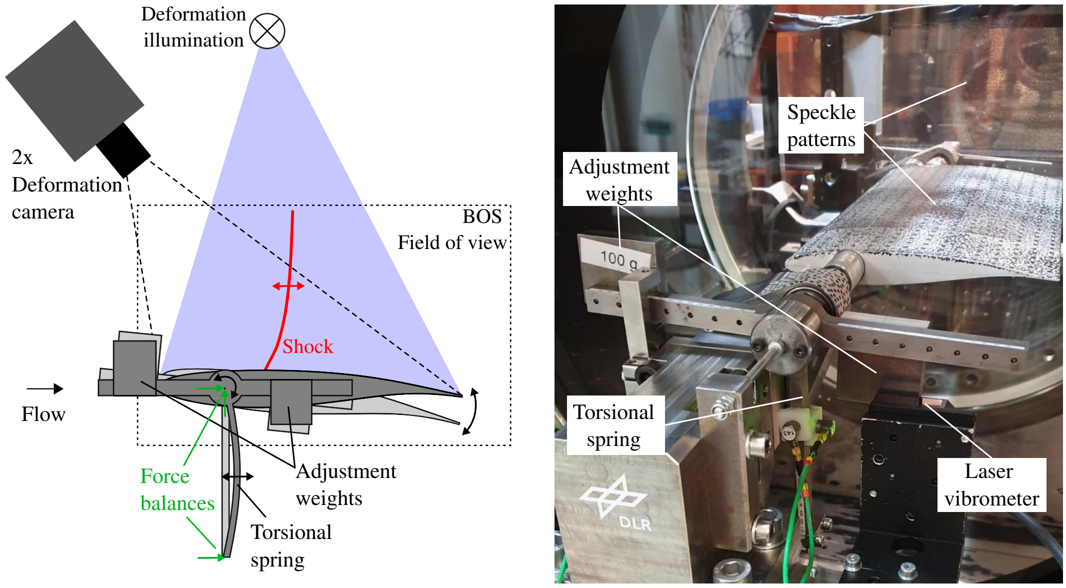

Fig. 1 Sketch (left) and photograph (right) of the mechanic implementation of the spring-mounted rigid wing with a pitching DOF and reduced heave DOF and applied measurement techniques.

aerodynamic moment measurements on either wing side while maintaining optical access was of major importance in the design process. The rectangular OAT15A wing model was manufactured from carbon-fiber-reinforced polymer by Weberschock Development in order to obtain a maximum of stiffness at lowest possible mass for a low experimental mass ratio. The model had a span width of $s = 298$ mm and chord length of $c = 152$ mm. The resulting aspect ratio of 1.96 does not necessarily allow the assumption of two-dimensional (2D) flow. Nevertheless, detailed investigations of the shock front have shown that 2D characteristics of shock buffet remain dominant, despite 3D effects closer to the walls. The boundary layer was tripped at 7% of chord on both, suction, and pressure side, by means of a line of circular stickers of 3 mm diameter and 60 μm thickness at 6 mm distance. An integrated steel shaft, with its center line located at 25% of chord, defined the rotational axis and was fed through circular holes in the side windows and supported by bearings outside the test section. A set of lever arms and adjustment weights was externally attached to the shaft, as shown in Fig. 1. These parts undertook the role of the torsional spring (vertical lever arm) and allowed the adjustment of moment of inertia and center of gravity (horizontal lever arms with trimming weights). The latter was set to coincide with the elastic/rotational axis as to decouple the structural modes in wind-off conditions for all flexible cases. Laser-vibrometer measurements on the downstream directed lever arm were used to complement the force measurements with online information about the current amplitude and frequency content of the pitching motion. A mechanical stop was used to limit the model pitching motion to a maximum AoA of ±2.5°. Approaching this limit, the wind-tunnel run was interrupted before exposing model and setup to excessive loads or causing structural failure.

III. Measurement Techniques

For the nonintrusive measurements of the shock-wave position, spanwise background-oriented schlieren (BOS) measurements were deployed. A random point pattern was positioned in the background of the test section and illuminated from the back by LED light (Luminus CBT-120-B-C11KM301, 462 nm). Images of the pattern were recorded from the opposite side of the test section by a high-speed camera (Phantom V2640) with an image rate of 1000 Hz. Density gradients and the corresponding change of refraction index led to a distortion of the dot pattern that allowed for a qualitative reconstruction of the density variations in the flow by windowwise cross-correlation with an undisturbed reference image, as described in [40]. Figure 2 (left) shows a raw BOS image with clear presence of a shock wave. In Fig. 2 (right), the resulting displacement map of the cross-correlation is displayed. Furthermore, the results of an algorithm-based detection of the shock position at different heights of the wing surface are visualized by means of black circles. Given the importance of its influence on the flow, structural deformations of the wing were detected via stereo digital image correlation (DIC) measurements (see [41]). A random speckle pattern was applied to the upper wing surface to optimize the correlation results. The pattern was illuminated from the top of the test section by four UV-LEDs (Luminus CBM-120-UVX, 410 nm). Two high-speed cameras (PCO Dimax HS4), mounted outside the test section side windows, observed the suction side under an angle of approximately 30°. Images were recorded synchronously with a recording rate of 1000 Hz. Making use of an a priori coplanar volume calibration of the stereo camera setup, a correlation-based 3D surface reconstruction was performed for every image pair. In Fig. 3 (left), an example result of the obtained

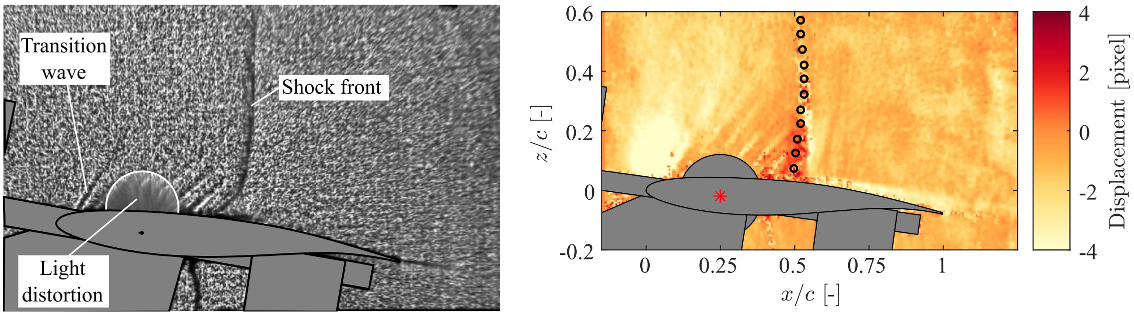

Fig. 2 Raw BOS image with clear presence of a compression shock (left). Exemplary processed BOS displacement field (right), representing density variations in streamwise direction. Black circles represent the automatically determined shock position at different heights.

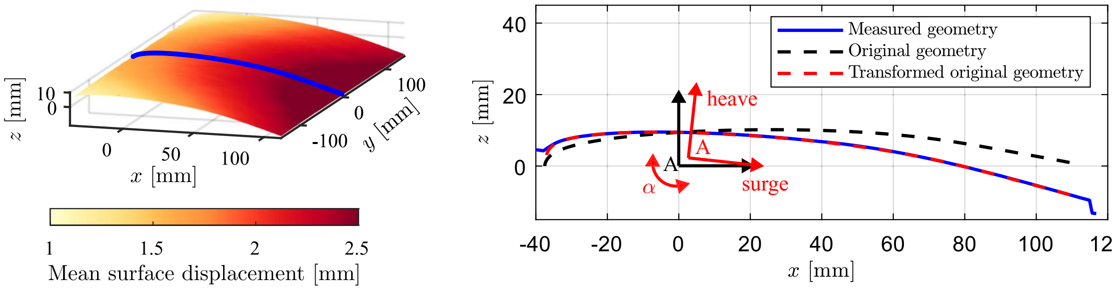

Fig. 3 Average wing surface displacement field obtained by DIC measurements (left). Extraction of α (pitch), heave, and surge motion from surface data in center cut by geometric transformation (right).

deformation field with respect to wind-off conditions is illustrated. The results clearly show the presence of a 3D wing deformation, constituted of a spanwise bending, resulting in higher displacements in the wing center, and a rotation/torsion around the elastic axis, which leads to higher displacements toward the trailing edge. As to separate the two effects, the cross section for each spanwise position was extracted and analyzed using an airfoil-shape fitting algorithm (see Fig. 3, right). The obtained spanwise distribution of local α, vertical (z_A, heave), and streamwise (x_A, surge) axis displacement showed average variations below 0.05°, 0.5% of chord, and 0.3% of chord, respectively. Based on this indication, the wing itself was deemed sufficiently rigid, while the shaft outside was the more flexible part and therefore the main reason for a minor heave motion. Nevertheless, given the minor variations within the wing, the extraction of the actual AoA and displacement values from the center cut (depicted in blue in Fig. 3) were used as the reference values for further evaluation.

The measurements of the integrated force balances played an important role for the determination of the inherent structural eigenfrequencies (Sec. IV) in wind-off conditions. Strong nonlinearities, most probably due to clearance in the bearing, led to major problems in the force balance calibration process and obstructed the dynamic evaluation and modal analysis based on the high-frequency force measurements. Nevertheless, raw signals were used as a backup measure to confirm the observed phenomena and frequency evaluations.

IV. Structural and Flow Parameters

The presented setup allowed for an adjustment of the pitching eigenfrequency via lever arm length (spring stiffness) and the shift of adjustment weights (variation of moment of inertia). The range of obtainable values was limited due to geometric constraints of the wind tunnel and the demand for optical accessibility. The pitch eigenfrequency variation in this campaign was chosen to be only realized by adjusting the weight positions to enable a maximum range.

Preliminary hammer tests, evaluated by force measurements, allowed the determination of the structural characteristics. Figure 4 shows the frequency spectral content of the raw force balance data for the four relevant configurations, namely, the rigid wing with the highest f_θ (top left) and the three lower pitching eigenfrequencies. Based on the frequency content of the vertical and streamwise components of the 3D force measurements at the axis bearing, $F_{3,z}$ and $F_{3,x}$, and the 1D measurement $F_{1,x}$ at the bottom of the spring lever arm, the predominant structural modes could be determined. As this representation was based on the raw signals, the force

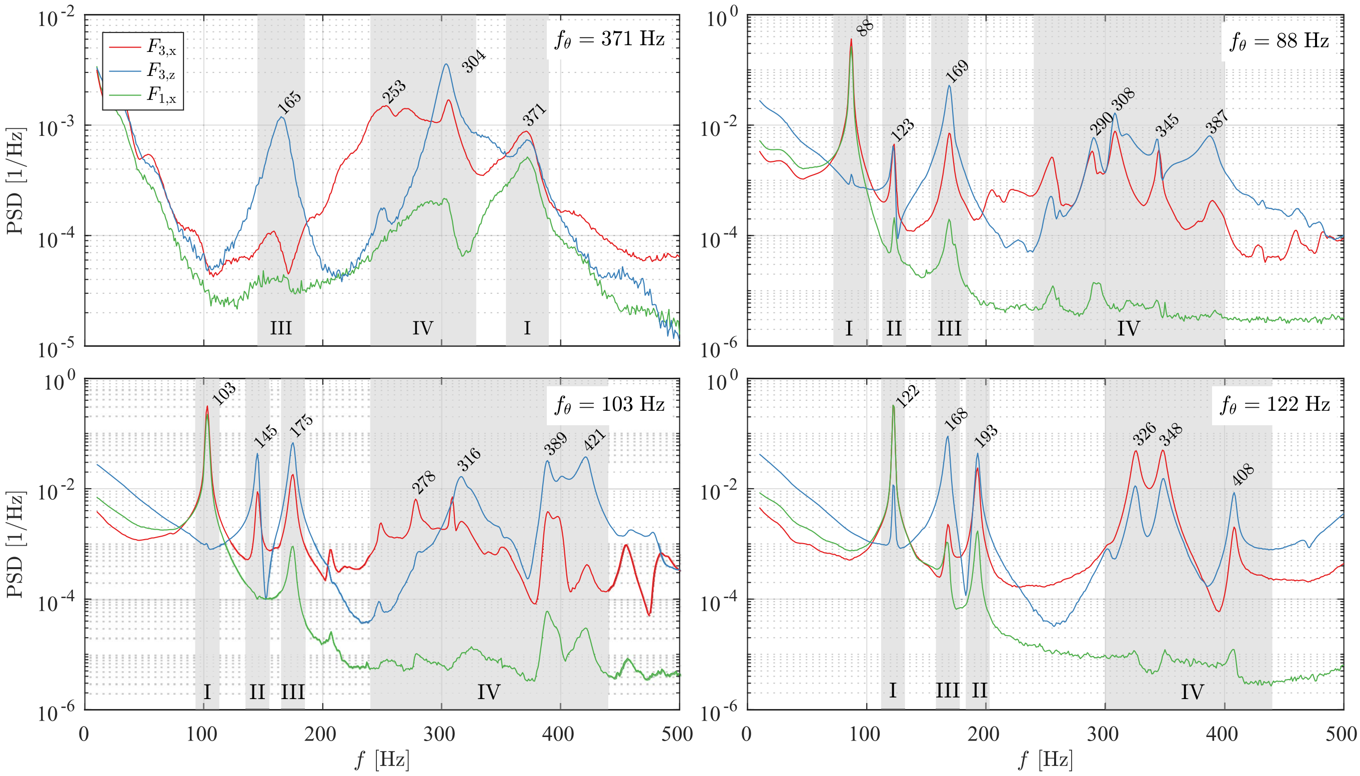

Fig. 4 Spectra of structural hammer tests of the four structural cases ($f_\theta = 371, 88, 103, 122$ Hz) in wind-off conditions evaluated with the raw signals of the force balances. Highlighted regions represent I, pitch mode; II, coupled heave–surge mode; III, heave mode; and IV, modes of higher frequency, based on external setup structure.

Table 1 Overview of the experimental parameters and the resulting reduced pitching eigenfrequencies based on the definition $k_\theta = \pi f_\theta c / u_\infty$

				Reduced pitching eigenfrequency k_θ at $\overline{M}$					
f_θ, Hz	$f_\theta/f_b \approx$	$\gamma \approx$	$\mu \approx$	0.72	0.73	**0.74**	0.745	0.75	0.76
88	0.9	0.15	335	0.178–0.180	0.175–0.178	**0.174–0.176**	0.173–0.175	0.172–0.174	0.169–0.172
103	**1.0**	**0.12**	**313**	**0.210–0.212**	**0.207–0.209**	**0.204–0.207**		**0.202–0.205**	**0.200–0.203**[a]
122	1.2	0.09	297			**0.241–0.244**[b]			
371	3.7					**0.743–0.735**[c]			

Bold entries mark the experimental runs for Mach number and pitch eigenfrequency variation.

[a] Intermittent behavior.

[b] Limitation by mechanical stop.

[c] "Rigid" wing from [5].

equilibrium led to similar contents in both streamwise (subscript x) measurements. Furthermore, cross-talk in the 3D force balance might account for minor artificial contributions. Nevertheless, under consideration of the peak levels, a clear distinction of the most important modes was possible:

I) Pitch mode
II) Coupled heave–surge mode
III) Heave mode
IV) Modes of higher frequency, based on external setup structure

The spectrum for $f_\theta = 122$ Hz (bottom right in Fig. 4) shows a minor contribution of $F_{3,z}$ at the desirably decoupled pitching eigenfrequency, inferring that the heave motion was not perfectly decoupled. The other spectra (top right, bottom left) exhibit well-decoupled pitching motion. Based on the geometric limitations of the facility, the distance from the spanwise wing limit to the bearing was considerably high and allowed for rather low heave and surge frequencies, despite the rather rigid wing. As the flow (wind-on conditions) can introduce some additional coupling coefficients, the decoupled wind-off state does not necessarily lead to a decoupling between heave and pitch in wind-on conditions.

Table 1 summarizes the performed experimental runs regarding the mean run Mach number $\overline{M}$, the structural pitching eigenfrequency f_θ, the inertia factor $\gamma = I_\theta/(c^2 m)$, the mass ratio $\mu = (m/s)/(\rho_\infty \pi (c/2)^2)$, and the resulting ranges of reduced frequencies based on the definition $k_\theta = \pi f_\theta c / u_\infty$. The total pressure was set to (1.5 ± 0.005) bar, resulting in a chord-based Reynolds number of $Re \approx 3 \times 10^6$ for the given Mach number range. The total temperature during the runs was (292 ± 4) K. Some runs unexpectedly exhibited intermittent or overly excessive pitch amplitude, as marked in Table 1. The reason for intermittence remained unclear but will be object of further investigations as the authors hope to draw conclusions about the buffet mechanisms from the anomalous behavior too. According to [31,32,42], very strong pitch responses, depending on the structural damping, were expected for some parameter settings. Consequently, the mechanical safety stop was utilized in order to limit the pitch amplitude artificially. Furthermore, the addressed run was interrupted prematurely as to minimize structural loads and the number of cycles. The authors expect that the point of buffet onset was not affected by these anomalies. Nevertheless, the specialty of these runs has to be considered in the upcoming comparison of detailed results.

V. Effect of Angle of Attack

Figure 5 illustrates the development of AoA and Mach number for a representing experimental run where the set AoA of the facility was continuously increased from 3 to 7°. Simultaneously, the blockage increased and led to a reduction of the Mach number from $M = 0.752$ to 0.743, which introduced a dampening effect on the buffet onset, opposing the effect of increasing AoA.

The pitching eigenfrequency was $f_\theta = 103$ Hz ($f_\theta/f_b \approx 1.0$), corresponding to a reduced frequency range of $k_\theta = \pi f_\theta c / u_\infty = 0.204$ to 0.207, where the inflow velocity u_∞ decreased from 241 to 238 $\mathrm{m \cdot s^{-1}}$. Given the fluid mode (buffet) eigenfrequency obtained from [5], of $f_b \approx 100$ Hz ($k_b \approx 0.2$), an intense FSI was expected. From the signal of the AoA (detailed in the zoomed region), one can clearly identify the point of onset, where the fluctuations of the AoA suddenly rise to a high level. For the detailed evaluation, the set AoA sweep was sectioned into intervals of $\Delta\alpha_{\mathrm{set}} = 0.1°$ for which the measured signals were decomposed into mean values and their fluctuations, e.g., $\alpha(t) = \overline{\alpha} + \alpha'(t)$. Figure 6a shows the development of $\overline{\alpha}$ with its standard deviation σ_α as error bars versus the set wind-tunnel AoA $\overline{\alpha}_{\mathrm{set}}$. Due to static structural deformation of the torsional spring and shaft torsion, the AoA was constantly reduced by approx. $\mathrm{d}\alpha_{\mathrm{st}} \approx 1.25°$. Therefore, all following results are referring to the actual, measured AoA instead of the set one, as the actual aerodynamic condition is expected to be accountable for the expected phenomena. Starting from $\overline{\alpha} = 4.6°$ a strong increase of fluctuations of the AoA can be observed, indicating the clear presence of a strong pitching motion (flutter). It reached a maximum level at 4.9° that remained constant up to the maximum tested incidence, indicating limit cycle oscillations. It must be noted that, despite a strong shock

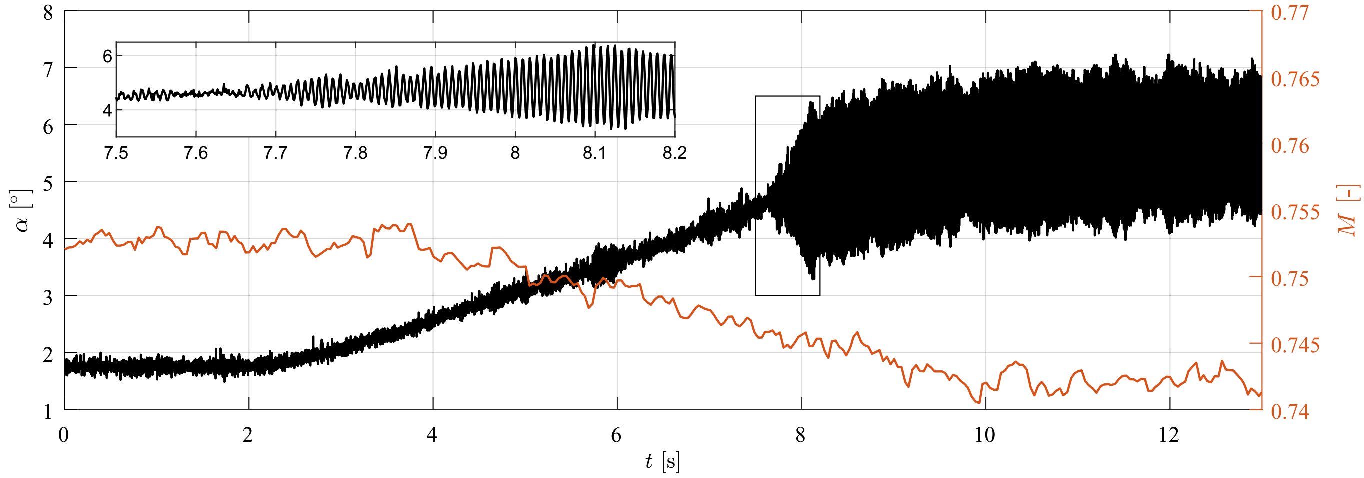

Fig. 5 Development of AoA and Mach number during a typical experimental run with buffet onset.

presence and resulting boundary-layer separation, the static deformation remained constant (constant slope). One can infer that the aerodynamic moment stayed constant with increasing set AoA too.

The results of frequency spectral analysis of the AoA fluctuations α' for each interval are presented in Fig. 6b. All representations of frequency content in this work are based on the signal fluctuations. The power spectral density (PSD) was determined by the method of Welch [43] with a window length of 100 samples and a Hamming window function with an overlap of 50%. Due to the fast increase of α_{set} throughout the experimental sweep run, each interval was restricted to a limited number of samples only, which led to reduced data for spectral averaging. Nevertheless, dominant regions can be clearly identified. For the presented case, one can observe a slightly prominent region at $f_{\alpha'} \approx 375$ Hz that is connected to eigenfrequencies of the external setup. Furthermore, a firstly weak peak can be identified at $f_{\alpha'} \approx 105$ Hz, which represents the structural pitch mode (I). That peak slightly shifts with continuously increasing AoA until it becomes very prominent at $\overline{\alpha} = 4.6°$ with $f_{\alpha'} \approx 115$ Hz. Together with the sudden onset of fluctuations, the peak height of the dominant frequency indicates flutter onset. The change in frequency (from 100 to 115 Hz) implies an influence by another structural mode that led to a change of frequency. In Figs. 6c and 6d, the evaluation of the shock position with respect to the AoA is presented. Due to inconsistent shock presence at lower AoA, the detected shock positions did not always resemble the shock but other regions of high-density gradients. This explains the high values of σ_{x_s} that are marked by the red region. In the plots illustrated in the following sections, these points have been removed for better clarity. Starting from $\overline{\alpha} \approx 2.7°$ a reliable shock detection was possible due to reduced fluctuations, and a downstream motion of the shock could be observed. The shock motion inversion point, indicating significant boundary-layer separation [16,20,44], and being a necessary but not sufficient criterion for buffet onset [5], was reached at $\overline{\alpha} \approx 4.3°$. A slight upstream motion of the shock was followed by a strong increase of fluctuations at $\overline{\alpha} \approx 4.7°$ that remained on a constant level. The frequency spectra do not exhibit any dominant peaks at low AoA. At the previously observed onset point, the shock position also shows the strongly dominant frequency of $f_{x_s'} \approx 115$ Hz together with the weak first higher harmonic. Figures 6e and 6f show the corresponding results for the normalized mean vertical position of the wing axis

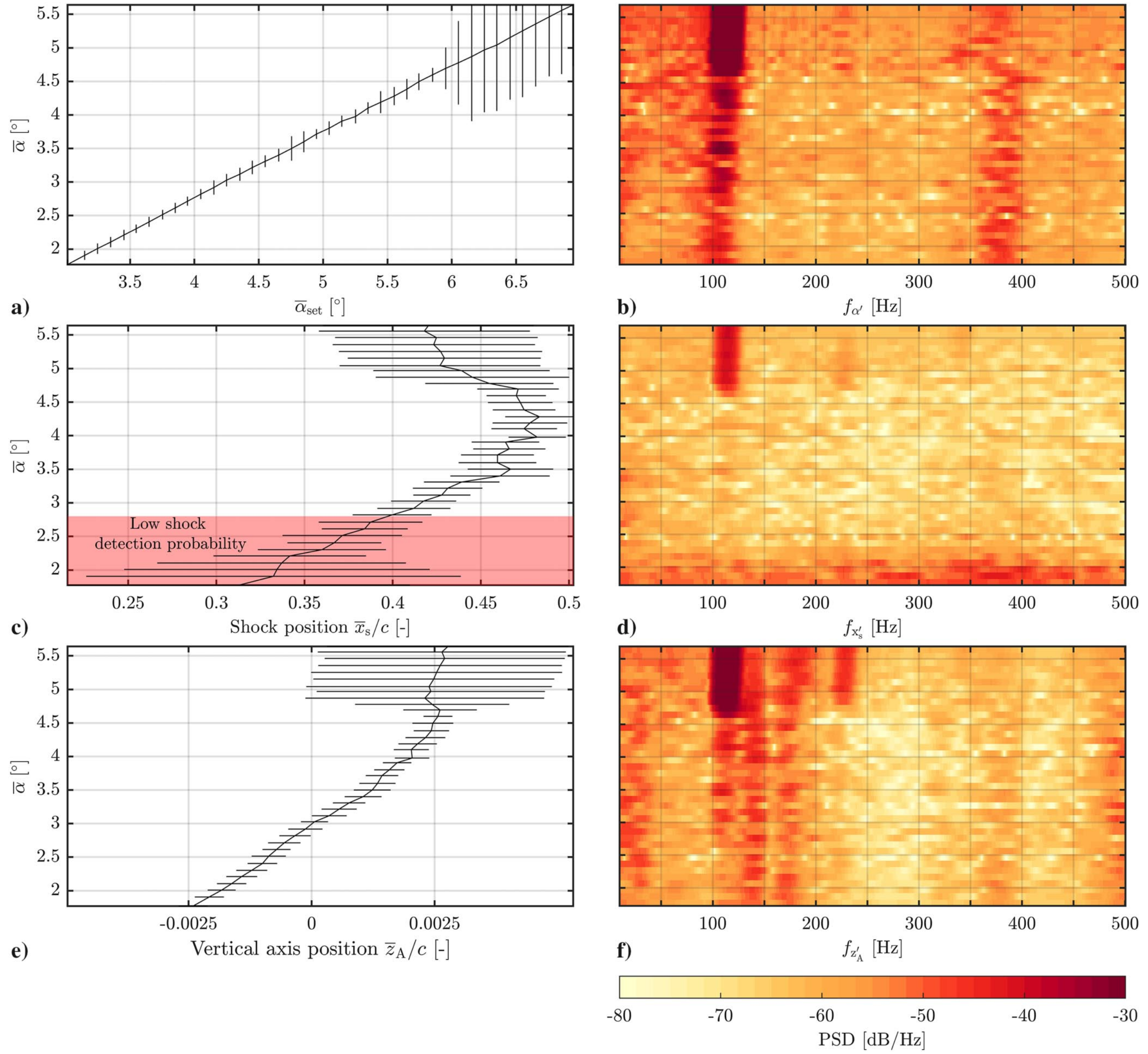

Fig. 6 **Development of pitch angle α, shock position x_s/c, and vertical axis position z_A/c by means of mean values with standard deviation (indicated by error bar, left) and frequency content (right); both evaluated for intervals of $\Delta\alpha_{\text{set}} = 0.1°$, $M = 0.752$ to 0.743, and $f_\theta = 103$ Hz ($f_\theta/f_b \approx 1$).**

z_A describing the heave motion of the wing. Negative values are attributed to a shaft mounting position below the coordinate system origin. By choosing this position, a free shaft motion was possible even at higher average heave values where the shaft was bent and lifted slightly outside the wing and test section. Up to $\overline{\alpha} \approx 4°$, a constant rise of vertical displacement with low fluctuations can be observed. The starting separation of the boundary layer led to limited increase of lift and, consequently, of the vertical axis position. The corresponding frequency spectrum shows permanently present but weak regions at $f_{z'_A} \approx 140$ Hz (coupled structural heave and surge motion, region II in Fig. 4) and 170 Hz (structural heave mode, region III in Fig. 4). Similarly to the pitch motion, starting from $\overline{\alpha} \approx 4.6°$ the presence of a highly dominant frequency at $f_{z'_A} \approx 115$ Hz is visible and indicates strong coupled pitch–heave motion. It has to be noted that the initial attempt of reducing the wing heave motion to an insignificant level could not be achieved.

The modal analysis and observation of stability boundaries by eigenvalue decomposition as proposed by [22] and applied by multiple research groups (e.g., [15,16,31,42]) created results that could be easily compared to coupled numerical simulations, given the presence of highly sampled, noise-free data from the computations. Due to the strong nonlinearity in the force balance measurement chain, the determination of the damping coefficients of the different modes was not reliably possible. Nevertheless, the authors expect the presented procedure based on the level of fluctuations and frequency content of a signal to be sufficient for the observation of different modes, their damping status (damped/undamped), and, thus, the onset boundaries. In the presented case, the firstly damped structural pitch mode underwent bifurcation at $\overline{\alpha} = 4.6°$ and became unstable. A coupled mode including shock, pitch and heave motion appeared, while the other previously observed modes remained damped on their low intensity level. An FSI was generated that synchronized with the coupled structural frequency, as observed and predicted by [31,32].

VI. Effect of Mach Number

In the following section, the influence of the Mach number on buffet and its onset is presented by means of a set of wind-tunnel runs at $f_\theta = 103$ Hz ($f_\theta / f_b \approx 1$). Since the shock motion and the structural motion were always coupled after onset as shown in Sec. V, and the point of onset always coincided, the main focus is set on the shock position, also regarding the onset determination.

A. Shock Position

Figure 7 shows for different Mach numbers the development of the mean shock position (left) and its fluctuations by means of the standard deviation (right). Points of inconsistent shock detection have been removed from the plot. The increase of the Mach number shifts all necessary steps for the establishment of buffet to lower AoA: firstly, the formation of a stable shock (low fluctuations in Fig. 7, right), the point of inversion (most downstream shock position in Fig. 7, left), and, finally, the onset (sharp rise of the fluctuations in Fig. 7, right). The reverse mean shock motion after onset seems to accelerate after the buffet onset, as one can see in change of slope in Fig. 7 (left). The rather constant level of shock fluctuations after onset does not seem to be significantly affected by the Mach number in the observed range.

B. Amplitude

In Fig. 8, the maximum peak-to-peak amplitudes for shock position, AoA, and heave motion in each interval are presented. Obviously, the development of the peak-to-peak of the shock position, which represents the maximum shock traveling distance, partially resembles what has already been shown in Fig. 7. Nevertheless, after onset, all curves seem to stagnate on the same level of $2\hat{x}_{s/c} \approx 0.2$ before exhibiting an excessive increase of maximum shock motion at $\overline{\alpha} \approx 5.2°$. As the standard deviation in Fig. 7 remains on a high level right after the individual onset point, it can be concluded that, below a certain AoA (for this pitching eigenfrequency), the maximum shock traveling distance was limited independently from the Mach number. Above the limiting AoA of $\overline{\alpha} \approx 5.2°$, the shock traveled longer maximum distances while the standard deviation remained on a constant level, inferring that fewer but stronger fluctuations occurred. This could be an indication of atypical shock motions as described in [45] for deep buffet conditions. Furthermore, the appearance of these characteristics was found to be independent from the Mach number after a threshold of $M \gtrapprox 0.72$ too. Concerning the structural development, the curves of the maximum pitch amplitude with increasing mean AoA in Fig. 8 (center) did not show the same behavior. Instead, all regular cases exhibited a similar peak-to-peak amplitude of $2\hat{\alpha} \approx 3°$ after the individual onset point. The same was observed for the heave motion, reaching a level of approx. $2\hat{z}_A \approx 0.8\%$. The special case with intermittent behavior at $\overline{M} = 0.76$, however, reached the high level of maximum structural fluctuations exactly at the same AoA where the shock motion started to exhibit atypical shock motion. In addition, the intermitting behavior started exactly at that point, which allows the inference that the intermitting is connected to the atypical shock motion.

C. Predominant Frequencies

Despite the low number of samples per interval for the frequency analysis and the consequent low spectral quality, the overall observation of the predominant frequencies gave insight into existing modes and their development. For Fig. 9 the five most dominant peaks of each interval were extracted from the frequency spectra of the shock position after the point of reliable shock detection. The transparency of each marker expresses the normalized peak height. Consequently, dominant markers indicate a dominant shock motion. A conglomeration of these markers can be found at $k_{x_s} \approx 0.22$, 0.45, and 0.68, expressing the buffet shock motion with its higher harmonics after the individual onset. Higher harmonics

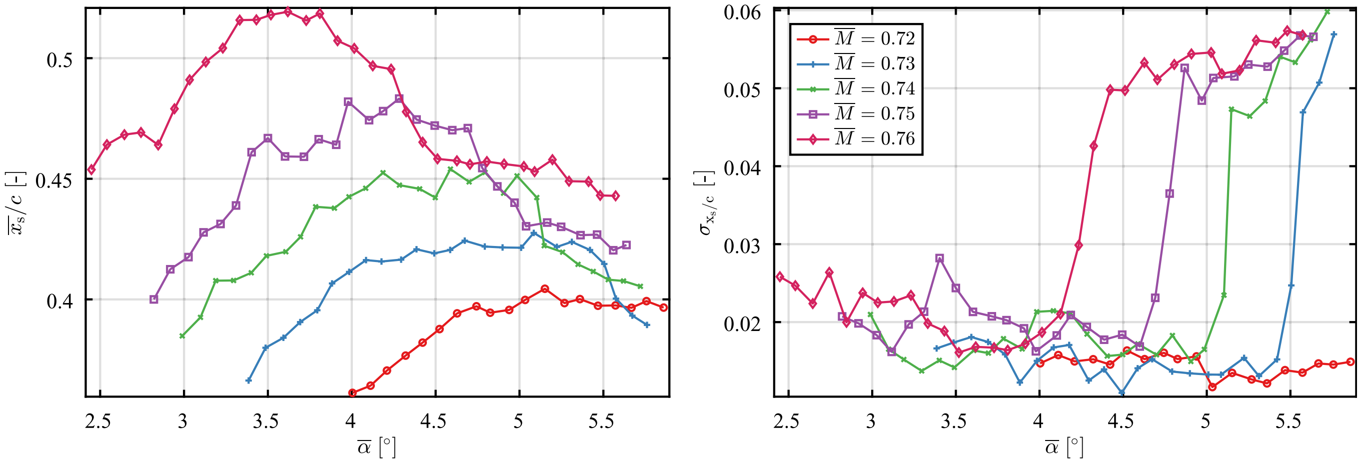

Fig. 7 **Development of mean (left) and standard deviation (right) of the shock position for different Mach numbers at $f_\theta = 103$ Hz ($f_\theta / f_b \approx 1$).**

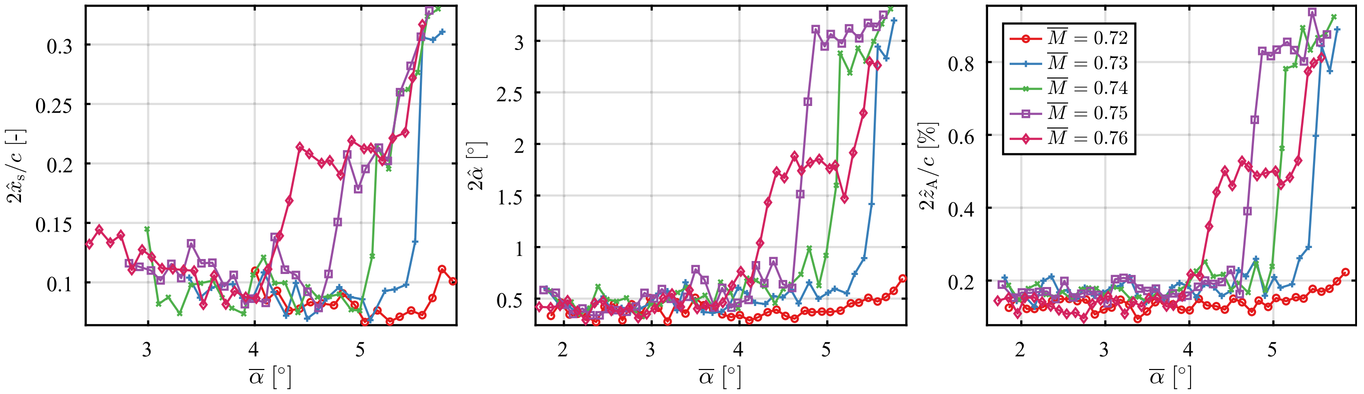

Fig. 8 Peak-to-peak amplitude in each interval for shock position (left), pitch (center), and heave (right) for different Mach numbers at $f_\theta = 103$ Hz ($f_\theta/f_b \approx 1$).

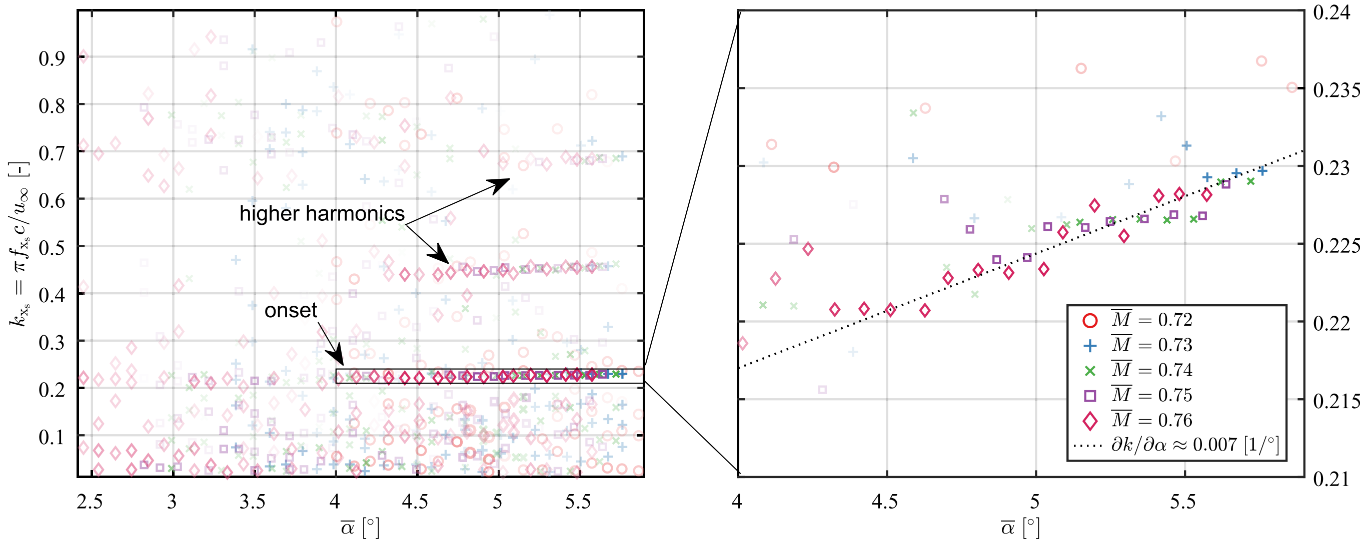

Fig. 9 Left: Overview of modal development of PSD of the shock position for different Mach numbers at $f_\theta = 103$ Hz ($f_\theta/f_b \approx 1$); amplitude of the five highest spectral peaks is qualitatively represented by transparency of markers. Right: Zoomed region of left plot with AoA-based frequency increase.

only appear delayed with respect to the AoA, indicating an increase of intensity with AoA. Besides the previously observed Mach number dependency of the onset, a manifestation of the most dominant motion centered around $k_{x_s} \approx 0.225$ can be observed independently from the Mach number. The zoomed-in plot on the right displays the agreement in detail and, furthermore, exhibits a similar increase of frequency with AoA for all Mach numbers of $\partial k/\partial \alpha \approx 0.007\,[1/°]$. The increase of the dominant frequency with the AoA was observed by multiple research groups [5,24,28,34], whereas others did not report this finding [3,23]. More detailed investigations identified a reduction of $\partial k/\partial \alpha$ with increasing Mach number for a rigid wing [5,24]. There are two possible reasons for the nonpresence of the change of gradient: the simultaneous reduction of the Mach number throughout the run or, more plausibly, the lock-in effect, where the frequency is determined by the structure solely. In addition, one can recognize another pattern that has to be backed-up by higher sampled measurements in future work: The line of dominant frequency (dotted) always seems to be approached from higher dominant frequencies just before bifurcation.

D. Overview

Figure 10 gives an overview of the onset boundary of shock oscillations, the most dominant frequencies (color coded), and their qualitative intensities (marker size, normalized with maximum of each run) for the Mach number variations at $f_\theta = 103$ Hz ($f_\theta/f_b \approx 1$). In the red region no reliable shock detection was possible. The light-gray region indicates the presence of a steady shock. In the dark-gray region strong harmonic oscillations are visible, and buffet has set on. The dominant frequencies from Fig. 9 can be observed, as well as the fact that the same AoA leads to the same shock buffet frequency for all Mach numbers. The case of $f_\theta = 88$ Hz ($f_\theta/f_b \approx 0.9$) exhibited similar characteristics with increasing Mach number.

VII. Effect of Structural Pitch Eigenfrequency

In this section, the effect of the structural pitch eigenfrequency on buffet onset is presented. For an average Mach number of $\overline{M} = 0.74$ three flexible cases with pitching eigenfrequencies of $f_\theta = 88, 103,$ and 122 Hz and resulting frequency ratios of $f_\theta/f_b \approx 0.9, 1.0,$ and 1.2, respectively, were studied and compared to the reference case with $f_\theta = 371$ Hz ($f_\theta/f_b \approx 3.7$) that has been investigated in [5]. In the following, that reference case will be referred to as “rigid” although minor heave wing motions could not be completely prevented. Nevertheless, as the results clarified, pitch motions were successfully inhibited.

A. Shock Position

Figure 11 shows the development of the shock position (average, left) and its fluctuations (standard deviation, right) with increasing AoA, analogously to Fig. 7. In general, the case with the lowest ratio of $f_\theta/f_b \approx 0.9$ shows more similarities to the rigid case than to the

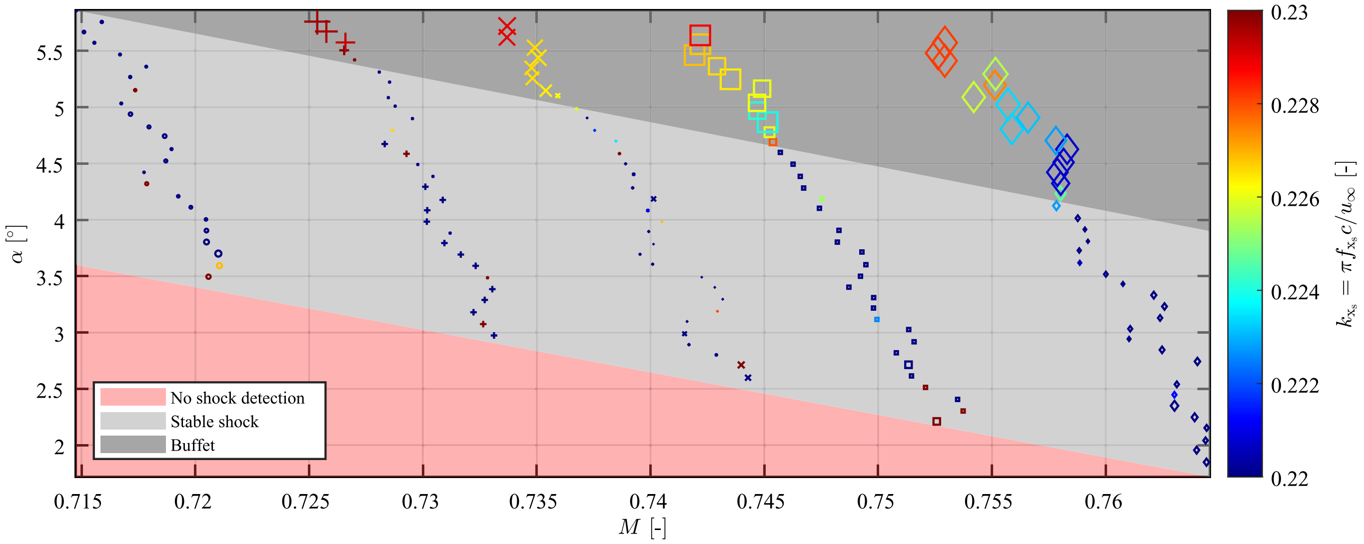

Fig. 10 Most dominant peaks of frequency spectrum (peak height qualitatively as marker size, normalized by maximum of each run) and corresponding frequencies (color coded) of the fluctuations of the shock position for the performed runs at $f_\theta = 103$ Hz ($f_\theta/f_b \approx 1$).

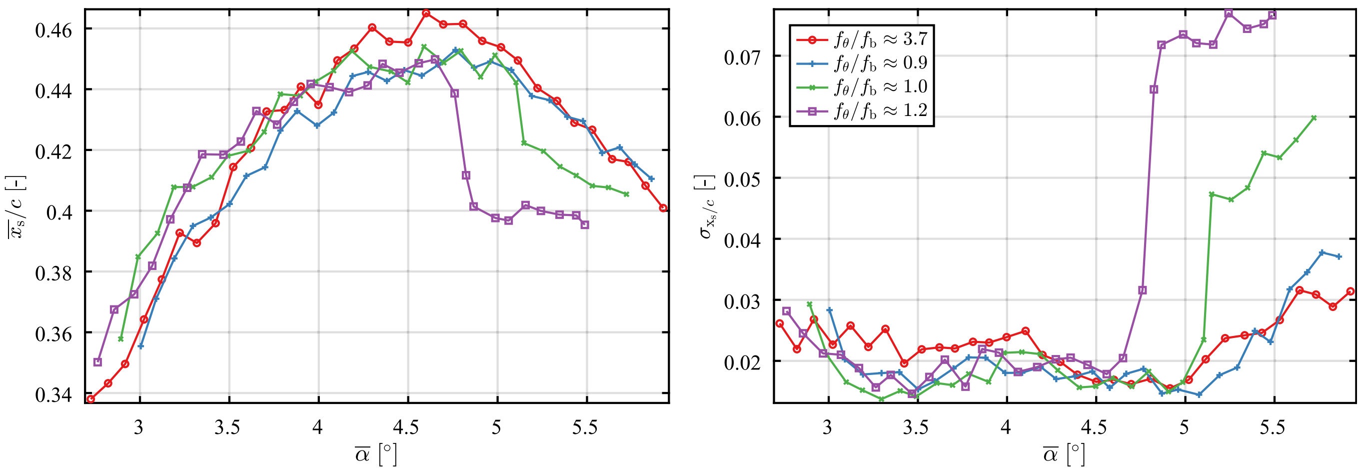

Fig. 11 Development of mean (left) and standard deviation (right) of the shock position for different structural pitch eigenfrequencies at $\overline{M} = 0.74$.

other two cases with released DOF. Despite only small differences, the rigid case presents a stronger gradient throughout the downstream shock excursion, resulting in a more upstream-located shock at lower and a further downstream-located shock at the inversion point. The average shock position does not show any anomalies in its steady behavior during the inverse shock motion, even after onset at $\overline{\alpha} \approx 5.1°$. The cases with released DOF exhibit a slightly more moderate downstream motion, and their inversion points are located further upstream. The case with lowest ratio ($f_\theta/f_b \approx 0.9$) reaches the inversion point at the highest AoA, compared to all other cases. Similarly to the rigid case, a steady inverse shock motion can be observed that was not harmed by the onset at $\overline{\alpha} \approx 5.2°$. However, the reverse shock motion of the other cases with ratios of $f_\theta/f_b \approx 1.0$ and 1.2 is strongly accelerated with the onset of strong fluctuations at $\overline{\alpha} \approx 5.0°$ and 4.6°, respectively. The level of fluctuations, as well as the onset point, is strongly dependent on the structural pitch frequency. The highest level is observed at $f_\theta/f_b \approx 1.2$. Since the mechanical limit had been reached during that run and introduced an artificial nonlinearity, the level of fluctuations was even limited on that high level. It has been proved that a premature onset can occur if structural stiffness is set in the right range, as predicted by [15,16]. Furthermore, the amplitude and buffet severeness for $f_\theta/f_b \approx 1.2$ is clearly higher than for $f_\theta/f_b \approx 0.9$ and 1, as has already been numerically observed in [31,32]. This confirms the observation of a nontypical, asymmetric excitation behavior.

B. Amplitude Development

Similarly to the previous comparison for different Mach numbers, Fig. 12 presents the maximum peak-to-peak amplitudes of shock position (left), pitch angle (center), and heave (right) with respect to the mean AoA and varying structural pitch eigenfrequencies. The higher values of the shock travel distance below $\overline{\alpha} \approx 3°$ were based on remaining spurious values of the shock detection algorithm. The amplitude remained on a low level for all cases until the individual point of onset was reached, which led to high fluctuations. The previously observed two-level characteristic can only be clearly identified for the rigid reference case that steps up to $2\hat{x}_s \approx 0.16$: first, at $\overline{\alpha} \approx 5°$, and remains on that level before increasing over again at $\overline{\alpha} \approx 5.6°$. The minor kink in the curve of $f_\theta/f_b \approx 1.0$ most probably represents the observed two-level phenomenon too, by just setting on the first level before the transition to the higher level fluctuations occurs. The case of $f_\theta/f_b \approx 0.9$ does not present the two-level behavior in the observed range. For $f_\theta/f_b \approx 1.2$ a statement is not possible due to the prior artificial amplitude limitation. The extent of the AoA amplitude varied strongly with the pitching eigenfrequency from no pitch motion (rigid case, $f_\theta/f_b \approx 3.7$), to minor pitch motion of $2\hat{\alpha} \approx 1°$ ($f_\theta/f_b \approx 0.9$), to high fluctuations of $2\hat{\alpha} \approx 3°$ ($f_\theta/f_b \approx 1.0$), and, finally, extreme pitch motion of up to $2\hat{\alpha} \approx 5°$ ($f_\theta/f_b \approx 1.2$), where the amplitude was limited by the mechanical stop. As the fluctuations of lift always increase with shock buffet, the amplitudes of the heave motion showed the same

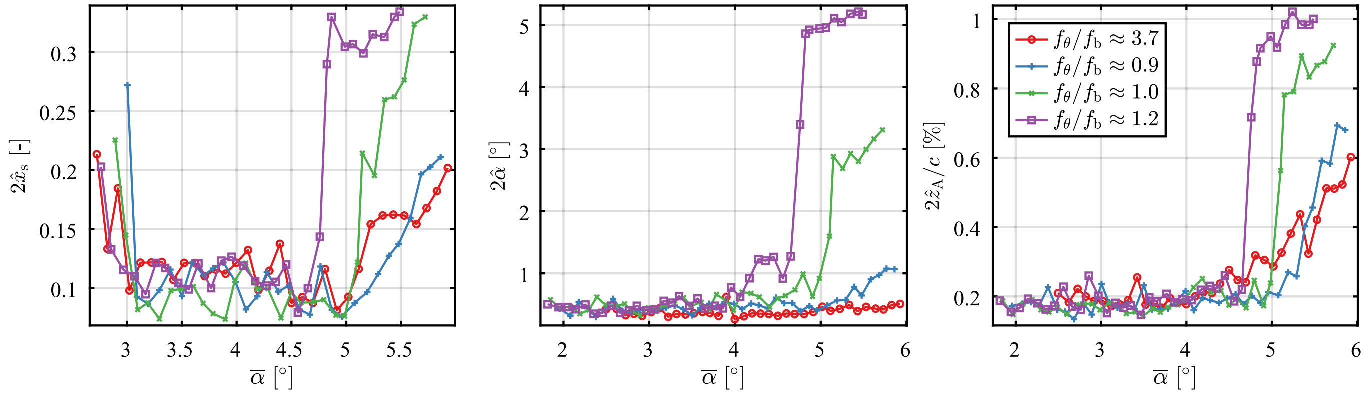

Fig. 12 **Peak-to-peak amplitude in each interval for shock position (left), pitch (center), and heave (right) for different structural pitch eigenfrequencies at $\overline{M} = 0.74$.**

characteristics. In particular, for the rigid case, a steady rise of fluctuations can be observed, already before clear buffet onset. After onset, all cases exhibit a strong increase of heave motion, where $f_\theta/f_b \approx 0.9$ and the rigid case range on the same level and $f_\theta/f_b \approx 1.0$ and 1.2 follow in increasing order.

C. Predominant Frequencies

Figure 13 gives an overview of the development of the five most dominant shock motion frequencies for the different cases of pitch stiffness. As the marker transparency stands for the relative spectral peak amplitude, most dominant regions, damped and undamped, and the individual onset for each case are visualized. The minor quality of the rigid case and thus the high dominance of spread out red markers are based on rather weak oscillations compared to the cases with released DOF. Nevertheless, onset points and corresponding frequencies, as well as their development, can be well distinguished. In the magnified region on the right, the presence of a damped mode can be recognized before onset too. The individual development of the frequency with increasing AoA is compared to the previously found, generally valid gradient of $\partial k/\partial\alpha \approx 0.007$ [1/°]. It can be concluded that the trend and approximate gradient remain valid, independently from the structural pitching eigenfrequency. Moreover, the case of ($f_\theta/f_b \approx 0.9$) appears very close to the rigid case, again. From this and the behavior of the shock, described in Figs. 11 and 12, one can infer that a ratio of $f_\theta/f_b < 1$ leads to a behavior very similar to the rigid case ($f_\theta/f_b \approx 3.7$) but with additional excitation of the structural motion. Consequently, the coupled motion is governed by buffet and can be denoted as "fluid mode flutter" [16,31]. The remaining small deviation may be accounted to the influence of the pitch–heave coupling that increases the resulting structural frequency marginally. The higher ratios $f_\theta/f_b \gtrsim 1$ appear to be far from the rigid buffet frequency; they represent the veering region and the lock-in phenomenon, resulting in a coupled motion governed by the structural eigenfrequency.

Figure 14 illustrates the resulting frequency maxima of the shock oscillation with respect to the set structural pitch eigenfrequency. The increase of AoA is represented by color code, and the transparency indicates the actual peak heights of the selected points. Furthermore, the different important frequency lines are shown: the approximate line of rigid buffet (dot-dashed), the pitch frequency line ($k = k_\theta$, dotted), and its shifted parallel ($k = k_\theta + \mathrm{d}k$, where $\mathrm{d}k \approx 0.19$). That parallel matches the frequencies of the two settings of higher frequency ratios (1.0 and 1.2) after onset. As all measured cases showed a coupling of shock motion and pitch with additional heave, the clean prediction with only one degree of freedom (dotted) of [31,32] is not valid here. Nevertheless, the present observations seem to agree with the predictions at least partly, when assuming that the influence of the heave motion lifts the structural line to higher frequencies. The coupled motion for higher ratios of $f_\theta/f_b \approx 1.0$ and 1.2 seems to lock into the structural eigenfrequencies rather than the buffet frequency, coinciding with the dashed line in Fig. 14. The case of $f_\theta/f_b \approx 0.9$, however, deviates from that behavior. As [31,32] stated,

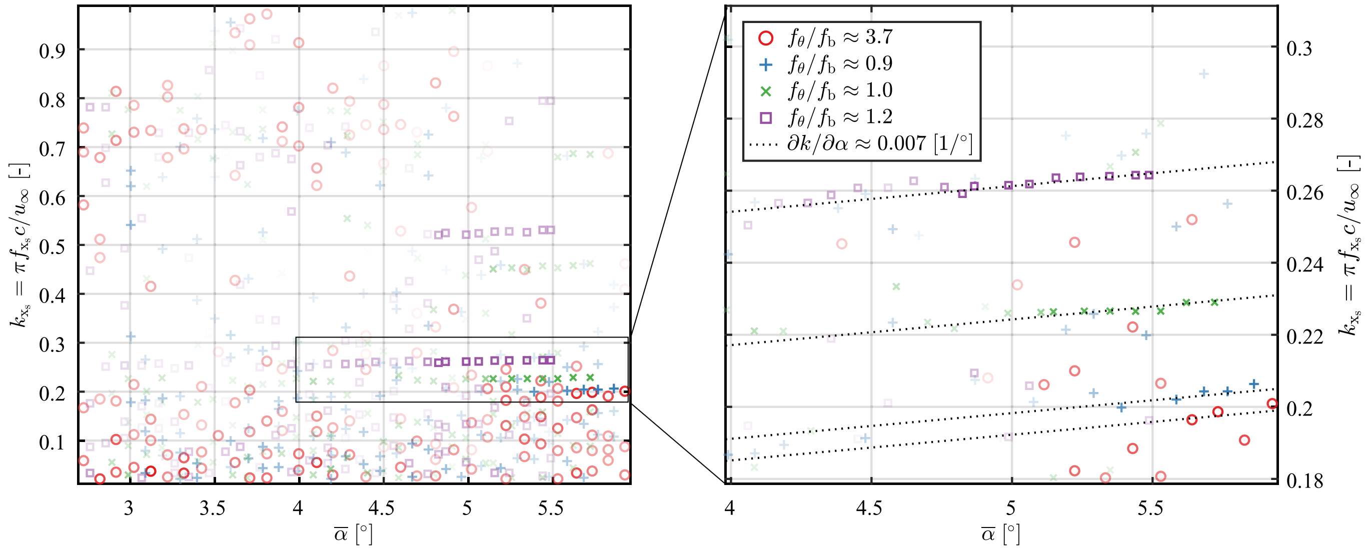

Fig. 13 **Left: Overview of modal development of PSD of the shock position for different structural pitch eigenfrequencies at $\overline{M} = 0.74$; amplitude of the five highest spectral peaks is qualitatively represented by transparency of markers and normalized for each interval. Right: Zoomed region of left plot with AoA-based frequency increase.**

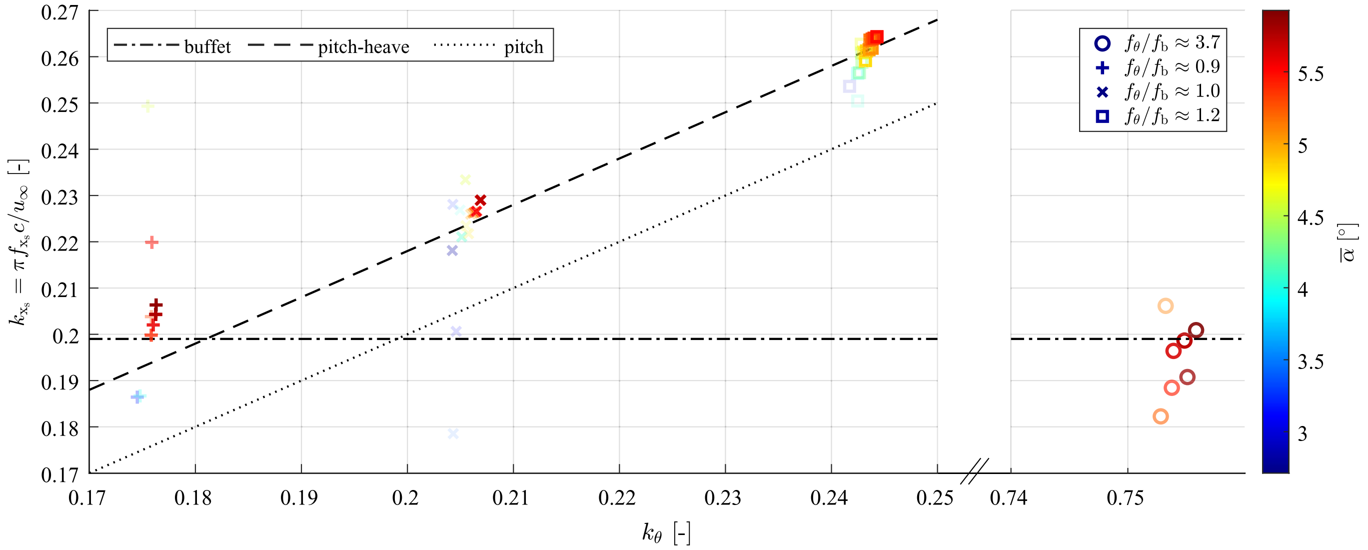

Fig. 14 Development of the most dominant frequencies in the shock position signal for increasing AoA (colored) with respect to different structural pitch eigenfrequencies. Different markers represent the variations of the pitch-to-buffet ratio. The marker transparency qualitatively stands for the corresponding peak height in the spectrum.

a sufficiently low mass ratio leads to a noticeable extent of the transition region from fluid-dominated to structurally dominated coupled motion. The presented case of lower ratio (and possibly the ratio of 1.0) could be located in this very transition region, in between fluid mode flutter and lock-in phenomenon. Again, the uncertainty of the given observations remains on a considerable level due to the low spectral quality. Nevertheless, the presented results oppose the classical, symmetrical resonance theory where the maximum response amplitude should appear at a pitch-to-buffet ratio of 1 and the resulting coupled frequency should be the buffet frequency, independently from the structural pitch eigenfrequency.

VIII. Onset Boundaries

In this section, a summary of the determined onset boundaries is given. Multiple research groups have investigated onset boundaries up to this point, mainly based on rigid wing buffet; see, e.g., [3,5,24]. As it has been shown numerically by [15,16], not only the Mach number and AoA but also structural characteristics have an influence on the boundary. Most often, onset criteria were defined on the basis of an increase in fluctuations of aerodynamic values, such as the lift coefficient. Since the shock oscillations are directly linked to variations in lift, the standard deviation of the shock position was chosen as suitable metric for the present campaign. For this, the standard deviation was averaged over an interval of $\overline{\alpha} \pm 0.1°$. The first increase of this moving average by more than 10% was defined as onset. Figure 15 shows the collected onset AoA values for the investigated pitch eigenfrequencies and Mach numbers. The linearity of the boundaries with respect to Mach number and AoA can be confirmed for all frequency ratios in the observed range. A release of the pitch degree of freedom leads to a decrease of the onset slope (rotation of the boundary). Consequently, at higher Mach numbers, the onset is reached at lower AoA. For lower Mach numbers, on the other hand, the onset is inhibited and appears with a delay. Furthermore, increased pitching eigenfrequencies shift the whole boundary to lower AoA and, thus, lead to premature buffet onset, in the range of observation. Some reader may ask why the onset boundaries are located at higher AoA than in the well-known measurements of [3]. Beside the fact of differing onset identification methods, major differences in the facilities (e.g., divergent vs adaptive walls or boundary-layer suction) account for that. As numerical simulations are very prone to discrepancies by different turbulence modeling [16] and other facilities used varying correction methods, the absolute position of the boundaries has to be treated with caution. A detailed discussion of the influencing factors is given in [5]. Nevertheless, the presented trends stem from one facility with the same boundary conditions and are deemed to be valid.

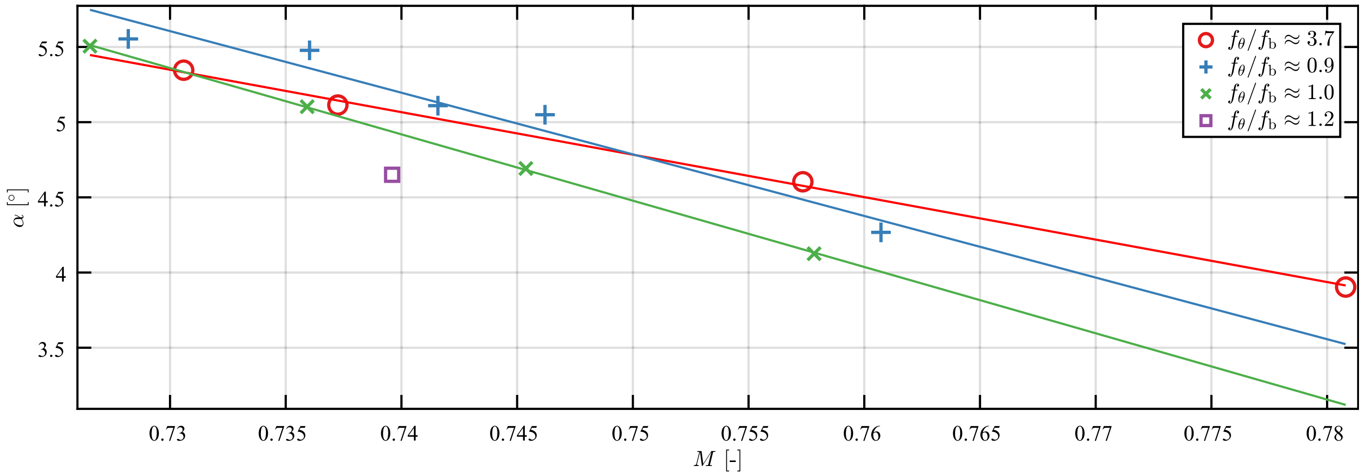

Fig. 15 Onset boundaries based on an increase of the standard deviation of the shock position of 10%; evaluated for all experimental runs at different Mach numbers and structural pitch eigenfrequencies.

IX. Summary and Conclusions

For the detailed investigation of buffet, its onset boundaries, and the transonic FSI (buffeting), an experimental wind-tunnel setup was designed and manufactured. The spring-mounted wing (OAT15A) with focus on a pitching degree of freedom allowed for a variation of the pitching eigenfrequency in the vicinity of the rigid-wing buffet frequency. Wind-tunnel runs were performed, increasing the AoA continuously for different transonic Mach numbers and pitching eigenfrequencies. High-speed optical measurement techniques, BOS and deformation, were deployed to nonintrusively observe structural and fluid modes.

For all runs, a *constant mean aerodynamic moment*, based on a constant static rotational deformation, could be observed throughout the whole AoA sweep. The steady increase of lift-based wing bending was interrupted once the region of shock inverse motion was reached, supposedly coinciding with *significant boundary-layer separation*. At higher AoA, a strong increase of fluctuations of pitch, heave, and shock position was observed, implying buffet onset in the form of a coupled FSI (buffeting). The limitation of amplitudes for most runs indicated the presence of limit-cycle oscillations, which the authors primarily attribute to the nonlinear character of the fluid flow as the corresponding measurements points were located within the linear range of the structure.

An increase of the Mach number at unaltered structural settings led to a decrease in the buffet onset AoA, where its boundary showed linear behavior in the observed range, which is in good agreement with other research groups. The *structural pitching eigenfrequency*, exhibited a *significant influence on the onset boundary* too. It altered the boundary slope: at higher Mach numbers the introduced flexibility led to earlier buffet onset; at lower Mach numbers it played an inhibiting role, delaying the onset to higher AoA. Furthermore, an increase of pitching eigenfrequency shifted the whole boundary to lower AoA and led to premature buffet onset for all Mach numbers. This is the experimental proof of the numerical findings in [15,16] and emphasizes the importance of consideration of structural characteristics in the process of transonic aircraft design.

Frequency and amplitude analysis of the shock motion revealed differing behavior for different pitch-to-buffet frequency ratios. The ratio of 0.9 resembled the characteristics of the rigid case regarding the coupled frequency and level of shock oscillation amplitudes. With high probability, it can be attributed to the *transition/veering region* in between fluid mode flutter and lock-in phenomenon. The coupled motion for ratios of 1.0 and 1.2 presented high similarity with lock-in behavior, synchronizing with the structural eigenfrequency, and exhibited large pitching amplitudes, as predicted in [28,31,32]. The influence of the heave motion could not be prevented completely and is suspected to lift the coupled structural frequency to a slightly higher level.

Subject to upcoming studies will be parametric variations of structural and fluid parameters at constant conditions with an increased number of samples to ensure higher quality spectra and to set particular focus on the observed interaction patterns.

Acknowledgments

Financial support in the frame of the project Holistic Optical Metrology for Aero-Elastic Research (HOMER) from the European Union's Horizon 2020 research and innovation program under grant agreement no. 769237 is gratefully acknowledged. Additional financial support from the Universität der Bundeswehr München is also gratefully acknowledged. The authors thank Jens Nitzsche, Yves Govers, Johannes Dillinger, Johannes Knebusch, and Tobias Meier from the DLR Institute of Aeroelasticity for their valuable contribution and expertise in design, manufacturing, and integration of the presented setup.

References

[1] Hilton, W. F., and Fowler, R. G., "Photographs of Shock Wave Movement," Aeronautical Research Council R&M 1312, 1947, https://naca.central.cranfield.ac.uk/bitstream/handle/1826.2/3237/arc-rm-2692.pdf?sequence=1&isAllowed=y.

[2] McDevitt, J. B., and Okuno, A. F., "Static and Dynamic Pressure Measurements on a NACA0012 Airfoil in the Ames High Reynolds Number Facility," NASA TP 2485, 1985, https://books.google.de/books?id=m8E5WqGU0MMC.

[3] Jacquin, L., Molton, P., Deck, S., Maury, B., and Soulevant, D., "Experimental Study of Shock Oscillation over a Transonic Supercritical Profile," *AIAA Journal*, Vol. 47, No. 9, 2009, pp. 1985–1994. https://doi.org/10.2514/1.30190

[4] Giannelis, N. F., Vio, G. A., and Levinski, O., "A Review of Recent Developments in the Understanding of Transonic Shock Buffet," *Progress in Aerospace Sciences*, Vol. 92, July 2017, pp. 39–84. https://doi.org/10.1016/j.paerosci.2017.05.004

[5] Accorinti, A., Baur, T., Scharnowski, S., and Kähler, C. J., "Experimental Investigation of Transonic Shock Buffet on an OAT15A Profile," *AIAA Journal*, Vol. 60, No. 11, Nov. 2022, pp. 6289–6300. https://doi.org/10.2514/1.J061135

[6] Badcock, K. J., Timme, S., Marques, S., Khodaparast, H., Prandina, M., Mottershead, J. E., Swift, A., Ronch, A. D., and Woodgate, M. A., "Transonic Aeroelastic Simulation for Instability Searches and Uncertainty Analysis," *Progress in Aerospace Sciences*, Vol. 47, No. 5, 2011, pp. 392–423. https://doi.org/10.1016/j.paerosci.2011.05.002

[7] Gao, C., and Zhang, W., "Transonic Aeroelasticity: A New Perspective from the Fluid Mode," *Progress in Aerospace Sciences*, Vol. 113, Feb. 2020, Paper 100596. https://doi.org/10.1016/j.paerosci.2019.100596

[8] Mabey, D., "Oscillatory Flows from Shock Induced Separations on Biconvex Aerofoils of Varying Thickness in Ventilated Wind Tunnels," TMemorandum, Royal Aircraft Establishment, 1981.

[9] Gibb, J., "The Cause and Cure of Periodic Flows at Transonic Speed," Ph.D. Thesis, Cranfield Univ., Cranfield, England, U.K., 1983.

[10] Lee, B. H. K., "Oscillatory Shock Motion Caused by Transonic Shock Boundary-Layer Interaction," *AIAA Journal*, Vol. 28, No. 5, 1990, pp. 942–944. https://doi.org/10.2514/3.25144

[11] Xiao, Q., Tsai, H. M., and Liu, F., "Numerical Study of Transonic Buffet on a Supercritical Airfoil," *AIAA Journal*, Vol. 44, No. 3, 2006, pp. 620–628. https://doi.org/10.2514/1.16658

[12] Hartmann, A., Feldhusen, A., and Schröder, W., "On the Interaction of Shock Waves and Sound Waves in Transonic Buffet Flow," *Physics of Fluids*, Vol. 25, No. 2, 2013, Paper 026101. https://doi.org/10.1063/1.4791603

[13] Hartmann, A., Klaas, M., and Schröder, W., "Coupled Airfoil Heave/Pitch Oscillations at Buffet Flow," *AIAA Journal*, Vol. 51, No. 7, 2013, pp. 1542–1552. https://doi.org/10.2514/1.J051512

[14] Crouch, J., Garbaruk, A., Magidov, D., and Travin, A., "Origin of Transonic Buffet on Aerofoils," *Journal of Fluid Mechanics*, Vol. 628, June 2009, pp. 357–369. https://doi.org/10.1017/S0022112009006673

[15] Gao, C., Zhang, W., and Ye, Z., "Reduction of Transonic Buffet Onset for a Wing with Activated Elasticity," *Aerospace Science and Technology*, Vol. 77, June 2018, pp. 670–676. https://doi.org/10.1016/j.ast.2018.03.047

[16] Nitzsche, J., Ringel, L., Kaiser, C., and Hennings, H., "Fluid-Mode Flutter in Plane Transonic Flows," *International Forum on Aeroelasticity and Structural Dynamics (IFASD 2019)*, Curran Associates, Inc., June 2019, pp. 39–56, https://elib.dlr.de/128011/.

[17] Poplingher, L., Raveh, D. E., and Dowell, E. H., "Modal Analysis of Transonic Shock Buffet on 2D Airfoil," *AIAA Journal*, Vol. 57, No. 7, 2019, pp. 2851–2866. https://doi.org/10.2514/1.j057893

[18] Timme, S., "Global Instability of Wing Shock-Buffet Onset," *Journal of Fluid Mechanics*, Vol. 885, Jan. 2020, pp. 228–250. https://doi.org/10.1017/jfm.2019.1001

[19] Deck, S., "Numerical Simulation of Transonic Buffet over a Supercritical Airfoil," *AIAA Journal*, Vol. 43, No. 7, 2005, pp. 1556–1566. https://doi.org/10.2514/1.9885

[20] Pearcey, H., "A Method for the Prediction of the Onset of Buffeting and Other Separation Effects from Wind Tunnel Tests on Rigid Models," Advisory Group for Aeronautical Research and Development Paris, France, 1958, https://apps.dtic.mil/sti/citations/AD0248342.

[21] Mabey, D., "Buffeting Criteria for a Systematic Series of Wings," *Journal of Aircraft*, Vol. 26, No. 6, 1989, pp. 576–582.

[22] Crouch, J., Garbaruk, A., and Magidov, D., "Predicting the Onset of Flow Unsteadiness Based on Global Instability," *Journal of*

Computational Physics, Vol. 224, No. 2, 2007, pp. 924–940. https://doi.org/10.1016/j.jcp.2006.10.035

[23] Sartor, F., Mettot, C., and Sipp, D., "Stability, Receptivity, and Sensitivity Analyses of Buffeting Transonic Flow over a Profile," *AIAA Journal*, Vol. 53, No. 7, 2015, pp. 1980–1993. https://doi.org/10.2514/1.j053588

[24] Giannelis, N. F., Levinski, O., and Vio, G. A., "Influence of Mach Number and Angle of Attack on the Two-Dimensional Transonic Buffet Phenomenon," *Aerospace Science and Technology*, Vol. 78, June 2018, pp. 89–101, https://www.researchgate.net/profile/Nicholas-Giannelis/publication/326977265_On_the_effect_of_control_surface_deflections_on_the_aeroelastic_response_of_an_aerofoil_at_transonic_buffet_conditions/links/5b6ee86f92851ca65055d7ba/On-the-effect-of-control-surface-deflections-on-the-aeroelastic-response-of-an-aerofoil-at-transonic-buffet-conditions.pdf. https://doi.org/10.1016/j.ast.2018.03.045

[25] Iovnovich, M., and Raveh, D. E., "Reynolds-Averaged Navier-Stokes Study of the Shock-Buffet Instability Mechanism," *AIAA Journal*, Vol. 50, No. 4, 2012, pp. 880–890. https://doi.org/10.2514/1.J051329

[26] Nitzsche, J., "A Numerical Study on Aerodynamic Resonance in Transonic Separated Flow," *IFASD—International Forum on Aeroelasticity and Structural Dynamics*, 2009, https://elib.dlr.de/61964/.

[27] Raveh, D. E., "Numerical Study of an Oscillating Airfoil in Transonic Buffeting Flows," *AIAA Journal*, Vol. 47, No. 3, 2009, pp. 505–515. https://doi.org/10.2514/1.35237

[28] Raveh, D., and Dowell, E., "Frequency Lock-In Phenomenon for Oscillating Airfoils in Buffeting Flows," *Journal of Fluids and Structures*, Vol. 27, No. 1, 2011, pp. 89–104. https://doi.org/10.1016/j.jfluidstructs.2010.10.001

[29] Raveh, D. E., and Dowell, E. H., "Aeroelastic Responses of Elastically Suspended Airfoil Systems in Transonic Buffeting Flows," *AIAA Journal*, Vol. 52, No. 5, 2014, pp. 926–934. https://doi.org/10.2514/1.J052185

[30] Giannelis, N. F., Vio, G. A., and Dimitriadis, G., "Dynamic Interactions of a Supercritical Aerofoil in the Presence of Transonic Shock Buffet," *Proceedings of the 27th International Conference on Noise and Vibration Engineering*, KU Leuven - Departement Werktuigkunde, Heverlee, Belgium, 2016, pp. 467–470, http://past.isma-isaac.be/downloads/isma2016/papers/isma2016_0584.pdf.

[31] Gao, C., Zhang, W., Li, X., Liu, Y., Quan, J., Ye, Z., and Jiang, Y., "Mechanism of Frequency Lock-in in Transonic Buffeting Flow," *Journal of Fluid Mechanics*, Vol. 818, Dec. 2017, pp. 528–561. https://doi.org/10.1017/jfm.2017.120

[32] Giannelis, N., and Vio, G., "Aeroelastic Interactions of a Supercritical Aerofoil in the Presence of Transonic Shock Buffet," *Proceedings of the 54th AIAA Aerospace Sciences Meeting*, AIAA, Reston, VA, 2016.

[33] Schewe, G., Mai, H., and Dietz, G., "Nonlinear Effects in Transonic Flutter with Emphasis on Manifestations of Limit Cycle Oscillations," *Journal of Fluids and Structures*, Vol. 18, No. 1, 2003, pp. 3–22. https://doi.org/10.1016/S0889-9746(03)00085-9

[34] Dietz, G., Schewe, G., and Mai, H., "Amplification and Amplitude Limitation of Heave/Pitch Limit-Cycle Oscillations Close to the Transonic Dip," *Journal of Fluids and Structures*, Vol. 22, No. 4, 2006, pp. 505–527. https://doi.org/10.1016/j.jfluidstructs.2006.01.004

[35] Scharnowski, S., Kokmanian, K., Schäfer, C., Baur, T., Accorinti, A., and Kähler, C. J., "Shock-Buffet Analysis on a Supercritical Airfoil with a Pitching Degree of Freedom," *Experiments in Fluids*, Vol. 63, No. 6, 2022. https://doi.org/10.1007/s00348-022-03427-4

[36] Accorinti, A., Baur, T., Scharnowski, S., Knebusch, J., Dillinger, J., Govers, Y., Nitzsche, J., and Kahler, C. J., "Measurements of Deformation, Schlieren and Forces on an OAT15A Airfoil at Pre-Buffet and Buffet Conditions," *IOP Conference Series: Materials Science and Engineering*, Vol. 1024, Jan. 2021, Paper 012052. https://doi.org/10.1088/1757-899x/1024/1/012052

[37] Kokmanian, K., Scharnowski, S., Schäfer, C., Accorinti, A., Baur, T., and Kähler, C. J., "Investigation of Transonic Shock Buffet over a Supercritical Airfoil Using Particle Image Velocimetry," *Experiments in Fluids*, Vol. 63, 2022, p. 149. https://doi.org/10.1007/s00348-022-03499-2

[38] Scharnowski, S., Bross, M., and Kähler, C. J., "Accurate Turbulence Level Estimations Using PIV/PTV," *Experiments in Fluids*, Vol. 60, No. 1, 2018, pp. 1–8. https://doi.org/10.1007/s00348-018-2646-5

[39] Scheitle, H., and Wagner, S., "Influences of Wind Tunnel Parameters on Airfoil Characteristics at High Subsonic Speeds," *Experiments in Fluids*, Vol. 12, Nos. 1–2, 1991, pp. 90–96. https://doi.org/10.1007/bf00226571

[40] Raffel, M., "Background-Oriented Schlieren (BOS) Techniques," *Experiments in Fluids*, Vol. 56, No. 3, 2015. https://doi.org/10.1007/s00348-015-1927-5

[41] Chu, T., Ranson, W., and Sutton, M. A., "Applications of Digital-Image-Correlation Techniques to Experimental Mechanics," *Experimental Mechanics*, Vol. 25, No. 3, 1985, pp. 232–244. https://doi.org/10.1007/BF02325092

[42] Giannelis, N., and Vio, G., "A Modal Approach to Shock Buffet Lock-in Analysis," *Proceedings of the 29th International Conference on Noise and Vibration Engineering*, KU Leuven, Dept. of Mechanical Engineering, Heverlee, Belgium, 2020, pp. 247–260, https://www.researchgate.net/profile/Nicholas-Giannelis/publication/344196923_A_modal_approach_to_shock_buffet_lock-in_analysis/links/5f5aaa0ea6fdcc1164092c7b/A-modal-approach-to-shock-buffet-lock-in-analysis.pdf.

[43] Welch, P., "The Use of Fast Fourier Transform for the Estimation of Power Spectra: A Method Based on Time Averaging over Short, Modified Periodograms," *IEEE Transactions on Audio and Electroacoustics*, Vol. 15, No. 2, 1967, pp. 70–73. https://doi.org/10.1109/TAU.1967.1161901

[44] Lee, B., "Self-Sustained Shock Oscillations on Airfoils at Transonic Speeds," *Progress in Aerospace Sciences*, Vol. 37, No. 2, 2001, pp. 147–196. https://doi.org/10.1016/S0376-0421(01)00003-3

[45] Giannelis, N. F., Levinski, O., and Vio, G. A., "Origins of Atypical Shock Buffet Motions on a Supercritical Aerofoil," *Aerospace Science and Technology*, Vol. 107, Dec. 2020, Paper 106304. https://doi.org/10.1016/j.ast.2020.106304

D. E. Raveh
Associate Editor

Journal of Fluids and Structures 122 (2023) 103975

Contents lists available at ScienceDirect

Journal of Fluids and Structures

journal homepage: www.elsevier.com/locate/jfs

Experimental investigation of transonic buffeting, frequency lock-in and their dependence on structural characteristics

Tim Korthäuer [*], Alessandro Accorinti, Sven Scharnowski, Christian J. Kähler

Institute for Fluid Mechanics and Aerodynamics, Universität der Bundeswehr München, Werner-Heisenberg-Weg 39, Neubiberg, 85577, Germany

ARTICLE INFO

Article history:
Received 5 March 2023
Received in revised form 17 July 2023
Accepted 20 August 2023
Available online xxxx

Keywords:
Transonic buffeting
Frequency lock-in
Experimental aero-elasticity
Fluid–structure interaction

ABSTRACT

Transonic buffet is a phenomenon that appears in compressible flow around an airfoil and plays a substantial role in the limitation of the flight envelope of commercial aircraft. If the structural natural frequencies of the wing are similar to the buffet frequency, the oscillation of the compression shock, fluid, and structure may interact (transonic buffeting) and lead to strong loads and potential structural failure. Numerical research has shown that structural parameters can have a significant effect on the onset point of shock oscillations as well as on the typology of the fluid–structure interaction, which presented classical structural excitation, modal veering, or frequency lock-in.

The aim of this research is a systematic experimental investigation to examine the structural effects and the lock-in phenomenon. It provides a partial validation of the numerical results available in the literature. A lightweight, elastically-suspended wing model (OAT15A profile) was tested in the Trisonic Wind Tunnel Munich. Optical measurement techniques were deployed to non-intrusively observe the flow-induced density gradient field (background-oriented Schlieren) and the structural deformation and displacement of the wing (digital image correlation). Mass ratios varied from 282 to 322 and the half-chord-based, reduced natural pitch frequency ranged from 0.169 to 0.280. The experimental results confirm the existence of frequency lock-in, an interaction dominated by the structural mode that presents high but limited pitch amplitudes for natural pitch frequencies above the natural buffet frequency. The effects of mass ratio and natural pitch frequency on the interaction are discussed. A substantial effect of the mass ratio on the onset of buffeting and the resulting pitch amplitude for frequency lock-in was discovered.

1. Introduction

The flight envelope of commercial aircraft at transonic speeds is affected by the phenomenon of transonic shock buffet. With increasing angle of attack (AoA) and/or Mach number the initially steady compression shock, which forms on the suction side of a supercritical airfoil, becomes unsteady. The shock starts to oscillate and induces strong load variations on the wing structure, which endanger aircraft and passenger safety. The phenomenon has been studied for decades, but a comprehensive physical explanation of its root cause remains missing (Giannelis et al., 2017). In the case of unswept wings or small sweep angles, the chord-wise shock oscillation is homogeneous along the span. On the other hand, wings with a sweep angle larger than 15° present the so-called span-wise buffet cells. Due to pressure perturbations traveling along the

---

[*] Corresponding author.
E-mail address: tim.korthaeuer@unibw.de (T. Korthäuer).

https://doi.org/10.1016/j.jfluidstructs.2023.103975

wing's span, the shock oscillations in the buffet cells are not in phase over the entire span (Iovnovich and Raveh, 2015). The present work focuses on investigating shock buffet occurring on unswept 2D wings. The phenomenon, observed on a fixed, rigid wing in the same facility in a previous work (Accorinti et al., 2022), will be referred to as "natural" buffet and will serve as the reference case for the upcoming investigations.

1.1. *Fluid-structural coupling in transonic buffet flow*

If the structural natural frequencies of the 2D wing are close to the dominant natural buffet frequency, the structure may be excited, leading to the fluid–structure interaction known as transonic buffeting. Given the non-linear character of the buffet phenomenon itself, the corresponding fluid–structure interaction (FSI) exhibits limit-cycle oscillations (LCO), where the amplitudes of the oscillation stagnate on a certain level (Dowell et al., 2003). Nevertheless, that level of wing oscillations might be above the structural capabilities and could lead to severe failure. At the least, it will induce high fatigue loads into the structure and limit the component life cycle.

Several studies on this FSI have been made in the last decades. A major distinction between them can be made based on the excitation method (self-induced or forced by pitch motion, heave motion, or deflection of control surfaces). Furthermore, the investigation of the effects of Mach number, angle of attack, flutter index, mass ratio, natural pitch and/or heave frequency, and dynamic pressure can be found throughout the literature.

1.1.1. *Forced excitation*

In his substantial work regarding transonic buffet, Tijdeman (1977) conducted experiments to investigate the effect of sinusoidal flap motions of a NACA 64A006 airfoil on the shock wave without presence of separation. The study identified three different modes of shock motion of which Type A presented a sinusoidal shock oscillation, synchronized with the flap motion. The relationship between frequency and phase lag between wing and shock motion was found to be linear. In the early 1980s, Davis and Malcolm (1980) performed detailed experiments on an oscillating airfoil in a transonic buffet flow. They focused on the effect of the unsteady shock-wave-boundary-layer interaction (SWBLI) on lift, moment, and pressure distribution, resulting from forced pitching motions of different amplitudes and frequencies. At higher incidence, with the presence of shock-induced boundary layer separation ('shock-stall conditions'), the airfoil presented strongly affected pressure distributions that deviated significantly from linear modeling. The frequency response of lift and moment coefficients with respect to the harmonic excitation showed a peak response at the reduced, chord-based natural pitch frequency $k_\theta \approx 0.2$, indicating a resonance peak. Furthermore, a change in phase-lead was observed in both coefficient responses at the mentioned excitation frequency. Good agreement with the observations of Davis and Malcolm (1980) and Tijdeman (1977) was found in succeeding numerical investigations regarding the effect of structural excitation by flap, pitch, or heave motions in (pre-)buffet conditions. The consequent response functions of aerodynamic coefficients matched and the potential of initiating a premature onset of shock oscillations was observed (Nitzsche, 2009). For buffet conditions, Raveh (2009) found compliant results regarding the response functions of aerodynamic coefficients. She first mentioned the phenomenon of frequency lock-in (FLI) in the transonic regime, which describes a synchronization of the shock oscillation with the structural excitation frequency if the latter was set sufficiently close to the natural buffet frequency and the excitation amplitude exceeded a certain threshold. Special emphasis was put on the ratio of the natural pitch and the natural buffet frequency f_θ/f_b, as $f_\theta/f_b > 1$ promoted frequency lock-in at lower excitation amplitudes compared to $f_\theta/f_b < 1$. Hartmann et al. (2013) experimentally studied the coupling of a forced heave-pitch airfoil motion with shock oscillations in transonic buffet flow. A good agreement with the previously mentioned numerical results was found. At excitation frequencies in the buffet range, the shock oscillation locked into the excitation frequency.

1.1.2. *Self-induced excitation*

Schewe et al. (2003) and Dietz et al. (2006) performed early self-induced, aero-elastic experiments close to the transonic dip - an unfavorable deviation from the flutter boundary based on linear theory. The focus was set on the limit-cycle oscillations and the corresponding energy exchange and (de)stabilizing effects of shock oscillations on the flutter boundary. The buffeting regime was reached but most experimental points included a change of several parameters at the same time or the natural pitch frequency was set too low to observe FLI. Nevertheless, the potential destabilizing effect of the shock wave was reported, just like for Nitzsche (2009).

In the last years, the research effort on transonic buffet has significantly increased, being accompanied by the approach of the buffeting phenomenon from the flow (buffet) rather than from the structural (flutter) side. Besides the forced excitation, Hartmann et al. (2013) conducted self-sustained experiments, where the airfoil was excited by the flow only ($k_\theta \approx 0.12$, $k_b \approx 0.34$). The resulting coupled frequency was found to be in the range of the natural buffet frequency, which agrees well with today's theory regarding structural natural frequencies located below the natural buffet frequency.

Several numerical groups investigated the interplay between shock buffet and different structural modes by modal analysis. Classical structural excitation would show a symmetrical, exponential response peak centered around the exciting natural buffet frequency f_b, where the equality of the natural pitch frequency and the natural buffet frequency $f_\theta = f_b$ would correspond to the resonance case, resulting in large amplitudes depending on structural damping. It has been shown that the pitching response of an elastically suspended airfoil in fluid–structure interaction is not generally based on the principle of classical structural excitation (Gao et al., 2017). The pitch motion is not always excited by the flow phenomenon (the shock buffet oscillations) and does not necessarily synchronize with the buffet frequency. The interaction rather follows the principle of modal coupling as shown by Nitzsche (2009), Gao et al. (2017) and others. This approach also confirms the premature onset given particular structural settings, firstly observed by Nitzsche (2009) and emphasizes the importance of the topic (Gao et al., 2018). It has to be noted that the results published by Gao et al. (2017, 2018) are based on a NACA0012 airfoil, but Giannelis et al. (2016) found a compliant behavior for the OAT15A.

The interaction exhibits typical characteristics of modal "veering", where the coupled motion switches from one mode to another, after the two modes approached each other without intersecting (Gao et al., 2017). For the investigated OAT15A airfoil, structural to natural buffet frequency ratios $f_\theta/f_\mathrm{b} \lessapprox 0.8$ result in a coupled frequency similar to the natural buffet frequency resembling classical dynamic excitation (dominant fluid mode, FM). The adjacent veering region can be found at $0.8 \lessapprox f_\theta/f_\mathrm{b} \lessapprox 1.2$, depending on mass ratio and structural damping (Giannelis et al., 2016). For $1.2 \lessapprox f_\theta/f_\mathrm{b} \lessapprox 1.7$ the coupled motion locks into the now-dominant structural mode (SM), which is the previously mentioned phenomenon of transonic frequency lock-in (Raveh and Dowell, 2011). In that frequency range, a strong rise in the pitch amplitude can be observed with increasing frequency ratios. A further increase in f_θ/f_b is accompanied by an abrupt drop in pitch amplitudes and indicates the end of the FLI region.

Just lately, Nitzsche et al. (2022) presented extensive numerical results that allow a classification of the different types of flutter that may occur in transonic flow depending on AoA, natural pitch frequency, and mass ratio (by variation of the dynamic pressure). Nevertheless, the investigated structural natural frequencies were lower or approximately equal to the natural buffet frequency and could not reach the FLI region.

In order to experimentally validate the numerically observed typologies of buffeting (e.g. FLI) and their characteristics in dependency on the mass ratio, the transonic flow around a supercritical airfoil for different aerodynamic and structural conditions was investigated. Besides the observation of buffet onset (Korthäuer et al., 2023), particular attention was paid to the manifestation of the FSI in the different regions (FLI, veering, classical dynamic excitation), and furthermore, the particular effects of structural characteristics, namely the natural pitch frequency f_θ and the mass ratio μ.

Section 2 gives an overview of the experimental facility and the setup designed for the experiments. In Section 3, a summary of the applied measurement techniques is given. The experimental conditions, namely the reference buffet case and the varied parameters are presented in Section 4. Section 5 extensively presents the results with respect to the effects of AoA, the structural parameters, and the consequent FSI. Finally, in Section 6, a brief summary of the work is given and corresponding conclusions are drawn.

2. Experimental setup

2.1. Facility

The presented experiments are based on the same experimental setup outlined in Korthäuer et al. (2023). They were conducted in the Trisonic Wind Tunnel of the Bundeswehr University in Munich (TWM). The blow-down type wind tunnel has a rectangular test section of 0.3 m × 0.68 m (width × height). By adjusting two throats, a Laval nozzle upstream of the test section and a diffuser downstream, it allows the operation at Mach numbers in the range of 0.2 to 3.0. By setting the total pressure of the incoming dry air from the pressure vessels in the range from 1.2 bar to 5.0 bar, the Reynolds number is controlled. The free-stream turbulence level for the here-discussed Mach number range was determined to be approximately 1.3%, based on the velocity fluctuations in stream-wise direction (Scharnowski et al., 2018). The following measures were taken to reduce the effects of boundary layer growth along the test section walls: the horizontal walls were set to a divergence angle of 0.08° along the complete test section of 1.8 m length, while a boundary layer suction was applied on the vertical walls. Both settings were optimized in order to obtain a constant distribution of the stream-wise wall pressure in the whole test section for all relevant Mach numbers. More detailed characterization and description of the facility and its features were reported in Scharnowski et al. (2018) and Scheitle and Wagner (1991).

2.2. Model and test stand

After having become a benchmark for the investigation of the buffet phenomenon (Jacquin et al., 2005), the OAT15A airfoil shape was selected for the presented measurement campaign. With a thickness of 18 mm ($0.12c$), the airfoil introduced a maximum blockage of 3.5% in the test section at the highest angle of attack. For the boundary layer tripping, a line of circular stickers (∅3 mm, thickness of 60 μm, span-wise spacing of 6 mm) was applied at 7% of chord on both the suction and the pressure side.

The two-dimensional rectangular wing was manufactured from carbon-fiber-reinforced polymer (Weberschock Development, Gleichen, Germany) to maintain maximum stiffness at a low experimental mass ratio. With a span width of $s = 298$ mm, a chord length of $c = 152$ mm and the resulting aspect ratio of 1.96 the presence of a clean 2D flow cannot be assumed. Detailed investigations of the span-wise shock front have revealed that despite 3D effects closer to the walls, the 2D characteristics of shock buffet remain dominant (Accorinti et al., 2023). Three-dimensional effects based on wing deformation are deemed to be negligible as will be reported in Section 3.2.

The design of the test stand focused on the realization of a spring-mounted wing with pitching DOF that allowed for the separate adjustment of the moment of inertia, mass distribution, and pitch spring stiffness. Fig. 1 shows a sketch and

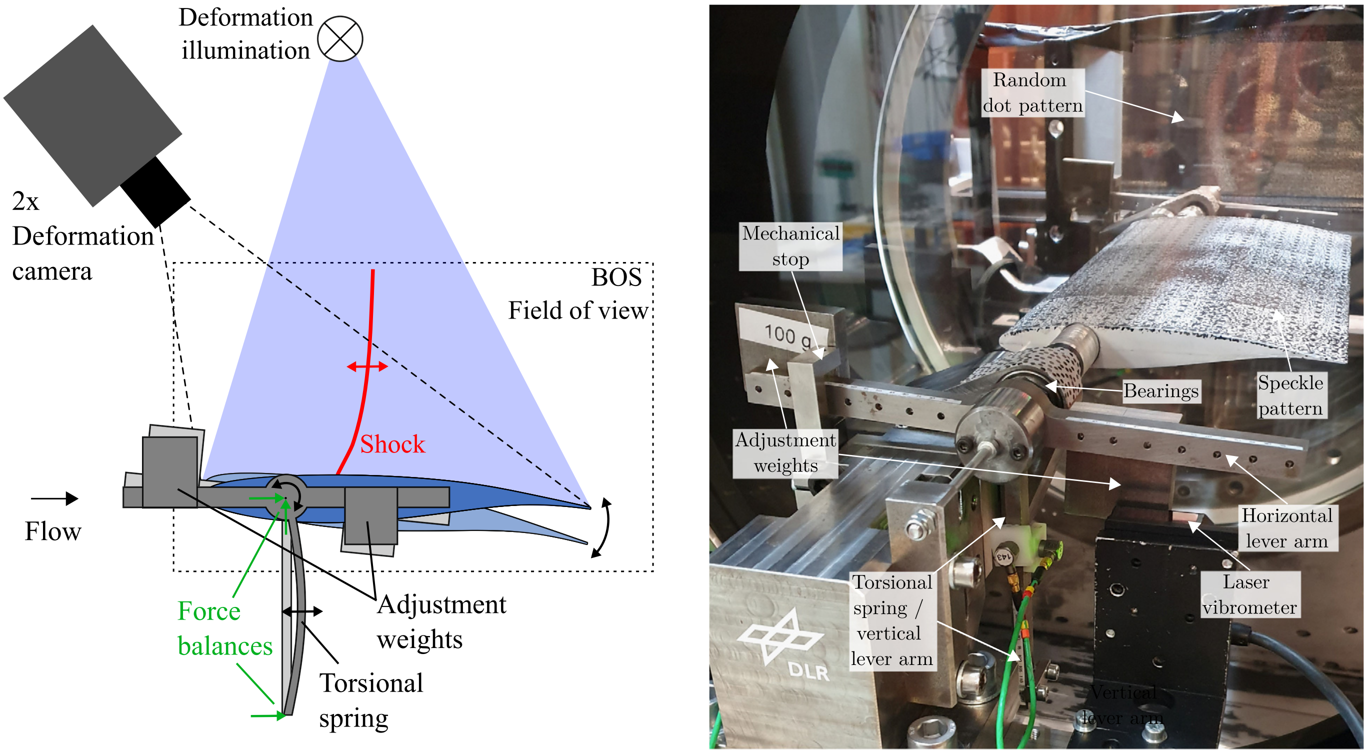

Fig. 1. Sketch (left) and photo (right) of the spring-mounted rigid wing with a pitching DOF and reduced heave DOF and applied measurement techniques, Korthäuer et al. (2023).

a photograph of the experimental setup used for the buffeting experiments with reduced degrees of freedom (DOF). The rotational axis was defined by a steel shaft, located at 25% of chord. It was fed through both circular side windows of the test section and supported in the plenum chamber by self-aligning bearings before being connected to a set of lever arms. The lower, vertical lever arm overtook the role of the torsional spring which could be adjusted by setting its length. Trimming weights were connected to the side arms in order to adjust the moment of inertia and the center of gravity. To reduce structural coupling, the latter was set to coincide with the rotational axis for all flexible cases. Furthermore, a laser-vibrometer was used on the lever arms to get online information about the current amplitude and frequency of the pitch motion. At high amplitudes, the wind tunnel runs were interrupted prematurely to avoid structural damage. Furthermore, a mechanical stop was used on the lever arms to limit the pitch amplitude to $\hat{\alpha} \leq 2.5°$.

In wind-off conditions, the integrated force balances were used to determine the inherent structural natural frequencies. Due to strong non-linearity, supposedly based on clearance in the self-centering bearings, a fruitful dynamic calibration and its application on the measured forces was not possible. As the bearing remained also for testing in “natural buffet” mode, this affected all wind-on measurements.

3. Optical measurement techniques

Two optical measurement techniques were deployed in order to non-intrusively measure flow and structural characteristics.

3.1. Background-oriented Schlieren: shock location

For the determination of the shock wave position, background-oriented schlieren (BOS) measurements were performed. Based on a conventional Schlieren setup, parallel light (Luminus LED CBT-120-B-C11KM301, 462 nm) was sent through the test section after having passed a random point pattern. The pattern was observed by a high-speed camera (Phantom V2640) with an image rate of 1000 Hz from the opposite side of the test section. This rate ensures a sufficiently high resolution for the observation of the shock motion, which is expected at $f_{x_s} \approx 100\,\text{Hz}$. Given the presence of compressible flow, depending on the density gradients in the flow, a change of refraction index was introduced, which consequently led to a distortion of the dot pattern corresponding to the flow structures. The cross-correlation of the recorded images with an undisturbed reference image at wind-off conditions allowed for a qualitative reconstruction of the density gradients in the flow, as shown in the color-coded displacement map in Fig. 2, left. Based on the assumption that the shock-wave represents the strongest density gradient in the flow, the shock location could be detected at different heights above the wing. The black circle represents the rotational axis. Due to the manufacturing process of the axis hole

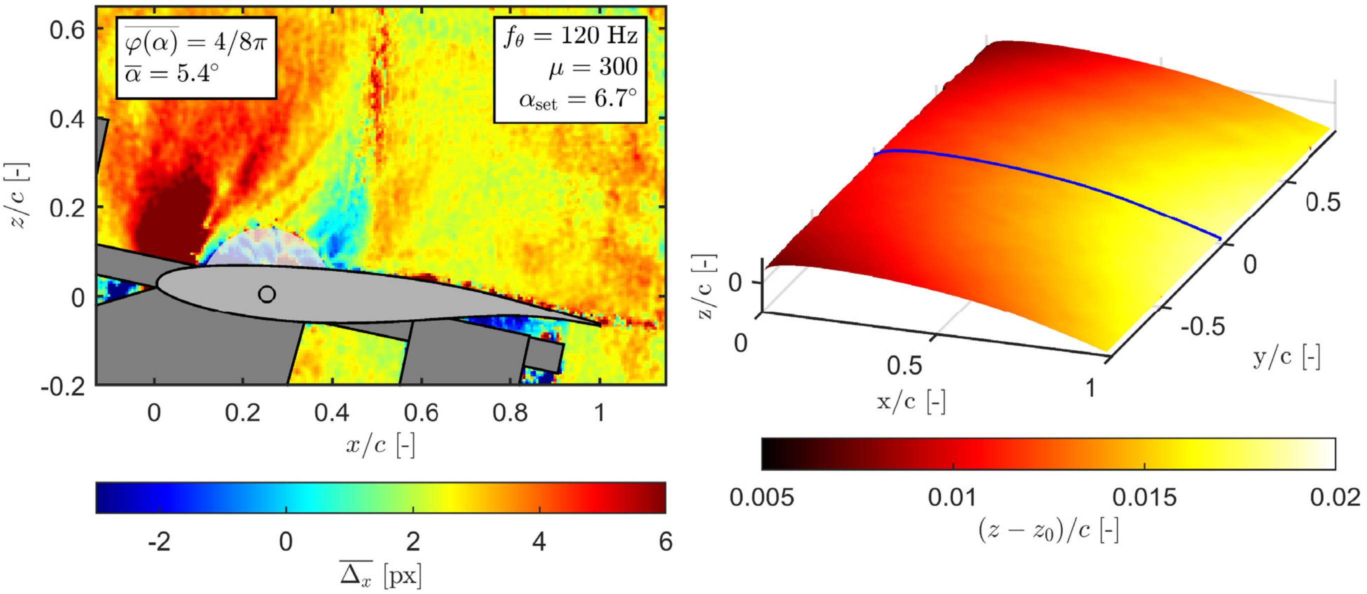

Fig. 2. Left: Exemplary phase-averaged BOS displacement field, presenting the color-coded stream-wise pixel displacement due to density gradients. The black circle marks the rotational axis. Right: Average wing surface displacement field obtained by DIC measurements with center cut highlighted in blue (right). $M = 0.74$. (For interpretation of the references to color in this figure legend, the reader is referred to the web version of this article.)

in the window, density gradients in the window material introduced erroneous values marked by the circular gray region. A more comprehensive description of the technique is given in Raffel (2015). As the shock location is the most important fluid feature in the buffet(ing) interaction, it will be used as the representation of the "fluid mode" (FM).

3.2. Digital image correlation: Structural deformation

For the observation of the structural behavior of the wing, stereo digital image correlation (DIC) measurements were applied (Chu et al., 1985). A random speckle pattern was painted on the upper wing surface to allow and optimize the correlation results. Four high-power LEDs (Luminus CBM-120-UVX, 410 nm) were set up on top of the test section to illuminate the pattern in pulsed mode to allow unblurred images. Two high-speed cameras (PCO Dimax HS4), mounted on either side of the test section, observed the wing surface under an angle of approx. 30°. The images were recorded with an image rate of 1000 Hz. An apriori, coplanar volume calibration of the stereo camera setup set the basis for the post-processing, where a correlation-based 3D surface reconstruction was performed for every image pair, resulting in a time-resolved surface representation of the wing. Fig. 2, right, shows the obtained deformation field for an exemplary run with respect to wind-off conditions (Korthäuer et al., 2023). The results clearly show a three-dimensional wing deformation, which is constituted of a span-wise bending that leads to higher displacements in the wing center, and a rotation/torsion around the elastic axis, which results in increased displacements towards the trailing edge.

Fig. 3 presents the mean vertical surface displacement and its fluctuations relative to wind-off conditions in natural buffet conditions for two chord-wise positions, $x/c = 0.25$ (position of the rotational axis) and $x/c = 0.91$ (close to the trailing edge), under high load at $M = 0.74$ and $\overline{\alpha} = 6.46°$ (buffet conditions). $x/c = 0.25$ represents the wing bending without the influence of the pitch motion. One can infer that the major part of the average bending (approx. 0.9% of chord) appears outside of the test section between wing and bearing, whereas the difference inside the wing is less than approx. 0.4% of chord. Under the effect of the static pitch deformation, $x/c = 0.91$ shows a higher mean deviation with respect to wind-off conditions. Both chord-wise positions present a significant amount of fluctuations ($0.1\% < \sigma_{z/c} < 0.2\%$), which means that also the bending motion is dynamically excited by the buffet phenomenon. Given the low level of wing bending inside the test section, the authors deem the 3D effect of wing bending on the flow negligible, compared to the strong pitch motions in the experiments. The vertical motion of the whole rigid wing will therefore be addressed by the term "heave".

In order to analyze the surface data with respect to the aerodynamically important quantities, an airfoil-shape-fitting algorithm was applied to each span-wise cross-section. A detailed description is given in Korthäuer et al. (2023). As a result, the span-wise distributions of local α, vertical (z_A, heave), and stream-wise (x_A, surge) displacement of the rotational axis were obtained and showed average variations below 0.05°, 0.5% and 0.2%, respectively. The authors deem the wing sufficiently rigid as the major driver for the displacement originates outside the test section. Consequently, the aerodynamic quantities were extracted from the span-wise center of the wing, as highlighted in blue in Fig. 2 (right), and will be the basis for further evaluations and the determination of the structural mode (SM).

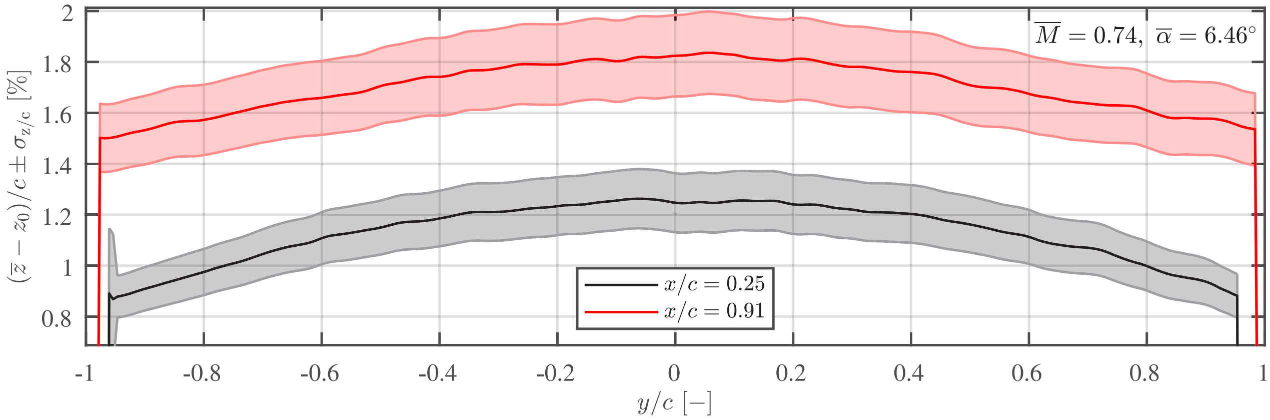

Fig. 3. Span-wise wing deformation for a run without released pitching DOF. Solid lines represent the average deviation from the wind-off wing position normalized by the chord length for two different positions of chord $x/c = 0.25$ and 0.91. The shaded area represents the corresponding fluctuations as standard deviation $\sigma_{z/c}$.

4. Experimental conditions

4.1. Natural buffet case

In the following section, an overview of the different aerodynamic and structural parameters will be given. Particular focus is set on the natural buffet case that will be used for comparison with the flexible cases. Detailed measurements were conducted on this configuration and are presented in Accorinti et al. (2022). The relevant reference case for the Mach number $M = 0.74$ will be presented briefly. Fig. 4 highlights the evolution of the detected shock statistics and frequency content at a height above the wing of 10%, x_s, for different α_{set}. On the left, the median shock location $\tilde{x}_s/c$ together with its corresponding shock motion range is presented over the mean measured angle of attack $\overline{\alpha}$. The shock motion range is represented by the 5–95 percentile range (error bar) of all samples. By this, excessive spurious values are filtered out from the results. Filled markers represent cases with established buffet, i.e. harmonic strong shock oscillations. The right plot shows the corresponding power spectral densities $P_{x_{s,x_s}}$, determined by the method of Welch (1967) with a window length of 100 samples and a Hamming window function with an overlap of 50%. The resulting frequency resolution of 10 Hz may lead to masking of eventually appearing neighboring peaks. As those peaks were found to range two orders of magnitude below the highest peak and this work focuses on the characteristics of the highest peak, the given settings were deemed sufficient. In particular in the spectral overviews, the readability is improved. Future work could benefit from longer measurement duration to increase the frequency resolution. All successive evaluations of the shock location in this work are based on this method.

As one can see by comparison of the set and the resulting angles of attack, the static deformation is $\alpha_{\text{set}} - \overline{\alpha} \approx 0.5°$, which originates from the static torsion of the shaft between the wing and outer support. The median shock location exhibits an inversion of the previously downstream-directed shock motion at $\overline{\alpha} \approx 5°$ after which a further increase in the AoA leads to a dominant frequency (in the spectrum on the right) together with increased shock fluctuations, indicating buffet onset. Occasionally, the shock can be found quite far upstream, which results in a skewed distribution of the detected shock location. After $\overline{\alpha} = 6°$ the fluctuations decrease and the spectral peak reduces, inferring the approach of the buffet offset boundary. Due structural limitations, a further increase in AoA was not possible. A future measurement campaign could focus on the determination of exact location of the offset boundary by adaptations of the setup.

Based on the wind-off structural tests, the reason for the spectral peak around $k_{x_s} \approx 0.75$ for low AoA is expected to emanate from structural natural frequencies of the setup outside the test section (see Korthäuer et al. (2023)). As to why a structural excitation appears at these low AoA, further investigations with possibly higher sampling rate have to be conducted.

4.2. Experimental parameters

Table 1 summarizes the tested structural settings. Three combinations of trimming weights were used, as indicated by the inertia factor $\gamma = I/(c^2\ m)$, where I is the moment of inertia and m represents the total moving mass of the setup including the wing. The variations in the mass ratio $\mu = 4m/(\rho_\infty \pi s c^2)$, where ρ_∞ denotes the inflow density for equal γ stem from minor variations in the Mach number. For each combination of trimming weights, three different values of spring stiffness (adjusted by the length of the lever arm) were selected to maximize the overall range of natural pitch frequencies. For each of those structurally fixed points, the set AoA was increased in steps of 0.3° within the range indicated in the last column. During all runs, the diffuser was adjusted to obtain a Mach number of $M = 0.74$ at a total pressure of $p_0 = 1.5$ bar. The resulting chord-based Reynolds number was $Re_c = 3 \times 10^6$. The total temperature was rather constant at (292 ± 3) K.

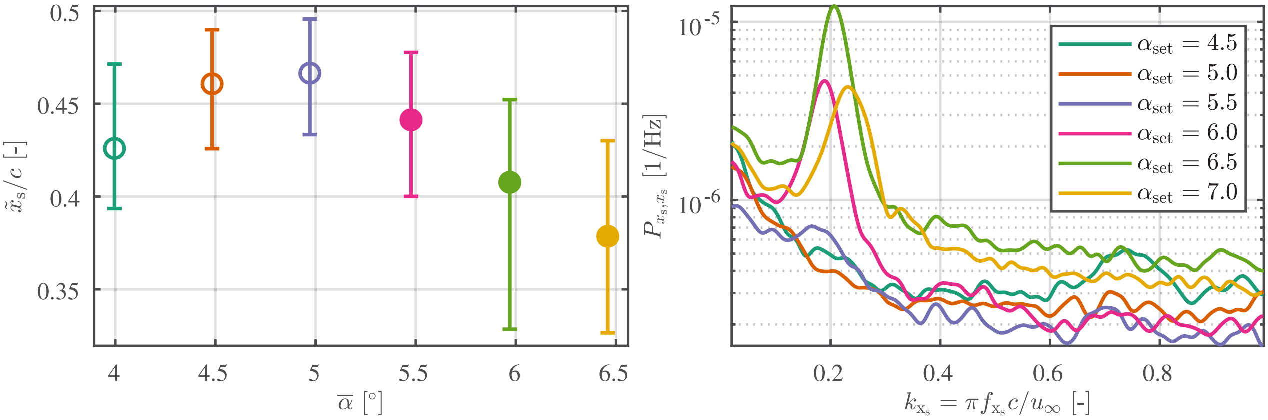

Fig. 4. Left: median shock location and 5–95 percentile range as error bars for the natural buffet case at different set AoA. Right: corresponding frequency spectra (PSD) based on the shock location at a height of 10%. (For interpretation of the references to color in this figure legend, the reader is referred to the web version of this article.)

Table 1
Overview over the experimental parameters and the resulting reduced natural pitch frequencies k_θ and mass ratios μ. The last row represents the natural buffet case as reference from Accorinti et al. (2022).

f_θ [Hz]	$k_\theta = \pi f_\theta c/u_\infty$ [−]	$\gamma = I/(c^2\ m)$ [−]	$\mu = 4m/(\rho_\infty \pi s c^2)$ [−]	α_{set} [°]
84	0.169	0.145	322 ± 1	5.5 to 6.7
93	0.187	0.145	323 ± 1	5.5 to 6.7
102	0.205	0.145	323 ± 1	5.5 to 6.7
104	0.209	0.116	302 ± 1	5.2 to 6.7
113	0.227	0.116	301 ± 1	5.2 to 6.7
120	0.241	0.116	301 ± 1	5.5 to 6.7
115	0.232	0.091	284 ± 1	5.5 to 6.7
121	0.244	0.091	282 ± 1	5.5 to 6.4
139	0.280	0.091	284	5.5 to 6.7
371				4.5 to 7.0

5. Results

5.1. Effect of AoA on FSI

With the increase of α_{set}, the region of buffet(ing) was slowly approached. In Fig. 5 the evolution of all selected quantities with increasing AoA is presented, namely the shock location (top row), the measured AoA (center row) and the heave position (bottom row). The structural settings for that particular run were $f_\theta = 102\,\text{Hz}$, $\mu = 322$ and $\gamma = 0.145$, i.e. the natural pitch frequency was set in the vicinity of the natural buffet frequency at which a strong interaction was to be expected. The left column shows the time signals for the different α_{set} in color code. In particular α and z_A, but also x_s for higher α_{set}, present periodic behavior. The center column shows the median values together with the 5–95 percentile range, whereas the frequency spectra based on the PSD are displayed in the right column, similar to the plots presented in Fig. 4 for the natural buffet case. The inversion of the shock motion appears to be equally pronounced, whereas the 5–95 percentile range of motion is only similar ($x_{s,0.95-0.05}/c \approx 6\%$) up to the point of established buffeting. In Korthäuer et al. (2023), the points of onset were defined by the detection of a substantial increase (more than 10%) in the standard deviation of the shock location. Considering this criterion the hereby-found onset points show a good agreement. The range of shock motion strongly increases for the points after onset (indicated by filled markers) compared to the natural buffet case ($x_{s,0.95-0.05}/c \approx 14\%$ vs. 8% at $\overline{\alpha} = 5.5°$).

Despite the inverse mean shock motion (upstream-directed), the most downstream shock excursion is extended further, whereas the natural buffet case exhibited an excessive upstream-directed excursion of the shock front. The frequency spectra present a very dominant peak at the natural pitch frequency for all cases just before and after onset. The shock motion has therefore locked into the structural frequency.

The median values appear centered in the 5–95-percentile range, speaking for a non-skewed statistical distribution. The pitch angle motion range varies from 0.25° to 1.2° for an increase from $\overline{\alpha} \approx 4.5°$ to 5.6°. This accentuates the effect of established buffeting. The frequency spectrum presents a dominant peak for all cases, even far before buffet onset, which indicates sole structural excitation of the wing by the flow.

The median heave position rises with increasing AoA up to the point of shock motion inversion and buffeting onset. This speaks for a strong separation, which reduces the lift, being the reason for the heave in the first place. Buffeting

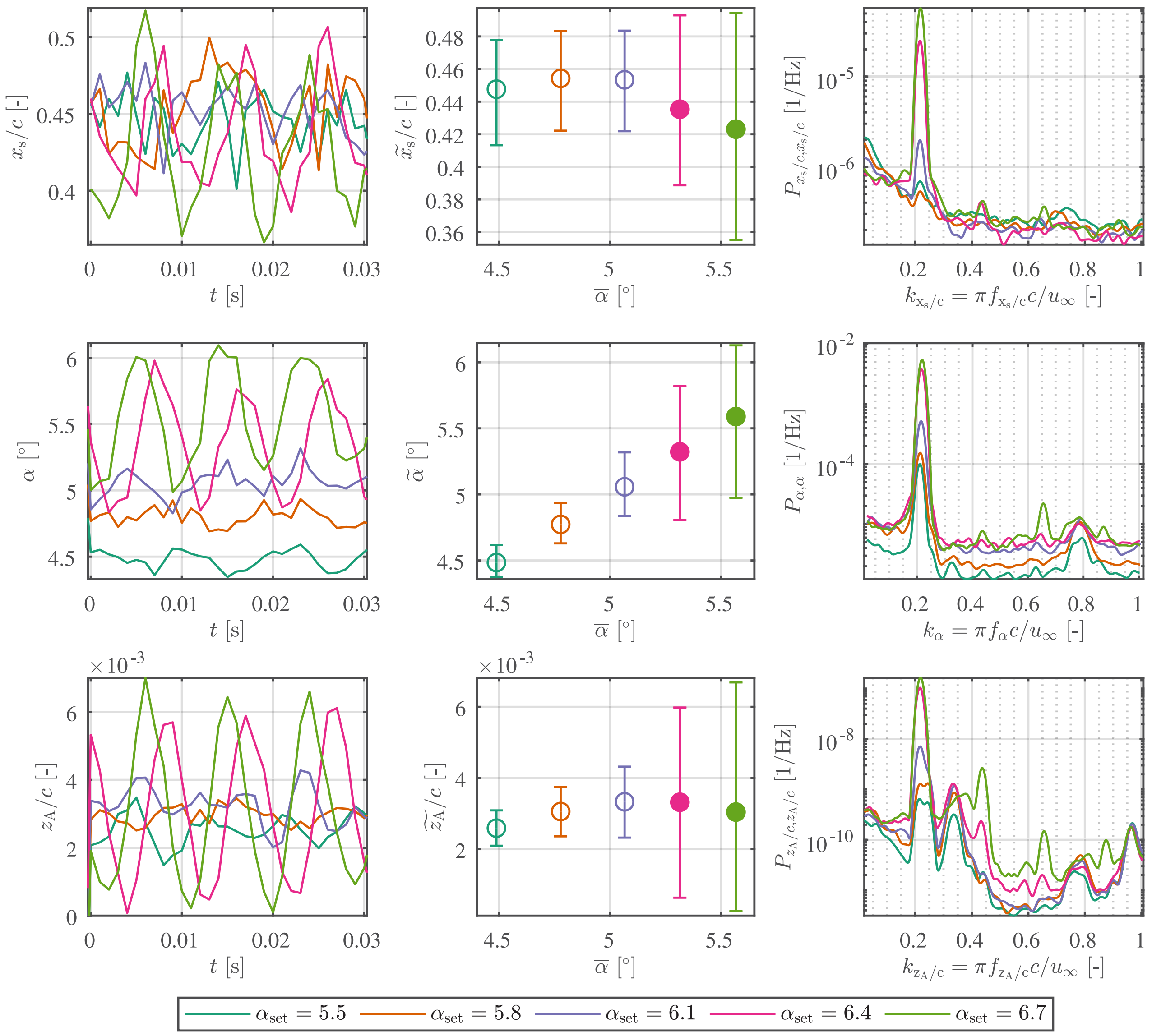

Fig. 5. Representation of time-signals (left column), median values and 5–95 percentile range (center column) and frequency content as PSD (right column) for shock location (top row), measured AoA (center row) and heave position (bottom row) and multiple set AoA (color-coded). Structural values: $f_\theta = 102\,\text{Hz}, \mu = 322, \gamma = 0.145$. (For interpretation of the references to color in this figure legend, the reader is referred to the web version of this article.)

onset results in an increased heave motion of up to $z_{A,0.95-0.05}/c \approx 0.7\%$. The frequency spectrum shows the same peak as before, indicating a coupled shock-pitch-heave motion. At low AoA a second peak is found close by at $k_{z_A/c} \approx 0.25$ being ascribed to a structurally coupled pitch-heave mode. Furthermore, for all AoA the isolated heave mode is present at $k_{z_A/c} \approx 0.34$.

Given the highly harmonic pitch oscillation, even at low AoA, a phase-locked evaluation of the quantities was carried out to obtain a representative characterization of the coupled motion. For this, a sine-function was fitted to the signal of α in moving windows of 0.05 s length to take into account a slight phase variation over time. Cleared by this phase shift, all measured quantities were phase-averaged. In Fig. 6 the phase-locked mean values of shock location (left) and heave position (right) are presented over the corresponding measured AoA. The color code represents the phase angle of α. The resulting Lissajou plots circulate around the previously shown median values expressing well the periodicity for all cases where the amplitude increases significantly after onset. As for the shock location, a variation in the phase relation becomes visible, i.e. for $\alpha_{set} = 6.4°$ the values wander along the same line during up- and downstream excursion, speaking for a zero phase shift. Whereas for $\alpha_{set} = 6.7°$ (and also lower set AoA), a more-elliptic shape is presented, speaking for a phase lag of the shock with respect to α. This is mainly attributed to the accelerated upstream and decelerated shock-foot excursion at the lowest and highest AoA, respectively, agreeing well with the evolution described in Scharnowski et al. (2022). The heave and pitch motion (right plot), on the other hand, present a rather constant phase lag throughout the increase of α_{set}.

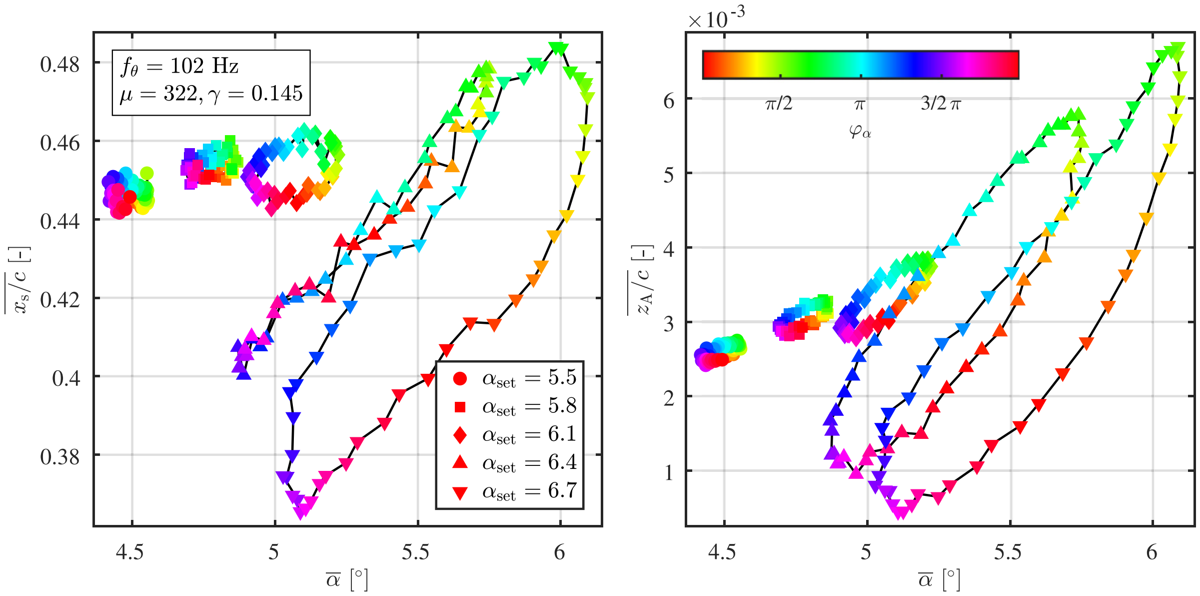

Fig. 6. Phase-locked values of shock location at a surface-height of 10% and heave position over corresponding measured AoA for different set AoA. (For interpretation of the references to color in this figure legend, the reader is referred to the web version of this article.)

5.2. *Effect of natural pitch frequency and mass ratio*

5.2.1. *Statistics of shock and structural oscillation*

In order to illustrate the effect of mass ratio and natural pitch frequency on buffeting, Fig. 7 presents an overview of the development of the shock location, the AoA and the heave position with increasing AoA (from top to bottom). The left column shows the mean values (for AoA the mean deviation from the set AoA), whereas the right column presents the amplitudes of shock and wing motion represented by the 5–95 percentile range. The black line stands for the natural buffet reference case. Green, blue, and red represents increasing mass ratios. Different symbols indicate the natural pitch frequency, which was varied for each setting of mass ratio. Due to excessive heave motion and consequent structural contact between shaft and window, the case of $f_\theta = 139$ Hz presented an extraordinary behavior and related conclusions have to be treated with care (dashed line).

The top left plot presents the mean shock location for which the following conclusions can be drawn:

The mass ratio affects the mean shock location before inversion. The lower the mass ratio the farther downstream the shock is located. The natural pitch frequency does not seem to have an effect. The AoA of shock motion inversion is mainly dependent on the mass ratio. A lower mass ratio introduces a premature inversion compared to the reference case. An exception is found for the set of lowest frequencies (highest mass ratio), which are supposedly located below the buffet frequency and therefore subject to FM-dominated FSI. Lower mass ratios (green and blue) present high gradients for the inverse shock motion. The highest mass ratio (red), however, shows a similar inverse motion as the reference case. Again, the discrepancy in the FSI can account for that. The “accelerated” inverse shock motion is limited by a mean upstream shock location that is approached asymptotically. A lower mass ratio results in a more upstream final location. For $\mu = 322$ the supposedly asymptotic region has not been covered by the measured points.

The centered left plot allows for the investigation of the static deformation, which can be seen as an indirect measure of the mean aerodynamic moment: The reference case presented a static deformation of approx. 0.5° with a slight dependency on α. This reduction in the AoA indicates that the pressure point was located aft of the rotational axis, i.e. a positive aerodynamic moment was present. Due to reduced pitch stiffness in the flexible cases with lower f_θ, the static deformation was on a higher level, ranging from 1° to 1.5°. In general, the static deformation (and the aerodynamic moment) increased with an increase in $\overline{\alpha}$. Particularly after buffeting onset, the static deformation of some cases rose significantly. An exception is found for $f_\theta = 104$ Hz and 113 Hz, where the increase of the AoA initially reduces static deformation. A decrease in mass ratio led to a higher static deformation. The actual structural pitch stiffness, varied by the length of the lower lever arm sometimes played an unexpected role. For $\mu \approx 322$ an increase in f_θ (reduced lever arm length) resulted, as expected, in reduced static deformation for all AoA. For $\mu \approx 302$ the increase firstly confirms this trend (from $f_\theta = 104$ Hz to 113 Hz). A further increase to $f_\theta = 120$ Hz, however, led to a higher static deformation. Also, for the lowest mass ratio of $\mu \approx 284$ the trend seems to be reversed. In Section 5.2.2 this topic will be addressed in more detail.

In the bottom left plot, the mean heave position of the airfoil is presented. In general, the mean heave position increased with the AoA until the point of buffeting onset was reached. The level of heave stagnates in the buffeting region, which is

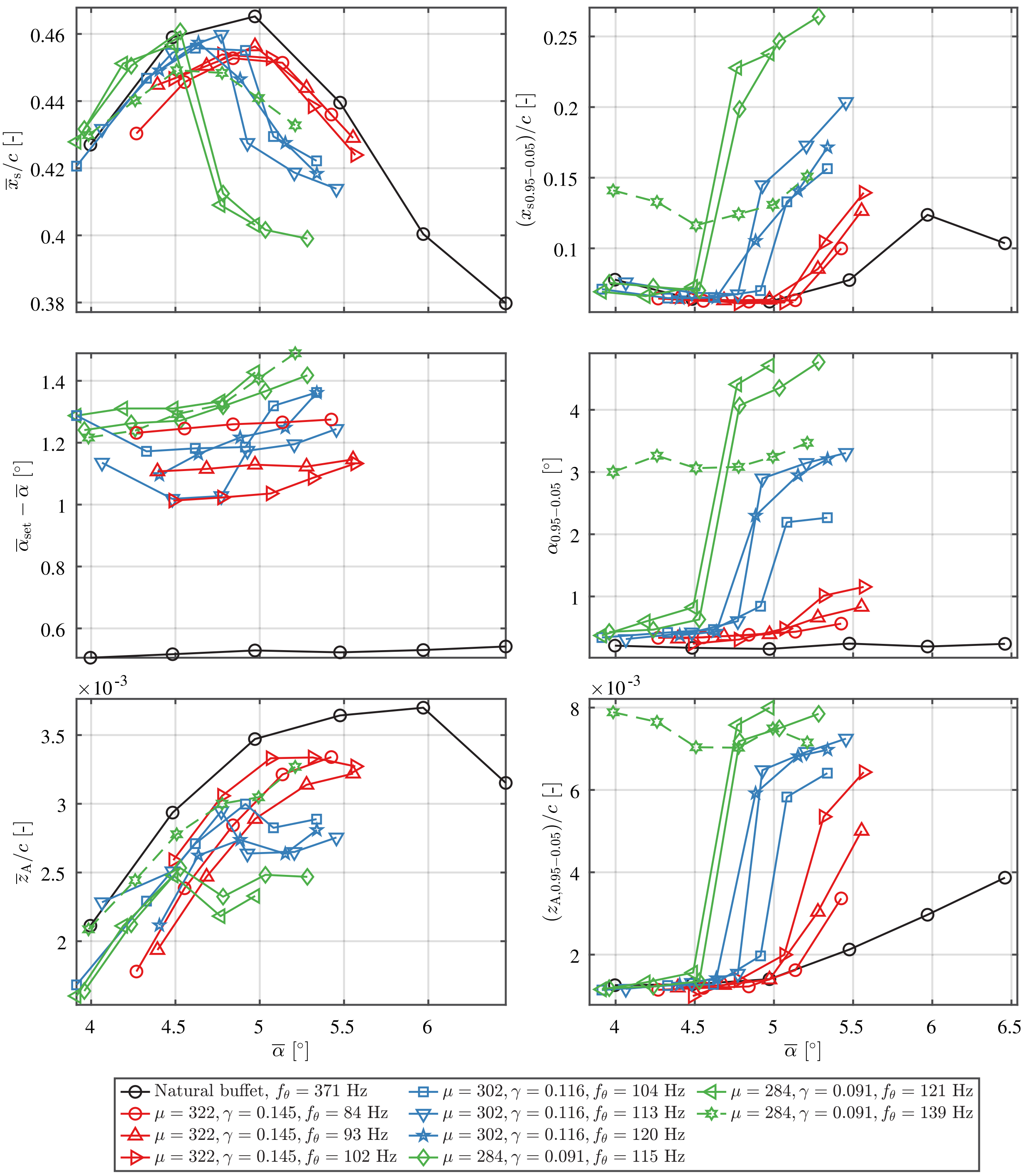

Fig. 7. Statistical values for shock position (top row), AoA (center row), and heave position (bottom row). Left column: mean values over AoA, right column: amplitudes represented by the 5–95 percentile range. Line colors and symbols represent variations of natural pitch frequency f_θ, mass ratio μ (and inertia factor γ).

most probably caused by the partially strong BL separation during the upstream excursion of the shock. Given the lower onset AoA, low values of mass ratio stagnate on lower heave levels than those of higher mass ratio.

Regarding the amplitudes of shock, pitch, and heave motion (right column), the following points can be derived: An increase in natural pitch frequency f_θ and a reduction in inertia factor or mass ratio independently lead to a reduction of the buffet onset boundary towards lower AoA. All amplitudes increase significantly with a reduction of the mass ratio (inertia factor), which is contradictory to the findings of Giannelis et al. (2016). An increase in f_θ has a small but rising effect on the shock amplitude, whereas the structural amplitudes, in particular the pitch amplitude, are more strongly affected. For high AoA a maximum level of pitch and heave amplitude seems to be approached, where the level is strongly

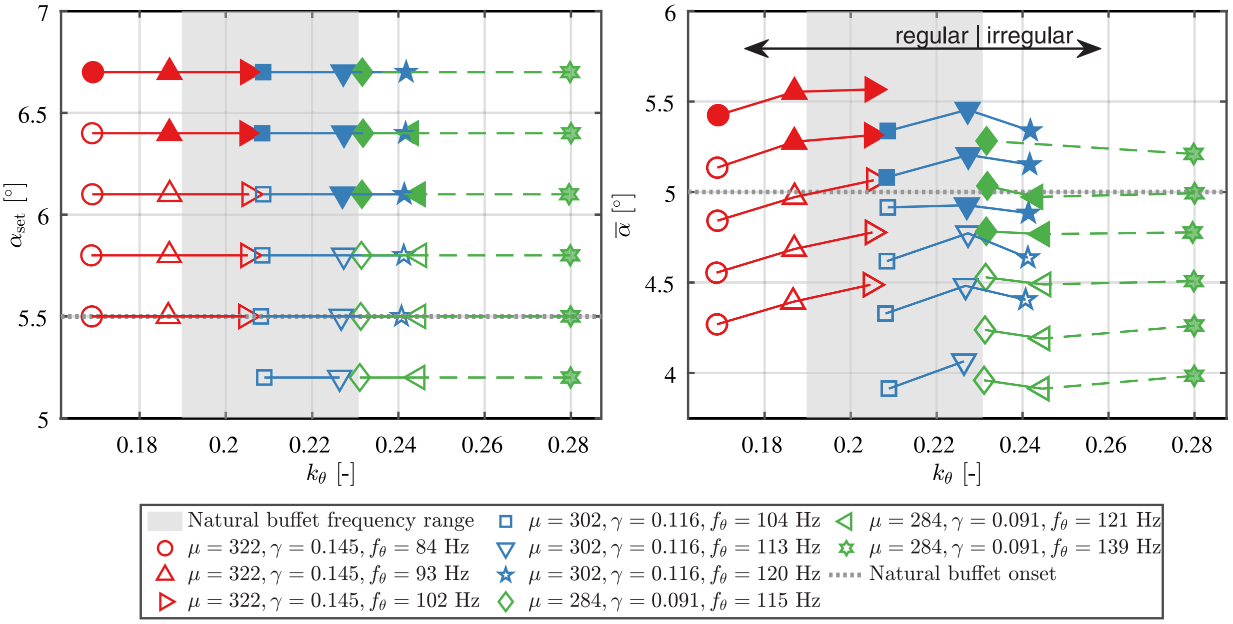

Fig. 8. Comparison of the relevance of α_{set} and α with respect to k_θ for static deformation and buffeting onset. Filled symbols represent cases of established buffeting.

dependent on both mass ratio and natural pitch frequency for the pitch, and mostly dependent on the mass ratio for the heave amplitude.

5.2.2. Onset and static deformation

In Fig. 8, all measurement points are displayed with respect to k_θ for α_{set} (left) and α (right). Points of established buffeting are marked by filled symbols. Lines connect measurement conditions of equal α_{set}. The left plot shows that the onset point does not depend on the mass ratio but only on the natural pitch frequency when considering the set AoA. Points of equal k_θ but different μ show onset at the same α_{set}. In comparison to the gray-dotted line of natural buffet onset, the onset points are located at higher α_{set} as the higher static deformation of the flexible cases is not represented in this plot. Under consideration of the actual measured AoA (right plot), the mass ratio plays a role for the onset. One can notice the partially inhibiting (for high μ) and facilitating (for low μ) effect on the onset. This adds up to the onset-varying effect of the natural pitch frequency, shown in Korthäuer et al. (2023). Points of equal k_θ can show established buffeting when the mass ratio is sufficiently low (compare $f_\theta = 102$ Hz and 104 Hz). This effect is based on the additional static deformation at lower mass ratios, which has yet to be explained.

As mentioned in Section 5.2.1, another irregularity can be observed when moving into the FSI region at natural pitch frequencies higher than the natural buffet frequency: Where an increase in k_θ by increasing the actual structural stiffness (shortened spring lever arm) usually leads to a reduced static deformation, it now enhances the static deformation leading to lower measured AoA. A possible reason for this might be the presence of a separation bubble leading to increased curvature and higher lift in the aft section of the airfoil, which in turn results in an increased aerodynamic moment. Additionally, dynamic effects and the interaction with the shock might play a role. Additional boundary-layer-resolving measurements, e.g. by the use of particle image velocimetry as in Scharnowski et al. (2022), could bring forth insights on this aspect.

5.2.3. Established FSI

Natural pitch frequency. As to supplement the previous findings, for Figs. 9 and 10 a number of cases of well-established FSI were selected, namely those of high α_{set}, in order to illustrate the effects of mass ratio and natural pitch frequency on the motion of wing and the whole shock front throughout one cycle. As a variation of the moment of inertia always induced a change in the natural pitch frequency, the setup with its limited mounting space only allowed a few combinations where the effect of the two structural parameters could be investigated separately. Fig. 9, left, presents the phase-locked location of wing and shock front for three natural pitch frequencies, namely $f_\theta = 84$ Hz, 104 Hz and 120 Hz and $\alpha_{\text{set}} = 6.7°$. The highest frequency was only reached by lowering the moment of inertia (and consequently the mass ratio). On the right, the corresponding bi-variate histograms are shown for the shock and heave position with respect to the measured AoA, respectively. The color code represents the number of samples throughout one wind tunnel run. The case of lowest $f_\theta = 84$ Hz exhibits a small pitch motion, while the shock front travels a substantial distance of approx. 10% of chord. The shape of the shock front shows a slight curvature but no evidence of phase-related distinctions. For the highest α at $\varphi_\alpha = \pi/2$, the shock front is found at the most downstream position, and for the lowest α at $\varphi_\alpha = 3\pi/2$, the shock is

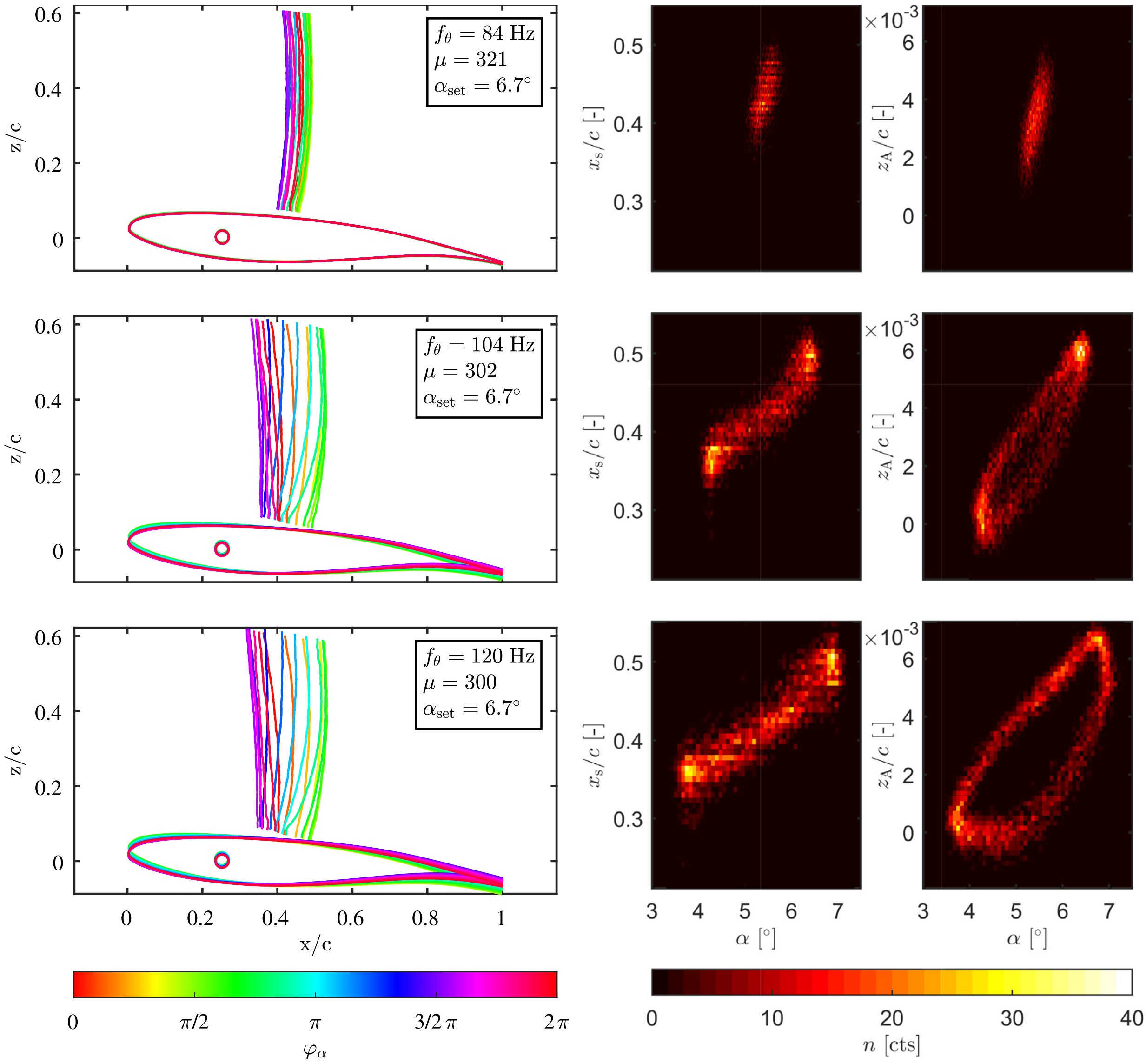

Fig. 9. Left: Phase-locked locations of the shock front and the wing based on the color-coded phase of the sinusoidal pitch motion for different natural pitch frequencies. Right: Corresponding bi-variate histograms of shock location at 10% of height and heave position with respect to the pitch angle, respectively. The color code indicates the number of samples found at the specific positions. (For interpretation of the references to color in this figure legend, the reader is referred to the web version of this article.)

found most upstream. Similar observations can be made for the heave position. Shock, heave, and pitch motion appear to have a negligible phase shift. With increasing f_θ to 104 Hz, the shock oscillation exhibits high amplitudes, which show an extended excursion in both down- and upstream directions. A further increase to $f_\theta = 120$ Hz mainly affects the upstream excursion, where the shock can occasionally be found even at $x_s/c = 0.3$. As the mass ratio could be maintained between $f_\theta = 104$ Hz and 120 Hz the latter trend can be attributed to the increase in natural pitch frequency solely. If at all, the phase relation of the shock front at 10% of height and pitch only shows a minor delay of the shock front compared to pitch, when inspecting the histogram. This can be traced back to the stronger upstream-directed shock curvature close to the wing surface at higher f_θ. Regarding the shock front above that lower region of strong curvature (e.g. at $z/c = 0.3$), an increased phase lag of the shock can be detected. The heave amplitude rises quickly on a high level, where it remains also for a stronger increase in f_θ. The phase relation, however, presents a lag between z_A and α of approx. $1/4\pi$ for higher f_θ, Regarding this aspect, it can be concluded that the region of FLI may lead to a phase delay of the shock front and heave relative to the pitch motion.

Mass ratio. In order to investigate the effect of the mass ratio (or inertia factor), additional cases are compared, namely those of equal f_θ with varying mass ratio μ. Fig. 10 displays the approximately equal cases of $f_\theta = 102$ Hz and 104 Hz with varying $\mu = 322$ and 302 in the upper two rows. Despite the rather low difference in mass ratio compared to Giannelis et al. (2016), the reduction of the mass ratio leads to an obvious increase in shock and pitch amplitude, whereas the heave amplitude remains similar, as can be seen from the histogram on the right side of the figure. The shock extends

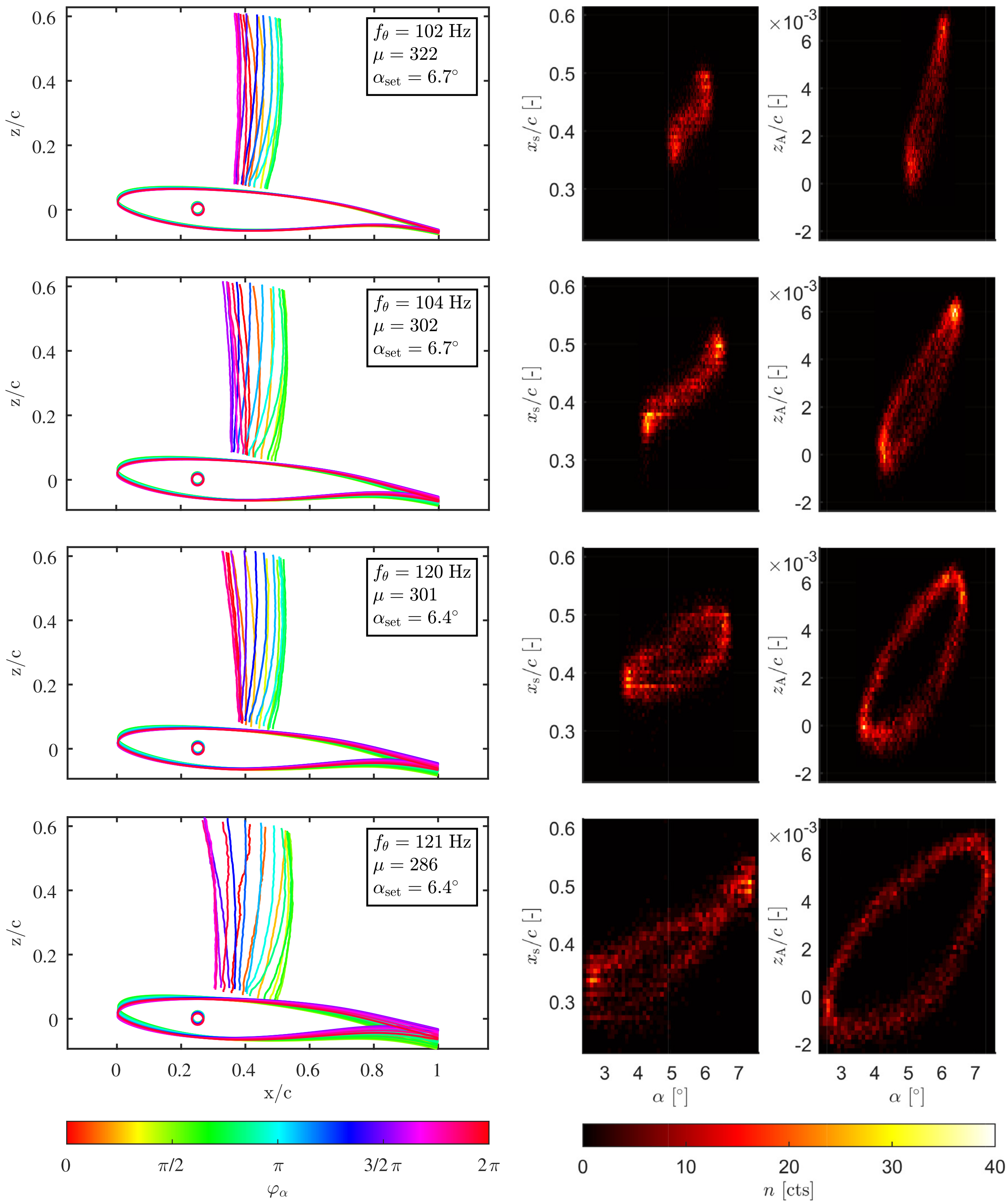

Fig. 10. Left: Phase-locked locations of the shock front and the wing based on the color-coded phase of the sinusoidal pitch motion for different mass ratios. Right: Corresponding bi-variate histograms of shock location at 10% of height and heave position with respect to the pitch angle, respectively. The color code indicates the number of samples found at the specific positions. (For interpretation of the references to color in this figure legend, the reader is referred to the web version of this article.)

both its extreme positions for $f_\theta \approx 103$ Hz. Both cases present an "S-shape" distribution in the histogram indicating an inequality in turnaround time between shock and pitch. This may be caused by the higher reactivity potential of the flow compared to "slow" structural reactivity given its inertia. Furthermore, a slight variation in the phase relation can be detected, again, only for the upper part of the shock front. The higher mass ratio leads to a small delay of the shock motion, whereas the lower mass ratio presents a mostly phase-equal shock-pitch motion. The shock appears in a neutral

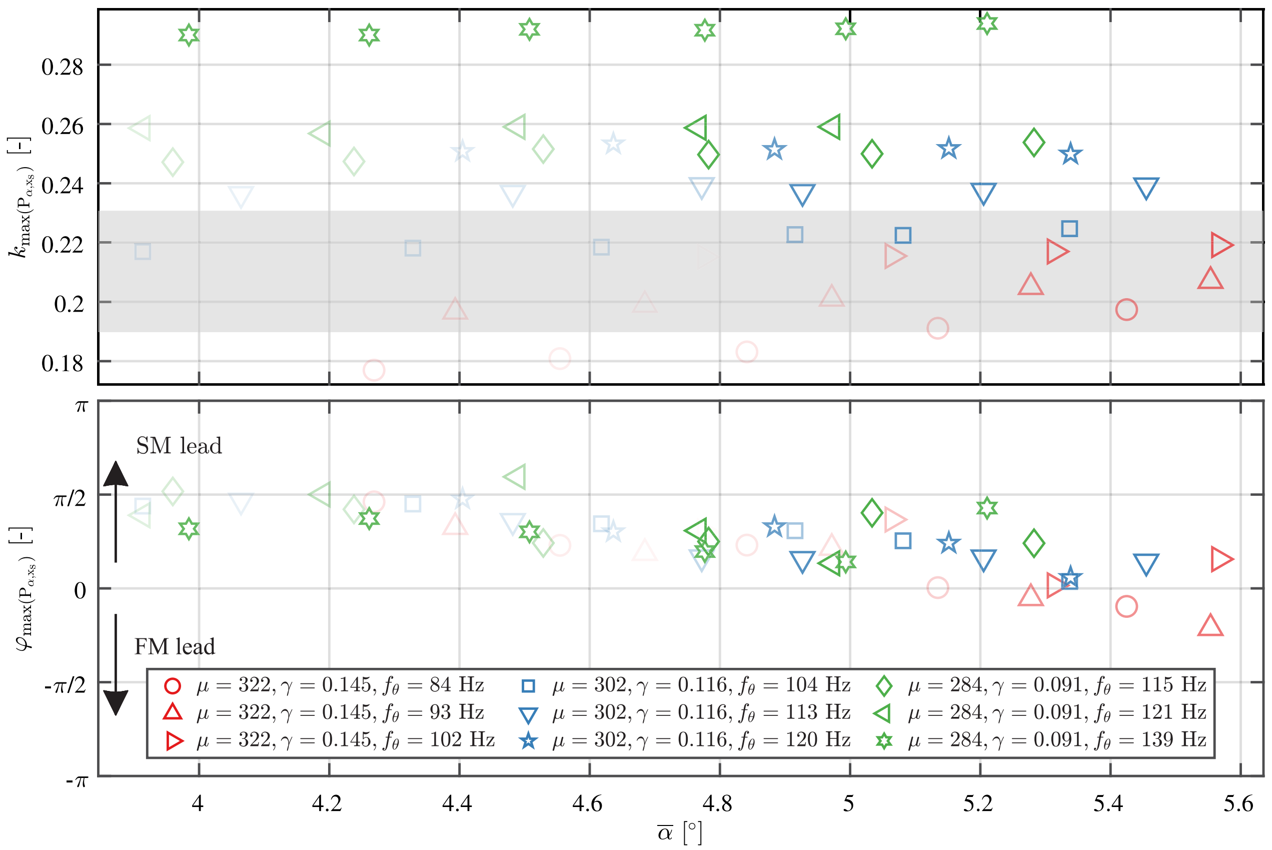

Fig. 11. Most dominant frequencies (top) and corresponding phase relation (bottom) from cross-correlation of α and x_s (height of 10%) for increasing AOA. Colors represent different mass ratios, symbols identify varying natural pitch frequencies. Transparency qualitatively stands for the normalized peak height in the spectrum. The gray range marks the natural buffet frequency range. (For interpretation of the references to color in this figure legend, the reader is referred to the web version of this article.)

pitch position centered about its own motion range (red and cyan). A reason for this could be the localization in the veering (transition) region, where lock-in might not yet be fully established and no prominent phase lead is present.

The lower two rows allow for a similar comparison at higher values of $f_\theta \approx 120\,\mathrm{Hz}$, where all amplitudes are found to be on a higher level. In particular, the upstream excursion of the shock wave increases significantly with lower μ. Both cases present a phase lead of the pitch motion compared to shock and heave motion. The bivariate histogram exhibits an intersection of the higher shock and pitch amplitude, indicating an uneven shock or pitch speed.

5.2.4. Coupled frequency, phase, and pitch amplitude

In order to investigate the phase relation of the coupled shock-pitch motion in more detail, a cross-power spectral density analysis based on Welch (1967) was applied. Fig. 11 shows the most dominant frequencies (top) and the corresponding phase relation (bottom) between α and x_s at a height of 10% above the surface for increasing AOA, derived from the cross-power-spectral-density analysis. Colors represent different mass ratios, symbols identify varying natural pitch frequencies and transparency represents the normalized peak height in the spectrum. The gray range marks the natural buffet frequency range. As one can see in the top plot, the rising effect of the AoA on the coupled frequency diminishes with increasing f_θ. For the red cases of $f_\theta = 84\,\mathrm{Hz}$, a strong dependency can be found ($\partial k/\partial\alpha \approx 0.017$ [1/°]), whereas starting from $f_\theta = 113\,\mathrm{Hz}$, hardly any effect of the AoA can be detected ($\partial k/\partial\alpha \approx 0.002$ [1/°]). This confirms the findings of Gao et al. (2017) and Giannelis et al. (2016) as the lower frequencies show a behavior dominated by the FM, whose dominant frequency depends on α. The FM is present and dominant in the flow far before buffet onset as shown by the transparent symbols, and can be detected in the minor coupled oscillation of the wing and the supposedly steady shock. That confirms the presence of a global flow instability as predicted by Crouch et al. (2009). For higher f_θ the SM, being independent of the AoA, becomes the dominant coupling partner. Also here, the oscillation can be detected before onset. The lower plot strengthens the theory as the corresponding phase relation between pitch and shock motion also depends on f_θ. The FM-dominated cases present a tendency of phase lead of the shock (like in the work of Tijdeman (1977) and Nitzsche (2009)), whereas SM-dominated measurement points exhibit the trend of a leading pitch motion. Given the temporal variation and the curved character of the shock front, the height of evaluation as well as the measurement technique itself may have a substantial influence on the absolute phase values. Nevertheless, the authors deem the trend

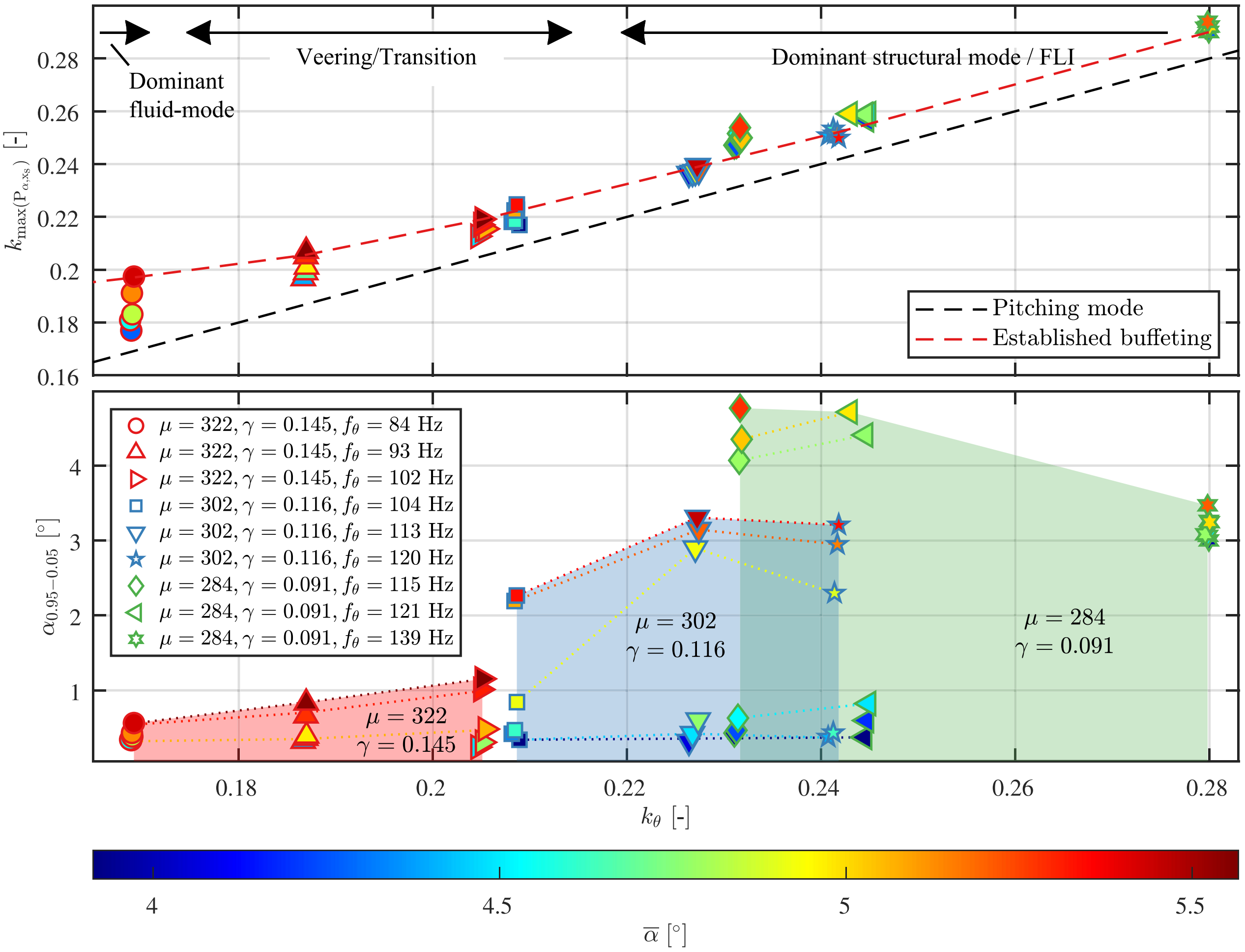

Fig. 12. Reduced peak frequencies of coupled shock and pitch motion (top) and the corresponding pitch amplitude (bottom) over the structural pitch frequency. The black dashed line represents the SM, and the red one indicates the trend of the coupled frequency for established buffeting cases. Symbol face colors represent the corresponding measured AoA, supported by the dotted lines. The edge color and symbol type are used for the identification of mass ratio and frequency, respectively. (For interpretation of the references to color in this figure legend, the reader is referred to the web version of this article.)

to be valid for the confirmation of numerical findings. Future investigations with methodological variations regarding the determination of phase relations will allow a more detailed, quantitative evaluation.

In Fig. 12, the resulting coupled reduced frequency (top) and the corresponding pitch amplitude (bottom) are presented over the natural pitch frequency. The symbol edge color represents the corresponding mass ratio, whereas the face color indicates the mean measured AoA. The black dashed line represents the natural pitch frequency, and the gray and colored dashed lines indicate the trends for established FSI cases.

In the top plot, starting from $k_\theta \approx 0.21$ a linear increase of the coupled frequency can be observed, whereby the SM is approached. A good agreement with Giannelis et al. (2016) and Gao et al. (2017) is shown, regarding the range of dominant SM and FLI. As all points almost collapse in that region, it has to be noted that even at low AoA, before buffeting onset, the structural lock-in frequency is dominant. The corresponding amplitudes (bottom plot) may even be low, which contradicts the finding of Raveh and Dowell (2011) regarding a necessary threshold amplitude for lock-in under forced excitation. Apparently, the shock already synchronizes with the minor, flow-excited structural motion before the onset point (see also frequency spectrum in Fig. 5, top right). The small offset of the linear trend (gray) compared to the SM accounted for the effect of the minor heave contribution in the interaction, lifting the coupled frequency to a slightly higher level. Furthermore, in Gao et al. (2017) a similar offset was reported for a coupled numerical simulation of computational fluid-structural dynamics (CFD/CSD).

For lower values of k_θ, the measurement points at different AoA do not collapse anymore. The coupled frequency progressively deviates with increasing AOA from the SM-line and approaches the range of the natural buffet frequency around $k \approx 0.2$. The coupled frequencies of $f_\theta = 84$ Hz present a clear influence of the FM as the coupled frequency rises with an increase in the AoA (as already shown in Fig. 11). For the highest $\mu = 322$ low pitch amplitudes are visible. With increasing k_θ, divergence can be recognized, separated by the effect of buffeting onset. Blue symbols with lower AoA remain at low amplitudes, whereas higher AoA present high pitch amplitudes. A further increase of k_θ intensifies this divergence, where a sudden strong rise of the pitch amplitude can be detected for each structural setting. This strong increase of the pitch amplitude with higher k_θ is the most significant indicator of the FLI region. The measurement points of $\mu = 302$ show a maximum pitch amplitude of $\alpha_{0.95-0.05}$ at $k_\theta \approx 0.23$, whereas cases of $\mu = 284$ present a significantly higher pitch amplitude at similar k_θ. Consequently, the mass ratio appears to have a significant effect on the pitch amplitude, which contradicts the numerical work of Giannelis et al. (2016), where only minor differences in the pitch amplitude in the FLI zone were detected, despite comparatively very high variations of mass ratio ($\mu = 50$ to 200).

6. Summary and conclusions

Transonic buffeting experiments were conducted on a quasi-two-dimensional wing with a supercritical airfoil (OAT15A) in the Trisonic Wind Tunnel Munich. The setup offered the option of an operation with or without a variable, elastically-suspended pitching degree of freedom. In the flexible setup configuration and for a Mach number of 0.74, the variation of the AoA, the natural pitch frequency, and the mass ratio (by adjusting the inertia factor) allowed for the investigation of the effects of structural settings on the FSI in pre-buffet and developed conditions.

The optical measurement techniques BOS and DIC were deployed for the time-resolved, non-intrusive observation of the shock and wing oscillations. The observed FSI were characterized by statistical, spectral, and phase analysis of pitch, heave, and shock motion of the wing. To the authors' best knowledge, this is the first experimental confirmation of the numerically-based findings regarding the manifestation and development of transonic frequency lock-in on a supercritical wing for $k_\theta > k_b$. The coupled frequency of shock and pitch motion followed the natural pitch frequency k_θ rather than the natural buffet frequency k_b. The coupled frequency was found to be dominant already at low AoA, i.e. lock-in exists even before buffeting onset, being present as a damped mode before bifurcation. For $k_\theta < k_b$ a coupled motion, dominated by the fluid mode (natural buffet), was observed. The region of modal veering (Gao et al., 2017) was identified, being characterized by the smooth transition from FM-dominated to SM-dominated (FLI) coupling.

It was found that the natural pitch frequency k_θ is the main determinator of the limits of FLI as predicted by numerical simulations of Giannelis et al. (2016) and Gao et al. (2017). The abrupt switch back to FM-dominated coupling for high k_θ could not be observed in the investigated parametric space due to spatial confinements of the configuration and facility. Depending on the dominant coupling partner, a shifting trend from a shock-led phase (FM-dominance) to a pitching-led coupled motion (SM-dominance) was confirmed. Maxima in the pitch amplitudes were detected for established buffeting at ratios of $k_\theta \approx 0.24$.

The mass ratio played a more dominant role in the interaction than expected. In the FLI region, the amplitude of the pitch motion was strongly affected by the mass ratio, which contradicts numerical findings (Giannelis et al., 2016). The static deformation, being the result of the mean effective aerodynamic moment, appeared to be increased by lower mass ratios at the same natural pitch frequency. This introduced, in addition to the already favoring effect of higher k_θ, additional prematurity of the buffeting onset under consideration of the actual mean AoA of the wing. Furthermore, an increase in the pitching stiffness throughout the region of FLI introduced an irregular, higher static deformation, which was unexpected by the authors. Dynamic effects or the substantially-separated boundary layer are deemed to cause these observations, but a detailed explanation remains to be found in future research.

Open questions may be addressed in future measurement campaigns by a more extensive parametric space. Minor adaptations in the setup should allow for lower and higher values of the natural pitch frequency k_θ in order to address the limits of the FLI region. A more isolated variation of μ and γ might also be of interest for a clear separation of the coinciding effects. As Giannelis et al. (2016) has shown, structural damping plays a significant role in the severity of the phenomenon and could be another interesting parameter for future investigations. More detailed examinations of the flow field and the interaction of shock, structure, and separated boundary layer for both cases of natural buffet and buffeting may shed some more light on the physical mechanisms of transonic buffet.

CRediT authorship contribution statement

Tim Korthäuer: Writing – original draft, Visualization, Software, Data curation, Formal analysis, Conceptualization, Methodology. **Alessandro Accorinti:** Writing – review & editing, Conceptualization, Methodology, Software. **Sven Scharnowski:** Supervision, Writing – review & editing, Conceptualization, Methodology. **Christian J. Kähler:** Writing – review & editing, Conceptualization, Funding acquisition.

Declaration of competing interest

Data availability

Data will be made available on request.

Acknowledgments

Financial support in the frame of the project HOMER (Holistic Optical Metrology for Aero-Elastic Research) from the European Union's Horizon 2020 research and innovation program under grant agreement No. 769237 is gratefully acknowledged. The authors like to thank Jens Nitzsche, Yves Govers, Johannes Dillinger, Johannes Knebusch, and Tobias Meier for their contributions to the model design and for fruitful discussions during the project. We acknowledge financial support by Universität der Bundeswehr München.

References

Accorinti, A., Baur, T., Scharnowski, S., Kähler, C.J., 2022. Experimental investigation of transonic shock buffet on an OAT15A profile. AIAA J. 1–12. http://dx.doi.org/10.2514/1.j061135.

Accorinti, A., Korthäuer, T., Scharnowski, S., Kähler, C.J., 2023. Characterization of transonic shock oscillations over the span of an OAT15A profile. Exp. Fluids 64 (61), http://dx.doi.org/10.1007/s00348-023-03604-z.

Chu, T., Ranson, W., Sutton, M.A., 1985. Applications of digital-image-correlation techniques to experimental mechanics. Exp. Mech. 25 (3), 232–244. http://dx.doi.org/10.1007/BF02325092.

Crouch, J., Garbaruk, A., Magidov, D., Travin, A., 2009. Origin of transonic buffet on aerofoils. J. Fluid Mech. 628, 357–369. http://dx.doi.org/10.1017/S0022112009006673.

Davis, S.S., Malcolm, G.N., 1980. Transonic shock-wave/boundary-layer interactions on an oscillating airfoil. AIAA J. 18 (11), 1306–1312. http://dx.doi.org/10.2514/3.50886.

Dietz, G., Schewe, G., Mai, H., 2006. Amplification and amplitude limitation of heave/pitch limit-cycle oscillations close to the transonic dip. J. Fluids Struct. 22 (4), 505–527. http://dx.doi.org/10.1016/j.jfluidstructs.2006.01.004.

Dowell, E., Edwards, J., Strganac, T., 2003. Nonlinear aeroelasticity. J. Aircr. 40 (5), 857–874. http://dx.doi.org/10.2514/2.6876.

Gao, C., Zhang, W., Li, X., Liu, Y., Quan, J., Ye, Z., Jiang, Y., 2017. Mechanism of frequency lock-in in transonic buffeting flow. J. Fluid Mech. 818, 528–561. http://dx.doi.org/10.1017/jfm.2017.120.

Gao, C., Zhang, W., Ye, Z., 2018. Reduction of transonic buffet onset for a wing with activated elasticity. Aerosp. Sci. Technol. 77, 670–676. http://dx.doi.org/10.1016/j.ast.2018.03.047.

Giannelis, N.F., Vio, G.A., Dimitriadis, G., 2016. Dynamic interactions of a supercritical aerofoil in the presence of transonic shock buffet. In: Proceedings of the 27th International Conference on Noise and Vibration Engineering, Leuven, Belgium. KU Leuven - Departement Werktuigkunde, Heverlee (Belgium), pp. 457–470.

Giannelis, N.F., Vio, G.A., Levinski, O., 2017. A review of recent developments in the understanding of transonic shock buffet. Prog. Aerosp. Sci. 92, 39–84. http://dx.doi.org/10.1016/j.paerosci.2017.05.004.

Hartmann, A., Feldhusen, A., Schröder, W., 2013. On the interaction of shock waves and sound waves in transonic buffet flow. Phys. Fluids 25 (2), 026101. http://dx.doi.org/10.1063/1.4791603.

Iovnovich, M., Raveh, D.E., 2015. Numerical study of shock buffet on three-dimensional wings. AIAA J. 53 (2), 449–463. http://dx.doi.org/10.2514/1.J053201, arXiv:https://doi.org/10.2514/1.J053201.

Jacquin, L., Molton, P., Deck, S., Maury, B., Soulevant, D., 2005. An experimental study of shock oscillation over a transonic supercritical profile. In: 35th AIAA Fluid Dynamics Conference and Exhibit. American Institute of Aeronautics and Astronautics, http://dx.doi.org/10.2514/6.2005-4902.

Korthäuer, T., Accorinti, A., Scharnowski, S., Kähler, C.J., 2023. Effect of mach number and pitching eigenfrequency on transonic buffet onset. AIAA J. 61 (1), 112–124. http://dx.doi.org/10.2514/1.j061915.

Nitzsche, J., 2009. A numerical study on aerodynamic resonance in transonic separated flow. In: IFASD – International Forum on Aeroelasticity and Structural Dynamics. Seattle, WA, USA, URL https://elib.dlr.de/61964/.

Nitzsche, J., Otte, J., Kaiser, C., Hennings, H., 2022. The effect of shock control bumps on the the transonic flutter and buffeting characteristics of a typical wing section. In: IFASD – International Forum on Aeroelasticity and Structural Dynamics. Madrid, Spain, URL https://elib.dlr.de/188433/1/IFASD_2022_149.pdf.

Raffel, M., 2015. Background-oriented schlieren (BOS) techniques. Exp. Fluids 56 (3), http://dx.doi.org/10.1007/s00348-015-1927-5.

Raveh, D.E., 2009. Numerical study of an oscillating airfoil in transonic buffeting flows. AIAA J. 47 (3), 505–515. http://dx.doi.org/10.2514/1.35237.

Raveh, D., Dowell, E., 2011. Frequency lock-in phenomenon for oscillating airfoils in buffeting flows. J. Fluids Struct. 27 (1), 89–104. http://dx.doi.org/10.1016/j.jfluidstructs.2010.10.001.

Scharnowski, S., Bross, M., Kähler, C.J., 2018. Accurate turbulence level estimations using PIV/PTV. Exp. Fluids 60 (1), http://dx.doi.org/10.1007/s00348-018-2646-5.

Scharnowski, S., Kokmanian, K., Schäfer, C., Baur, T., Accorinti, A., Kähler, C.J., 2022. Shock-buffet analysis on a supercritical airfoil with a pitching degree of freedom. Exp. Fluids 63 (6), http://dx.doi.org/10.1007/s00348-022-03427-4.

Scheitle, H., Wagner, S., 1991. Influences of wind tunnel parameters on airfoil characteristics at high subsonic speeds. Exp. Fluids 12–12 (1–2), 90–96. http://dx.doi.org/10.1007/bf00226571.

Schewe, G., Mai, H., Dietz, G., 2003. Nonlinear effects in transonic flutter with emphasis on manifestations of limit cycle oscillations. J. Fluids Struct. 18 (1), 3–22. http://dx.doi.org/10.1016/S0889-9746(03)00085-9.

Tijdeman, H., 1977. Investigations of the Transonic Flow Around Oscillating Airfoils. NLR-TR 77090 U, Nationaal Lucht-en Ruimtevaartlaboratorium.

Welch, P., 1967. The use of fast Fourier transform for the estimation of power spectra: A method based on time averaging over short, modified periodograms. IEEE Trans. Audio Electroacoust. 15 (2), 70–73. http://dx.doi.org/10.1109/TAU.1967.1161901.

5

Summary and Outlook

5.1. Summary of Research Results

In the frame of this doctoral thesis, transonic buffeting experiments were conducted in the Trisonic Wind Tunnel Munich on a two-dimensional wing with supercritical airfoil (OAT15A). The aim was a systematic experimental characterization of transonic buffet(ing) and the effects of aerodynamic and structural parameters. The following three research objectives were defined and adressed by individual measurement campaigns and published in the corresponding scientific publications:

1. The experimental determination of the facility-specific buffet boundaries and shock motion characteristics (Accorinti et al., 2022).
2. The experimental determination of the onset boundaries of a wing with elastically-suspended pitching DoF in dependence of the natural pitch frequency (Korthäuer et al., 2023a).
3. The experimental verification of the regions of transonic FLI, the fluid-dominated structural excitation, and the intermediate veering region on a wing with elastically-suspended pitching DoF (Korthäuer et al., 2023b).

A wind-tunnel test stand was designed, manufactured and set up, as specified in the steps 1a and 2a (see Section 2.3). The test stand provided the options of an operation with or without an elastically-suspended pitching DoF. In flexible mode, the natural pitch frequency and mass ratio were adjustable. Although undesired, a minor heave DoF remained, for which the natural frequency was higher than the investigated natural pitch frequencies but not high enough to be negligible. The light-weight wing and structural setup was designed to allow a low but variable mass ratio, while maintaining the center of gravity in the rotational axis.

Besides complementary measurements by force balances, accelerometers and laser vibrometers, the focus was set on the deployment of two optical measurement techniques, BOS and DIC, in order to accurately track fluid and structural behavior during the experiments. Both techniques proofed to be reliably providing the required information about the shock location as well as the wing motion and deformation (defined as steps 1b and 2b in Section 2.3). The wing rigidity was assessed by the structural deformations of the wing without applied pitching flexibility. The wing itself presented high stiffness, whereas the shaft outside the wing structure was twisted and bent. This led to a reduced AoA and a slightly curved wing surface, although the low level of curvature was not deemed to introduce major three-dimensional flow characteristics.

The respective results for each research objective are summarized briefly and put into the context of the frame of this thesis:

⇒ **Research objective 1:**
The systematic analysis of transonic buffet on the pitch-inhibited wing outlined in Accorinti et al. (2022) provided a thorough overview about the phenomenon in the specific experimental facility, the Trisonic Wind tunnel Munich. The resulting data served as an essential reference for the subsequent experimental campaigns with released pitching flexibility. The influence of AoA and Mach number on the onset as well as the flow development, shock features and the dominant buffet frequency was examined.
At various Mach numbers, the AoA was continuously increased to determine the onset boundary. It presented a mostly linear behavior with the Mach number in the observed range of Mach numbers and AoA. With respect to literature, buffet onset and its development occurred at considerably higher AoA. A comparison among reference results revealed a general sensitivity of buffet to both numerical, and experimental boundary conditions. For this reason, the influences of gap flow between model and side windows as well as the boundary layer suction on the side walls were investigated but not found to be the major driver of the delayed onset. Another influencing factor may be the altered pressure distribution due to the interaction of the transonic flow with the wall boundary layer suction. A conclusive explanation remains to be determined in future investigations.
The frequency in established buffet conditions was found to linearly depend on the AoA, where the slope decreased with increasing Mach number. Fully developed buffet flows were only detected at mean shock positions aft the location of the maximum profile thickness. The shock inversion proved to be a necessary (but not sufficient) condition for buffet onset.

⇒ **Research objective 2:**
The introduction of the pitching DoF enlarged the parametric space considerably. Therefore, a first corresponding campaign was carried out, focusing on the onset variations induced by the structural flexibility (Korthäuer et al., 2023a). The AoA was continuously increased at various Mach numbers to track the development of shock and wing motion. The procedure was repeated for three settings of natural pitch frequency, namely below, approximately equal and above the natural buffet frequency.
After onset, a coupled oscillation of wing and shock with limited amplitudes was observed. The non-linear character of the flow was deemed responsible for the LCO. Window-wise frequency analysis provided low-quality but important information about the modal development and dominant frequencies in dependence of the AoA for different Mach numbers. After onset, shock, pitch, and heave presented a coupled motion. The Mach number appeared not to have a substantial effect on the obtained frequencies and amplitudes. The presence of the heave

motion was accounted to classical structural excitation as the natural heave frequency was located too close to the natural pitching frequency.
The comparison of the onset boundaries with and without pitching DoF revealed a persistent linear relation between Mach number and onset AoA, where the pitching flexibility reduces the slope of the boundary. Natural pitch frequencies above the natural buffet frequency shift the onset boundary substantially towards lower AoA and consequently to premature onset of the phenomenon. This finding emphasizes the necessity of a fully coupled analysis of the buffet(ing) characteristics early in the process of transonic aircraft design, as proposed by Nitzsche et al. (2019) and Gao and Zhang (2020).

⇒ **Research objective 3:**
A more detailed investigation of the actual nature of transonic buffeting was conducted in Korthäuer et al. (2023b). The focus was hereby set on the independent variation of structural parameters at a fixed Mach number of 0.74. For each structural combination, the AoA was incrementally increased from the pre-buffeting into the buffeting region. Measurements of higher duration at constant conditions provided spectral information of improved quality and allowed the additional investigation of phase relations, besides dominant frequencies and amplitudes of the interacting entities.
The results of Gao et al. (2018) regarding the onset variation by natural pitch frequency and mass ratio were confirmed. Both paremeters affect buffeting onset, where the former appeared with stronger influence than the latter, in the observed range of values. Substantial proof of transonic FLI was provided, as the coupled motion of wing and shock locked into the natural pitch frequency when the latter was set above the natural buffet frequency. If it was set below, the coupling was dominated by the fluid mode and followed the natural buffet frequency. In between the two, the veering region could be identified, where the coupled oscillation steadily begins to transition from fluid- to structurally-governed mode. The AoA affected the coupled frequency only in the fluid-dominated region. At low AoA the structural mode was dominant; an increase in AoA induced a shift towards the fluid mode up to the point of onset. In the FLI region, even low AoA presented damped coupled oscillations at the structural frequency, speaking for a weakly damped structural mode before bifurcation (in agreement with the modal development in Nitzsche et al. (2019)).
The natural pitch frequency was found to be the main determinator of the FLI range, which agrees well with literature. The upper limit, however, could not be reached due spatial limitations of the setup. Analysis of the phase relations between shock and pitch motion revealed the trend of a phase shift from leading shock to leading pitch motion during the increase of the natural pitch frequency. Throughout the veering region towards FLI, a substantial rise of the pitch amplitude was observed, as expected for FLI behavior. The highest pitch amplitudes were obtained at considerably higher natural pitch than the natural buffet frequency.
The variation of the mass ratio presented a rather unexpected effect in this regard. A minor reduction of this parameter significantly increased the pitch amplitude, which opposed the expectations from numerical results. However, the influence

of altered structural damping could not be precluded in this context and has to be subject of future clarification.

In conclusion, all of the obtained experimental campaigns provided substantial insight into the nature of transonic buffet and buffeting. Multiple numerical findings of the recent years could be confirmed and validation data for advanced numerical methods has been provided. The presented results emphasize the importance of FSI in presence of transonic buffet and support the demand of coupled fluid-structure simulations and/or early experiments in the aircraft design process, as proposed by Nitzsche et al. (2019) and Gao et al. (2018).

5.2. Future Research Prospects

The variable applicability of the designed test stand and the provision of a second wing with integrated pressure sensors allow for various prospective investigations to deepen the insight on transonic (aeroelastic) phenomena. Some ideas and open points for an enhancement and extension of the presented experiments will be given here.

- After having proved the safe operation of the setup, the PMMA windows could be replaced by high-quality glass windows to allow the use of conventional schlieren measurements. A further benefit could be gained by the application of focusing Schlieren, which reduces the distortion effects of the shock front by span-wise integration (Schauerte and Schreyer, 2023). At the same time, the setup remains less complex than comparable PIV measurements.
- Future sampling rates for the optical techniques, in particular BOS, should exceed 2.5 kHz for the given chord length. This should allow a precise observation and analysis of underlying mechanisms, such as upstream traveling waves/shocklets (D’Aguanno et al., 2021).
- As shown in Accorinti et al. (2023a), the side walls induce three-dimensional effects in the shock front in the pre-buffet regime. Therefore, a variation of aspect ratio is recommended in order to investigate the effects on the flow formation and onset characteristics.
- The setup could be adapted to extend the parametric space, in particular for the natural pitch frequency. Modifications of the lever arm and a redesign of the bearing mount (possibly without force balances) could increase the space and allow capturing of the whole FLI region.
- A higher range of values for the mass ratio could be obtained by two options. Firstly, the integration of trimming weight in the leading edge (see Fig. 3.6) could allow a more symmetric set of weights on the lever arms. By this, lighter and heavier combinations of weights could be utilized to enlarge the range, while keeping the center of gravity in the elasic axis. Furthermore, a variation of the total pressure of the facility could be used to vary the denominator of the mass ratio (see Eq. (2.7)). As Fig. 3.2 shows, up to more than threefold of the presented total pressure is feasible, at the cost of an alternating Reynolds

number. In particular in combination with higher aspect ratios (reduced chord length), a variation in total pressure may allow a constant Reynolds number. For all variations, it needs to be ensured to keep the mass ratio below the threshold to avoid classical bending-torsion flutter as shown in Nitzsche et al. (2022).

- The mass ratio and the moment of inertia are often coupled (as in the presented experiments). The rotational motion of an object, however, is typically determined by the moment of inertia (see Eq. (2.6)), rather than the total mass (considered in the mass ratio). Therefore, the hypothesis has to be advanced that the mass ratio only displays the actual effects of an altered moment of inertia (considered in the inertia factor). The presented setup actually allows a separate variation of the two parameters. By maintaining the same set of trimming weights on the side lever arms, a variation in their location changes the inertia factor but not the mass ratio. The insertion of the leading edge trimming weight should be supportive for this too.
- As shown by Giannelis et al. (2016), the structural damping has a substantial effect on the pitching amplitudes of transonic buffeting. It is therefore crucial for future works to implement a mechanism for damping control and to measure the obtained values.
- As shown by Nitzsche et al. (2022), also for natural pitch frequencies below the natural buffet frequency a structurally-dominated interaction can be obtained. For this, the Mach number needs to be sufficiently high. During a continuous rise of the AoA, first a bifurcation of the fluid mode should be observed, being followed by a stable region. Ultimately at higher AoA, the structural mode experiences bifurcation and dominates the interaction with a fluid mode. For an experimental proof of this, a more extensive variation of Mach numbers is essential.
- As Bendiksen (2011) has theoretically advanced, the phase relation between wing and shock front affects the damping. With increasing pitch frequency the lag increases, as does the negative damping. This results in rising amplitudes towards higher frequencies, as observed in the region of FLI. At some point, the structural frequency is too high (the pitch motion is too “fast”) to be followed by the shock front, whose adaptation still relies on the speed of sound to receive information. This leads to an increase in damping and ultimately a positive value, inhibiting the high amplitude oscillation. This point should coincide with the sudden termination of the FLI region. One way to prove this important role of the phase relation could be the application of forced excitation by a shaker unit and the consequent energy budget analsyis to ultimately determine the damping state.
- As a universal physical explanation of the buffet mechanism has yet to be found, the presented work may provide a solid basis for further in-depth investigation of the root cause of transonic buffet.
  - Focus on the point of onset
    The global location of the onset boundaries was thoroughly determined in the presented works both for natural buffet and for transonic buffeting. In a future campaign, the onset process could be investigated in detail. For this,

the AoA would continuously but slowly be increased just around the point of onset. A temporally highly-resolved observation by BOS or PIV during the onset process may then provide some insight in the buffet mechanism. The key question would be, which interaction partner starts the oscillation, is it the shock or the separated boundary layer (or the pitching airfoil in the case of pitching DoF)?

- Intermittent behavior in transonic buffeting
  The intermittent behavior presented in some of the runs of Korthäuer et al. (2023a) provides another point of vantage for deeper investigation. The intermittence might be caused by a mode being close to the bifurcation point of zero-damping. On the other hand, some additional influencing factor, such as additional non-linearity due to structural limitation, may intervene with the establishment of an LCO. Either way, focusing on these special cases may increase the knowledge about the phenomenon and its limitations.

- The propagation of pressure information
  Besides the widely accepted and multiply-advanced theory of Lee (2001) another hypothesis advanced in Raghunathan et al. (2008) and Accorinti et al. (2023b). It is based on the attempt of the shock to satisfy equality and compatibility conditions at the trailing edge. Due to the continuous change of the pressure field and the propagation lag due to the limitation by the speed of sound, this attempt fails and results in the unsteady response with an oscillating shock. It lies in the shock wave's nature to adapt its location and strength to the pressure conditions up- and downstream. The affection of its location by a breathing separation region or a moving wing is consequent. As Scharnowski et al. (2023) has proved, the phase relation between the shock front and the pitching motion is highly dependent of the considered height above the airfoil. Consequently, one can infer that the distance to some location of the airfoil plays a role in the interaction. This reinforces the above mentioned hypotheses. The ultimate answer could be provided by a pressure field reconstruction, possibly on the basis of highly resolved PIV data or unsteady PSP measurements. The time-averaged analysis of the propagation speeds (as determined in Scharnowski et al. (2022) and Kokmanian et al. (2022)), however, does not reveal the correlation of breathing boundary layer or moving wing as it varies throughout a buffet(ing) cycle. The integration of propagation speeds along individual propagation paths from boundary layer/airfoil to the shock could provide the required temporal information that ultimately determines the buffet(ing) frequency.
  Assuming the underlying mechanisms are preserved under the effects of a pitching DoF, the availability of multiple oscillations frequencies by inhibiting or varying the pitching flexibility provides various test points for validation of the hypothesis.

References

Accorinti, A., Baur, T., Scharnowski, S., and Kähler, C. J. (2022). "Experimental Investigation of Transonic Shock Buffet on an OAT15A Profile". In: AIAA Journal, pp. 1–12. DOI: 10.2514/1.j061135.

Accorinti, A., Korthäuer, T., Scharnowski, S., and Kähler, C. J. (2023a). "Characterization of transonic shock oscillations over the span of an OAT15A profile". In: Experiments in Fluids 64.3, p. 61. DOI: 10.1007/s00348-023-03604-z.

Accorinti, A., Korthäuer, T., Scharnowski, S., and Kähler, C. (2023b). "Analysis of the flow development towards shock buffet on an OAT15A profile". In: AIAA SCITECH 2023 Forum. American Institute of Aeronautics and Astronautics (AIAA). DOI: 10.2514/6.2023-0244.

Anderson, J. D. (2011). Fundamentals of Aerodynamics. 6th. McGraw Hill Education. ISBN: 978-1-259-12991-9.

Babinsky, H. and Harvey, J. K., eds. (2011). Shock Wave-Boundary-Layer Interactions. Cambridge Aerospace Series. Cambridge University Press. DOI: 10.1017/cbo9780511842757.

Badcock, K. J., Timme, S., Marques, S., Khodaparast, H., Prandina, M., Mottershead, J. E., Swift, A., Ronch, A. D., and Woodgate, M. A. (2011). "Transonic aeroelastic simulation for instability searches and uncertainty analysis". In: Progress in Aerospace Sciences 47.5, pp. 392–423. DOI: 10.1016/j.paerosci.2011.05.002.

Bendiksen, O. O. (2011). "Review of unsteady transonic aerodynamics: Theory and applications". In: Progress in Aerospace Sciences 47.2, pp. 135–167. ISSN: 0376-0421. DOI: 10.1016/j.paerosci.2010.07.001.

Braune, M. and Hebler, A. (2019). "Mechanisms of transonic single degree of freedom flutter of a laminar airfoil". In: International Forum on Aeroelasticity and Structural Dynamics 2019, IFASD 2019. URL: https://elib.dlr.de/128034/1/IFASD-2019-132.pdf.

Bungartz, H. and Schäfer, M. (2006). Fluid-Structure Interaction: Modelling, Simulation, Optimisation. Lecture Notes in Computational Science and Engineering. Springer Berlin Heidelberg. ISBN: 9783540345954. URL: https://books.google.de/books?id=6OaMOqfPOfEC.

Collar, A. (1978). "The first fifty years of aeroelasticity". In: Aerospace 5.2, pp. 12–20.

Crouch, J., Garbaruk, A., Magidov, D., and Travin, A. (2009). "Origin of transonic buffet on aerofoils". In: Journal of Fluid Mechanics 628, pp. 357 –369. DOI: 10.1017/S0022112009006673.

Crouch, J. D., Garbaruk, A., and Strelets, M. (2019). "Global instability in the onset of transonic-wing buffet". In: Journal of Fluid Mechanics 881, pp. 3–22. DOI: 10.1017/jfm.2019.748.

Crouch, J., Garbaruk, A., and Magidov, D. (2007). "Predicting the onset of flow unsteadiness based on global instability". In: Journal of Computational Physics 224.2, pp. 924–940. DOI: 10.1016/j.jcp.2006.10.035.

D'Aguanno, A, Schrijer, F., and Oudheusden, B. van (2021). "Spanwise organization of upstream traveling waves in transonic buffet". In: Physics of Fluids 33.10, p. 106105.

D'Aguanno, A. (2023). "Physics and Control of Transonic Buffet". In: DOI: 10.4233/UUID:7E4F868B-7716-4C36-8FA0-B55572D1572B.

Dandois, J. (2016). "Experimental study of transonic buffet phenomenon on a 3D swept wing". In: Physics of Fluids 28.1. 016101. ISSN: 1070-6631. DOI: 10.1063/1.4937426.

Doggett, R. V., Rainey, A. G., and Morgan, H. G. (1959). An experimental investigation of aerodynamic effects of airfoil thickness on transonic flutter characteristics. National Aeronautics and Space Administration.

Dowell, E. (2010). "Some Recent Advances in Nonlinear Aeroelasticity: Fluid-Structure Interaction in the 21st Century". In: 51st AIAA/ASME/ASCE/AHS/ASC Structures, Structural Dynamics, and Materials Conference. DOI: 10.2514/6.2010-3137.

Dowell, E., Edwards, J., and Strganac, T. (2003). "Nonlinear Aeroelasticity". In: Journal of Aircraft 40.5, pp. 857–874. DOI: 10.2514/2.6876.

EASA (2023). Easy Access Rules for Large Aeroplanes (CS-25). URL: http://web.archive.org/web/20080207010024/http://www.808multimedia.com/winnt/kernel.htm.

Frazer, R. A. and Duncan, W. J. (1931). The flutter of monoplanes, biplanes and tail units. Tech. rep. HM Stationery Office.

Gao, C. and Zhang, W. (2020). "Transonic aeroelasticity: A new perspective from the fluid mode". In: Progress in Aerospace Sciences 113, p. 100596. DOI: 10.1016/j.paerosci.2019.100596.

Gao, C., Zhang, W., Li, X., Liu, Y., Quan, J., Ye, Z., and Jiang, Y. (2017). "Mechanism of frequency lock-in in transonic buffeting flow". In: Journal of Fluid Mechanics 818, pp. 528–561. DOI: 10.1017/jfm.2017.120.

Gao, C., Zhang, W., and Ye, Z. (2018). "Reduction of transonic buffet onset for a wing with activated elasticity". In: Aerospace Science and Technology 77, pp. 670–676. DOI: 10.1016/j.ast.2018.03.047.

Giannelis, N. F., Vio, G. A., and Dimitriadis, G. (2016). "Dynamic interactions of a supercritical aerofoil in the presence of transonic shock buffet". In: Proceedings of the 27th International Conference on Noise and Vibration Engineering, Leuven, Belgium. KU Leuven - Departement Werktuigkunde, Heverlee (Belgium), pp. 457–470.

Giannelis, N. F., Levinski, O., and Vio, G. A. (2018). "Influence of Mach number and angle of attack on the two-dimensional transonic buffet phenomenon". In: Aerospace Science and Technology 78, pp. 89–101. DOI: 10.1016/j.ast.2018.03.045.. URL: https://www.researchgate.net/profile/Nicholas-Giannelis/publication/326977265_On_the_effect_of_control_surface_deflections_on_the_aeroelastic_response_of_an_aerofoil_at_transonic_buffet_conditions/links/5b6ee86f92851ca65055d7ba/On-the-effect-of-control-surface-deflections-on-the-aeroelastic-response-of-an-aerofoil-at-transonic-buffet-conditions.pdf.

Giannelis, N. F., Vio, G. A., and Levinski, O. (2017). “A review of recent developments in the understanding of transonic shock buffet”. In: Progress in Aerospace Sciences 92, pp. 39–84. DOI: 10.1016/j.paerosci.2017.05.004.

Gibb, J. (1983). “The cause and cure of periodic flows at transonic speed”. PhD thesis. Cranfield University.

Hartley, R. and Zisserman, A. (2004). Multiple View Geometry in Computer Vision. 2nd ed. Cambridge University Press. DOI: 10.1017/CBO9780511811685.

Hilton, W. F. and Fowler, R. G. (1947). “Photographs of shock wave movement”. In: Aeronautical Research Council Reports & Memoranda (1312). URL: https://naca.central.cranfield.ac.uk/bitstream/handle/1826.2/3237/arc-rm-2692.pdf?sequence=1&isAllowed=y.

Iovnovich, M. and Raveh, D. E. (2012). “Reynolds-Averaged Navier-Stokes Study of the Shock-Buffet Instability Mechanism”. In: AIAA Journal 50.4, pp. 880–890. DOI: 10.2514/1.J051329.

Iovnovich, M. and Raveh, D. E. (2015). “Numerical Study of Shock Buffet on Three-Dimensional Wings”. In: AIAA Journal 53.2, pp. 449–463. DOI: 10.2514/1.J053201.

Isogai, K. (1979). “On the Transonic-Dip Mechanism of Flutter of a Sweptback Wing”. In: AIAA Journal 17.7, pp. 793–795. DOI: 10.2514/3.61226.

Jacquin, L., Molton, P., Deck, S., Maury, B., and Soulevant, D. (2009). “Experimental study of shock oscillation over a transonic supercritical profile”. In: AIAA Journal 47.9, pp. 1985–1994. DOI: 10.2514/1.30190.

Kokmanian, K., Scharnowski, S., Schäfer, C., Accorinti, A., Baur, T., and Kähler, C. J. (2022). “Investigating the flow field dynamics of transonic shock buffet using particle image velocimetry”. In: Experiments in Fluids 63.9. DOI: 10.1007/s00348-022-03499-2.

Korthäuer, T., Accorinti, A., Scharnowski, S., and Kähler, C. J. (2023a). “Effect of Mach Number and Pitching Eigenfrequency on Transonic Buffet Onset”. In: AIAA Journal 61.1, pp. 112–124. DOI: 10.2514/1.j061915.

Korthäuer, T., Accorinti, A., Scharnowski, S., and Kähler, C. J. (2023b). “Experimental investigation of transonic buffeting, frequency lock-in and their dependence on structural characteristics”. In: Journal of Fluids and Structures 122, p. 103975. ISSN: 0889-9746. DOI: https://doi.org/10.1016/j.jfluidstructs.2023.103975. URL: https://www.sciencedirect.com/science/article/pii/S0889974623001433.

Kou, J., Zhang, W., Liu, Y., and Li, X. (2017). “The lowest Reynolds number of vortex-induced vibrations”. In: Physics of Fluids 29.4, p. 041701. DOI: 10.1063/1.4979966.

Lee, B. (2001). “Self-sustained shock oscillations on airfoils at transonic speeds”. In: Progress in Aerospace Sciences 37.2, pp. 147 –196. ISSN: 0376-0421. DOI: 10.1016/S0376-0421(01)00003-3.

Leishman, G. (2022). Introduction to Aerospace Flight Vehicles. Embry-Riddle Aeronautical University. DOI: 10.15394/eaglepub.2022.1066.

Lin, M.-T., Sciammarella, C., Espinosa, H. D., Furlong, C., Lamberti, L., Reu, P., Sutton, M., and Hwang, C.-H. (2020). Advancements in Optical Methods & Digital Image Correlation in Experimental Mechanics, Volume 3. Springer International Publishing. DOI: 10.1007/978-3-030-30009-8.

Mabey, D. (1981). “Oscillatory flows from shock induced separations on biconvex aerofoils of varying thickness in ventilated wind tunnels”. In: Technical Memorandum, Royal Aircraft Establishment.

Mabey, D. (1989). “Buffeting criteria for a systematic series of wings”. In: Journal of Aircraft 26.6, pp. 576–582.

McDevitt, J. B. and Okuno, A. F. (1985). “Static and dynamic pressure measurements on a NACA0012 airfoil in the Ames high Reynolds number facility”. In: NASA Technical Paper. NASA technical paper 2485. URL: https://books.google.de/books?id=m8E5WqGU0MMC.

Nitzsche, J. (2009). “A numerical study on aerodynamic resonance in transonic separated flow”. In: IFASD – International Forum on Aeroelasticity and Structural Dynamics. Seattle, WA, USA. URL: https://elib.dlr.de/61964/.

Nitzsche, J., Otte, J., Kaiser, C., and Hennings, H. (2022). “The Effect of Shock Control Bumps on the the Transonic Flutter and Buffeting Characteristics of a Typical Wing Section”. In: IFASD – International Forum on Aeroelasticity and Structural Dynamics. Madrid, Spain. URL: https://elib.dlr.de/188433/1/IFASD_2022_149.pdf.

Nitzsche, J., Ringel, L., Kaiser, C., and Hennings, H. (2019). “Fluid-mode flutter in plane transonic flows”. In: IFASD – International Forum on Aeroelasticity and Structural Dynamics. Savannah, Georgia, USA. URL: https://elib.dlr.de/128011/.

Pearcey, H. (1958). A method for the prediction of the onset of buffeting and other separation effects from wind tunnel tests on rigid models. Tech. rep. Advisory Group For Aeronautical Research And Development Paris (France). URL: https://apps.dtic.mil/sti/citations/AD0248342.

Poplingher, L., Raveh, D. E., and Dowell, E. H. (2019). “Modal analysis of transonic shock buffet on 2D airfoil”. In: AIAA Journal 57.7, pp. 2851–2866. DOI: 10.2514/1.j057893.

Raffel, M. (2015). “Background-oriented schlieren (BOS) techniques”. In: Experiments in Fluids 56.3. DOI: 10.1007/s00348-015-1927-5.

Raffel, M., Willert, C. E., Scarano, F., Kähler, C. J., Wereley, S. T., and Kompenhans, J. (2018). Particle Image Velocimetry. Springer International Publishing. DOI: 10.1007/978-3-319-68852-7.

Raghunathan, S., Early, J., Tulita, C., Benard, E., and Quest, J. (2008). “Periodic transonic flow and control”. In: The Aeronautical Journal (1968) 112.1127, 1–16. DOI: 10.1017/S0001924000001949.

Raveh, D. and Dowell, E. (2011). “Frequency lock-in phenomenon for oscillating airfoils in buffeting flows”. In: Journal of Fluids and Structures 27.1, pp. 89–104. DOI: 10.1016/j.jfluidstructs.2010.10.001.

Rooij, A. van (2017). “Aeroelastic Limit-Cycle Oscillations resulting from Aerodynamic Non-Linearities”. PhD thesis. Delft University of Technology. DOI: 10.4233/uuid:cc2f32f8-6c6f-4675-a47c-37b70ed4e30c.

Rory Bigger, and et al. (2018). A Good Practices Guide for Digital Image Correlation. Tech. rep. DOI: 10.32720/idics/gpg.ed1.

Sartor, F., Mettot, C., and Sipp, D. (2015). “Stability, receptivity, and sensitivity analyses of buffeting transonic flow over a profile”. In: AIAA Journal 53.7, pp. 1980–1993. DOI: 10.2514/1.j053588.

Scarano, F. (2003). “Theory of non-isotropic spatial resolution in PIV”. In: Experiments in Fluids 35.3, pp. 268–277. DOI: 10.1007/s00348-003-0655-4.

Scarano, F. and Riethmuller, M. L. (2000). “Advances in iterative multigrid PIV image processing”. In: Experiments in Fluids 29.7, S051–S060. DOI: 10.1007/s003480070007.

Scharnowski, S., Accorinti, A., Korthäuer, T., and Kähler, C. J. (2023). “Comparison of shock-buffet dynamics on a supercritical airfoil with andwithout a pitching degree of freedom”. In: Reviewing process of CEAS Aeronautical Journal.

Scharnowski, S., Bross, M., and Kähler, C. J. (2018). “Accurate turbulence level estimations using PIV/PTV”. In: Experiments in Fluids 60.1. DOI: 10.1007/s00348-018-2646-5.

Scharnowski, S., Kokmanian, K., Schäfer, C., Baur, T., Accorinti, A., and Kähler, C. J. (2022). “Shock-buffet analysis on a supercritical airfoil with a pitching degree of freedom”. In: Experiments in Fluids 63.6. DOI: 10.1007/s00348-022-03427-4.

Scharnowski, S., Sciacchitano, A., and Kähler, C. J. (2019). “On the universality of Keane & Adrian’s valid detection probability in PIV”. In: Measurement Science and Technology 30.3, p. 035203. DOI: 10.1088/1361-6501/aafe9d.

Schauerte, C. J. and Schreyer, A.-M. (2023). “Experimental Analysis of Transonic Buffet Conditions on a Two-Dimensional Supercritical Airfoil”. In: AIAA Journal, pp. 1–17. DOI: 10.2514/1.j062349.

Scheitle, H. and Wagner, S. (1991). “Influences of wind tunnel parameters on airfoil characteristics at high subsonic speeds”. In: Experiments in Fluids 12-12.1-2, pp. 90–96. DOI: 10.1007/bf00226571.

Schewe, G, Mai, H, and Dietz, G (2003). “Nonlinear effects in transonic flutter with emphasis on manifestations of limit cycle oscillations”. In: Journal of Fluids and Structures 18.1, pp. 3–22. DOI: 10.1016/S0889-9746(03)00085-9.

Schlichting, H. and Gersten, K. (2006). Grundzüge Der Grenzschicht-Theorie. Springer.

Schreier, H., Orteu, J.-J., and Sutton, M. A. (2009). Image Correlation for Shape, Motion and Deformation Measurements. Springer New York, NY. ISBN: 978-1-4419-4622-5. DOI: 10.1007/978-0-387-78747-3.

Soloff, S. M., Adrian, R. J., and Liu, Z.-C. (1997). “Distortion compensation for generalized stereoscopic particle image velocimetry”. In: Measurement Science and Technology 8.12, pp. 1441–1454. DOI: 10.1088/0957-0233/8/12/008.

Sugioka, Y., Kouchi, T., and Koike, S. (2022). “Experimental comparison of shock buffet on unswept and 10-deg swept wings”. In: Experiments in Fluids 63.8. DOI: 10.1007/s00348-022-03482-x.

Sutton, M., Wolters, W., Peters, W., Ranson, W., and McNeill, S. (1983). “Determination of displacements using an improved digital correlation method”. In: Image and Vision Computing 1.3, pp. 133–139. ISSN: 0262-8856. DOI: 10.1016/0262-8856(83)90064-1.

Theodorsen, T. (1935). “General Theory Of Aerodynamic Instability And The Mechanism Of Flutter”. In: Annual Report of the National Advisory Committee for Aeronautics 268, p. 413.

Tijdeman, H. (1977). “Investigations of the transonic flow around oscillating airfoils”. In: NLR-TR 77090 U.

Timme, S. (2020). “Global instability of wing shock-buffet onset”. In: Journal of Fluid Mechanics 885. DOI: 10.1017/jfm.2019.1001.

Welch, P. (1967). “The use of fast Fourier transform for the estimation of power spectra: A method based on time averaging over short, modified periodograms”. In: IEEE Transactions on Audio and Electroacoustics 15.2, pp. 70–73. DOI: 10.1109/TAU.1967.1161901.

Willert, C. E. and Gharib, M. (1991). “Digital particle image velocimetry”. In: Experiments in Fluids 10.4, pp. 181–193. DOI: 10.1007/bf00190388.

Wright, J. R. and Cooper, J. E. (2008). Introduction to aircraft aeroelasticity and loads. Vol. 20. John Wiley & Sons.

Zhang, W., Gao, C., Liu, Y., Ye, Z., and Jiang, Y. (2015). “The interaction between flutter and buffet in transonic flow”. In: Nonlinear Dynamics 82.4, pp. 1851–1865. DOI: 10.1007/s11071-015-2282-z.